FACILITY FORM 602
N66-18020
(ACCESSION NUMBER)
177
(PAGES)
(NASA CR OR TMX OR AD NUMBER)
1
(THRU)
(CODE)
28
(CATEGORY)

NASA CR-54746
GE 214-252(Final)

GPO PRICE $ ______

CFSTI PRICE(S) $ ______

Hard copy (HC) 5.00

Microfiche (MF) 1.00

ff 653 July 65

INVESTIGATION OF PLASMA ACCELERATOR (CYCLOTRON RESONANCE PROPULSION SYSTEM)

by

D. B. Miller, G. W. Bethke, and G. F. Crimi

prepared for

NATIONAL AERONAUTICS AND SPACE ADMINISTRATION

contract NAS 3-6266

SPACE SCIENCES LABORATORY
GENERAL ELECTRIC
MISSILE AND SPACE DIVISION

Requests for copies of this report should be referred to

National Aeronautics and Space Administration
Office of Scientific and Technical Information
Attention: AFSS-A
Washington, D. C. 20546

NASA CR-54746
GE 214-252 (Final)

FINAL REPORT

INVESTIGATION OF PLASMA ACCELERATOR
(CYCLOTRON RESONANCE PROPULSION SYSTEM)

by

David B. Miller, George W. Bethke and Giles F. Crimi

prepared for

NATIONAL AERONAUTICS AND SPACE ADMINISTRATION

November 1, 1965

CONTRACT NAS 3-6266

Technical Management
NASA Lewis Research Center
Cleveland, Ohio
Spacecraft Technology Division
Dr. H. G. Kosmahl

GENERAL ELECTRIC COMPANY
SPACE SCIENCES LABORATORY
MISSILE AND SPACE DIVISION
P.O. Box 8555
Philadelphia, Pennsylvania 19101

INVESTIGATION OF PLASMA ACCELERATOR
(CYCLOTRON RESONANCE PROPULSION SYSTEM)

by

David B. Miller, George W. Bethke, and Giles F. Crimi

ABSTRACT

18020

Five different electron-cyclotron-resonance plasma accelerators have been tested. All are of the longitudinal-interaction type, where the r-f propagation vector is parallel to the plasma acceleration direction. Two feature axial injection of the propellant through a hole in the waveguide window; these were shown to have relatively low power efficiency* (< .42), and the window design is apparently weakened by the axial gas injection hole. The other three inject gas through oblique peripheral ports. Solid waveguide walls are used in two of these; the other uses screen waveguide, allowing gas pumping between the window and the injection point. High (up to .79) power efficiencies have been measured for these peripheral-injection accelerators. A thrust stand has been specially built for these accelerators. Preliminary thrust measurements at 912 watts r-f power indicate thrust efficiencies ($T^2/2\,\dot{m}P$) on the order of .4 at 3200 seconds. Mapping of the r-f field indicates that most efficient operation occurs when the r-f/plasma coupling takes place in a region removed from the window; an analytical model results in theoretical correlation with these mappings. Potential probes have been used to verify and measure the charge-separation electric field profile. A multigrid, retarding-potential probe has been used to measure the ion energy distribution.

Author

*Power efficiency = plasma stream power/incident r-f power.

TABLE OF CONTENTS

LIST OF FIGURES

Figure		Page

Figure		Page
46	Dependence of Power Efficiency on Magnetic Field Strength, Xenon, 2 kw, Accelerator-to-Calorimeter Distance 43 cm, #B5 Beryllium Oxide Half-Wavelength Window, Mark IV-S Accelerator	51
47	Power Density Contour Mark IV-S Accelerator Nitrogen, .42 mg/sec, 2 kw, 3840 Gauss Accelerator-to-Array Distance: 70 cm Ambient Pressure ~ 4 x 10^{-5} Torr	53
48	Power Density Profile; Mark IV-S Accelerator; Nitrogen, .42 mg/sec, 2 kw, 3320 Gauss Accelerator-to-Array Distance 70 cm Ambient Pressure ~ 4 x 10^{-5} Torr	53
49	Ion Flux Density Profile Mark IV-S Accelerator Nitrogen, .42 mg/sec, 2 kw, 3320 Gauss, Accelerator-to-Array Distance 70 cm, Ambient Pressure ~ 4 x 10^{-5} Torr	54
50	Typical Emitting Potential Probe Current Response with Accelerator Operating	58
51	Energy Analyser Probe Response Curve. Probe is Located 68 cm from Mark V-L Accelerator, with Probe Electron Repelling Grid Biased at -250 Volts	58
52	Dependence of Power Efficiency on Magnetic Field Strength	60
53	Dependence of Power Efficiency on Magnetic Field Strength	60
54	Power Density Contour Mark V-L Accelerator Argon, .28 mg/sec, 2 kw, 3730 Gauss Accelerator-to-Array Distance 70 cm, Ambient Pressure 2.5 x 10^{-5} Torr	61
55	Power Density Profile Mark V-L Accelerator Argon, .28 mg/sec, 2 kw, 3730 Gauss at Window Accelerator-to-Array Distance 70 cm Ambient Pressure 2.5 x 10^{-5} Torr	62
56	Ion Flux Density Profile Mark V-L Accelerator Argon, .28 mg/sec, 2 kw, 3730 Gauss at Window Accelerator-to-Array Distance 70 cm Ambient Pressure 2.5 x 10^{-5} Torr	62 62
57	Hot Potential Probe Emission Current in Vacuum Tank. No Plasma Present	66
58	Dependence of R-f Probe Signal on Magnetic Field Strength	69
59	Dependence of R-f Probe Signal on Magnetic Field Strength	69
60	Dependence of R-f Probe Signal on Magnetic Field Strength	70
61	Dependence of R-f Probe Signal on Magnetic Field Strength	
62	Exhaust Stream, Mark V-S Accelerator, Xenon 1500 watts r.f. Power; Exhaust Stream is Emerging from the Accelerator on the Left and is Flowing into the Open End of the 10" Diameter Calorimeter on the Right	71
63	Dependence of Power Efficiency on Magnetic Field Strength	73
64	Dependence of Power Efficiency on Magnetic Field Strength	75
65	Dependence of Power Efficiency on Magnetic Field Strength	75
66	Dependence of Power Efficiency on Magnetic Field Strength	76
67	Dependence of Power Efficiency on Magnetic Field Strength	76
68	Dependence of Power Efficiency on Magnetic Field Strength	77

1. SUMMARY

A new test facility, specially designed and built for this study, has been used to test several new types of electron-cyclotron-resonance plasma accelerators. All are of the "longitudinal interaction" type, where the propagation vector is parallel with the plasma acceleration direction and all utilize a circularly polarized TE_{11} mode at 8.35gc in a cylindrical guide which is below cutoff for higher order modes. Specifically, the following models have been evaluated:

Mark IV-L (Axial-injection, long version).
Gas is injected through an axial hole through the waveguide window. R-f probes and calorimeters are located in the accelerator walls. Power efficiency is low. Measured wall power loss is also low, but wall erosion is evident.

Mark IV-S (Axial-injection, short-version).
This accelerator utilizes the same injection scheme as for the Mark IV-L design but is much shorter, with no r-f probes or wall calorimeters. The shorter plasma chamber resulted in no significant increase in efficiency. Wall erosion continued to occur. Several dielectric windows failed, possibly caused by dimensional irregularities in the accelerator but also believed to reveal an inherent structural weakness in this window design. Potential probes, the energy analyser probe and the diode sampling probe array were first tested with this thrustor.

Mark V-L (Peripheral-injection, long-version).
In the Mark V devices, the gas is injected through peripheral holes drilled at an angle through the plasma chamber wall just beyond the waveguide wall. The long version has r-f probes and calorimeters in the plasma chamber wall. Power efficiency was about the same as for the Mark IV accelerators. (Although the diode sampling-probe array indicated power efficiency should be greater than for the Mark V-S accelerator). The wall calorimeters had too much thermal conductance, preventing sensible wall power measurements. Analysis of the r-f probes revealed a complex pattern requiring greater spacial resolution for proper interpretation. The energy analyser probe indicated ion energies less than for the Mark IV-S accelerator.

Mark V-S (Peripheral-injection, short-version).
Gas injection is the same as for the Mark V-L model, but the plasma chamber is much shorter. Ignition problems were solved by a short radial tungsten wire, which apparently reduced the breakdown point sufficiently. Power efficiencies were much better

than for any previous electron cyclotron resonance accelerator, with a high point of .79 and with repeated readings above .6. Initial thrust stand measurements were taken with this accelerator. Although the thrust stand has a number of inadequacies, thrust readings were obtained. Thrust efficiency of approximately .4 and greater at about 3200 second specific impulse were recorded. Extensive probing of the Mark V-S exhaust stream was carried out. The r-f/plasma coupling under most favorable operating conditions was shown to take place relatively far beyond the window. Plasma diamagnetism must be below 3%. Langmuir probes were used to map the potential profile, and a retarding potential energy analyser was employed to measure ion energies. Extrapolation of the potential proportional to magnetic field generally results in potential differences somewhat greater than measured ion energies.

Mark VIII (Screen waveguide)

The plasma chamber in this model is formed by a copper screen cylinder jutting out into the vacuum chamber. Gas is injected from peripheral tubes terminating some distance beyond the window (the Mark V window is used). This allows pumping between the window and the injection point, reducing the gas density next to the window and therefore hopefully reducing power passing from the plasma to the window. Although no direct measure of window heating was made, the power efficiency was found to be quite high (up to ~ .65). Erosion of the copper screen was noted.

In order to interpret r-f probe measurements as well as to obtain necessary information for proper evaluation of reflection coefficient data, analysis of a theoretical model has been carried out. In this model, a cylindrical waveguide having the same diameter as the experiment was assumed to be filled with a plasma whose electron density has an exponential position dependence. The experimental magnetic field contour was assumed, and the Doppler broadening process was taken as the damping mechanism. Plots of r-f electric field correlate well with experimental results. Reflection coefficient as a function of frequency was also calculated.

In summary it can be stated that considerable progress has been made during this contract year. Power efficiencies are higher. A thrust stand has been operated and has revealed that total thrust efficiency and specific impulse are in interesting ranges. Diagnostics and theoretical correlation have unveiled many of the important operating mechanisms and characteristics of this type of accelerator. Finally, new accelerator designs have shown promise.

Continued effort should be made on improvement of the accelerator configuration and of the thrust measurement. The mass flow metering technique should also receive careful attention. In addition, thrust and mass flow data should be corroborated by further ion energy analysis. This ion energy should in turn be confirmed by more quantitative potential profile mapping in order to verify basic operating principles. Direct measurement of the electron density and energy profiles should also be made for further revelation of basic mechanisms. Permanent magnet methods should be explored to replace the present electromagnet. Finally, more practical propellants, such as liquid metals, must be employed.

2. INTRODUCTION

Use of an electron-cyclotron-resonance, magnetic-expansion, plasma accelerator for space propulsion purposes was to our knowledge first proposed in late 1960 by General Electric (Reference 1). This proposal was accepted by NASA, who has continued to sponsor this work since 1961 (References 2, 3, 6, 8, 12, 15, 16, 21, 24). Independently, workers at RCA began development of a similar scheme soon thereafter (References 7, 11, 18, 20, 23). French researchers at Centre d'Etude de Saclay have been working on this type of plasma accelerator at least since 1963 for controlled thermonuclear reaction (fusion) purposes (References 9, 10, 13, 17, 22). An Oak Ridge National Laboratories group has made significant advancements in electron cyclotron heating for fusion (References 4, 5, 14), although their techniques do not directly involve macroscopic acceleration. Recently it has come to our attention that the Russians are also interested in this heating process (Reference 19).

Prior to this year's effort, three years of study by General Electric under NASA contract had been spent on the electron cyclotron resonance accelerator (see Final Reports, References 2, 6, 15). During these earlier periods, the basic operating principles were considered theoretically, steady-state c-w acceleration was experimentally accomplished at medium power (320 watts, S-band), an X-band c-w experiment was brought into service and used for high power (>4 kw, cw), steady-state (>250 seconds continuous), high power efficiency* (>.50) tests, and space propulsion applications were investigated.

Because of the favorable efficiency as well as the possibility of unique space mission applications, this fourth year of development was authorized. The objectives of this year's program have essentially been two-fold, first, to improve operating efficiency, and, second, to obtain a more complete measurement of the thrustor characteristics, especially measurements which would independently corroborate the earlier power efficiency result.

This report will first describe the experimental equipment: facilities, accelerators and diagnostics techniques. Results to date will then be presented for each accelerator. Finally, analysis of a theoretical model used to interpret measurements will be discussed.

*Power efficiency = plasma stream power/incident r-f power.

3. EXPERIMENTAL EQUIPMENT

3.1 TEST FACILITY

The experimental work for this contract is being carried out in a new Test Facility, financed by General Electric facility funds. This facility, shown in the accompanying photographs and diagram (Figures 1, 2 and 3) has the following specifications:

vacuum tank: 4' diameter, 6' long, full-sized hinged doors each end, stainless steel.

pumping system: (2) oil diffusion pumps, each rated at 18,000 liters per second; estimated total pumping capacity (taking into account flow resistance due to right angle valves and baffles) is 9000 liters per second (20,000 liters per second without the baffles).

ultimate attained pressure: 1.6×10^{-7} mm Hg (without liquid nitrogen in baffles).

high voltage power supply: 12.5 - 16 k v d c, 3 amperes maximum. (three phase full-wave bridge circuit).

3.2 THRUSTORS

New accelerator designs are shown in Figures 4 - 11. Continuing the accelerator designation system begun for X-band accelerators during Contract NAS3-3567, these will be referred to as the Marks IV-VIII designs.

The Mark IV-L thrustor (Figures 4-6; the L designation indicating the long version) is an axial-injection configuration in which the propellant gas is injected from a pressure chamber into the plasma acceleration chamber through a small diameter hole drilled completely through the ceramic dielectric window. The smallest hole which the window vendor was able to put through these ceramic pieces was approximately .015 inches in diameter. In order to reduce the propellant flow to the desired levels, however, the pressure chamber had to be held down at such a low pressure ($\sim$ 50 torr absolute) that a shielding (and damaging) discharge formed in this interwindow region. This undesirable phenomenon was cured by filling the original .015 gas hole with a high-temperature, electrically-insulating cement (Sauereisen type DW-30), leaving a small ($<$ .001 diameter) through hole. This resulted in interwindow pressures greater than an atmosphere, high enough in general to prevent interwindow discharges, although occasional spurious electrical effects still did take place in this region. These latter phenomena might have been related to behavior of the cement, which was

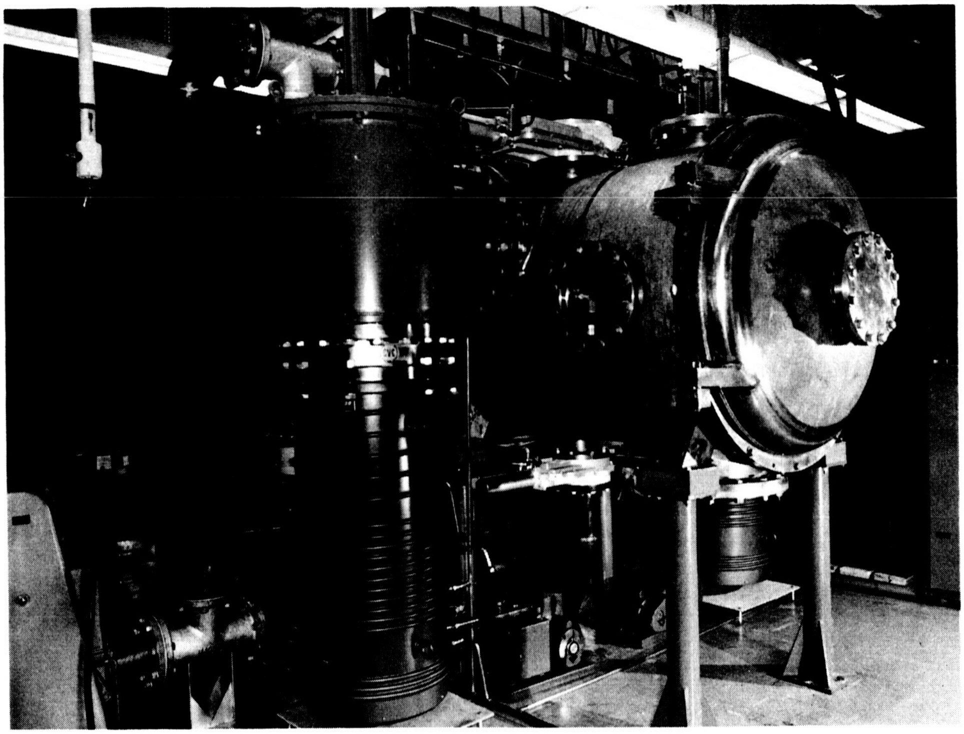

Figure 1. Vacuum Facility

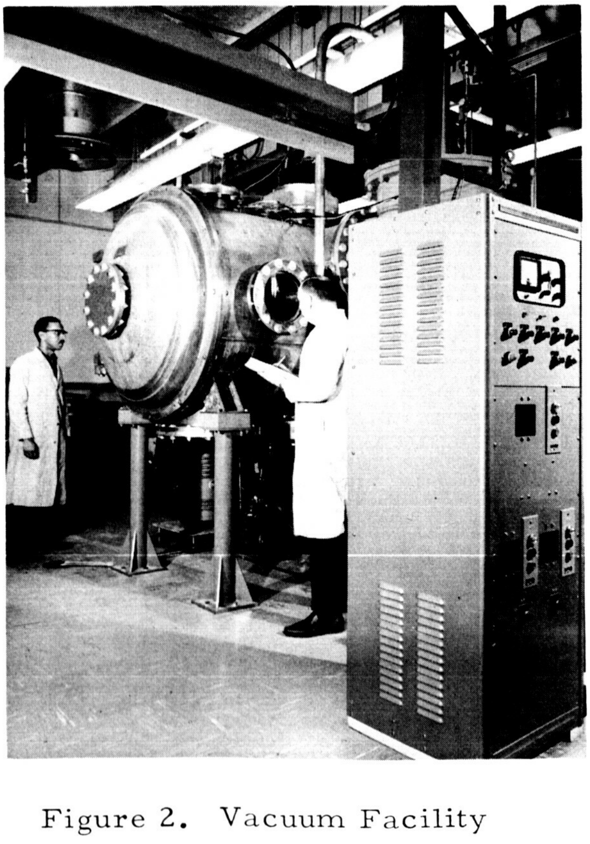

Figure 2. Vacuum Facility

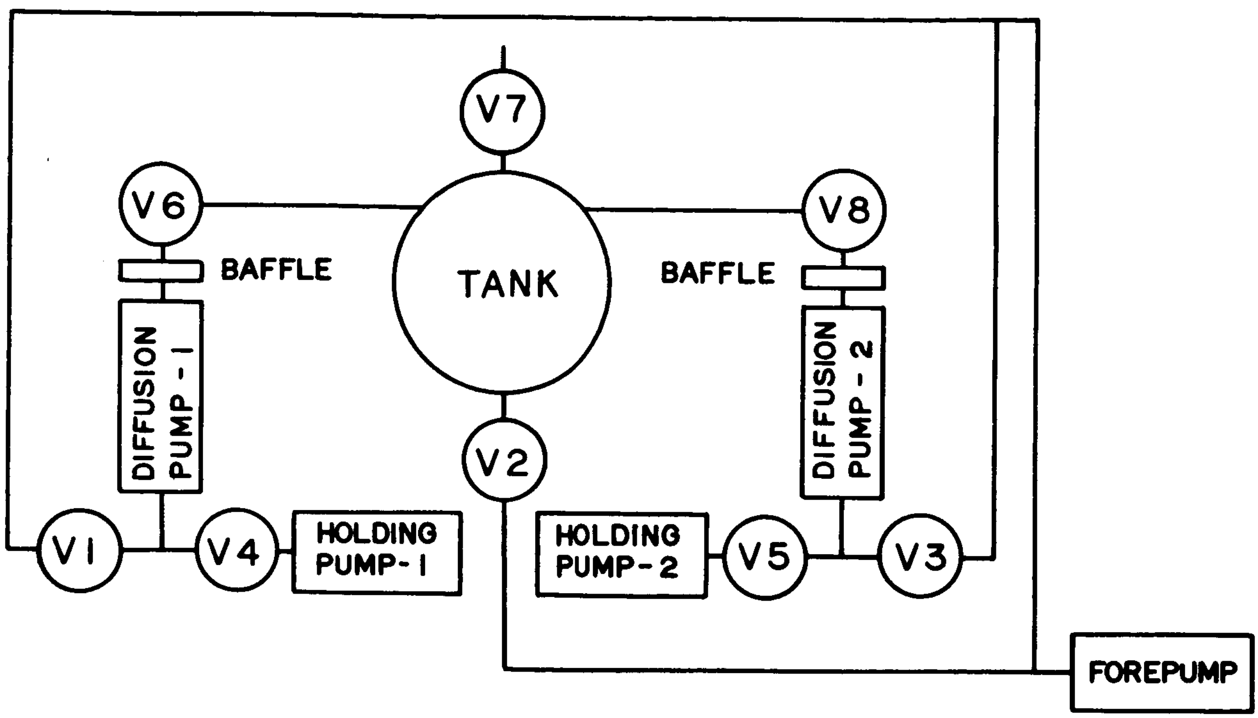

Tank: 4' Dia x 6' Long

Baffles: CVC BC210

Pumps:

Diffusion: CVC PMC 18000
Fore: Stokes 212H
Holding: Welch 1403B

Valves:

V1, V2, V3: 6" Gate, CVC VST 63M2
V4, V5: 2" Gate, CVC VST 23M2
V6, V8: 20" Rt. Angle, CVC VRA 216
V7: 10" Gate, CVC VST 103M2

Figure 3. Vacuum System - Microwave Physics Laboratory

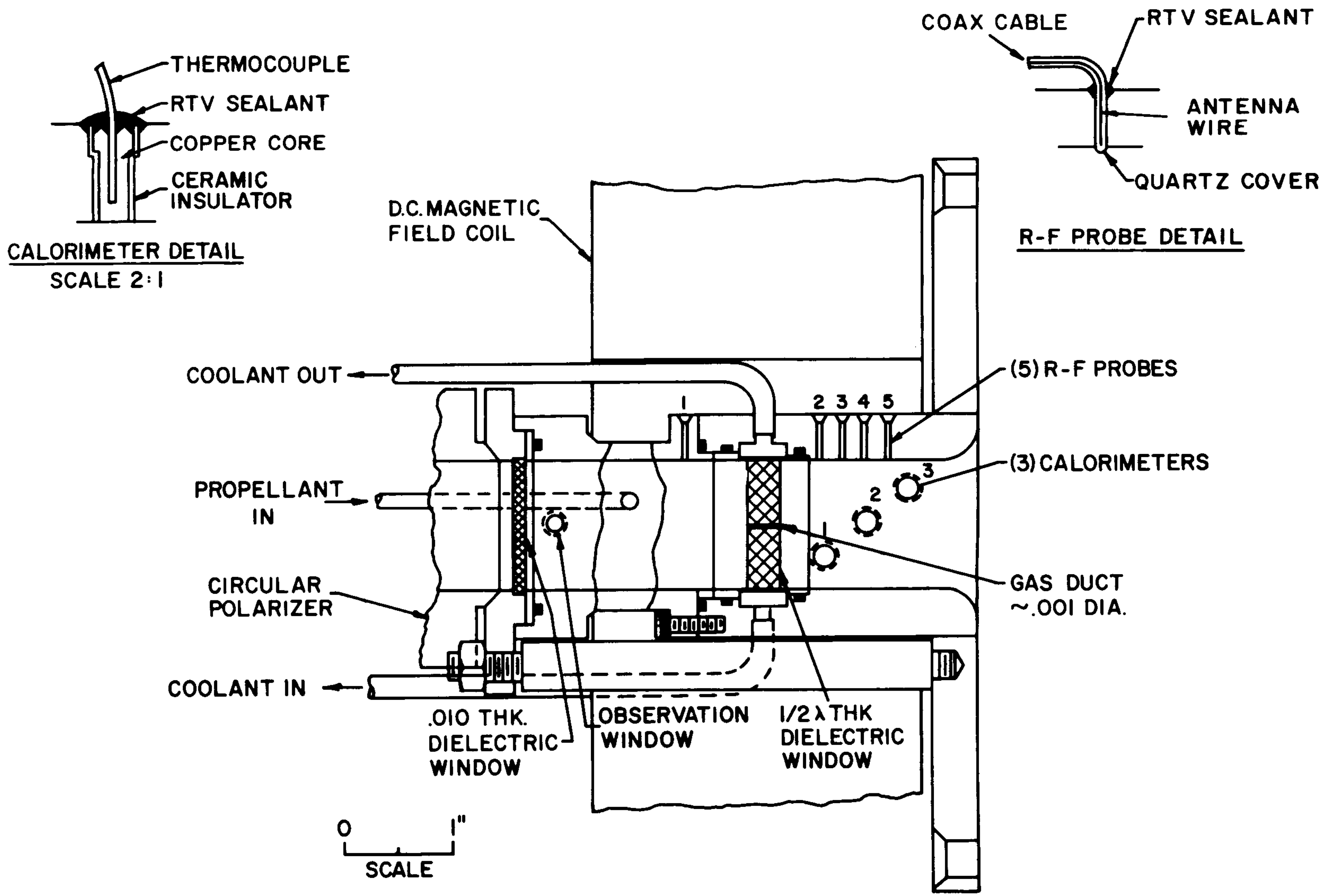

Figure 4. X-Band Longitudinal - Interaction Accelerator; Axial Injection (Mark IV)

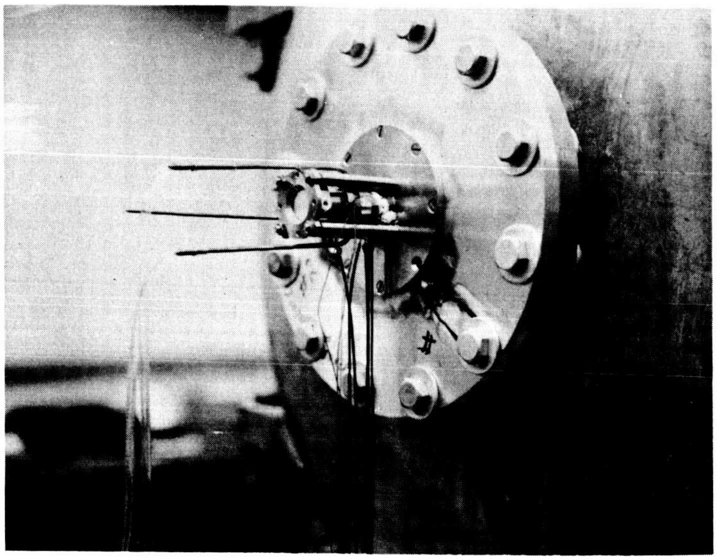

Figure 5. Mark IV (Axial Injection) Accelerator, Mounted on Vacuum Tank

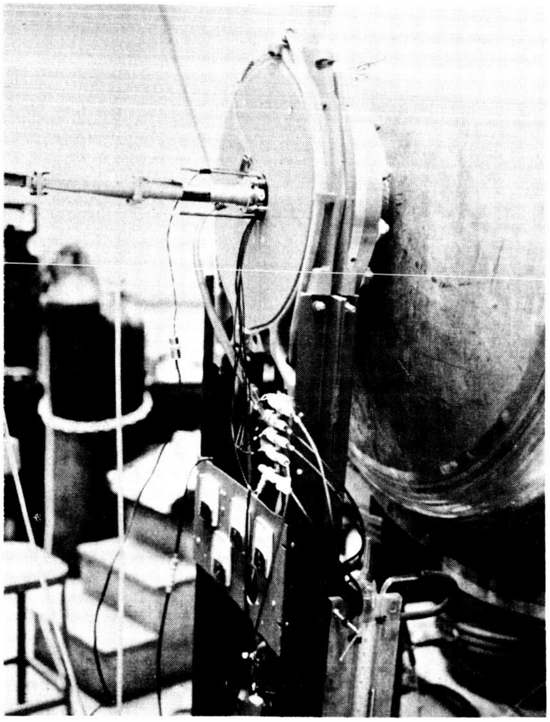

Figure 6. Photograph of Assembled Axial-Injection (Mark IV) Accelerator

observed to exhibit some small amount of reaction to the high-power r-f. Over the course of perhaps 10^3 seconds operation, erosion of the cement, indicated by increased flow for a given pressure, was also observed. Thus if this technique were to be employed in a final engine, a much more satisfactory filling material must be found.

Both high purity alumina and beryllia were employed for the thick ($1/2\lambda$) window in the Mark IV accelerator. Apparently the hole through the window weakened it structurally since in all cases the window eventually developed hairline radial cracks which penetrated through the entire window thickness. The alumina windows failed very rapidly while the beryllia units lasted considerably longer. Note that the window flange was designed with a thin section adjacent to the ceramic and the water cooling. This section was to have been sufficiently flexible to take up any radial strains which might appear in the window, but apparently this measure was inadequate.

The inside diameter of the waveguide through the pressure and plasma chambers is maintained at the 1.152 inch polarizer dimension. Although this results in considerably higher window power density loading than in the two inch diameter Mark I accelerator (see Final Report, NAS3-3567), it is below cutoff for modes above the fundamental TE_{11} mode and so will be less affected by multiple modes and "ghost" modes within the window.

Views of the Mark IV accelerator mounted in operating position on the vacuum tank are shown in Figures 5 and 6.

The short version of the axial injection accelerator (Mark IV-S) is identical with the unit shown in Figure 4 except that the plasma chamber (between the $1/2\lambda$ window and the right-hand exit plane) has been shortened to one inch. In addition, the wall calorimeters and r-f probes have been eliminated, and the plasma chamber is made of stainless steel rather than copper.

The Mark V-L accelerator is shown in Figure 7. In this geometry a single solid dielectric window is used, and the propellant gas is injected peripherally through six angling holes in the plasma chamber wall just on the vacuum side of the window. The same 1.152 inch inside diameter is employed as for the Mark IV design. The short version (Mark V-S), shown in Figure 8 again has a one-inch-long stainless steel plasma chamber without probes and wall calorimeters.

Alumina, beryllia and sapphire windows have been used with the Mark V accelerators, the latter (sapphire) being only 0.10 inch thick, while the ceramic windows are one-half wavelength thick. The alumina windows were again noted to crack under any significant plasma loading (e.g., 1 kw)

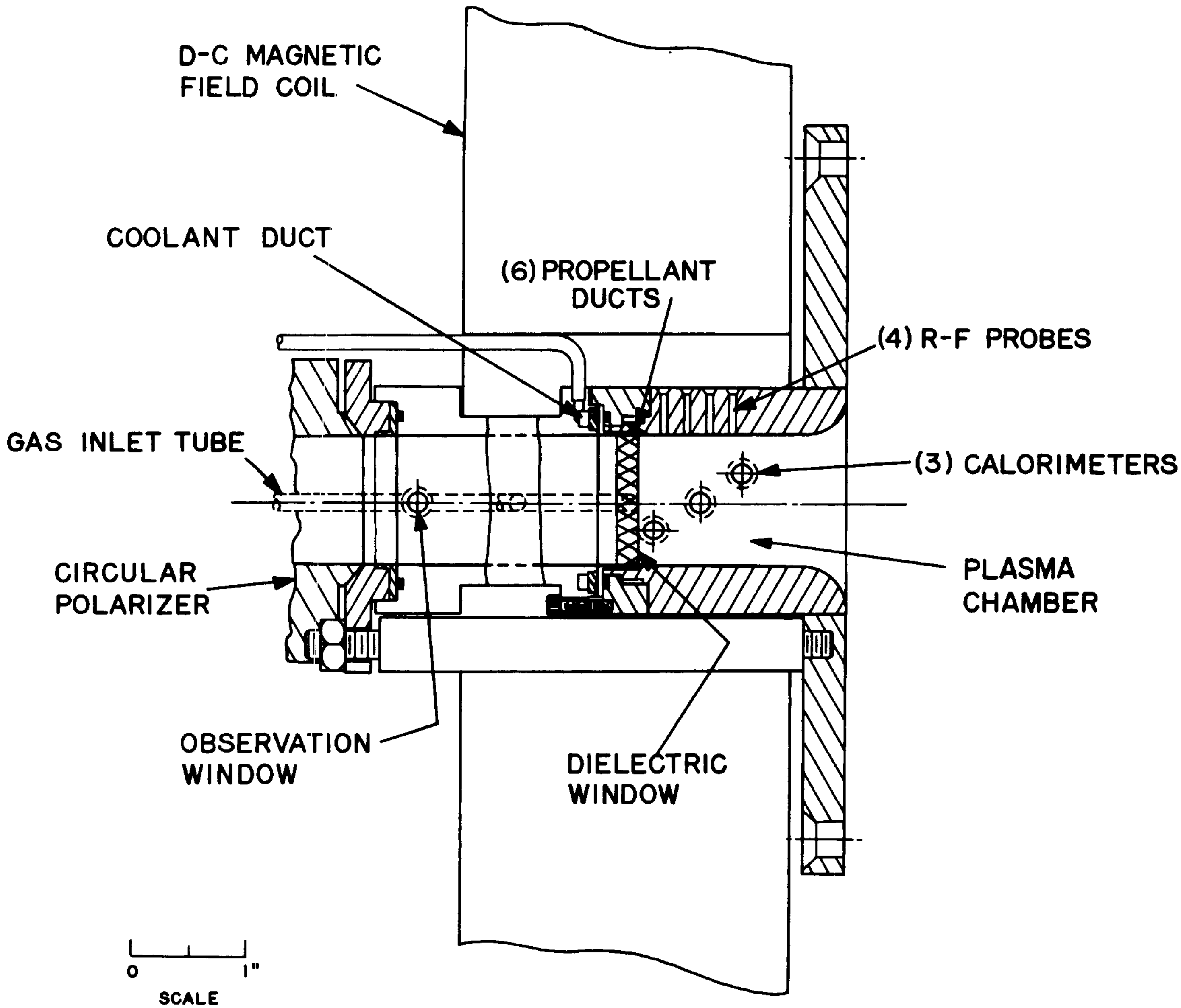

Figure 7. X-Band Longitudinal-Interaction Accelerator; Peripheral Injection, Long Version (Mark V-L)

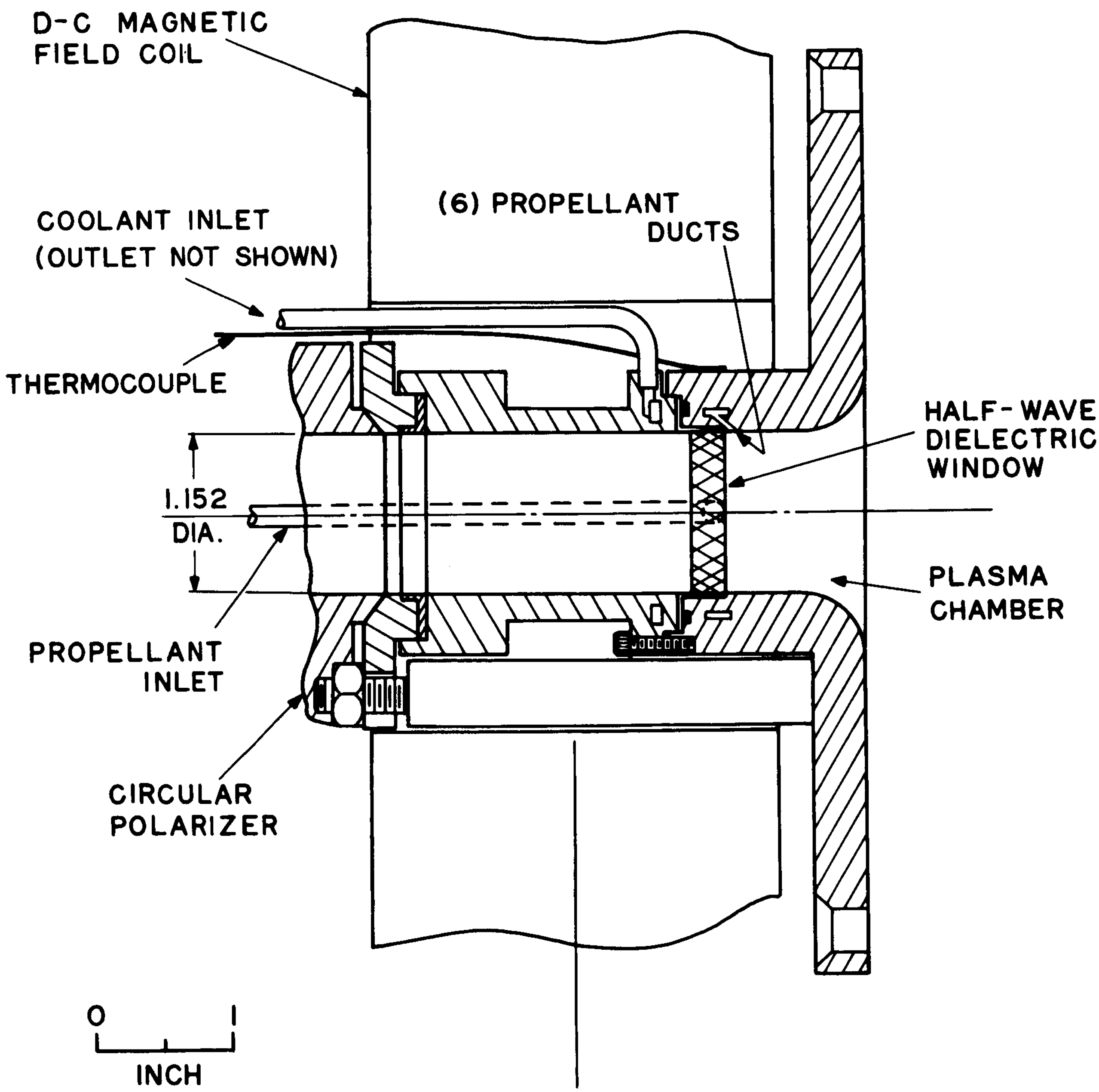

Figure 8. X-Band Longitudinal-Interaction Accelerator; Peripheral Injection; Short Version (Mark V-S)

as did the sapphire design. Extensive testing has been performed with eight beryllia windows, failures occurring only when the window temperature* was allowed to rise too high.

The Mark VI Thrustor, shown in Figure 9 uses the Mark V window but expands to a larger diameter plasma chamber in hopes of reducing wall loss. The length of chamber is also adjustible in order to determine optimum accelerator length. This unit has been built but not yet tested.

A Mark VII design has been constructed but also not yet tested. This is essentially the same as the Mark V-S design except that a boron nitride window is used.

The Mark VIII accelerator is shown in Figures 10 and 11. Note that the Mark V window is again employed but that the injection point is quite far away from the window. This is done in order to reduce the window heating by removing the plasma from the region immediately adjacent to the window. Using copper screen to guide the r-f wave allows pumping between the window and the injection point so that the gas density and plasma density in this region will indeed be low.

3.3 MAGNETIC FIELD

A single coil (Magnion "plasma flux" coil, type PF3-285-175) is used with these accelerators. The resulting on-axis field distribution is plotted in Figure 12. A three-phase bridge rectifier circuit has been built to supply the d-c (up to 292a, 88 v) for this coil.

3.4 R-F SYSTEM

The r-f system to generate the microwave power is shown in Figure 13. Note that the input r-f power to the accelerator is continuously monitored by a calorimetric power meter. The system, with this power meter, has also been operated into a calibrated water load/calorimeter (Varian, Model V-4045F, Ser. #19), comparing the two absolute power meters up to 5 kw. Using the measured value for the DBH631 30 db directional coupler (29.6 db at 8.35 gc), the HP434A calorimetric power meter was found to read accurately within 5% up to 5000 watts. The polarizer is a special unit built by DeMornay-Bonardi Company, designed for 8.35 gc. The radiation pattern is still measured to have ellipticity, however, as discussed in Appendix IV. A photographic view of the overall system is shown in Figure 14.

3.5 REFLECTION COEFFICIENT

A pair of thermistor power meters in a standard waveguide reflectometer arrangement (see Figure 13) is used to compare incident and reflected power. In addition, these two powers are chart recorded continuously during each run using crystal detectors. In all tests, the tuner is used to minimize

* A thermocouple is located in the plasma chamber wall adjacent to the window flange.

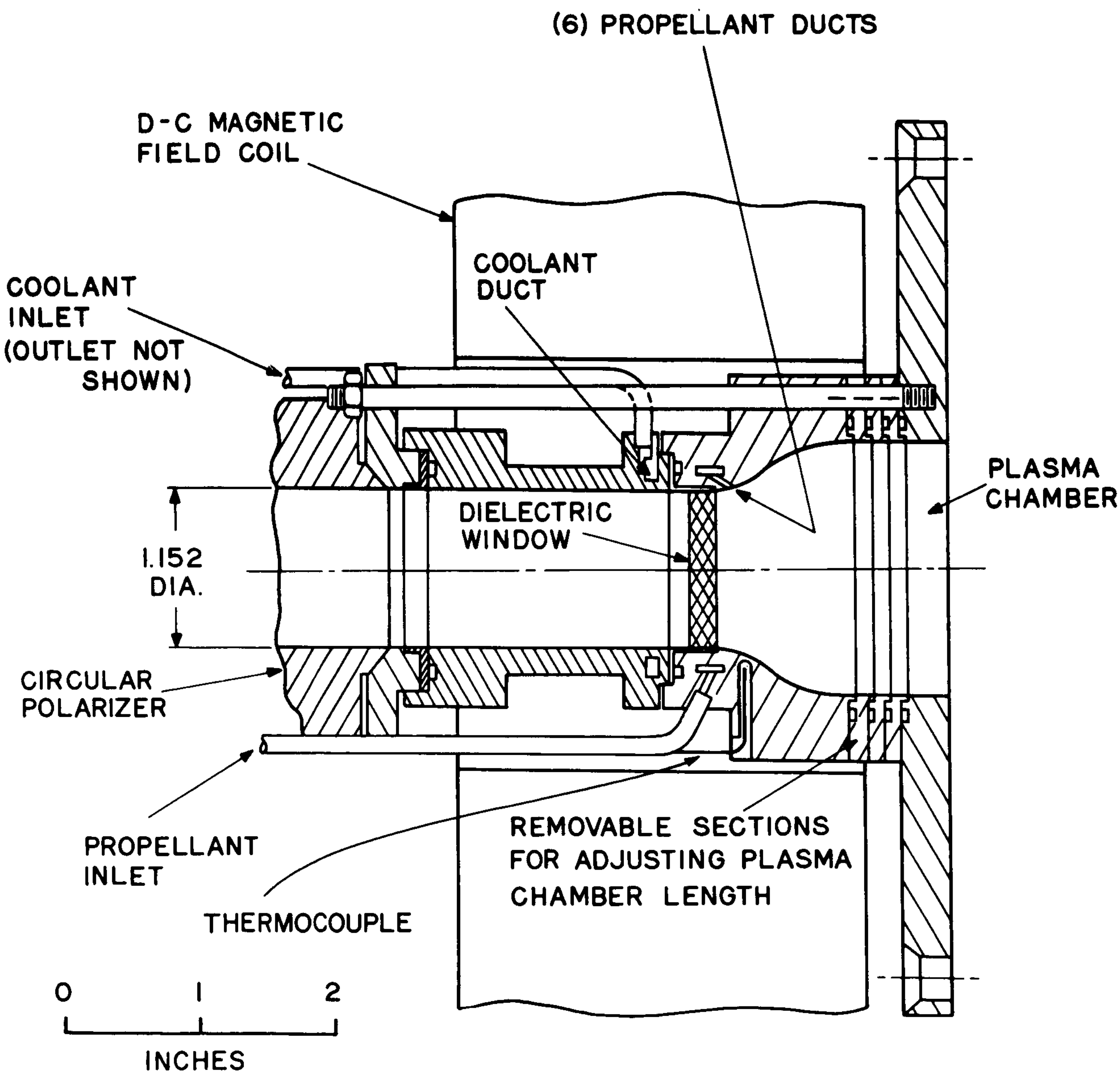

Figure 9. X-Band Plasma Accelerator - Mark VI, with Expanded Adjustible Plasma Chamber

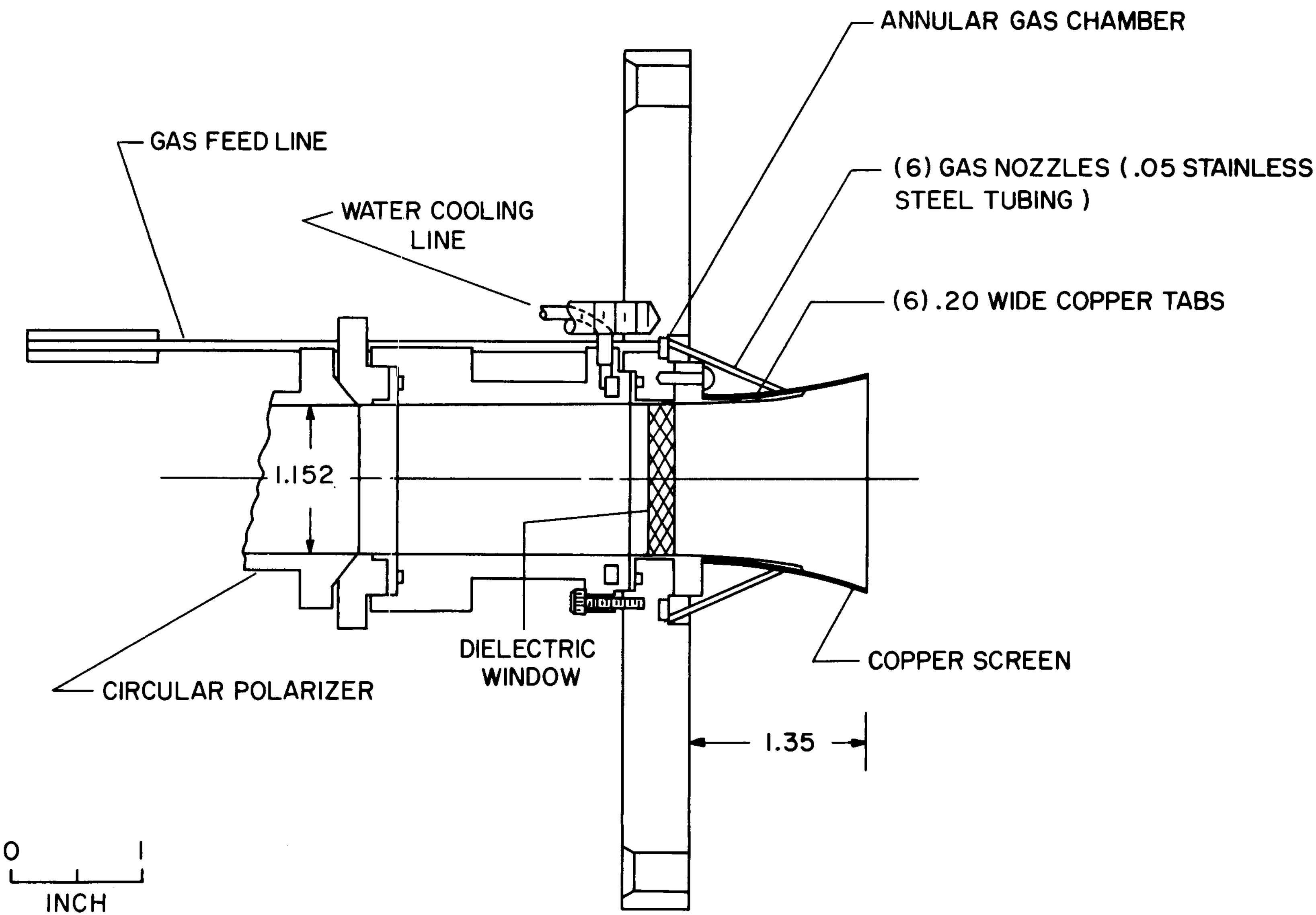

Figure 10. X-Band Screened-Waveguide Accelerator (Mark VIII)

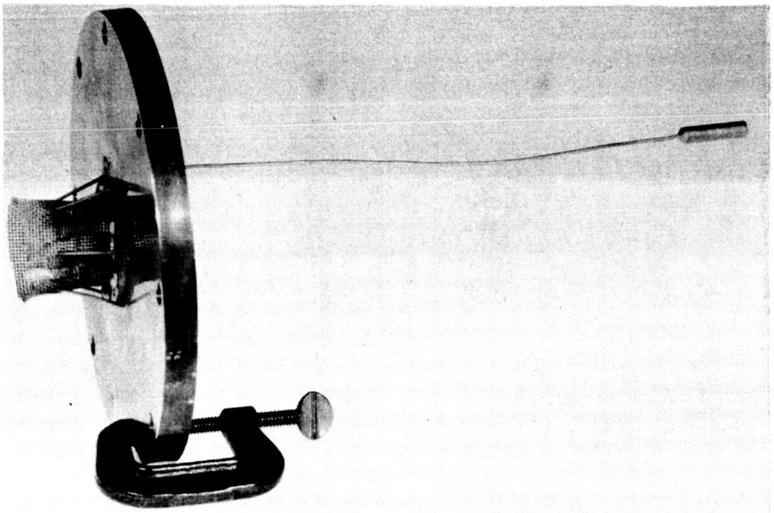

Figure 11. Mark VIII Accelerator

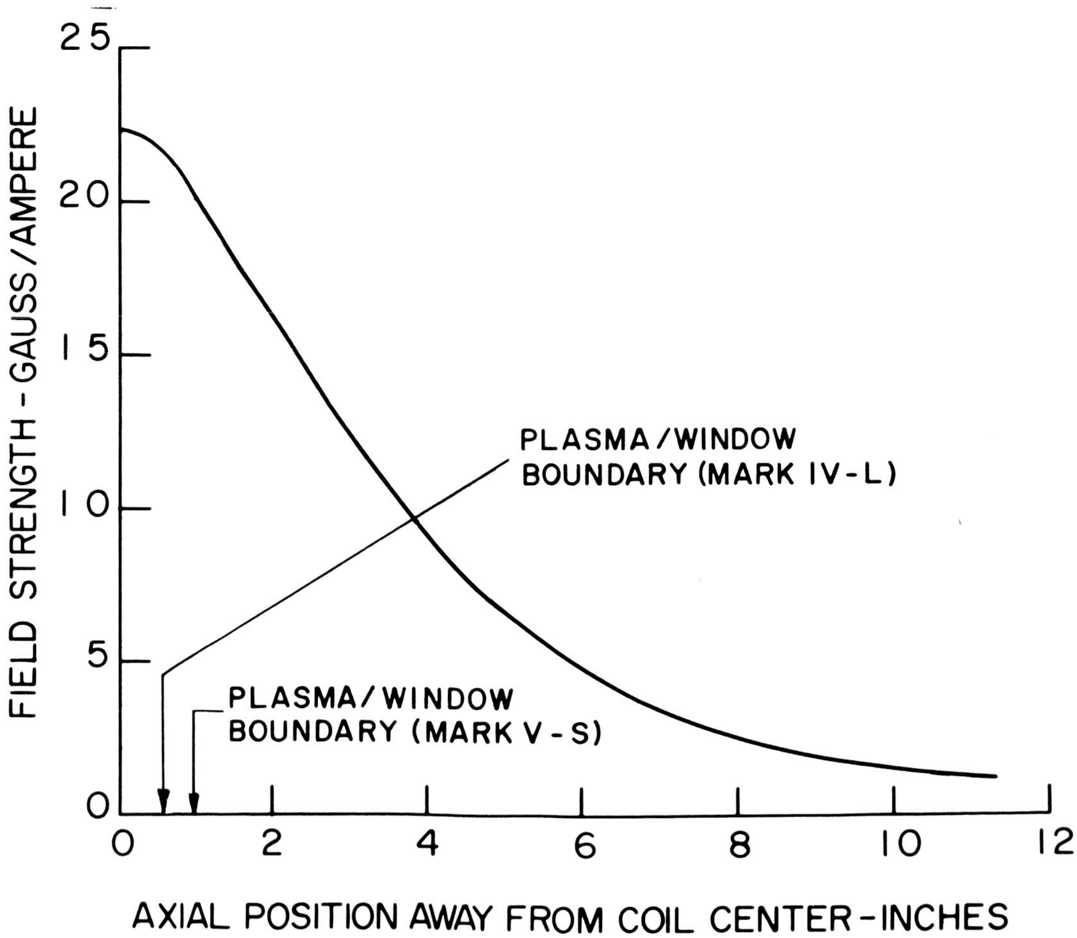

Figure 12. Magnetic Field Distribution on Axis; Magnion "Plasma Flux" Coil, Type PF3-285-175.

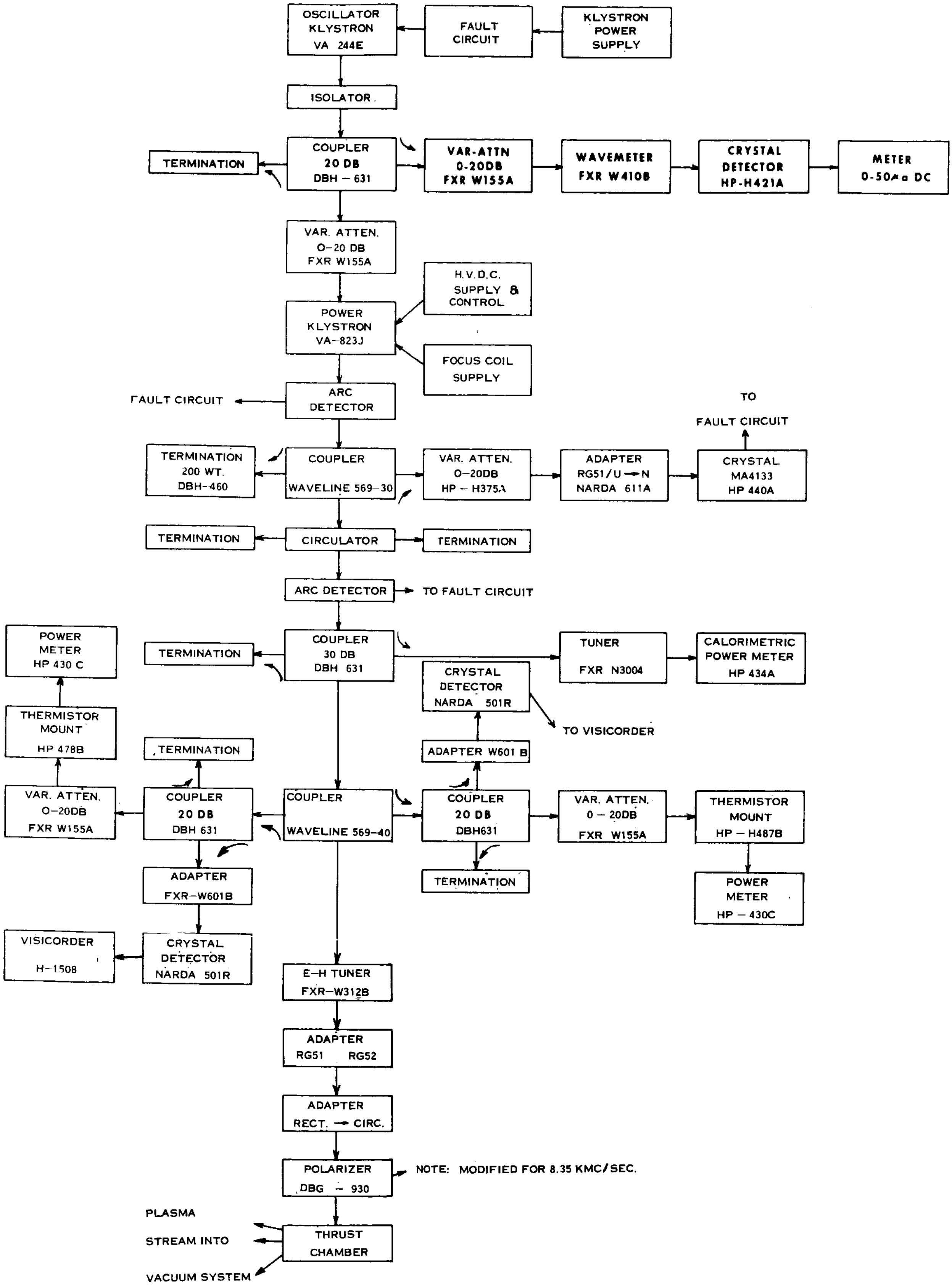

Figure 13. R-f System, Microwave Magnetic Accelerator, 8.35 kmc/sec.

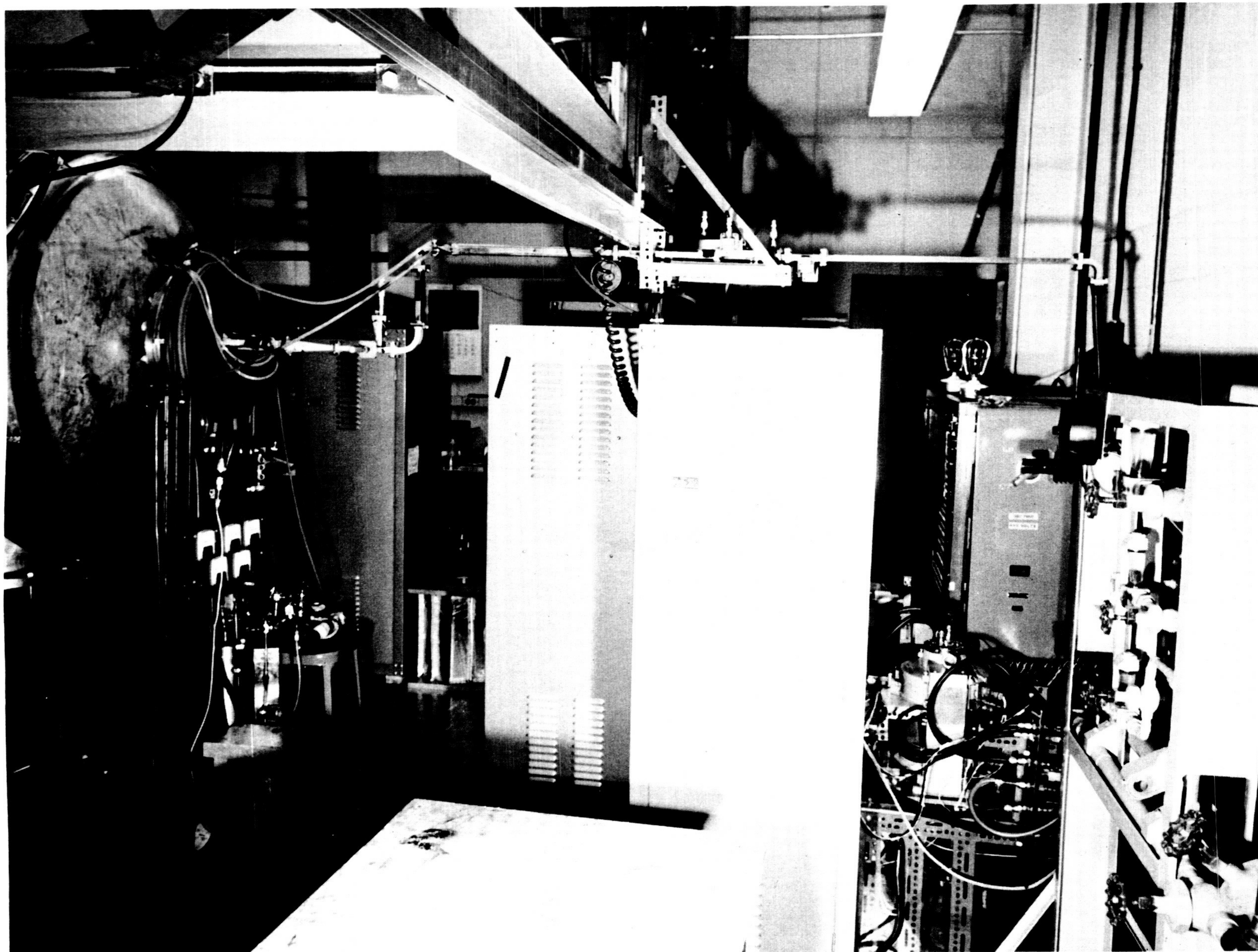

Figure 14. Photographic View of R-f System, Showing Source on the Right and Accelerator on the Left

the power appearing in the reflected wave traveling back toward the klystron. Because this reflectometer is located several waveguide feet back from the accelerator, power lost in heating the walls of the connecting waveguide is not taken into account either in determining power incident on the plasma or in determining the plasma reflection coefficient. Since losses along such a waveguide are generally small, this inaccuracy should also be small.

3.6 R-f PROBES (FIXED AND MOVABLE)

R-f probes located in the accelerator walls (see Figures 4 and 7) respond to the r-f electric field in the vicinity of the probe. The induced signal is rectified through a crystal detector and then recorded on the chart recorder. These probes will behave much like the moving probe in a slotted standing wave detector, and the separate probe signals must be interpreted as responding at any instant to the standing wave pattern existing within the accelerator at that instant. It must be remembered, however, that this wave pattern will exist within a lossy medium (plasma) so that the field strength will ultimately go to zero as depth within the plasma increases. Although an attempt was made to make all probes as identical as possible, they will not have identical sensitivities and so will have to be calibrated before they can be used on a comparative basis.

In order to overcome the difficulties discussed above, the movable r-f probe shown in Figure 15 was installed. Since this is a single probe, there is now no problem of probe dissimilarity. It also measures continuously with axial position through <u>and beyond</u> the plasma diameter. Finally, it is applicable to all accelerators, eliminating the need for installing probes in the accelerator walls.

3.7 WALL CALORIMETERS

Three button calorimeters are located in the plasma chamber walls of the Mark IV-L and Mark V-L accelerators as shown in Figures 4 and 7. Construction details are shown in Figure 4. These calorimeters are not sufficiently insulated so that they continue to gain temperature throughout a test, but rather they rapidly attain an equilibrium temperature indicative of the power incident on them from the plasma. This power may be calculated from the cooling curve:

$$\Delta T = \Delta T_o \, e^{-t/\tau}$$

where ΔT is the temperature (relative to ultimate) at time t, and ΔT_o is the initial temperature at t = 0.

The time constant τ is found to be different for each calorimeter and to be somewhat a function of temperature but is approximately 30 seconds. From

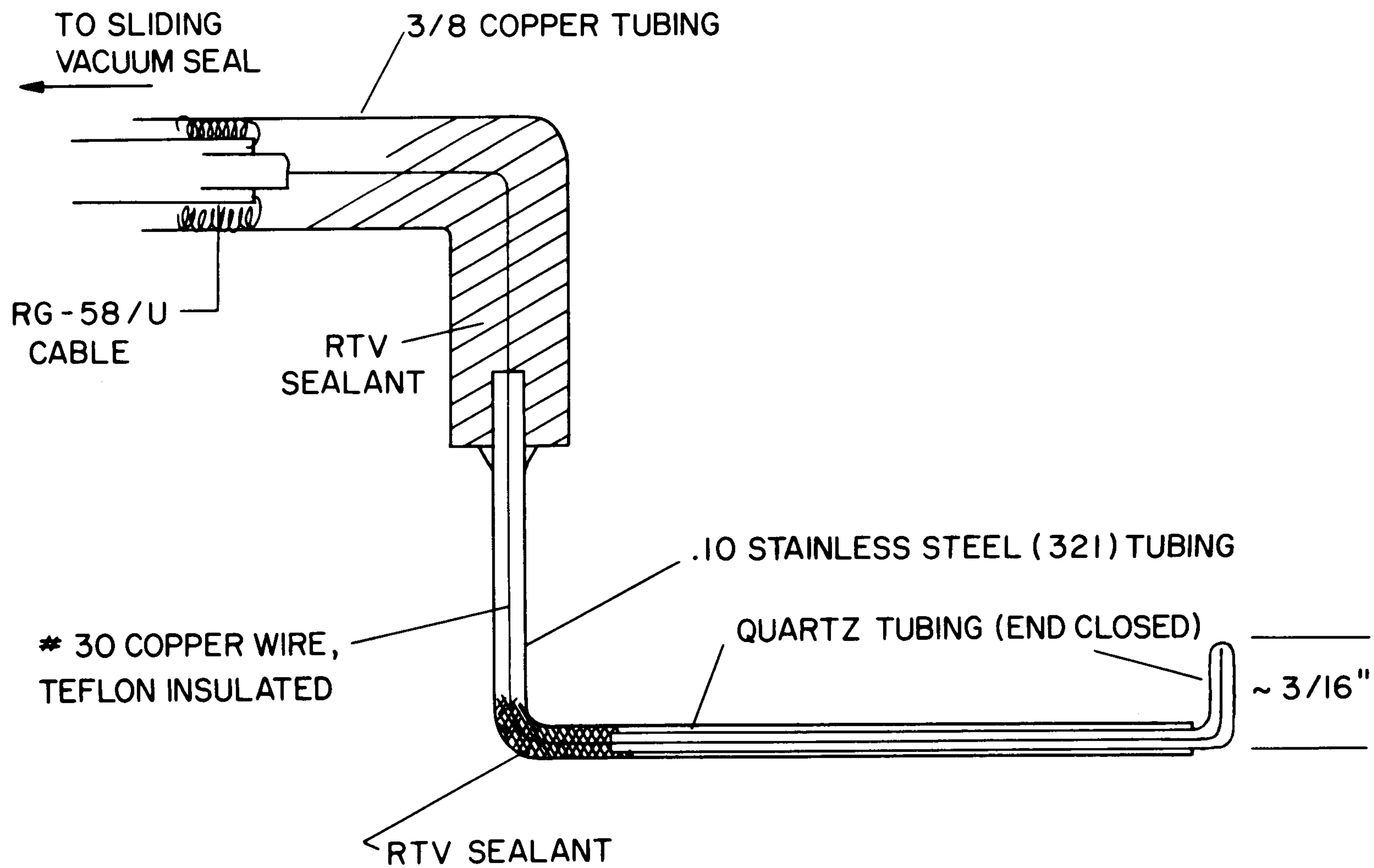

Figure 15. Movable R-f Probe

the cooling expression, the power being lost at any temperature (and therefore the absorbed power) can be derived as:

$$P = -\frac{\sigma M}{\tau} \Delta T$$

where σ is the specific heat (~ .09 cal/gm - $^{\circ}$C for copper) and M is the mass of the calorimeter. Since the calorimeters have a mass of .77 gm, this amounts to a power loss of about .97 watt from each calorimeter per 100°C calorimeter temperature (ΔT). Converting this to power density by dividing by the known exposed area of the calorimeters (.31 cm^2) and then multiplying by the accelerator wall area (41 cm^2) yields a power of about 1.3 watts going to the accelerator walls per 1° C ΔT.

3.8 TOTAL CALORIMETERS

Measurement of the total power carried by the accelerated plasma stream is a relatively simple, accurate and revealing technique. The plasma is impinged on a collector, which, if properly designed, receives essentially all of the plasma energy. The heating rate of the calorimeter, or the steady state temperature rise of a metered calorimeter coolant flow, then yields power. One must take care that the total plasma power is transferred to the calorimeter rather than being carried away by reflected particles, although this is a relatively easy criterion to meet. Radiation and conduction may also carry significant power away from the collector. Interpretation of the measurement is not as simple, however, since <u>total</u> plasma power is measured, including excitation and ionization energies, energy in transverse particle motion and energy in oscillatory motion. Estimates and independent measurements aid in evaluating the relative importance of these quantities.

The first total calorimeter used this year is the 2 ft diameter by 10 in deep one shown in Figure 16. This is water cooled so that steady-state power measurements are made. It is mounted on a movable shaft and platform so that the plasma power can be measured as a function of distance away from the accelerator.

The inlet and outlet water temperatures are measured with electrically insulated thermocouples immersed in the water lines at points a few inches before entry into and after emergence from the calorimeter collector. Ice baths are used for the reference junctions. A millivolt recorder (Leeds and Northrup "Speedomax" or Photovolt "Microcord") is used to measure and record the thermocouple e.m.f., as shown in Figure 17. Note that, at a water flow rate of 1500 cc/min, the calorimeter has a time constant of approximately one minute.

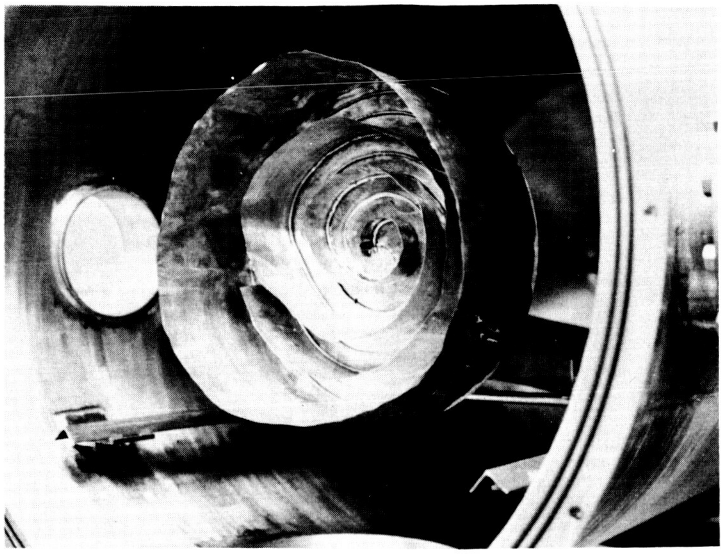

Figure 16. 2ft Diameter x 10'' Deep Total Calorimeter Mounted on Movable Base in Vacuum Tank

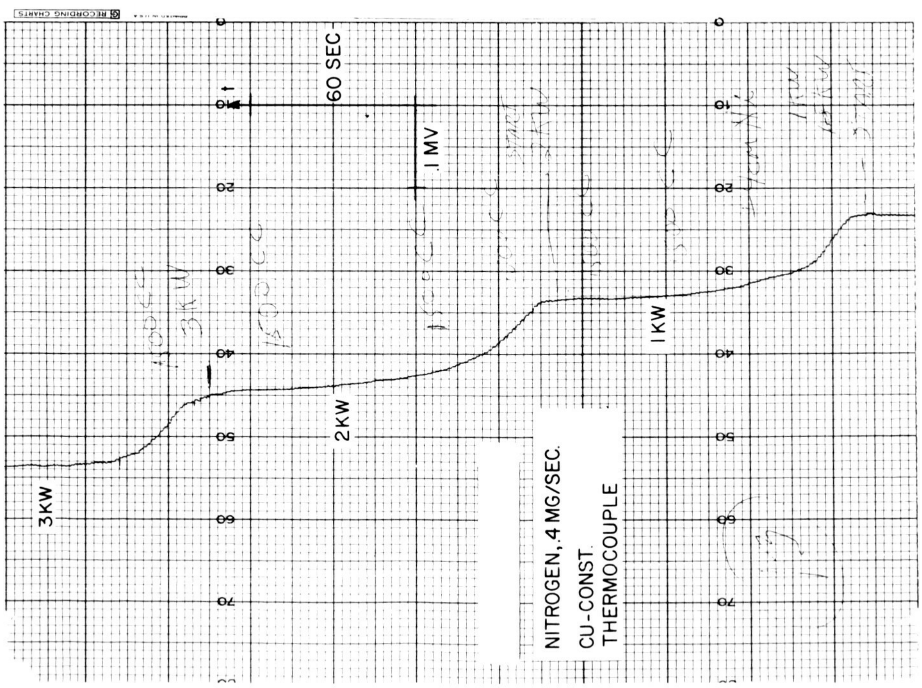

Figure 17. Typical Total Calorimeter Outlet Temperature Record During a Test; 1500 cc/min. Water Flow; 2' diameter x 10'' deep Calorimeter

The large exposed frontal surface and the relative shallowness of the 24" diameter calorimeter were felt to be detrimental to efficient absorption of the plasma stream power. The deeper, smaller diameter calorimeter shown in Figure 18 was therefore constructed. Note that it consists basically of a thin-walled copper cylinder with the back end closed off. The water cooling line is wrapped along the entire cylinder length in order to minimize local hot spots. The water line is brought through the vacuum wall at the insulated coupling which attaches the calorimeter to the horizontal drive shaft, also visible in Figure 18. The calorimeter is supported by the same movable platform used previously for the 24" calorimeter, so that the calorimeter position can be easily changed. It is electrically insulated so that it may be operated either electrically floating or grounded.

The water flow rate is continuously monitored by a calibrated flow meter, and the temperature rise of this water is measured by thermocouples in the water inlet and outlet lines. The inlet thermocouple is used as the reference junction so that a thermocouple signal proportional to the temperature difference is obtained. Water flow rates are in the range 1000-1500 cc/min., resulting in temperature rises of only a few degrees, thereby reducing radiation losses to a negligible level. At these small temperature differences, the conduction of heat away through the insulated support coupling is also negligible compared with the rate at which heat is carried away by the water.

A typical 10" calorimeter record is shown in Figure 32. Note that the response speed is approximately the same as for the 24" calorimeter (Figure 17).

3.9 DIODE PROBES

An array of diode probes has been used to map the exhaust stream flux density and power density distributions. The probe design is shown in Figure 19. A 28-unit array of these probes is illustrated in Figure 20. The probe circuit is shown in Figure 21. These probes are identical to those developed during an earlier contract (see Final Report NAS3-3567).

Power density is measured by measuring the temperature rise of the collector cup during a test of known duration. Knowing the heat capacity of the collector, the time, and the temperature change allows calculation of the energy and the average power absorbed by the cup. The thermocouple leads from each probe pass through the vacuum wall at the central hub of the array. An ice-bath cold junction is employed, and a stepping switch is then used to connect the probe e.m.f.'s sequentially to a recording millivoltmeter (Photovolt "Microcord" Model 44). The temperature decay rate of each probe collector is sufficiently small so that all 28 temperatures can be recorded without any significant change in collector temperature taking place during the recording time.

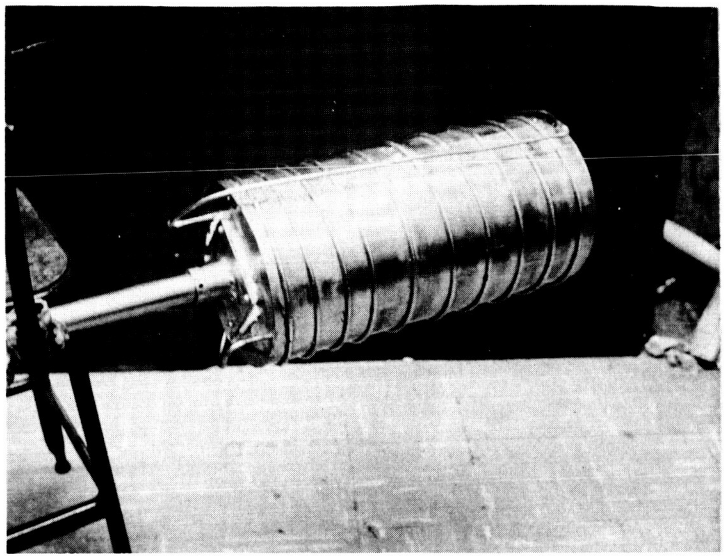

Figure 18. 10" Diameter by 20" Long Steady State Calorimeter, Mounted on Support Shaft

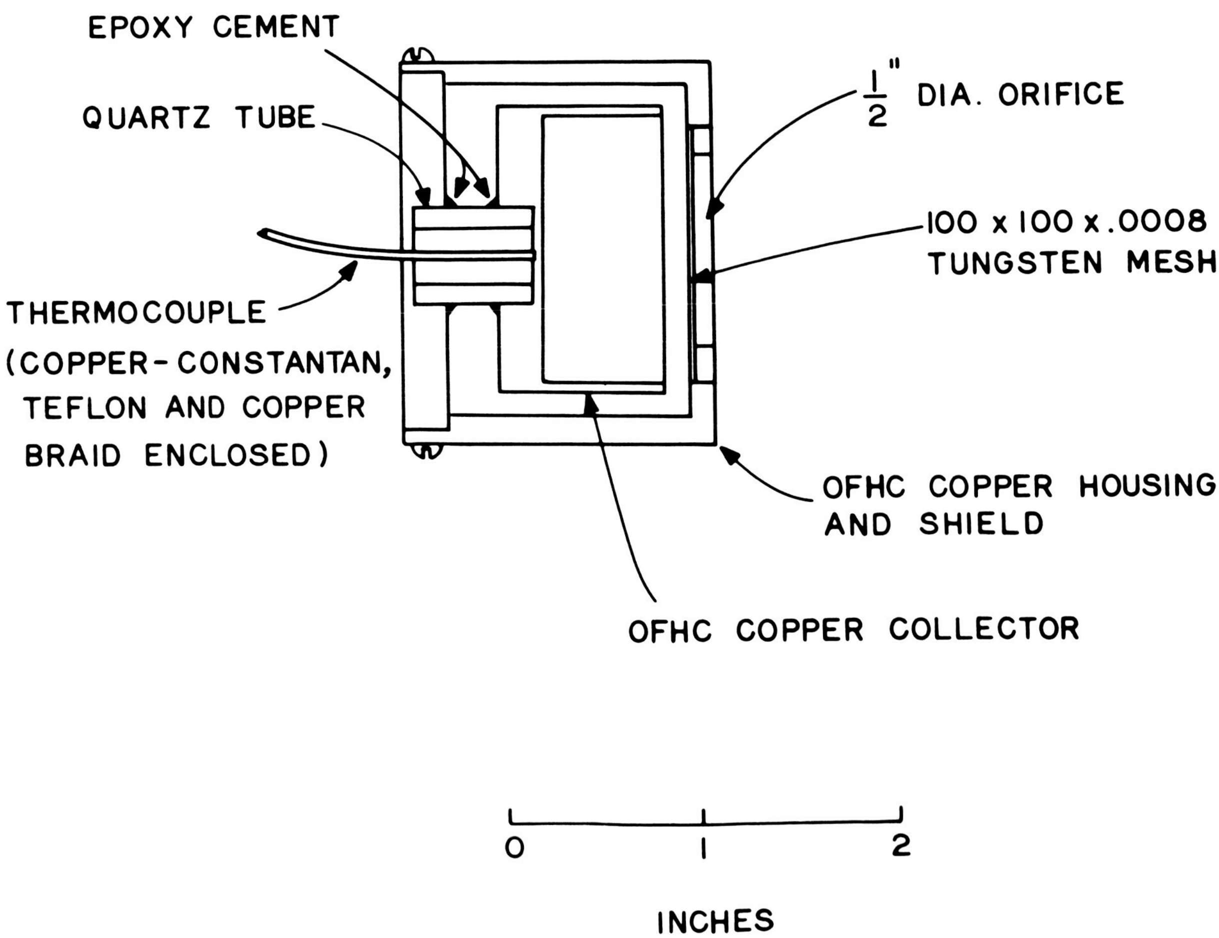

Figure 19. Diode Probe

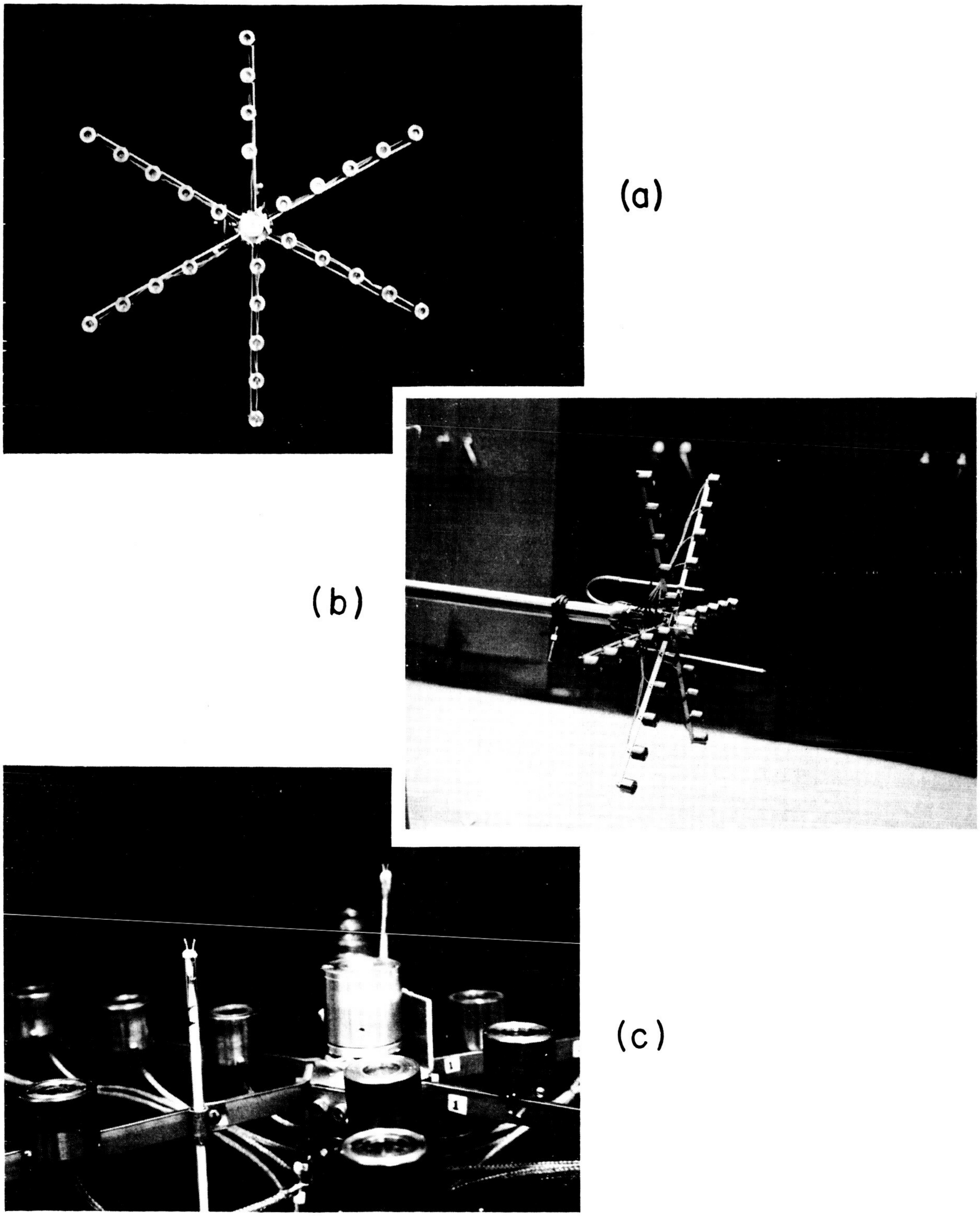

Figure 20. Multichannel Sampling-Probe Array
a. Frontal view, showing star pattern
b. Array mounted on support shaft
c. Close-up view, showing details of the velocity-analyser probe (on center), the potential probes (with emitting filaments at tips) and the diode (ion/power flux) probes.

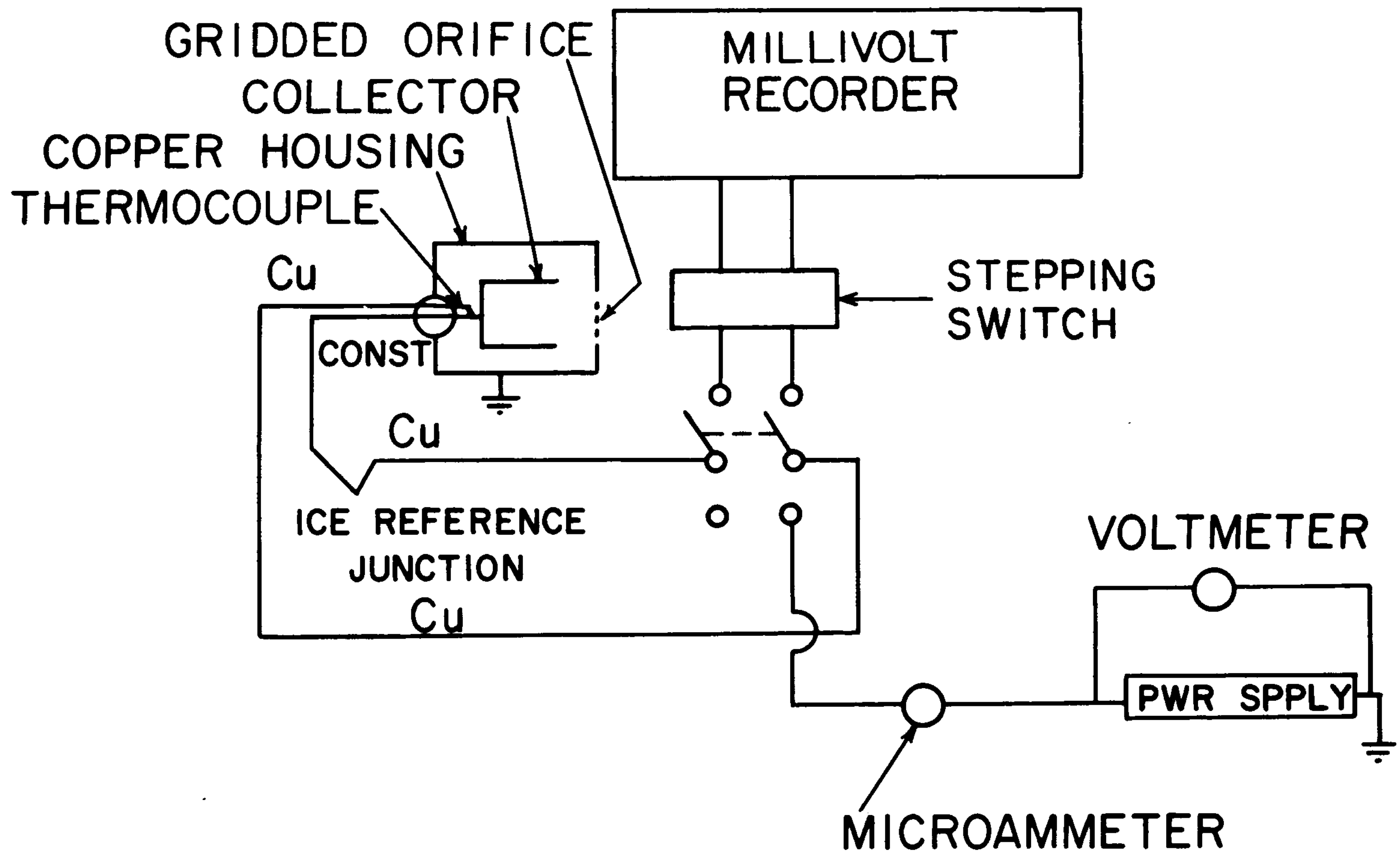

Figure 21. Sampling Probe Circuit (Typical of Sixteen)

Ion flux density is measured by biasing the collector strongly negative with respect to the enclosure and entrance grid so that all electrons are removed from the stream. The recorded collector current (through the copper thermocouple wire) then gives the ion arrival rate, and division by the probe entrance area (1.26 cm^2) yields ion flux density (ions/cm^2-sec). The gridded entrance causes approximately an 8% shadow but prevents the retarding field from extending out into the space beyond the probe and thereby increasing the effective ion collection area.

There are 16 microammeters so that ion currents to sixteen probes can be measured simultaneously. Currents are recorded by taking a photograph of the 16-meter panel, as shown in the photographs of Figure 22. It can be noted from the data in Figure 22 that ion currents are taken for several (in this case three) collector bias voltages, and the saturation currents are interpreted from the resulting curves. Although only a few tenths of a volt should be needed to reflect the plasma electrons, it is seen that on the order of two hundred volts is needed to reach ion saturation current. This is explained by realizing that, after the electrons have been reflected, the probe acts as an ion diode and is space-charge limited, governed by the well-known Child-Langmuir relation. The large collector voltage is required to "pull across" to the collector all the ions arriving at the grid.

3.10 POTENTIAL PROBES

Potential probes were used on the exhaust of three different accelerators, Mark IV-S, Mark V-L, and Mark V-S. Since both the probes and their mounting for the Mark IV-S and V-L accelerators were different than for the Mark V-S accelerator, the two types of probe systems will be discussed separately.

3.10.1 Mark IV-S and Mark V-L Accelerators

The plasma potential probe as used here consisted of a heated emitting filament. If the probe current response curve near plasma potential is determined both with and without the probe emitting, the plasma potential presumably can be determined by either the "break" in the I-V curve or by the potential at which the emitting and non-emitting I-V curves (of the same probe) start to diverge. Here, I is probe current and V is probe bias voltage.

Since only relative probe currents are needed for the determination of plasma potential, the probe shape is not critical. Thus ordinary miniature light bulb filaments were used as a conveniently available source of emitting tungsten probes.

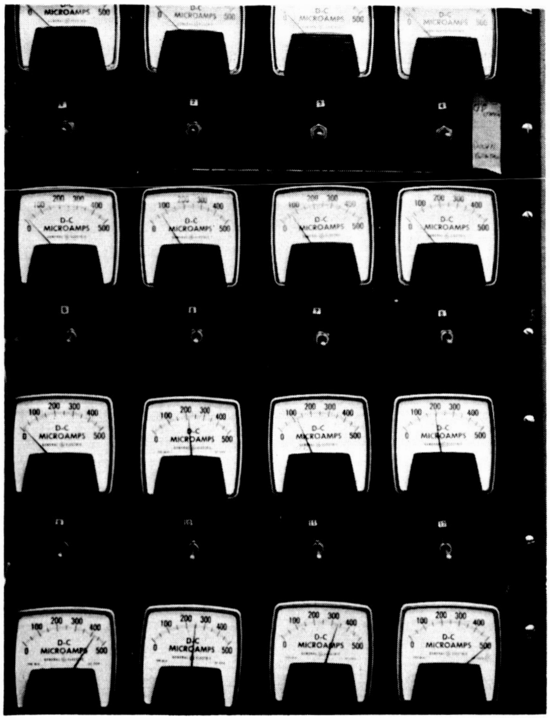

70v

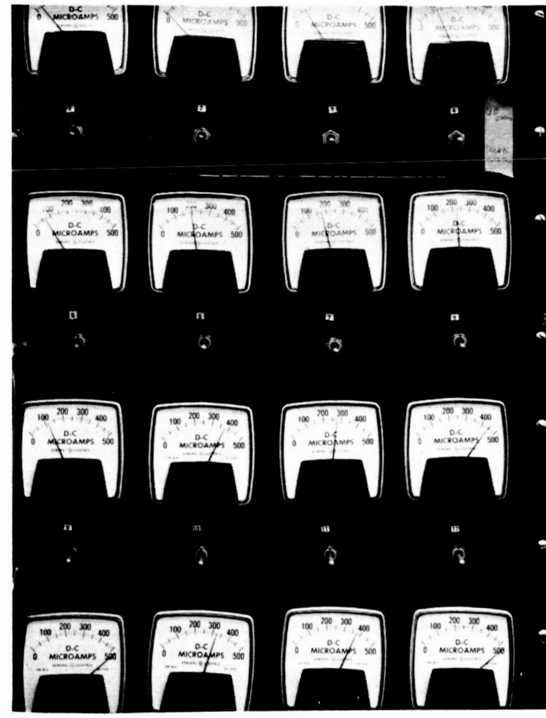

105v

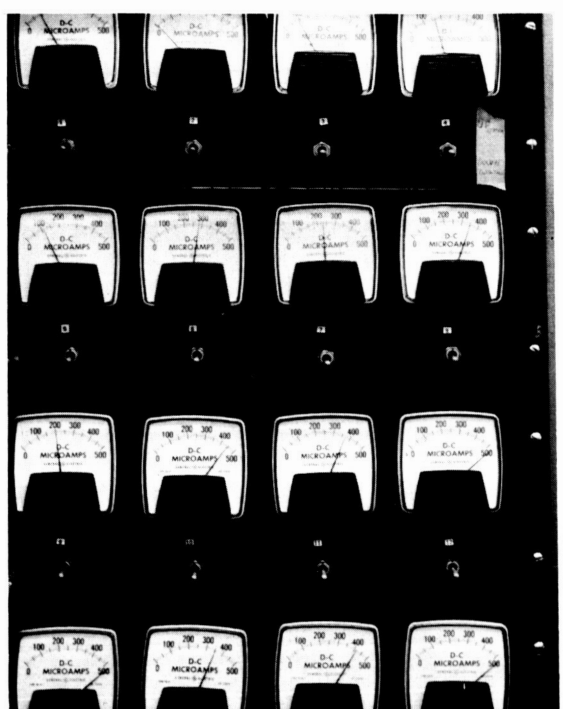

160v

Figure 22. Typical 16-Channel, Sampling Probe Data

The plasma potential probes thus far used each consist of a GE #43 miniature lamp filament cemented to the end of a glass tube as shown in Figure 23. On testing several such filaments within an anode and in vacuum, they were found to give satisfactory life and 23-40 milliamps electron emission current at 75% filament overvoltage (4.4 volts AC).

Two of the above potential probes were mounted on the "multi-channel probe array" frame as shown in Figure 20. Both probes were mounted 7 cm from the center of the array, with the filament of one of them (probe A) being 2 cm ahead of the diode probes, and the filament of the other potential probe (probe B) being 8.5 cm ahead of the diode probes.

3.10.2 Mark V-S Accelerator

For the Mark V-S accelerator measurements, three potential probes of different types were mounted nearly on-axis on a special probe carriage such that the three probes could be moved towards and away from the accelerator. Simultaneously two potential probes (and the energy analyser probe) were located somewhat off-axis and adjacent to each other on a stationary part of the probe carriage. This probe carriage assembly is shown in Figure 24.

The above-mentioned five potential probes consist of three types: an emitting heated filament probe, small diameter tungsten wire (cylindrical) Langmuir probes, and larger diameter rod probes with only a small exposed side surface. The emitting heated filament potential probe is the same as used for the Mark IV-S and Mark V-L accelerators (see above and Figure 23), except that quartz tubing was used in place of glass. Small-diameter cylindrical Langmuir potential probes were constructed of quartz tubing drawn at one end to a fineness which just passed a .002 inch diameter gold-coated tungsten "grid" type wire. This wire extended 6-11 mm beyond the quartz drawn end into the plasma, this exposed distance being a function of where the probes were to be mounted. Finally, .065 inch diameter non-magnetic stainless steel rod potential probes were constructed by cementing (Sauereisen) the rod in a quartz tube and coating the projecting exposed end of the rod with boron nitride insulating "paint." The sides of these coated sections were then scraped clean to expose the metal over a 1 x 2 or 3 mm area so as to somewhat approximate a flat probe.

Using the special probe carriage mentioned above and shown in Figure 24, the energy analyser probe (discussed later), one .002 inch diameter Langmuir potential probe (11 mm long), and one thick ("flat") potential probe were positioned 10.6 cm off axis and 77.8 cm axial distance from the accelerator window; and the emitting filament potential probe, a .002 inch diameter Langmuir probe (6 mm long), and a thick ("flat") potential probe were positioned about 1.5 cm off axis and 12.5-42.5 cm from the accelerator window. By "window", is meant the plasma-window interface.

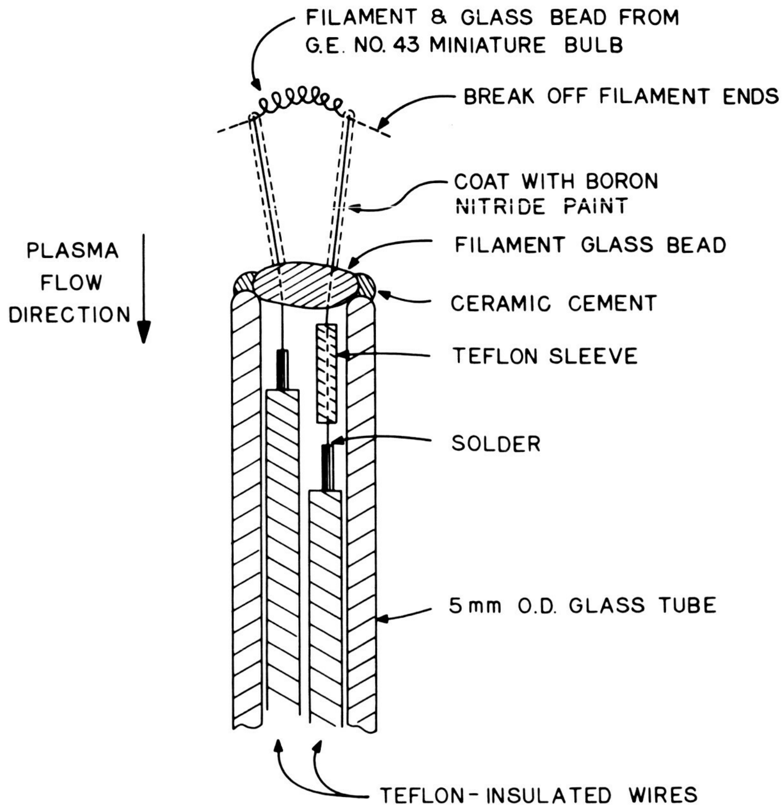

Figure 23. Emitting Plasma Potential Probe

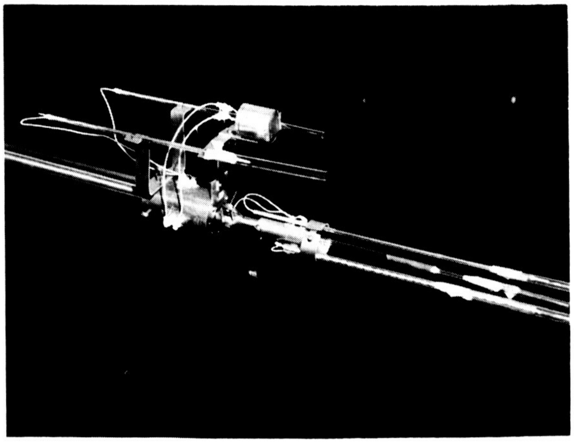

Figure 24. Energy Analyser and Potential Probe - Assembly. (note that the potential probes are enclosed in temporary glass protective covers)

Some potential probe currents were recorded as a function of voltage on an X-Y recorder, while most potential probe currents were recorded (logarithmicly) on a Visicorder while using a repeating 2 second sawtooth bias voltage generated by special circuitry. Using this automatic biasing circuitry, it was possible to obtain results from all potential probes at all distances from the accelerator during each accelerator run. In all cases, the probe voltages were referenced to the grounded vacuum tank test chamber.

During these runs, the moveable heated filament and (perhaps) thick ("flat") potential probes broke some Sauereisen seals, probably due to differences in thermal expansion of materials and the intense heat close to the accelerator. However, this breaking of seals did not necessarily affect the operation of these probes. The 0.002 inch diameter Langmuir probes survived and operated well, although the gold coating evaporated off the wire due to accelerator plasma heating. This loss of gold coat did not appear to affect these probes.

3.11 ENERGY ANALYSER PROBE

A two-gridded energy analysing probe has been constructed for determining ion velocities. As indicated in Figure 25 an inner ion collector plate is positively charged (variable) so as to collect only those ions above a certain energy, a grid adjacent to the above plate is negatively charged so as to repel all electrons, and an outer grid is at ground potential so as to limit the field from the negative grid.

Some earlier measurements[15] with a simple grid-less sampling probe indicated an exhaust ion current density of about 1.5 milliamps/cm^2. To successfully operate a multi-gridded ion velocity analysing probe with such a plasma, the probe must be designed so as to avoid space charge limitations.

The Langmuir-Child equation[25] can be used to determine the space charge-limited (i.e., maximum permitted) ion current through the negative grid to the positive collector: Assuming a monoenergetic beam of argon ions directed into the analysing probe, we find that the negative grid-positive collector spacing must be decreased to 0.09 cm (about 1/32 inch) and the collector-grid potential difference increased to 150 volts if the ion current limit is to be increased to 2.0 milliamps/cm^2.

Since it is difficult to reduce the grid-collector spacing to less than 1/32 inch without increasing the chances of forming grid ripples, touching, and shorting out, the analyser probe has grid-grid and grid-collector separations of 1/32 inch. Even maintaining the 1/32 inch spacings, the space-charge limitation can be further eased, if necessary, by increasing the negative grid potential. Also, the limited "transparency" of the grids will considerably reduce the actual ion current to the collector.

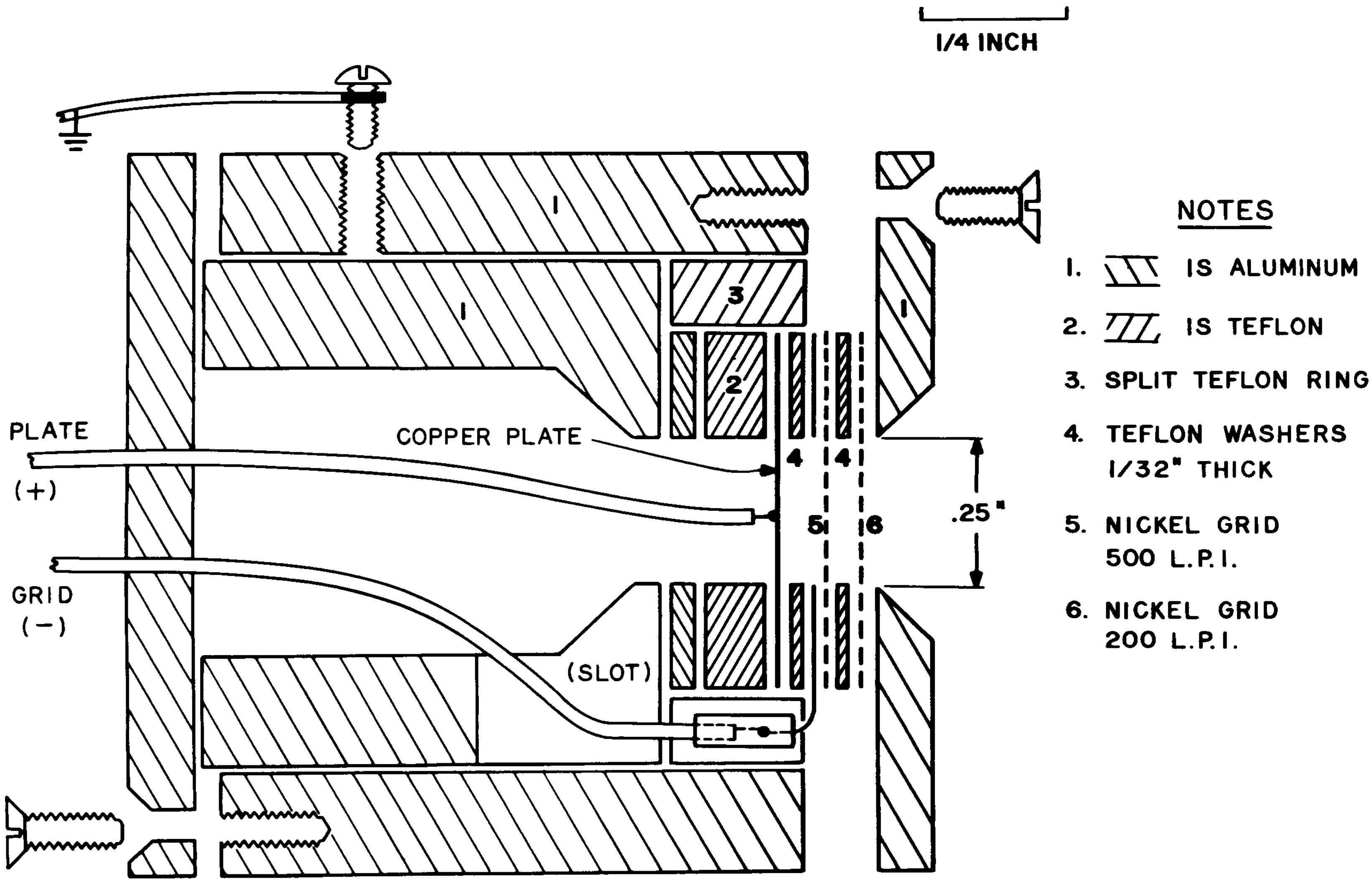

Figure 25. Energy Analysing Probe

The use of a simple flat collector plate results in the loss of some ion current due to the failure of a small fraction of the ions to neutralize before leaving the collector surface. This problem could be considerably reduced if the collector plate were replaced with a variably positive ion repelling grid followed by a negative (with respect to positive grid) ion collector plate. With a negative plate-positive grid spacing of 0.09 cm it can be calculated[25] as above that a potential difference of 150 volts would be required for a space charge current limitation of 2.0 milliamps/cm^2. [A negative collector cup of significant depth is thus not reasonable since the space charge current limitation is universely proportional to the square of the positive grid - negative collector surface spacing[25].] Since such additional grids and potentials considerably increase the practical problems of probe operation and data recording with relatively little increase in data quality, the energy analysing probe has been constructed with a positive plate and no positive grid as discussed in the previous paragraph and shown in Figure 25.

The ion energy analyser probe thus far used consists of a nickel 200 line per inch (l.p.i.) grounded grid, a nickel 500 l.p.i. negative (electron repelling) grid, and a positive ion selecting and collecting copper plate. The 200 and 500 l.p.i. grids are stated by the manufacturer to be 70% and 58% transparent, respectively. As shown in Figure 25, 1/32 inch thick Teflon washers separate the grids from each other and from the collector plate. Of the limited grid materials available, nickel has been initially employed because of its lower sputtering yield and higher melting point than copper. Similar copper grids are available for use if desired, as are grids with closer wire spacings.

For the Mark IV-S and Mark V-L accelerator runs, the above energy analyser probe was mounted at the center of the "multichannel probe array" frame as shown in Figure 20. This probe was mounted such that its grounded grid was about 2.0 cm ahead of the diode probes and even with one of the potential probes.

For the Mark V-S accelerator runs, the energy analyser probe has been modified slightly from the above description, in that larger inside diameter 1/32" thick Teflon washers were used than shown in Figure 25. This change was to reduce the chance of internal shorts or leaks resulting from sputtering by the accelerator exhaust. As indicated in the section on potential probes, for these runs the energy analyser probe was positioned 10.6 cm off axis and 77.8 cm axial distance from the accelerator plasma-window interface (see Figure 24). All Mark V-S energy analyser probe plate currents were recorded _vs_ plate voltage on an X-Y recorder.

3.12 THRUST STAND

A thrust stand for the cyclotron-resonance accelerator has been designed and built. An assembly drawing of this system is shown in Figure 26. Photographic views are shown in Figures 27-29. Its features are dominated by the large rectangular pressure box, which houses the coil and accelerator. This enclosure was necessitated by the inability of the coil to operate in vacuum. Note that, whereas the drawing, Figure 26, shows strengthening ribs on the coil box covers, the photographs reveal that thicker, unribbed covers were in fact used. Severe warppage during welding prevented satisfactory fabrication of the ribbed covers. The stand itself, below the box, consists primarily of positioning tracks for initial and final balancing of the stand. Four thin flexible legs (part #23) support the stand and are sufficiently loaded so that slight horizontal thrusts will cause appreciable bending of these legs. A linear motion transducer (Sanborn "Linearsyn Type 595DT025, supported by part #33) provides an electrical signal proportional to the displacement. This signal is then amplified (Sanborn Model 3114) and displayed on the Visicord recorder.

Electrical power, coolant water and propellant gas enter through the overhead couplings. Drain lines are attached through the base.

The photograph in Figure 28 shows the installed stand before attaching the cover plate. The water lines (coil and engine cooling), the electrical power lines (d-c for the coil) and the gas input line are visible in this photograph. Water drain lines leading out through the base were installed after these photographs were made. In addition to the normal coil and engine coolant drain lines, an open drain was also required because of coil leaking. Figure 29 shows the same assembly after installing the cover, polarizer and wave guide sections. The open (left) end of the waveguide attaches to one end of a vertical, 12", flexible waveguide section whose other end is fastened to the vacuum tank; the flexible waveguide section enables the stand to move laterally while maintaining a tightly coupled and pressurizable waveguide.

Calibration of the stand is achieved by a 1-1/2" x 3-1/2" x .010" piece of brass sheet attached to the waveguide. The spring constant of the brass piece has been measured (35 gram/in). A precision screw, passing through the vacuum wall and coaxial with the engine provides an accurate means of deflecting the brass piece and therefore of imposing a known, small, axial force on the thrust stand. This calibration can be carried out anytime, even while the engine is operating. Before completing assembly of the calibrator, it was determined that the thrust stand sensitivity was symmetric so that calibration is valid even though the calibrator force is anti-parallel to the engine force.

Each of the four flexible thrust stand legs is made up of one piece of .030" non-magnetic stainless steel sheet. The remainder of the stand is also constructed of non-magnetic material and magnetic pieces have as much as possible been removed from the neighborhood of the stand in order to minimize magnetic force effects.

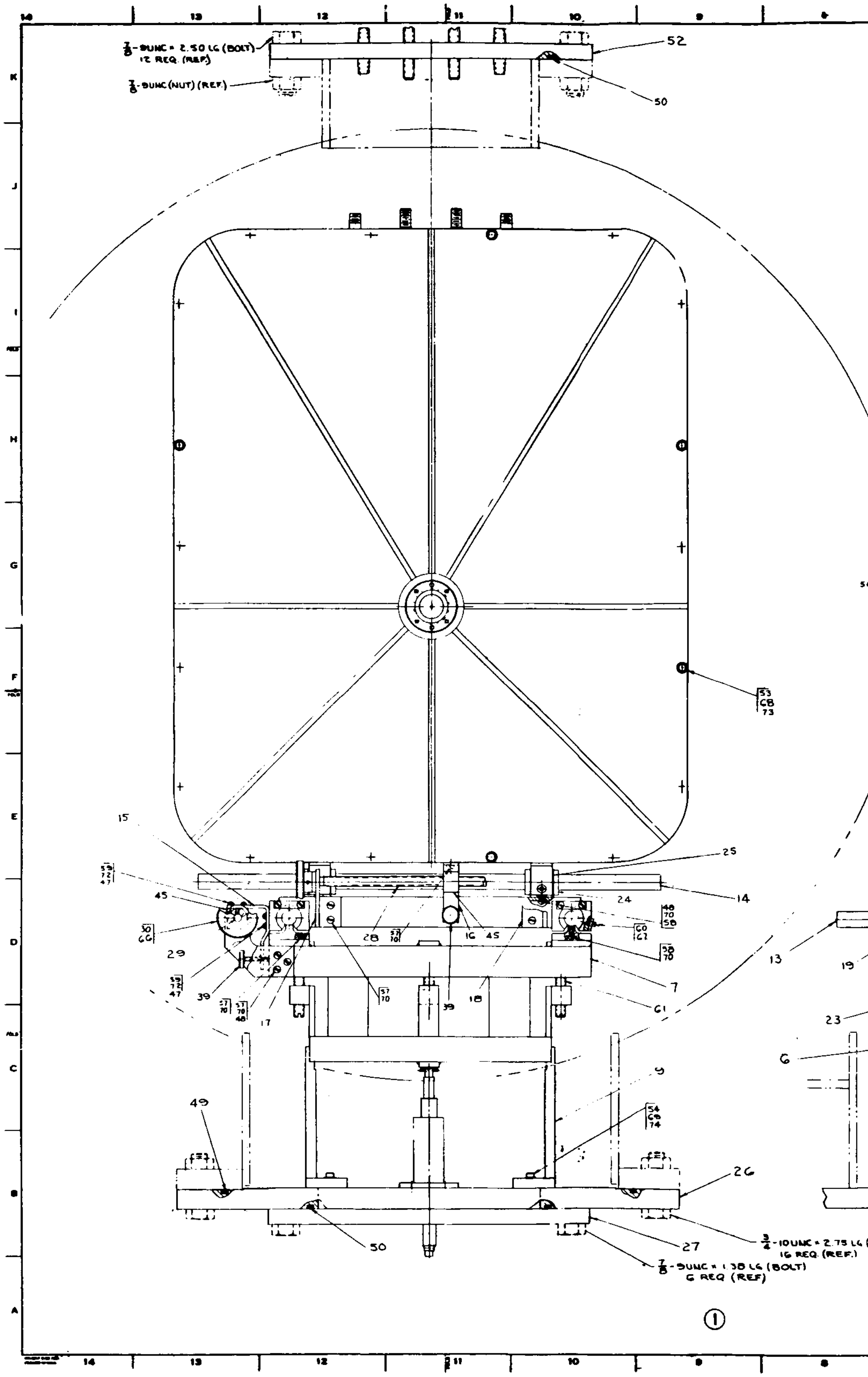
7/8-9UNC × 2.50 LG (BOLT) 12 REQ (REF)
7/8-9UNC (NUT) (REF)
52
50
53 68 73
15
25
14
45
24
28
16 45
18
7
61
29
39
17
13
19
23
6
9
49
26
27
50
54 68 74
3/4-10UNC × 2.75 LG
16 REQ (REF)
7/8-9UNC × 1.38 LG (BOLT)
6 REQ (REF)
①

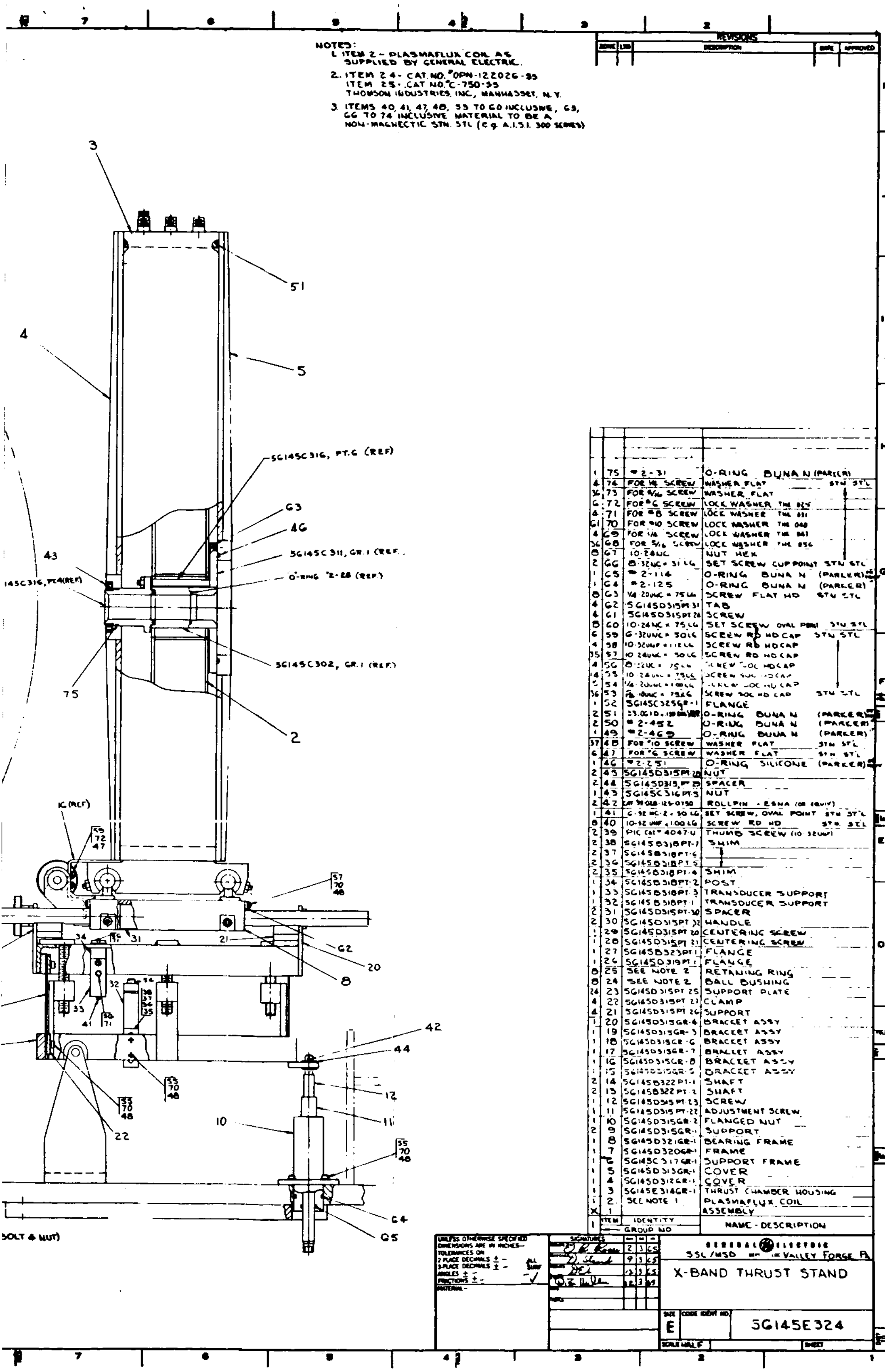

Figure 26. Thrust Stand Assembly Drawing

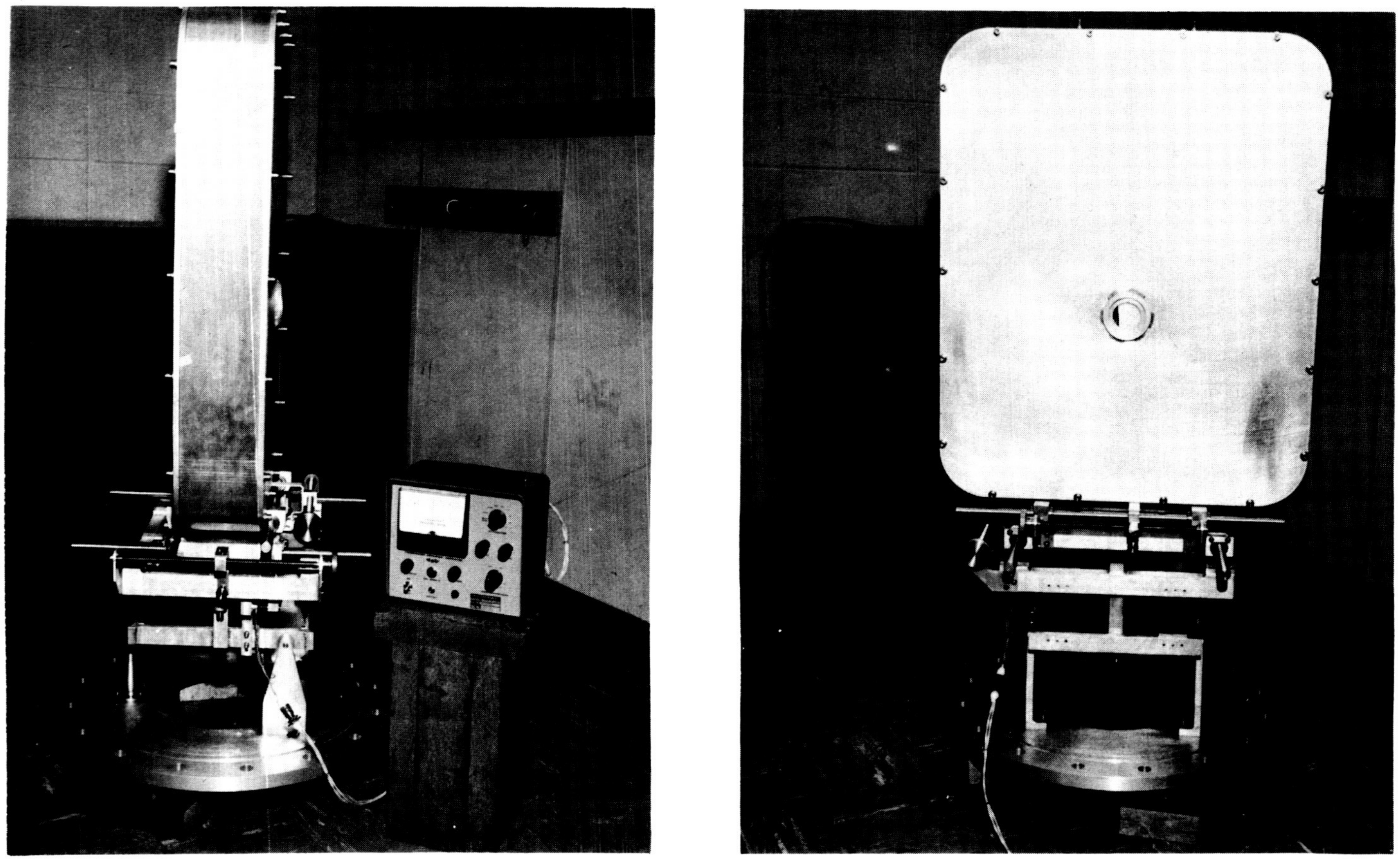

Figure 27. Thrust Stand, Side and Face Views

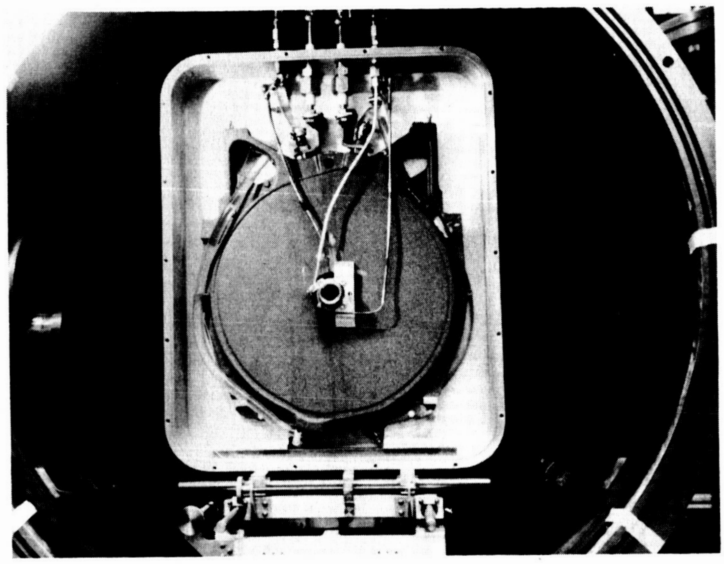

Figure 28. Thrust Stand with Cover Removed

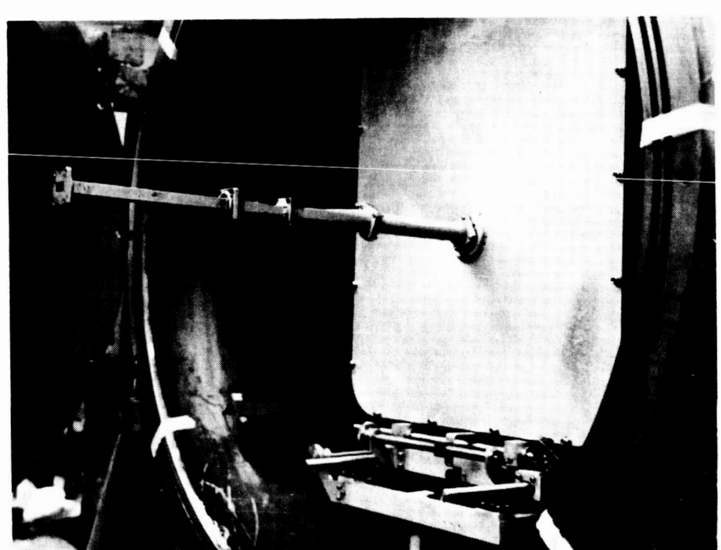

Figure 29. Thrust Stand with Waveguide Attached

Thrust stand operating procedures are described and discussed in Section 4.4.

3.13 MAGNETIC PROBE

R-f probes have revealed that r-f absorption takes place before the vacuum magnetic field has dropped to the resonance point (see Section 4.4.2). Since the plasma is diamagnetic, due to the cyclotron orbiting electrons, it is possible that the actual field strength in the plasma is in fact reduced by this plasma diamagnetism to resonance. A direct measurement of the magnetic field would therefore be helpful in verifying this hypothesis as well as yielding a measure of the electron transverse energy. For this purpose, the probe shown in Figure 30 was constructed. This probe is movable along the system axis. The combination of copper and quartz covers over the Hall sensor element permitted this probe to hold up for longer times immersed in the plasma, as compared with an original model, which only had the quartz cover. The copper cover in addition protects the sensor element from r-f damage and makes the high temperature vacuum seal problem easier. This probe was employed with the Mark V-S accelerator, using the following steps:

1) With probe removed, ignite plasma and adjust to desired power level and field strength.

2) Move probe to a position on center close to the window (1 or 2 cm).

3) Turn chart recorder to full speed (8 in/sec).

4) Turn off r-f.

5) Turn off recorder; look for change in magnetic field at instant r-f (and therefore plasma) is turned off.

By this procedure, a 3% change in magnetic field can be observed. The result was that, over a wide range of field strengths, for r-f powers up to 2500 watts, in He, Ar, and Xe no change in magnetic field at the turn-off instant could be detected.

The expected action can be estimated:

$$B = B_o - M$$

where B_o is the vacuum field, M is the magnetization.

$$M = n m \text{ (dipoles/m}^3 \text{ x magnetic moment/dipole)}$$

$$= n \left(\frac{1}{2} \mu_o \, e \, v \, r \right)$$

$$= n \left(\frac{1}{2} \mu_o \, e \right) \left(\frac{2\epsilon}{eB} \right)$$

where ϵ is the energy per electron in transverse orbiting motion.

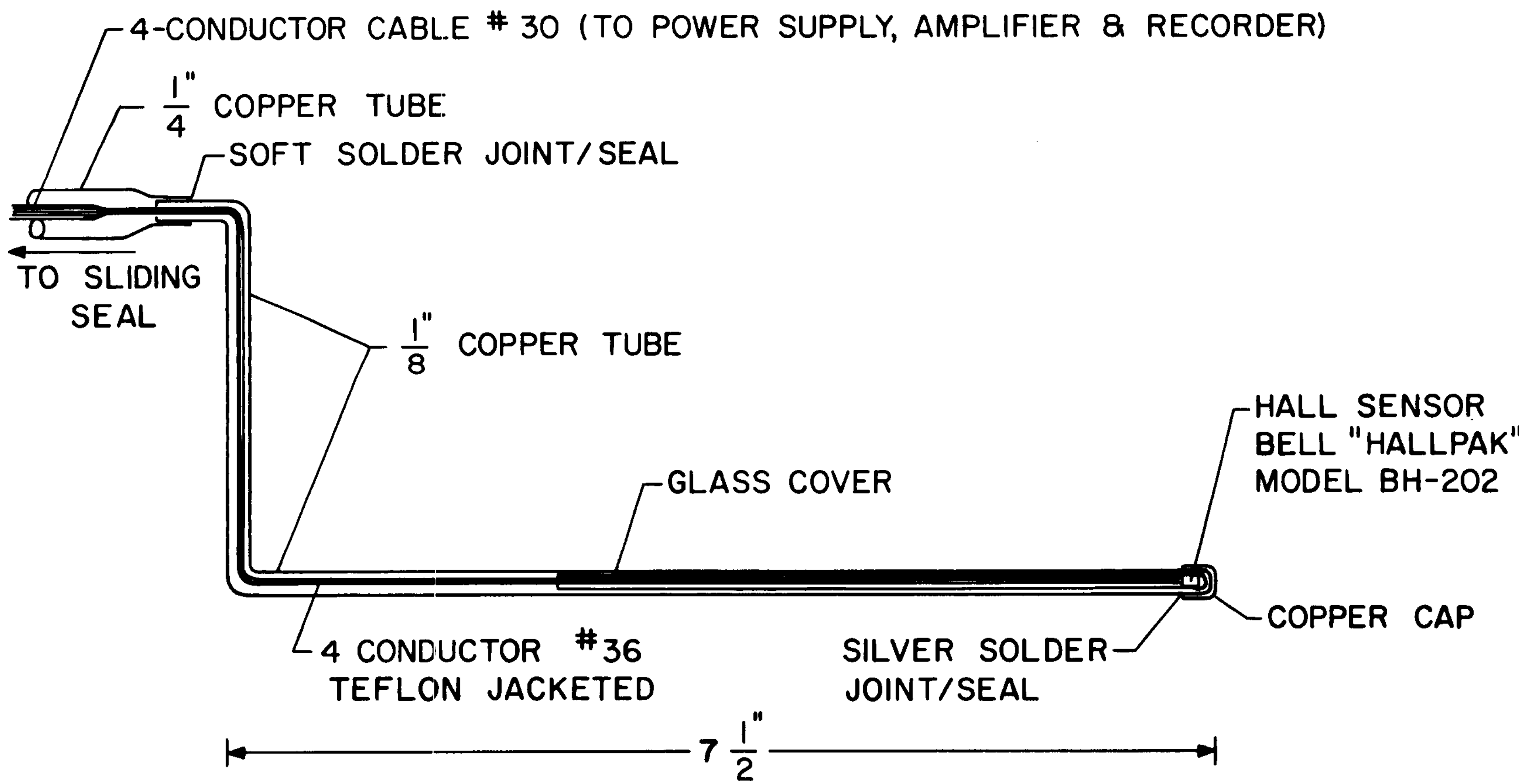

Figure 30. Magnetic Probe

$$B = B_o - \frac{\mu_o n\epsilon}{B}$$

or $$B = \frac{B_o}{2}\left[1 + \sqrt{1 - \frac{4\mu_o n\epsilon}{B_o^2}}\right]$$

Let $$\alpha = \frac{4\mu_o n\epsilon}{B_o^2} = 2\frac{\epsilon_p}{\epsilon_B}$$

where ϵ_p is the plasma energy density ($n\epsilon$) and ϵ_B is the vacuum field energy density ($B_o^2/2\mu_o$).

If $\alpha \ll 1$

Then $$\frac{B}{B_o} \cong 1 - \frac{1}{2}\frac{\epsilon_p}{\epsilon_B} .$$

Assume that the electron density is close to cutoff at 8350 mc, i.e., $\sim 10^{18}$ electrons/m^3. Now, if the average electron energy is 1 kev ($\sim 10^{-16}$ joule/electron), this gives a plasma energy density of about 10^2 joule/m^3. The field energy density at 3000 gauss, on the other hand, is approximately 10^4 joule/m^3, so the energy ratio is about 10^{-2} or 1%. Thus, it would appear that the lack of diamagnetic behavior in the experiment is not surprising since a resolution of better than 3% would be needed. Further tests should attempt to improve this lower detection limit, perhaps by some kind of "bucking" technique.

3.14 MASS FLOW MEASUREMENT; PROPELLANT HANDLING

The same basic propellant handling system has been used for all the accelerators tested this year. This consists of a cylindrical, brass gas reservoir (6" diameter x 24" long; 1.11×10^4 cm^3), with a capillary flow limiter in the gas line between the reservoir and the accelerator. Gas flow is controlled by the reservoir pressure. Mass flow rate was originally determined by measuring the rate of pressure drop in the reservoir. More recently, a calibrated flow meter (Brooks Instrument Co., glass tube, type 1A-15-1, stainless steel and aluminum floats) has been inserted in the gas line so that a continuous indication of flow is available. The old and new methods agree satisfactorily.

3.15 DATA RECORDING; TEST OPERATIONS

A multichannel, strip chart record (Honeywell "Visicorder" Model 1508) is made of each test. This record always contains continuous plots of the incident and reflected power, and may in addition contain additional information depending on the particular objective of the test. Typical examples are shown in Figures 31-33, where r-f probes, calorimeter measurements and thrust stand results, respectively, were being obtained. In Figure 32, the simultaneous engine and calorimeter temperature plots are also shown; the variations of reflection, engine temperature and plasma power with changes in magnetic field are quite evident.

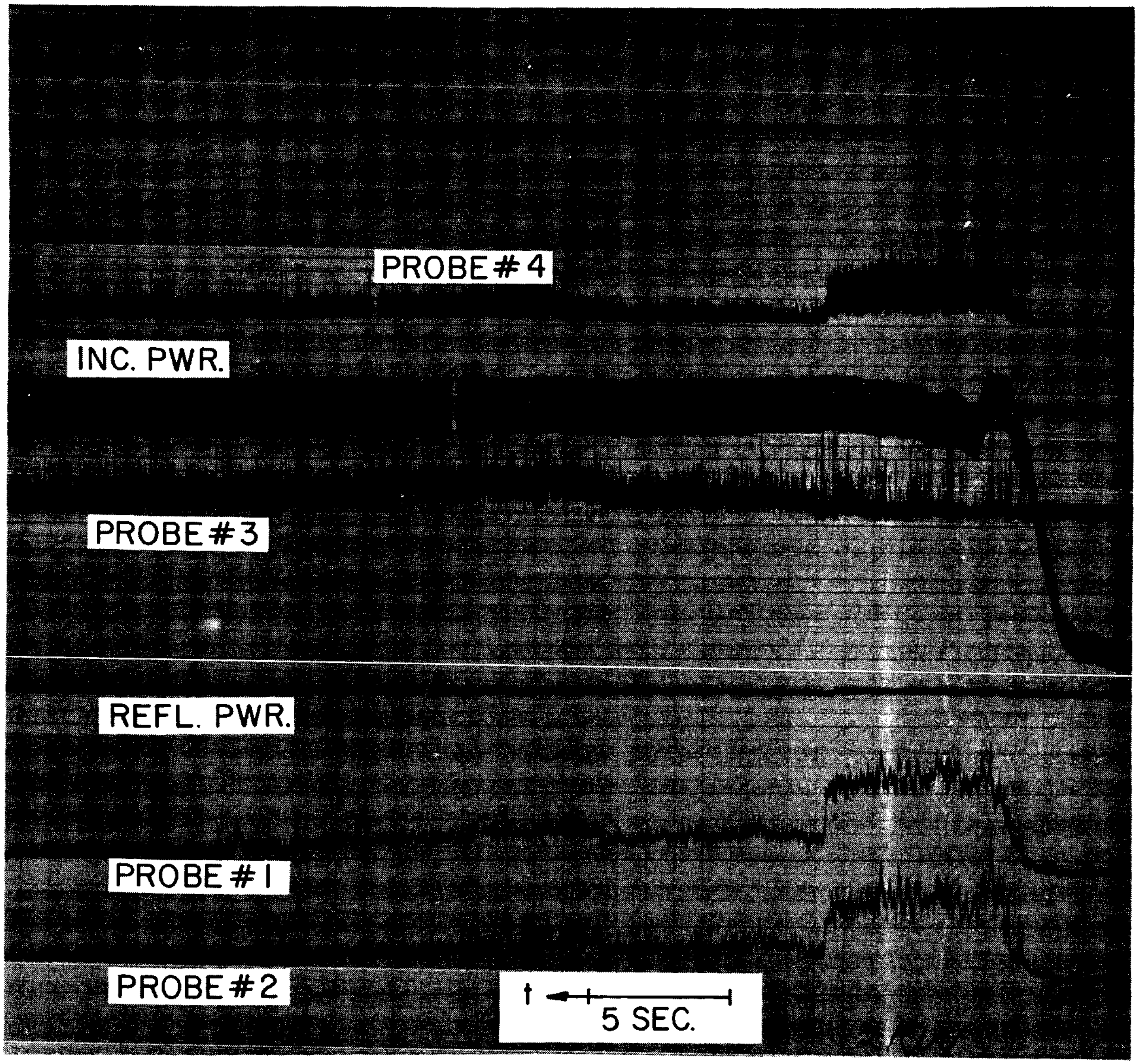

Figure 31. Typical Strip-Chart Recorder Record, Argon, 2 kw, .2 mg/sec, 4060 Gauss at r-f/Plasma Boundary, Mark V-L Accelerator

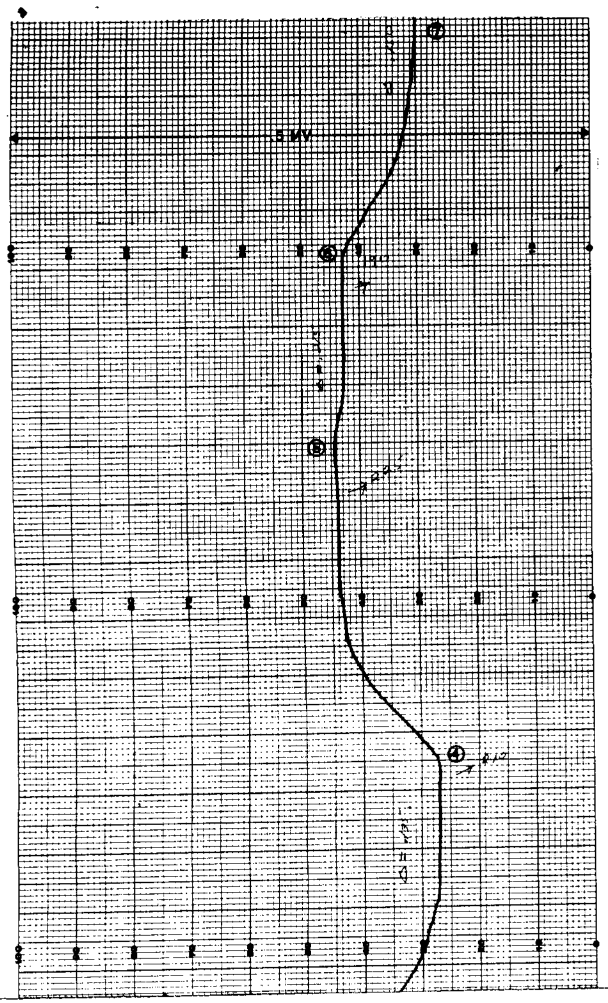

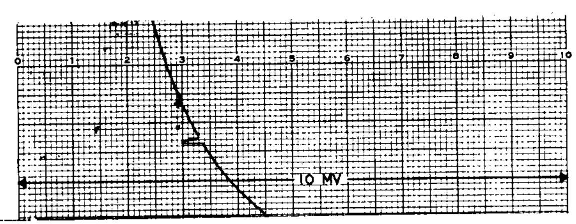

① : Accelerator on
② : Accelerator off
Total test duration (① - ⑦): 401 sec

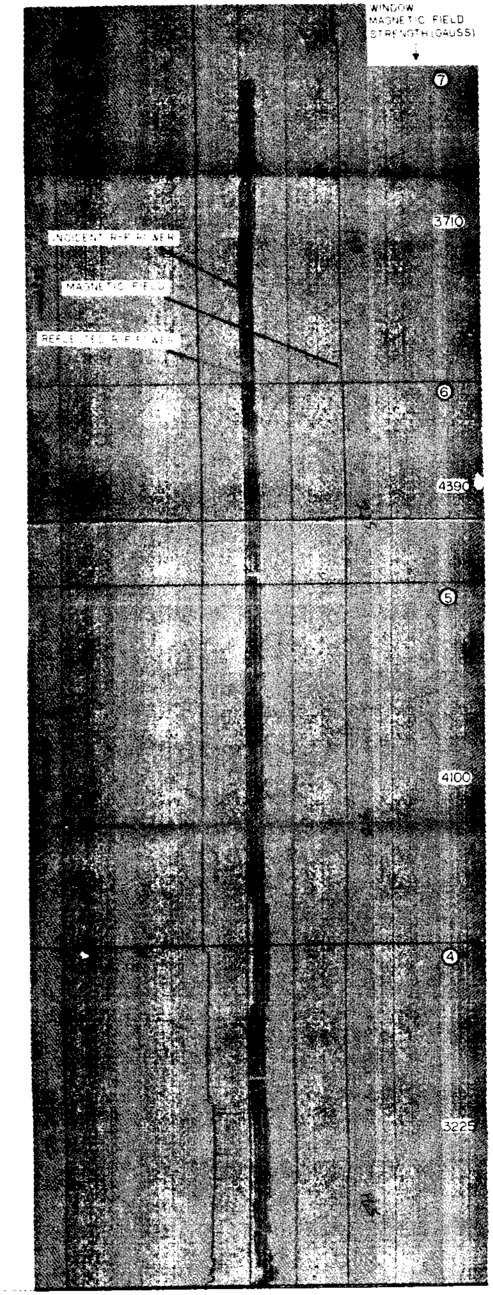

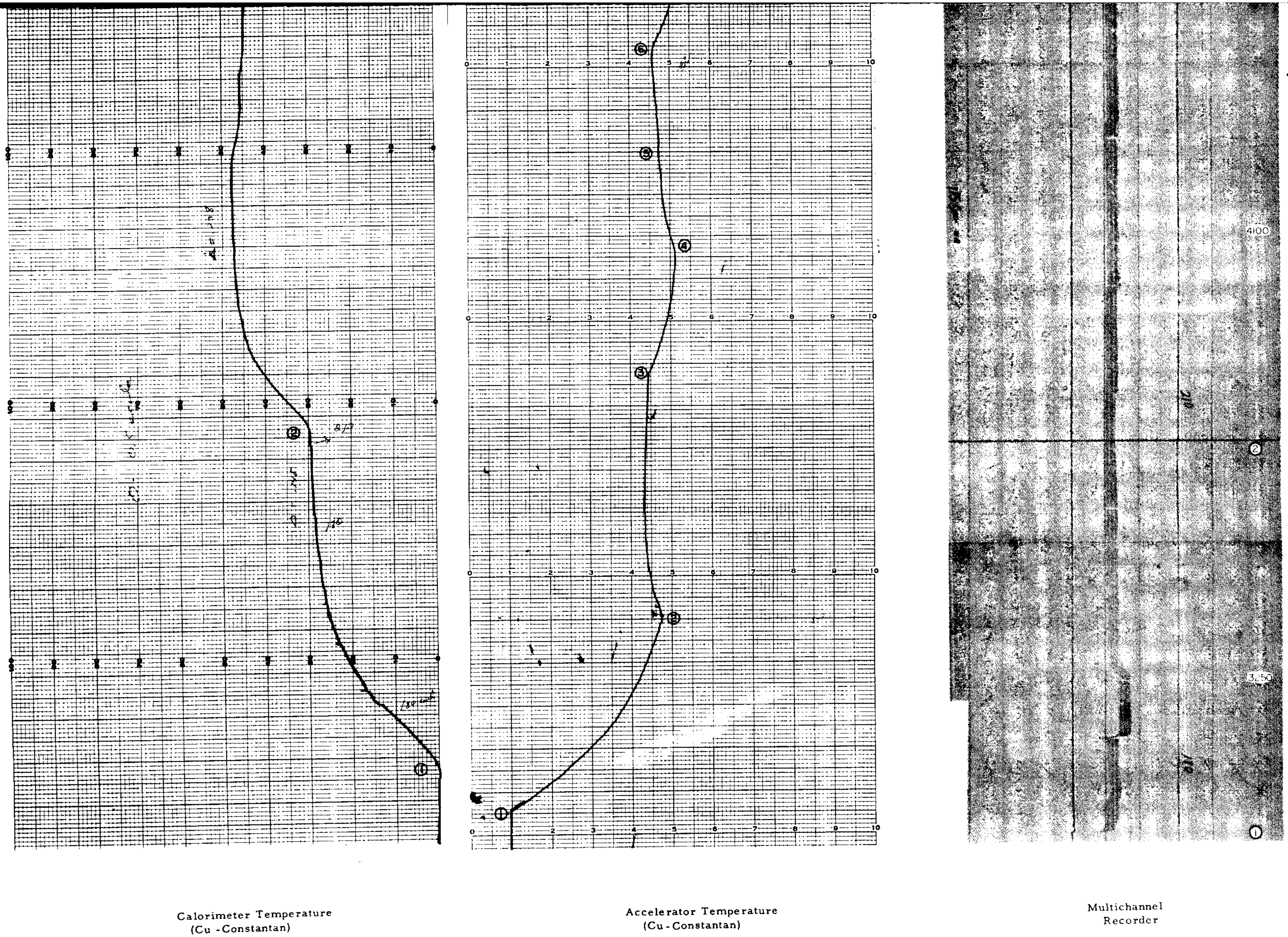

Figure 32. Chart Records of a Typical Test; Mark V-S Accelerator, Argon, .26 mg/sec, 1500 watts

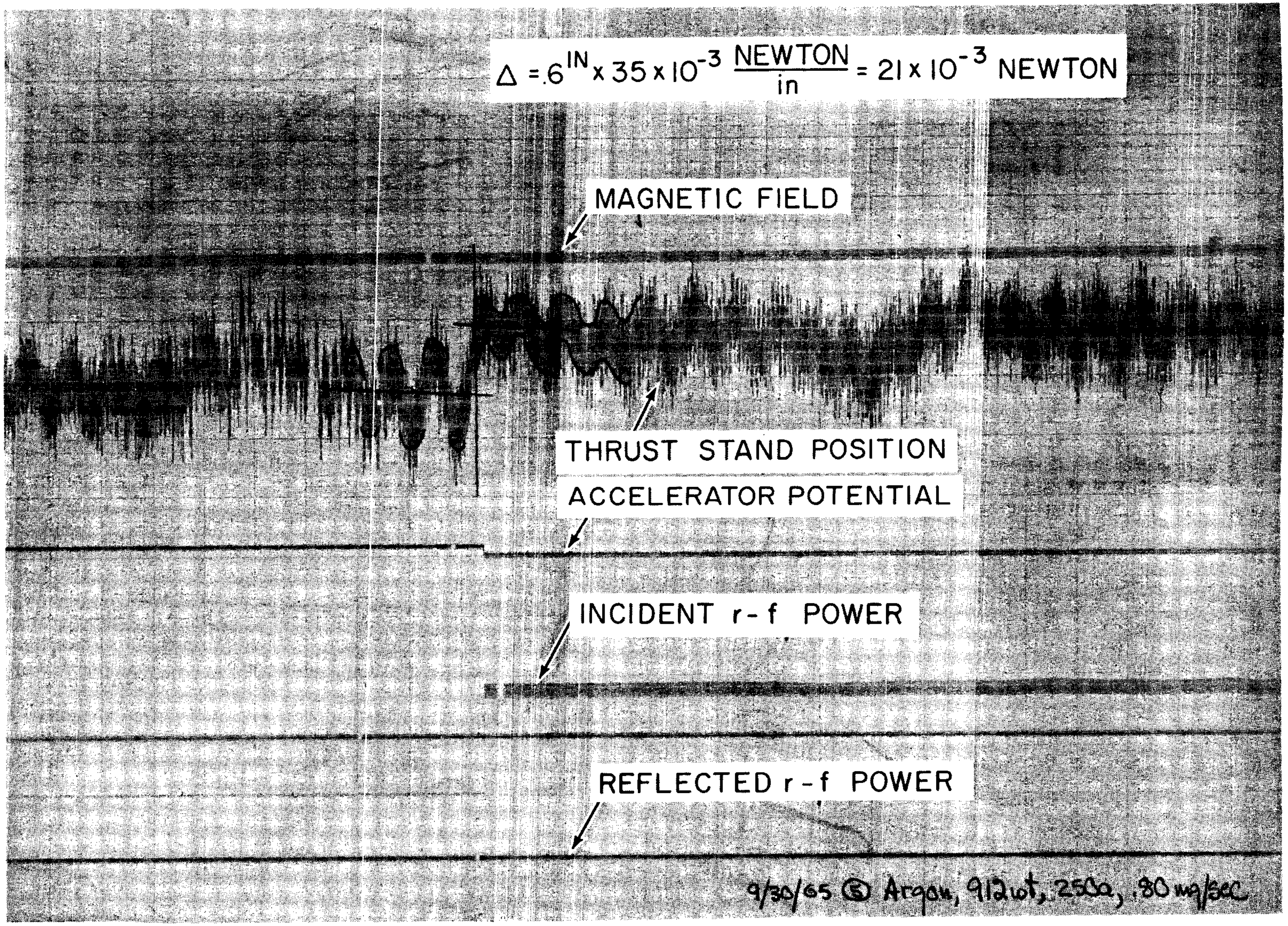

Figure 33. Typical Thrust Measurement Data Record, Mark V-S Accelerator

4. EXPERIMENTAL RESULTS

4.1 MARK IV-L ACCELERATOR (AXIAL-INJECTION, LONG VERSION)

A photograph of the Mark IV-L exhaust stream is shown in Figure 34. If the reasonable assumption is made that the luminous region indicates the approximate limits of the accelerator stream, then this illustration indicates that the plasma does not "fountain" back following the solenoidal field lines, although it does appear to continue spreading to some extent after leaving the engine. Quantitative measurements on the Mark IV-L accelerator are presented in Figures 35-40.

We note from Figure 35 that the reflection coefficient is very low (< 5%). This, of course, is a result of tuning, so that the plasma load is matched to the source; if tuning were to be carried out at each test, the reflection coefficient could in all instances be kept essentially zero. The r-f probe curves do not lend themselves to easy interpretation; undoubtedly the fact that the plasma probably has a cone shape, expanding away from the injection point, with propagation in the annular region between the cone and the waveguide wall, has much to do with the characteristics of these signals. In addition, a reasonably complex probe signal pattern is to be expected since these probes are indicative of the reasonably complex standing wave pattern which must exist within the accelerator. These probe signals with plasma are stronger than in the absence of plasma, probably due to both the annular propagation and standing wave effects. An additional point of interest is that one might have expected to have seen more clearly the enhancement of propagation with increased magnetic field strength, as predicted theoretically and as obtained in similar measurements on the Mark I accelerator during the NAS3-3567 studies.

The wall calorimeter temperatures indicated in Figure 36 exhibit the expected inverse relationship between the magnetic field strength and wall loss. For these calorimeters, the rate of heat lost is such that they rapidly reach an equilibrium temperature, and power received is a function of calorimeter equilibrium temperature, as was explained in Section 3.7. Using the 1.3 watt/degree figure stated in Section 3.7 yields wall power loss of only 100-500 watts at low fields, decreasing to less than half of this at the higher field strengths. Inspection of the engine after several days testing ($\sim 10^4$ seconds operating time) revealed, however, that the copper wall of the plasma chamber had suffered considerable erosion, with eroded copper ($\sim$0.19 gm) being redeposited on the face of the engine flange. Undoubtedly this erosion took place most severely during those tests conducted at low fields.

Total calorimeter power efficiency measurements are shown in Figures 37-40. The following items are interpreted from these curves:

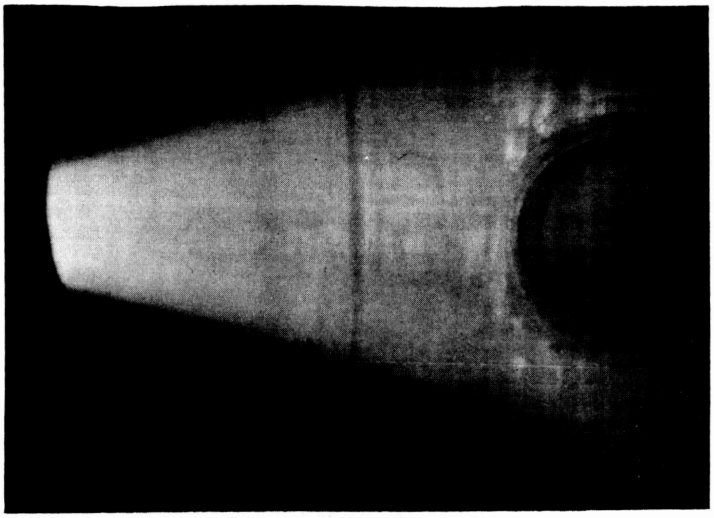

Figure 34. Exhaust Stream Emerging from Mark IV-L Accelerator (on the left) and Impinging on Calorimetric Collector (on the right), Argon, 2 kw, 5 x 10^{-5} torr Background Pressure

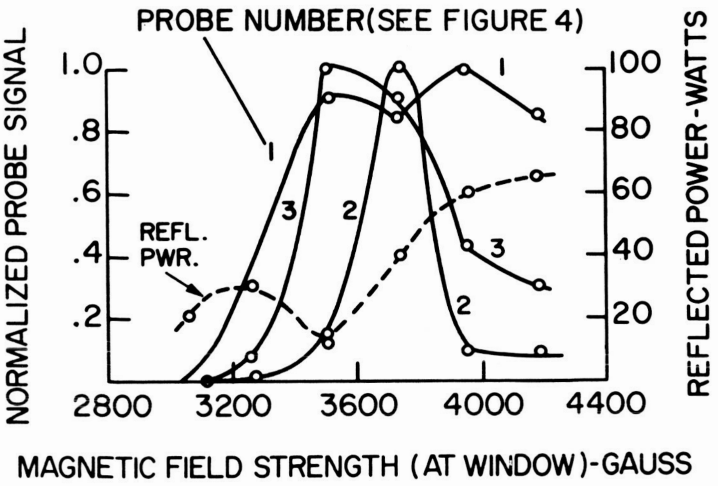

Figure 35. Dependencies of Reflected Power and R-F Antenna Probe Signals on Magnetic Field Strength. Nitrogen; .4 mg/sec, 2 kw R-F Power, Mark IV-L Acceleration

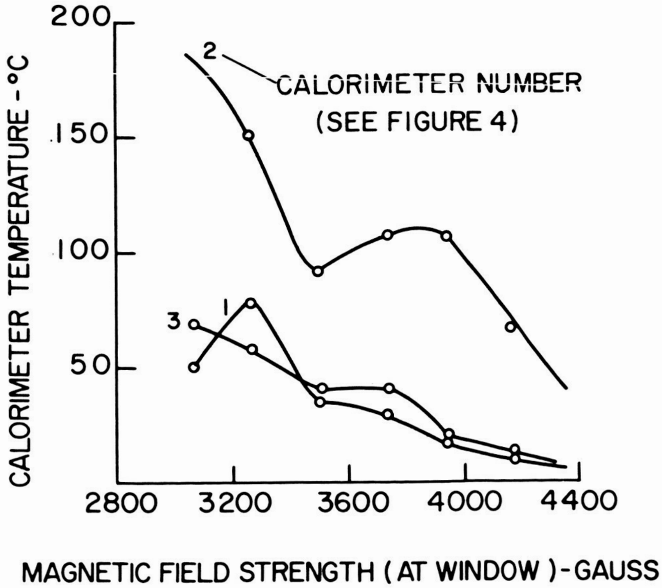

Figure 36. Dependencies of Wall Calorimeter Temperatures on Magnetic Field Strength. Nitrogen, .4 mg/sec, 2 kw R-F Power, Mark IV-L Accelerator

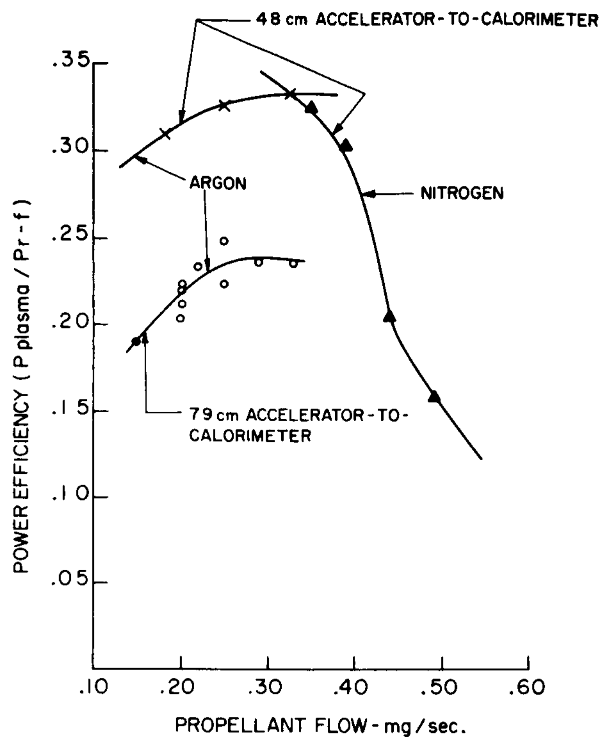

Figure 37. Dependence of Power Efficiency on Propellant Flow Rate, Propellant Species and Calorimeter Position, Mark IV-L Accelerator

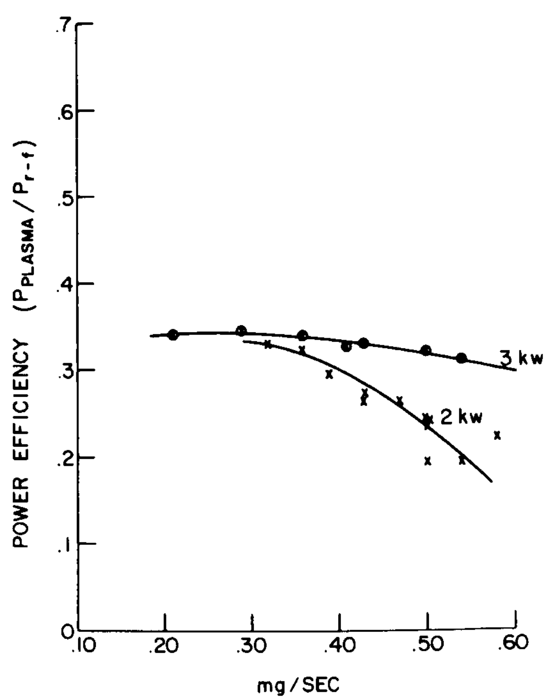

Figure 38. Dependence of Power Efficiency on Mass Flow Rate, Nitrogen, 3730 Gauss Window Magnetic Field Strength, Accelerator-to-Calorimeter Distance 33 cm Mark IV-L Accelerator

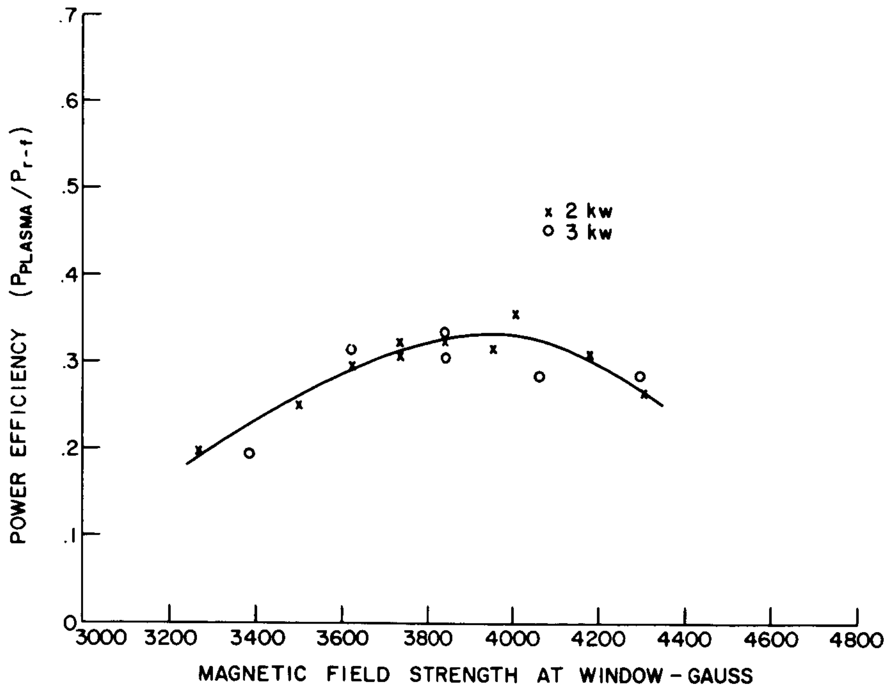

Figure 39. Dependence of Power Efficiency on Magnetic Field Strength, Nitrogen, .36 mg/sec, Accelerator-to-Calorimeter Distance 33 cm, Mark IV-L Accelerator

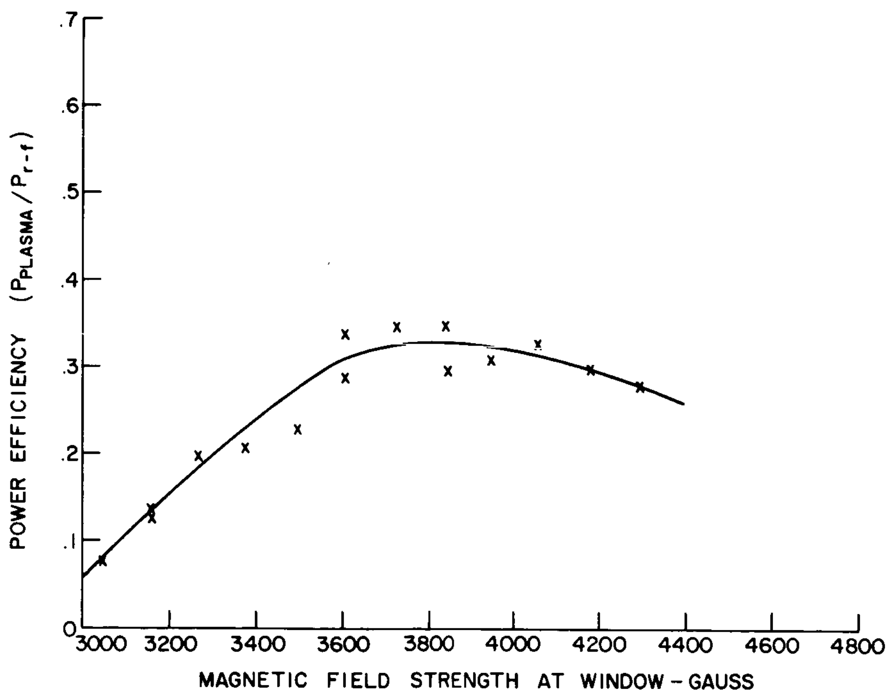

Figure 40. Dependence of Power Efficiency on Magnetic Field Strength, Argon, .19-.22 mg/sec, Accelerator-to-Calorimeter Distance 33 cm. 2 kw. Mark IV-L Accelerator

1. There is an optimum mass flow rate for maximum efficiency (Figures 37 and 38).

2. At high flow rates (> optimum) the efficiency holds up better at higher power, due possibly to frozen flow effects (Figure 38).

3. There is an optimum field for maximum efficiency (Figures 39 and 40).

4. This optimum field is considerably above resonance at the window. This was originally ascribed to plasma diamagnetism, but the magnetic probe has shown that the diamagnetic effect is very low (see Section 4.4). In addition, most of the r-f/ plasma interaction takes place some distance beyond the window. The decrease in wall loss with increasing field (Figure 36) would also aid in achieving higher efficiency at higher field.

5. The optimum field is approximately independent of power (Figure 39) but appears to occur at a higher value with nitrogen than with argon.

6. The best power efficiency for the Mark IV-L accelerator is approximately 35%, with this same peak achieved in both argon and nitrogen. Since the wall calorimeters reveal that less than ten percent of the power is going to the accelerator walls, there must be other avenues through which considerable power is being lost. Much power is undoubtedly going to the ceramic window. Radiation could account for further loss.

More extensive testing of the Mark IV-L accelerator could have been carried out, but the poor power efficiency and the severe wall erosion suggested that time would be better spent investigating other geometries.

4.2 MARK IV-S ACCELERATOR (AXIAL-INJECTION, SHORT VERSION)

The Mark IV-S exhaust stream photograph (Figure 41) reveals that shortening the accelerator has not grossly diminished the collimation of the plasma jet. Power efficiency data are presented in Figures 42-46.

This accelerator was more troubled by window failure than was the Mark IV-L device. It seems likely that the central axial hole through this window weakened it structurally, or there could have been slight dimensional irregularities which, under thermal expansion, caused intolerable stresses. No specific cause for these frequent failures was conclusively determined. As a result, however, significant tests were carried out with two windows, #B4 (Figure 42) and #B5 (Figures 43-46), differing only slightly in the size of the axial injection hole. The B4 window tests resulted in generally higher

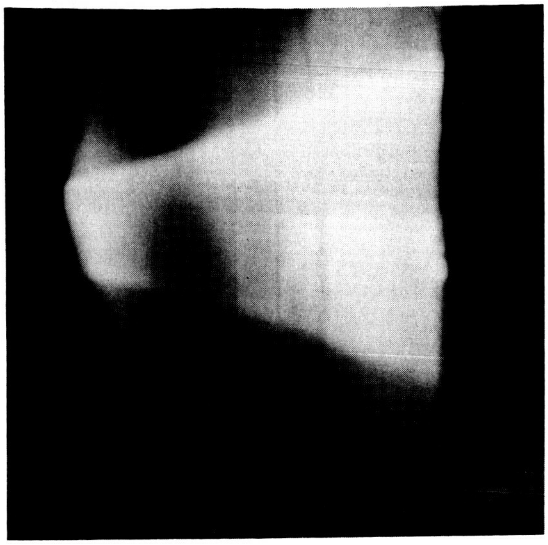

Figure 41. Exhaust Stream Emerging from Mark IV-S Accelerator, Nitrogen, 2 kw, 1 x 10^{-5} Torr Background Pressure

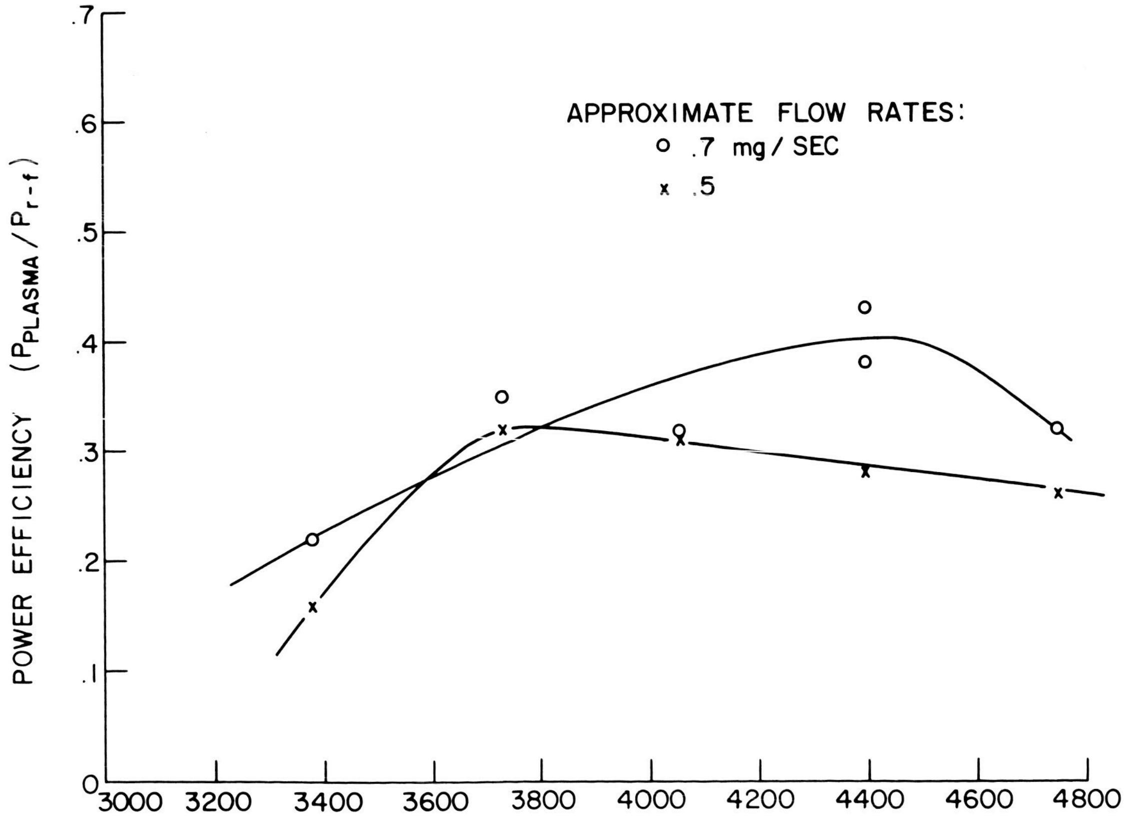

Figure 42. Dependence of Power Efficiency on Magnetic Field Strength, Krypton, 2 kw, Accelerator-to-Calorimeter Distance 43 cm, #B4 Beryllium Oxide Half-Wavelength Window. Mark IV-S Accelerator

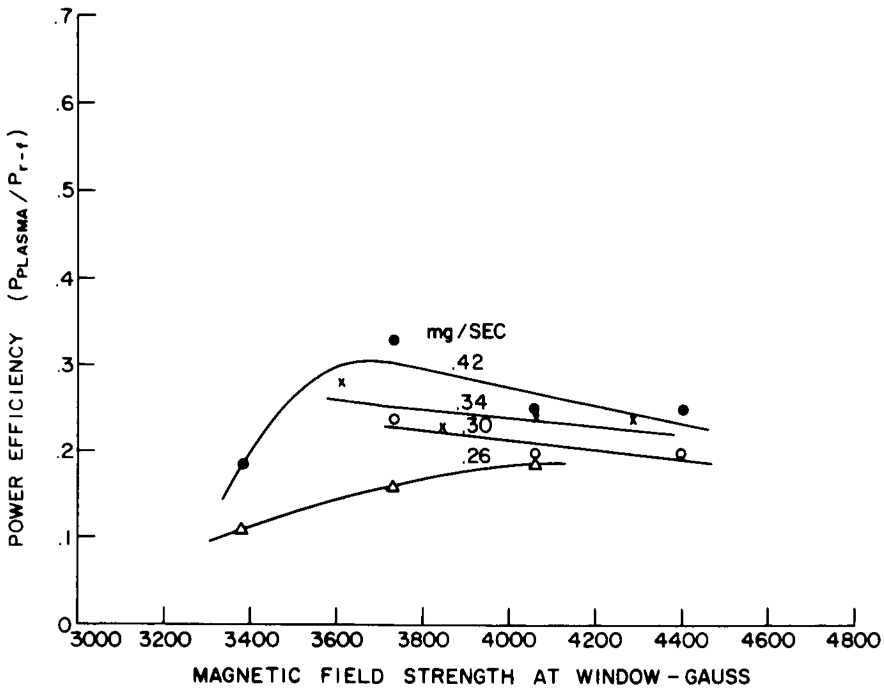

Figure 43. Dependence of Power Efficiency on Magnetic Field Strength, Nitrogen, 2 kw, Accelerator-to-Calorimeter Distance 43 cm, #B5 Beryllium Oxide Half-Wavelength Window, Mark IV-S Accelerator

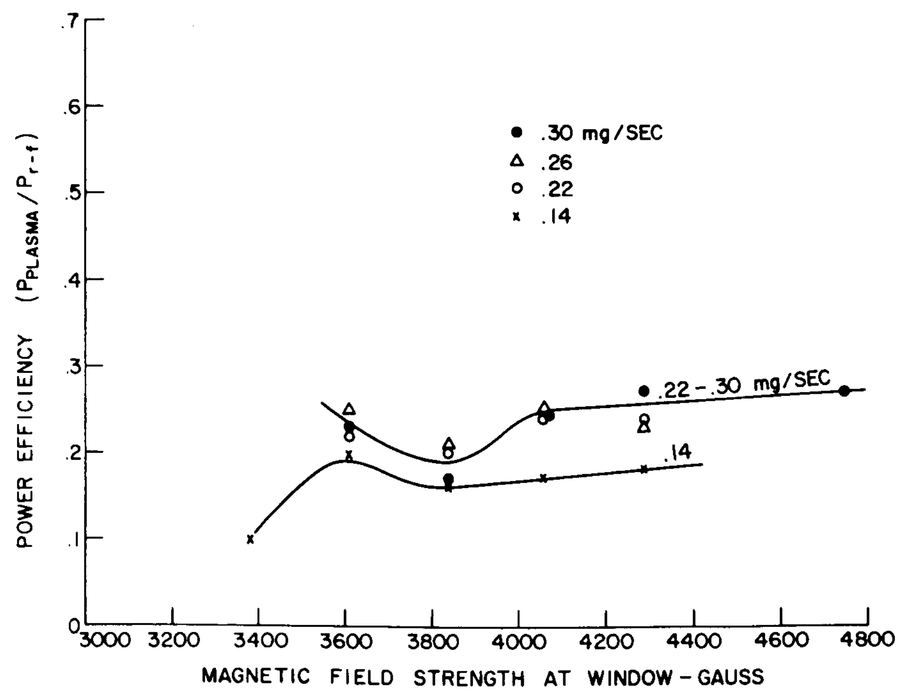

Figure 44. Dependence of Power Efficiency on Magnetic Field Strength, Argon, 2 kw, Accelerator-to-Calorimeter Distance 43 cm, #B5 Beryllium Oxide Half-Wavelength Window, Mark IV-S Accelerator

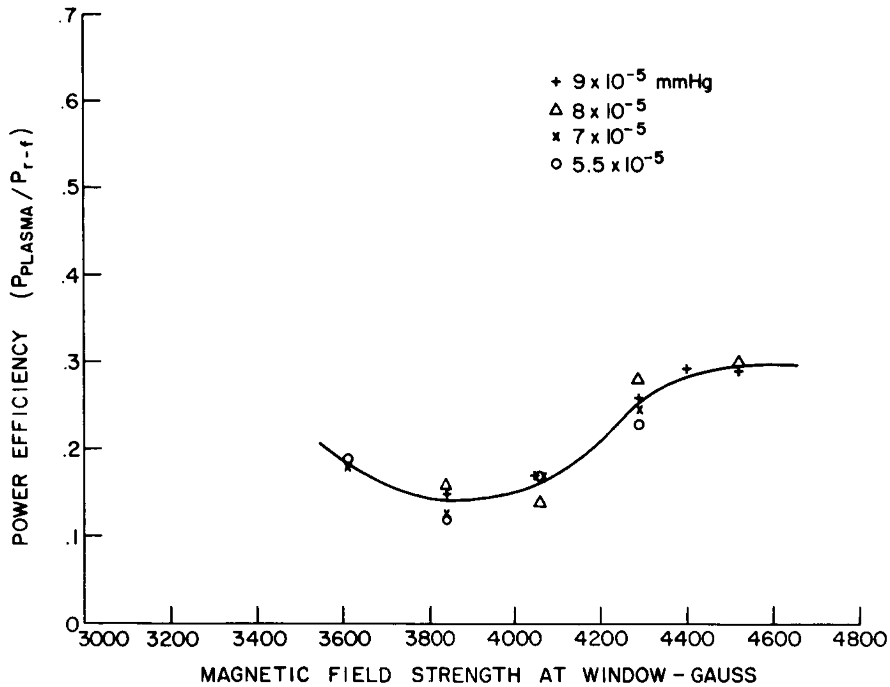

Figure 45. Dependence of Power Efficiency on Magnetic Field Strength, Krypton, 2 kw, Accelerator-to-Calorimeter Distance 43 cm, #B5 Beryllium Oxide Half-Wavelength Window, Mark IV-S Accelerator

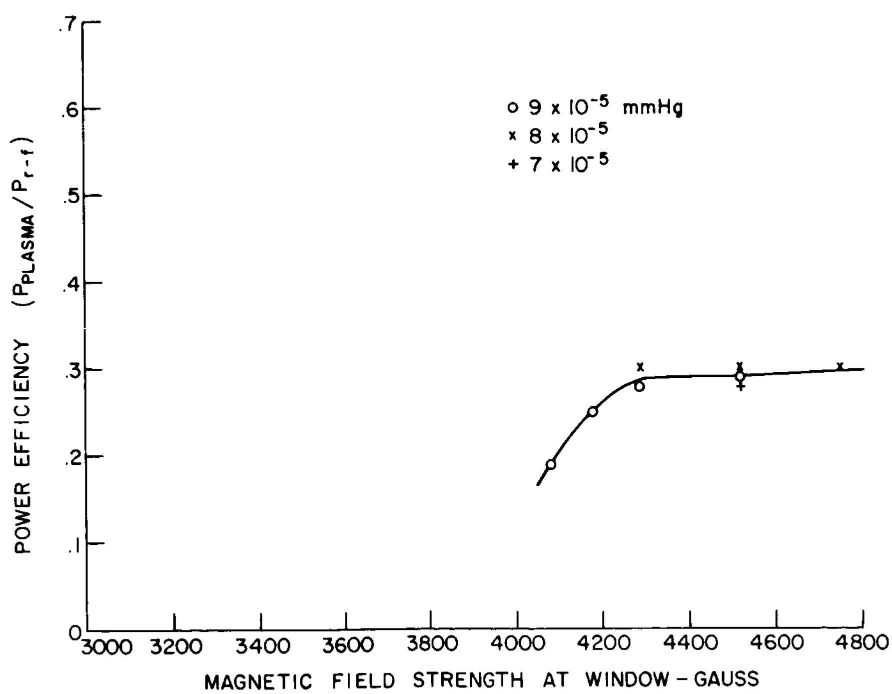

Figure 46. Dependence of Power Efficiency on Magnetic Field Strength, Xenon, 2 kw, Accelerator-to-Calorimeter Distance 43 cm, #B5 Beryllium Oxide Half-Wavelength Window, Mark IV-S Accelerator

efficiency, attaining on one test 42%, as shown in Figure 42. The series of tests using the B5 window and varying the propellant species (Figures 43-46) show that optimum efficiency is essentially independent of molecular weight but that the optimum field strength increases with increasing molecular weight. Since no startling increase in efficiency resulted from shortening of the accelerator, and since in addition wall erosion continued to occur (although the wall in this case was stainless steel), it was decided to turn to the peripheral injection (Mark V) accelerators. Before making this change, however, the sampling probe array was tested briefly with the Mark IV-S accelerator in order that direct comparison with the total calorimeter could be made.

Figure 47 illustrates a three-dimensional plot of the power density distribution as obtained by the diode probes for one set of accelerator operating conditions. An average power density profile taken from the Figure 47 data is shown in Figure 48, and an average ion flux density profile for these same conditions is included as Figure 49. Numerical integrations of these curves are performed in Tables I and II. The power (245 watts) comes out to be approximately equal to the power for these same conditions obtained with the total calorimeter (Figure 43). The ion flux (616.5 ma $\equiv 3.8 \times 10^{18}$ singly charged ions/sec) is approximately two-tenths of the injected neutral flux (.42 mg/sec $\equiv 1.8 \times 10^{19}$ nitrogen atoms/sec). The average particle energy is about 400 ev.

The facts that these total power and particle flux values correlate so well with the measured input flow and total stream power indicate that this type of probe and probe array can yield useful data.* Not only is an independent check on other measured parameters obtained, but also important new information, such as power and particle flux profiles and particle energies, is gathered. Charge exchange processes would cause a reduction in measured ion current but not in measured power. This may account for the ion flux being significantly less than the neutral input flux. This may also be a good method of measuring charge exchange cross section by measuring the decrease in intercepted ion current as a function of distance away from the accelerator.

The primary objection to using an array of this sort is the tediousness of data reduction. More automatic methods may be possible.

---

*Note that the data in Figures 48 and 49 were included in the Semiannual Report (NASA CR-54213; May 17, 1965). The abcissa scale was incorrect, however, causing invalid integrations and data interpretation. These errors have been corrected for this report.

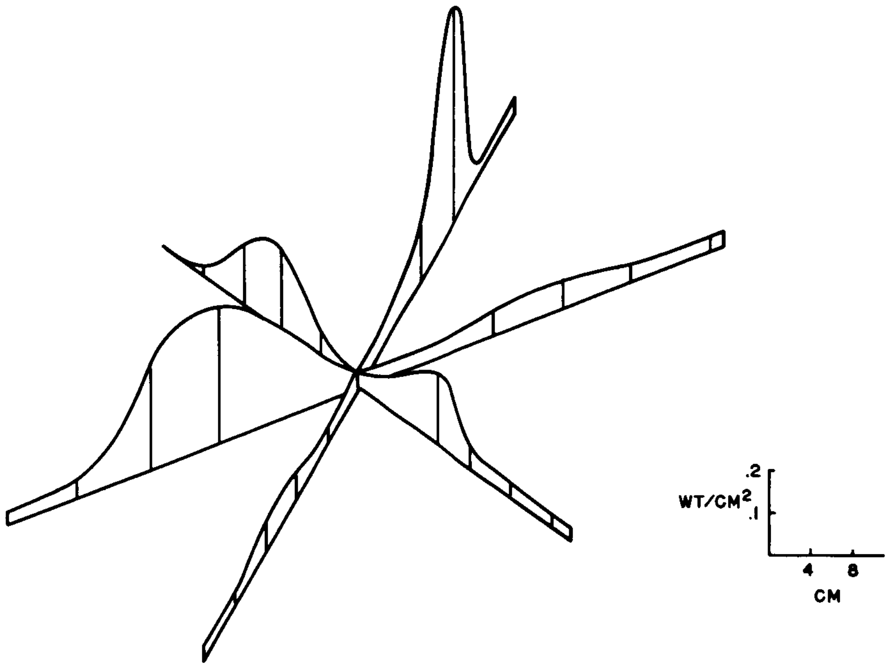

Figure 47. Power Density Contour Mark IV-S Accelerator Nitrogen, .42 mg/sec 2 kw, 3840 Gauss Accelerator-to-Array Distance: 70 cm Ambient Pressure ~ 4 x 10^{-5} Torr

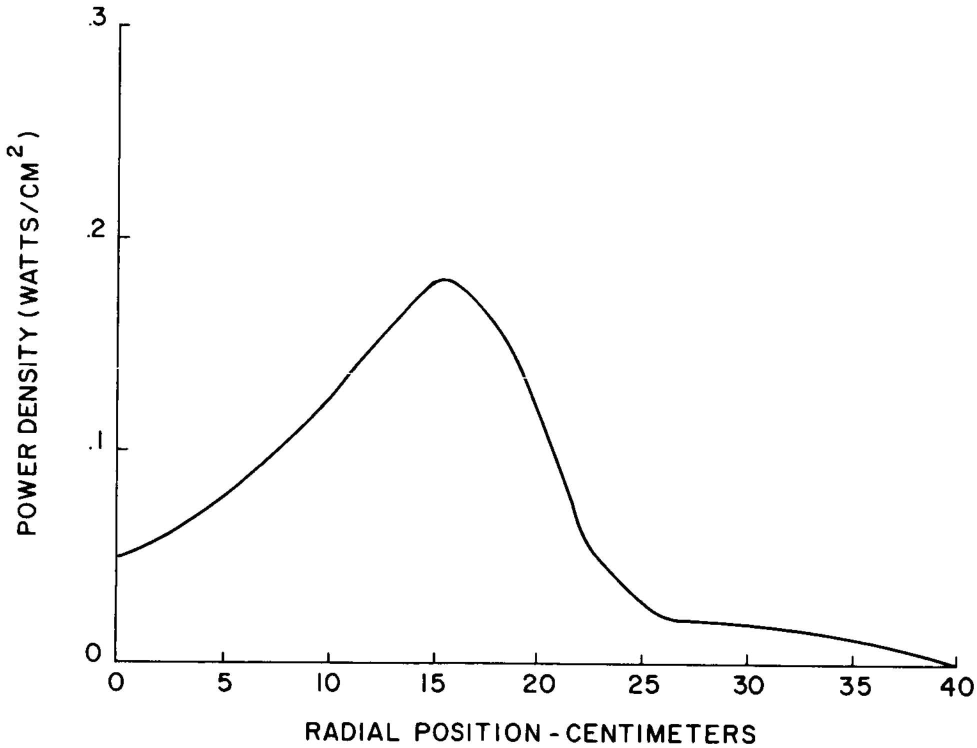

Figure 48. Power Density Profile; Mark IV-S Accelerator; Nitrogen, .42 mg/sec 2 kw, 3320 Gauss Accelerator-to-Array Distance 70 cm Ambient Pressure ~ 4 x 10^{-5} Torr

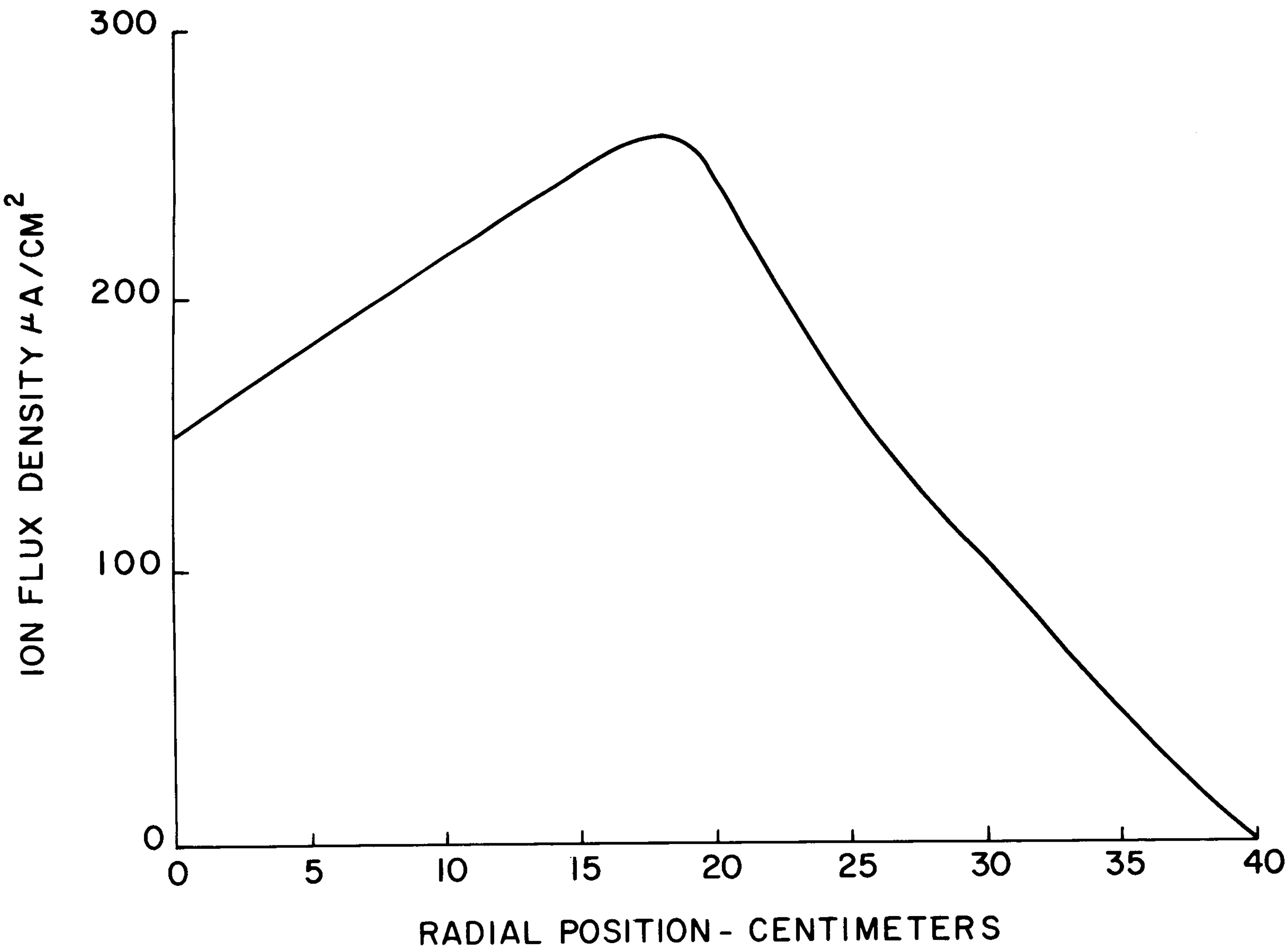

Figure 49. Ion Flux Density Profile Mark IV-S Accelerator Nitrogen, .42 mg/sec 2 kw, 3320 Gauss, Accelerator-to-Array Distance 70 cm, Ambient Pressure $\sim 4 \times 10^{-5}$ Torr

TABLE I.

Integration of Figure 48. Exhaust Stream Power, Mark IV-S Accelerator, nitrogen, .42 mg/sec., 2 kw, 3320 gauss, accelerator-to-array distance 70 cm.

r_n	$A_{n-(n-1)}$	$\bar{p}$	P
cm	cm^2	wt/cm^2	watts
2	13	.06	1
4	37	.07	3
6	63	.09	6
8	88	.11	10
10	113	.12	14
12	138	.14	19
14	163	.17	28
16	190	.18	34
18	215	.16	34
20	240	.12	29
22	260	.07	18
24	290	.03	9
26	320	.02	6
28	340	.02	7
30	370	.02	7
32	390	.02	8
34	410	.02	8
36	440	.01	4
38	460	.0	0
40	490	0	0
		Total	245 watts

TABLE II.

Integration of Figure 49. Exhaust Stream Ion Flux, Mark IV-S Accelerator, nitrogen, .42 mg/sec., 2 kw, 3320 gauss, accelerator-to-array distance 70 cm.

r_n	$A_{n(n-1)}$	$\bar{i}$	I
cm	cm^2	$\mu a/cm^2$	ma
2	13	160	2.1
4	37	175	6.5
6	63	190	12.0
8	88	200	17.6
10	113	215	24.3
12	138	230	31.8
14	163	240	39.2
16	190	255	48.5
18	215	260	55.8
20	240	245	61.3
22	260	210	54.6
24	290	175	50.7
26	320	150	48.1
28	340	125	42.5
30	370	105	38.9
32	390	80	31.2
34	410	60	24.6
36	440	40	17.6
38	460	20	9.2
40	490	0	0
		Total	616.5 ma

The potential probes were first used with the Mark IV-S accelerator. Since for these measurements the data were read from meters, only two sketchy sets of emitting and non-emitting curves were obtained during the limited times available. The forms of these curves are similar to those obtained from the Mark V-L accelerator (discussed later) and shown in Figure 50.

Although the breaks in the I-V (i.e., probe current vs. potential) curves were not as sharp as desired and did not necessarily agree with the probe voltage at which the emitting and non-emitting curves started to become mutually parallel, the plasma potentials appeared to be about +15 volts at the probes, and the probe currents were as great as 0.5 ma at +30 volts probe bias. Specifically, probe A indicated a local plasma potential of perhaps +14 volts during one accelerator run, while probe B (6.5 cm closer to accelerator than A) indicated a local plasma potential of perhaps +17 volts during the next accelerator run. Both of these values could be as high as +20 volts.

In these first measurements with the energy analyser probe, the probe data were obtained point-by-point from meters. Consequently, the few points that could be read during a run gave plots which showed only the gross features of the accelerator ion energy. The curves thus obtained followed the same general pattern as shown in Figure 51. Figure 51 shows an energy analyser probe I-V response curve which was obtained with an X-Y plotter in conjunction with the Mark V-L accelerator discussed in a later section. The ion energy distribution is determined from these I-V curves by taking their derivative and plotting dI/dV vs. $(V-V_p)$ where I is probe current, V is volts, and V_p is plasma potential. For this accelerator, the potential probe indicated a plasma potential of perhaps 15 volts.

The energy analyzer probe results are indicated in Table III below.

TABLE III.

Energy Analyser Probe Measurements - Mark IV-S Accelerator.
nitrogen, 0.42 mg/sec., 3840 gauss (at window)

Accel. r-f power (kw)	Plasma Jet Ions	
	Avg. Energy (ev)	Energy Spread (ev)
2	96	28
2	~110	~50
1	85	35
3	197	71

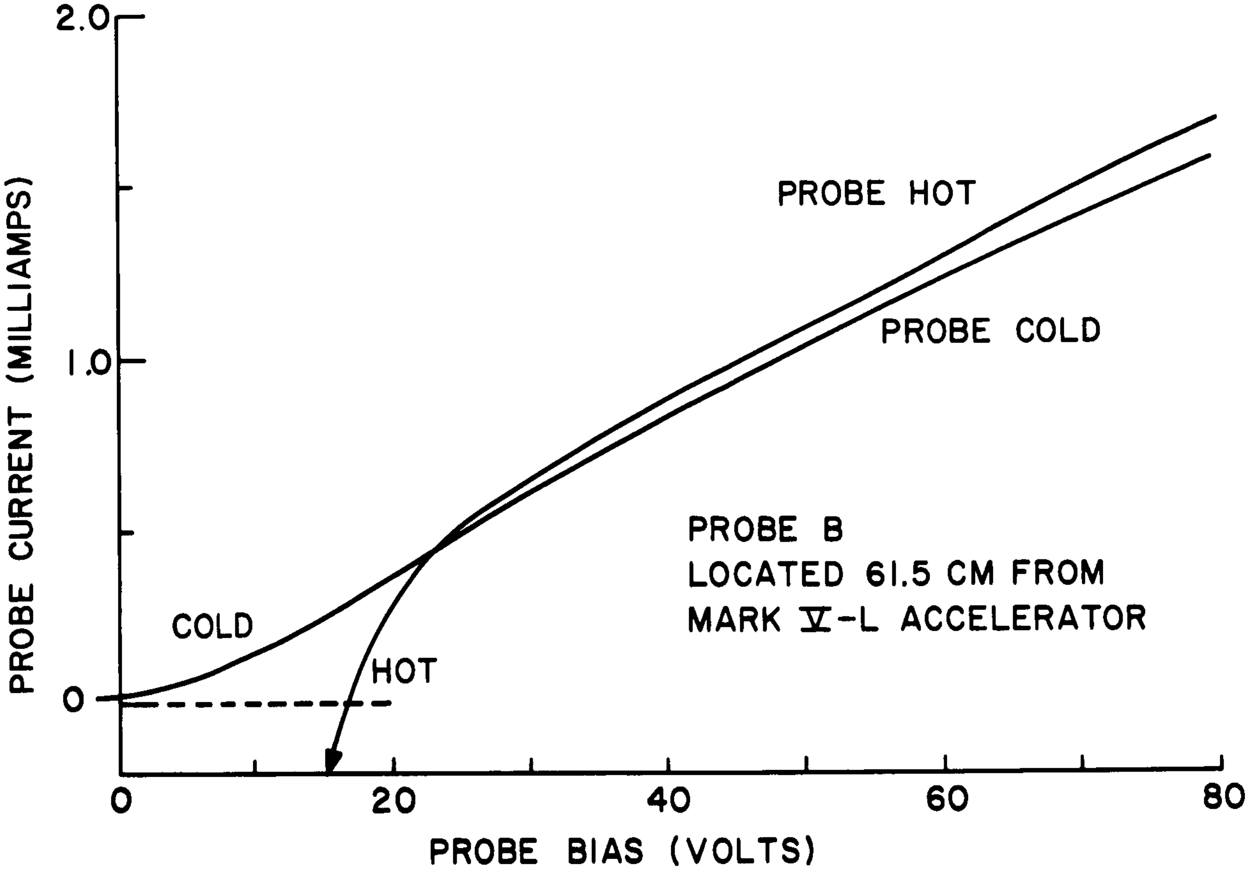

Figure 50. Typical Emitting Potential Probe Current Response with Accelerator Operating

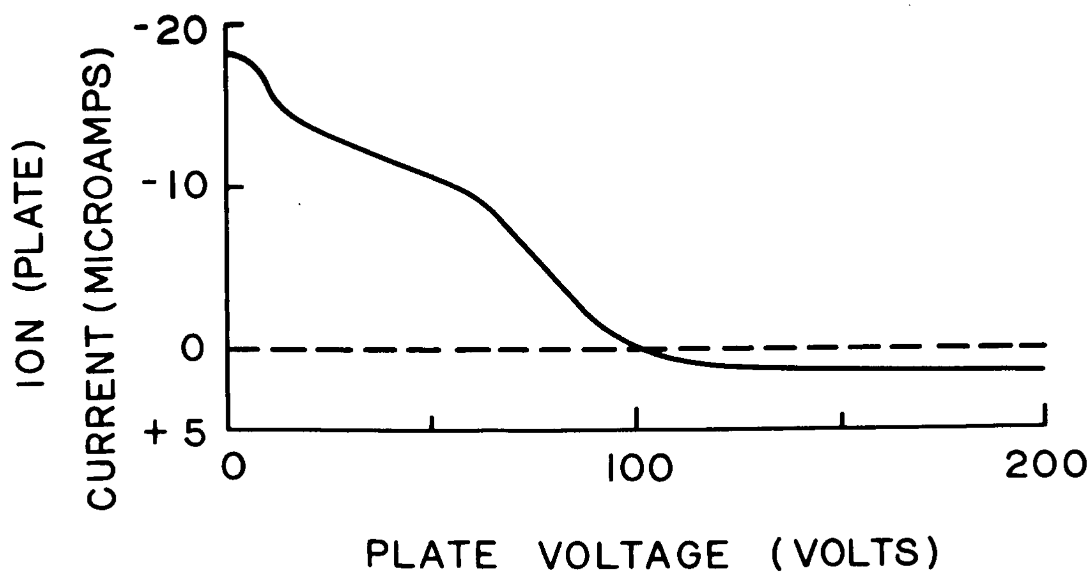

Figure 51. Energy Analyser Probe Response Curve. Probe is Located 68 cm from Mark V-L Accelerator, with Probe Electron Repelling Grid Biased at -250 Volts

Before obtaining the I-V curves which led to these results, it was determined that for a Mark IV-S two-kilowatt accelerator run, at least - 70 volts was required on the electron repelling grid to eliminate all electron current at the positive plate. Consequently, repelling grid potentials of -100 volts or - 150 volts (for 3 kw run) were used in all cases.

It can be concluded first that the energy analyser probe operated as expected. Since no ion current exceeded 30 microamperes total (< 0.1 milliamp cm^{-2}), no space charge limiting could have occurred. As discussed elsewhere, the space charge limit for this probe was calculated to be about 2 milliamps cm^{-2}.

As to the probe results, we see from Table III that the main body of ions tend to reach the energy analyser probe with energy spreads of 30-70 electron volts and average $e(V-V_p)$ energies of about 85-200 electron volts, the average energy increasing as the r-f power level is increased from one to three kilowatts. This trend is as expected. However, an interesting result is that the lowest r-f power level runs of the accelerator appeared to yield the highest ion currents.

4.3 MARK V-L ACCELERATOR (PERIPHERAL-INJECTION, LONG VERSION)

4.3.1 Total Calorimeter

The 24" diameter by 10" deep calorimeter (Figure 16) was used to measure the Mark V-L accelerator power efficiency. Results are plotted in Figures 52 and 53. The reader will note that no marked gain in efficiency has resulted by going back to the peripheral injection technique. Perhaps because this is a long accelerator, wall losses were again high. This unfortunately could not be checked directly since the wall calorimeters in this model did not give reliable results.

Further probe tests were carried out with this accelerator, as described below, before going on to another accelerator.

4.3.2 Diode Probe Array

Since there is considerable effort involved in setting up and removing the diode probe array, initial tests on the Mark V-L accelerator were made using the array, it being already in position from the final Mark IV-S tests. Power density and ion flux density curves for one operating point are shown in Figures 54, 55 and 56. The power and ion flux integrations are performed in Tables IV and V. The integrated probe array power is now found to be greater than the total calorimeter power, (compare Figure 53 and Table IV).

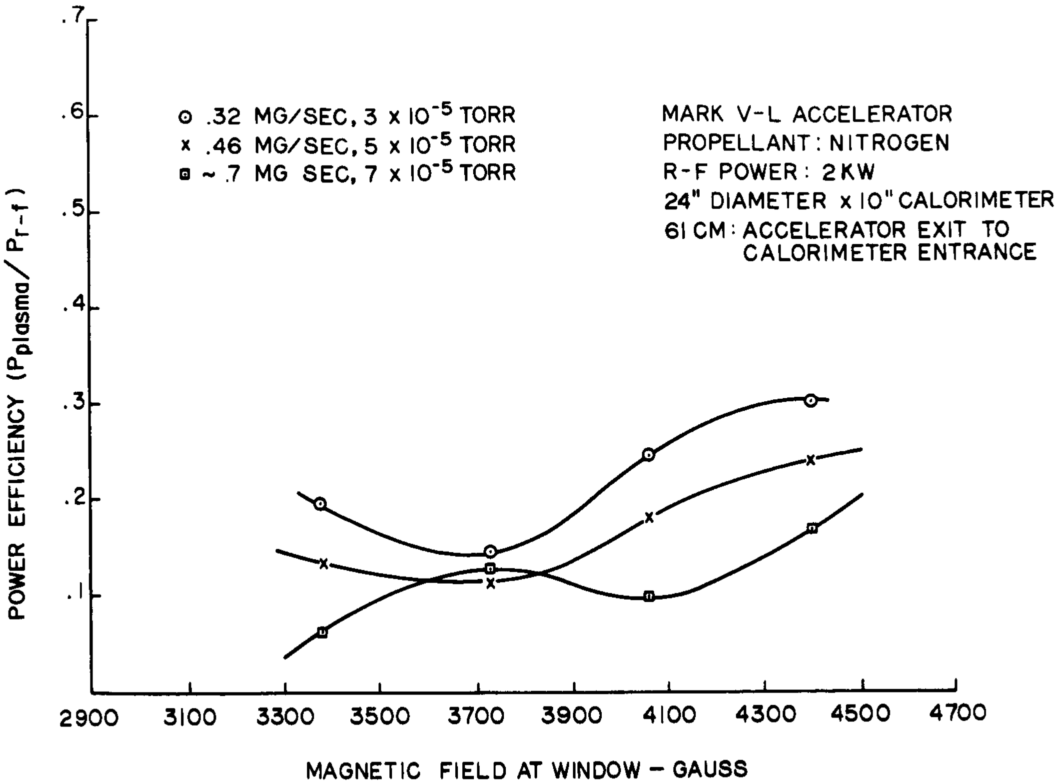

Figure 52. Dependence of Power Efficiency on Magnetic Field Strength

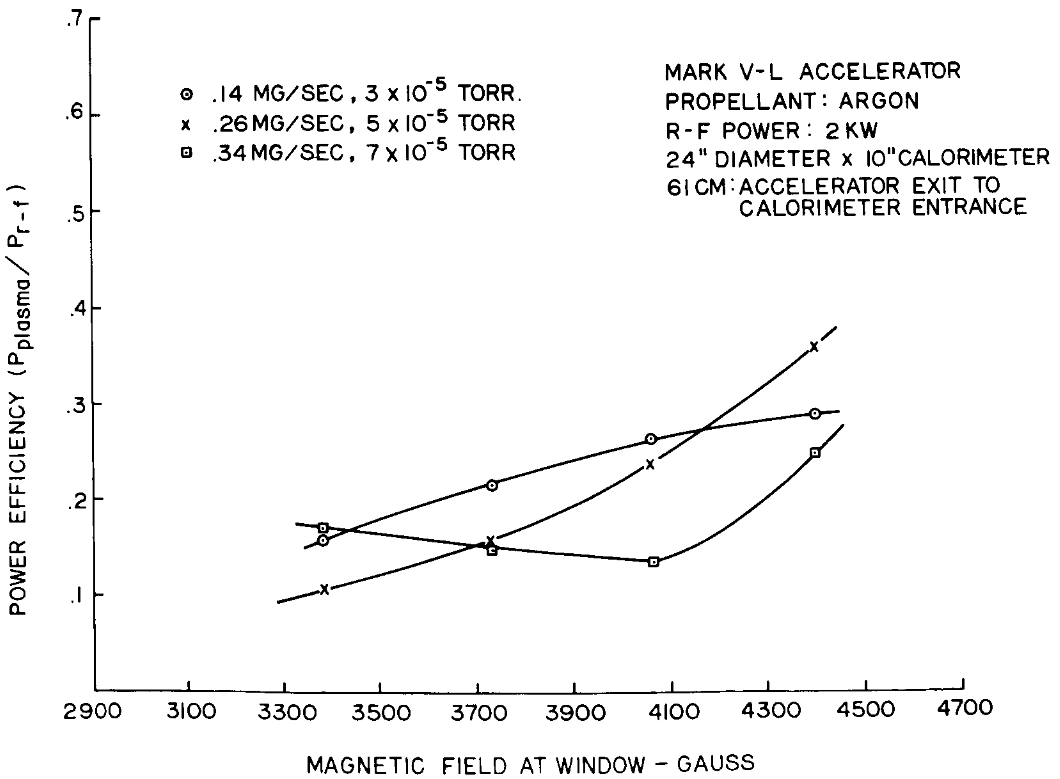

Figure 53. Dependence of Power Efficiency on Magnetic Field Strength

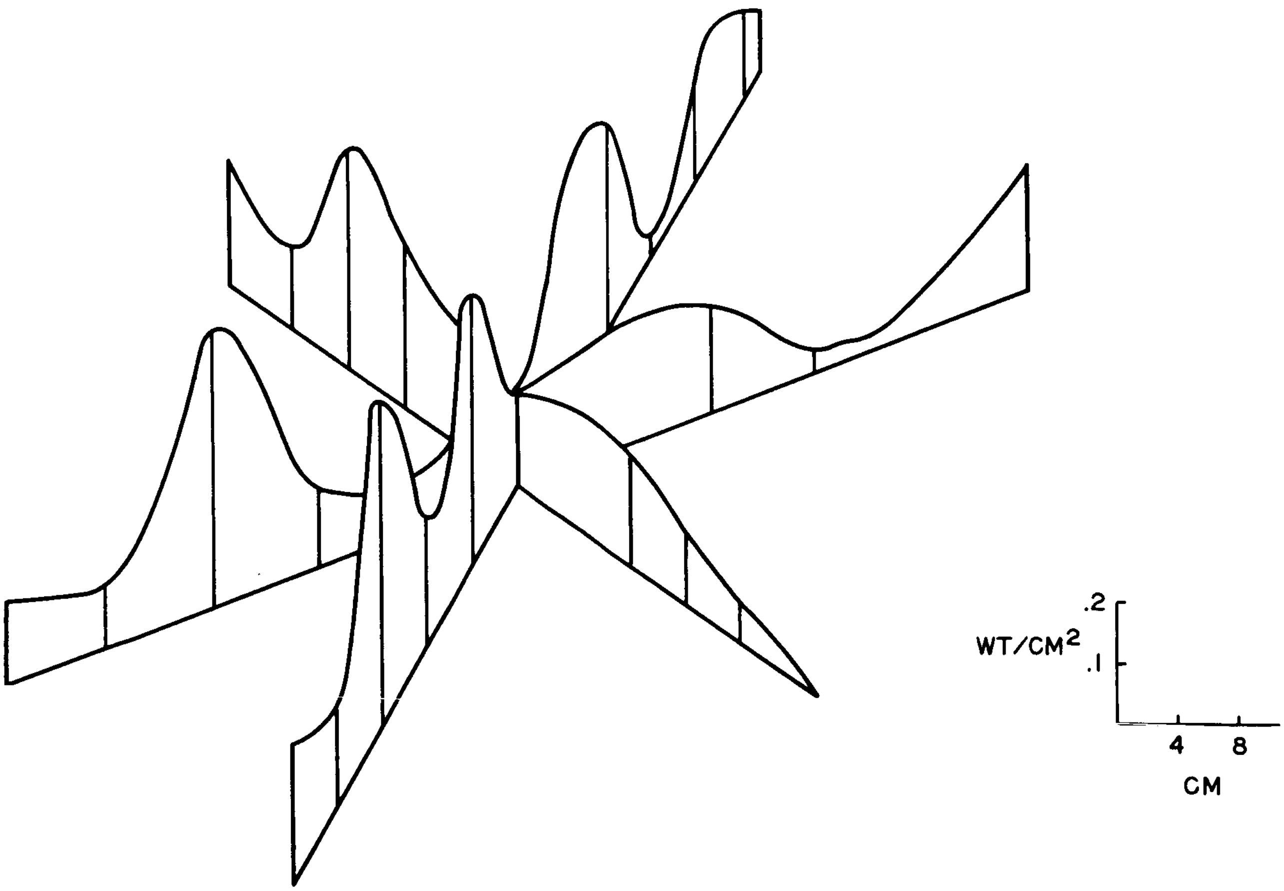

Figure 54. Power Density Contour Mark V-L Accelerator Argon, .28 mg/sec 2 kw, 3730 Gauss Accelerator-to-Array Distance 70 cm, Ambient Pressure 2.5 x 10^{-5} Torr

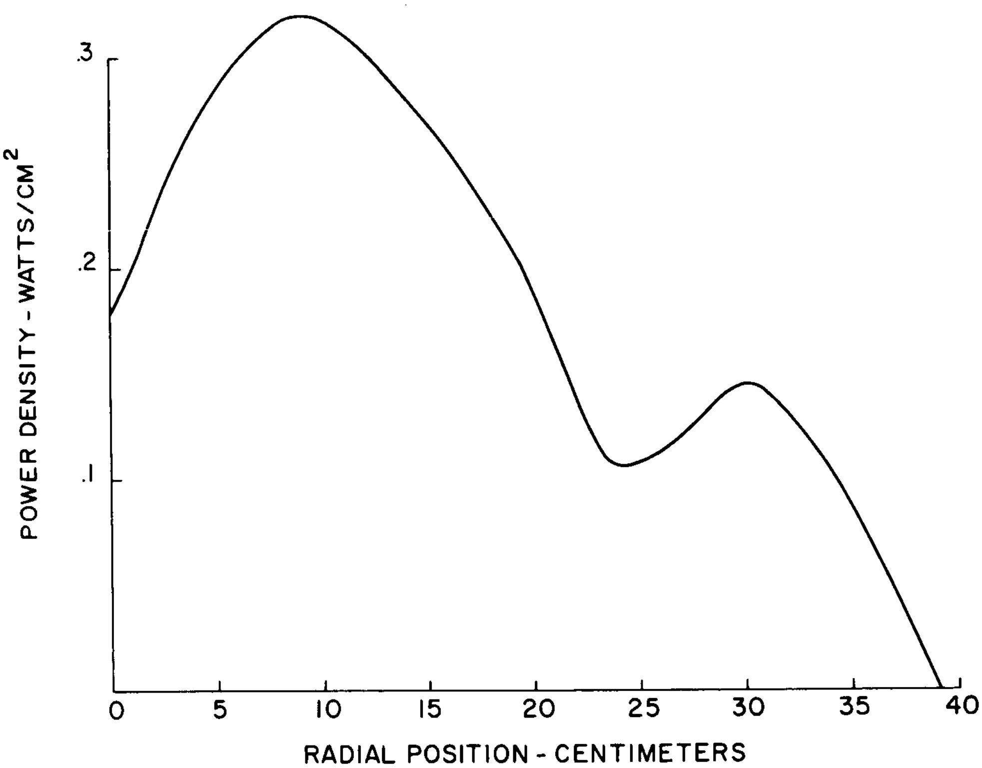

Figure 55. Power Density Profile Mark V-L Accelerator Argon, .28 mg/sec 2 kw, 3730 Gauss at Window Accelerator-to-Array Distance 70 cm Ambient Pressure 2.5 x 10^{-5} Torr

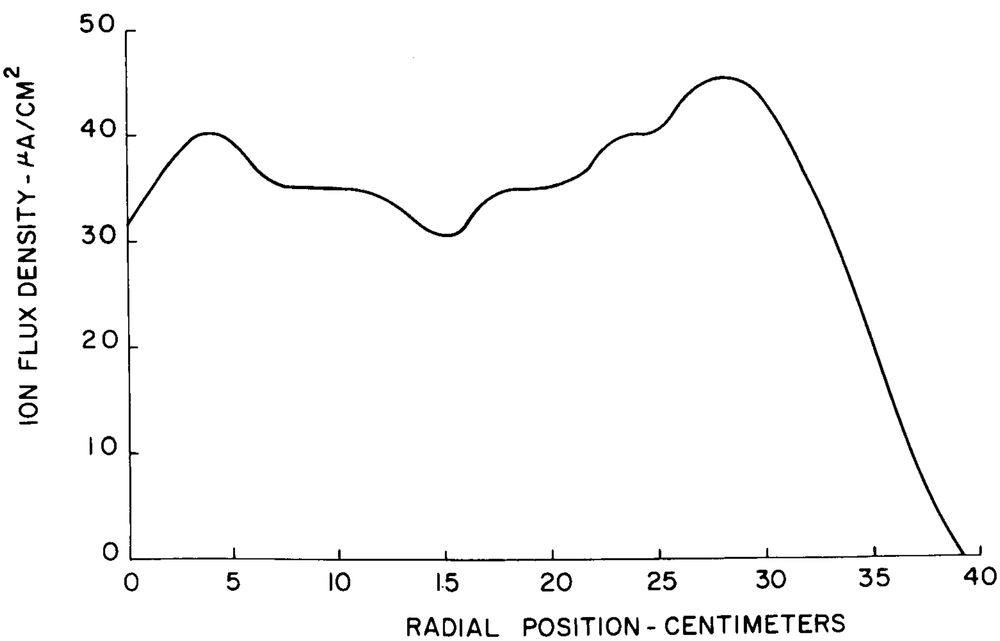

Figure 56. Ion Flux Density Profile Mark V-L Accelerator Argon, .28 mg/sec 2 kw, 3730 Gauss at Window Accelerator-to-Array Distance 70 cm Ambient Pressure 2.5 x 10^{-5} Torr

TABLE IV.

Integration of Figure 55. Exhaust Stream Power, Mark V-L Accelerator, argon, .28 mg/sec., 2 kw, 3730 gauss, accelerator-to-array distance 70 cm

r_n	$A_{n-(n-1)}$	$\bar{p}$	P
cm	cm^2	wt/cm^2	wt
2	13	.20	3
4	37	.25	9
6	63	.29	18
8	88	.31	27
10	113	.32	36
12	138	.31	43
14	163	.29	47
16	190	.27	51
18	215	.24	52
20	240	.21	50
22	260	.16	42
24	290	.11	32
26	320	.11	35
28	340	.12	40
30	370	.14	52
32	390	.14	55
34	410	.12	49
36	440	.09	40
38	460	.04	18
40	490	0	0
		Total	699 watts

TABLE V.

Integration of Figure 56. Exhaust Stream Ion Flux, Mark V-L Accelerator, argon, .28 mg/sec., 2 kw, 3730 gauss, accelerator-to-array distance 70 cm.

r_n	$A_{n-(n-1)}$	$\bar{i}$	I
cm	cm^2	μ a/cm^2	ma
2	13	35	.5
4	37	40	1.5
6	63	40	2.5
8	88	35	3.1
10	113	35	4.0
12	138	35	4.8
14	163	35	5.7
16	190	30	5.7
18	215	35	7.5
20	240	35	8.8
22	260	35	9.1
24	290	40	11.6
26	320	40	12.8
28	340	45	14.9
30	370	45	16.7
32	390	40	15.6
34	410	30	12.3
36	440	20	8.8
38	460	10	4.1
40	490	0	0
		Total	150 ma

The ion flux (150 ma ≡ 9.4×10^{17} singly-charged-ions/sec) is again somewhat less than the injected neutral flux (.28 mg/sec - 4.2×10^{18} argon molecules/sec), possibly due to charge exchange processes. The calculated ion energy, 4650 ev, is rather high, further supporting the possibility of significant charge exchange.

4.3.3 Potential Probe Measurements

The potential probes were used on several runs of the Mark V-L accelerator. Since for these runs the current and voltage data were recorded on an X-Y plotter, the curves are better and much more numerous than was the case with the Mark IV-S accelerator already discussed.

To determine the potential probe emission current (I) as a function of potential difference (V) between probe and surroundings, the probe I-V curves were measured when emitting in the accelerator testing tank, but with the accelerator not operating. These curves are shown in Figure 57 for both probes A and B. Since the emission current of both probes was -0.03 milliamps at V = 0 volts, this value was used at the "break" in the emitting probe plasma I-V curves so as to aid in estimating the plasma potential at the probe position. Of course, in a plasma the probe- "collector" distance (sheath thickness) is smaller than in the case of no plasma where the plasma sheath thickness is replaced by the probe-to-tank wall and probe support distance. Consequently, in a plasma the probe emission currents can be much greater than shown in Figure 57.

A typical plasma potential curve during accelerator operation is shown in Figure 50. In this series of measurements, saturated probe currents at +50 volts bias varied from 0.4 to about 7 milliamps. As shown in Figure 50, the emitting probe current normally did not coincide with the non-emitting current at bias voltage > V_p (local plasma potential), nor were the two curves always straight or parallel at bias voltage > V_p. Since the plasma potential was not always clearly indicated by the I-V curves, V_p was estimated (in order of credibility) first from the "break" in the emitting curve and second from the divergence from parallel of the emitting and non-emitting curves. Any "knee" in the non-emitting I-V curve was usually too ill-defined to be useful. As indicated earlier, probe A was 2 cm ahead of the diode probes and 68 cm from the accelerator exit, while probe B was 8.5 cm ahead of the diode probes and 61.5 cm from the accelerator exit. Part way through the runs, probe A developed a short to ground, after which only probe B data were obtained.

All but three of the 22 plasma potentials were between +16 and +25 volts from ground. In those few cases where both probes A and B were operated during the same run, probe B showed a 5-7 volt higher V_p than probe A.

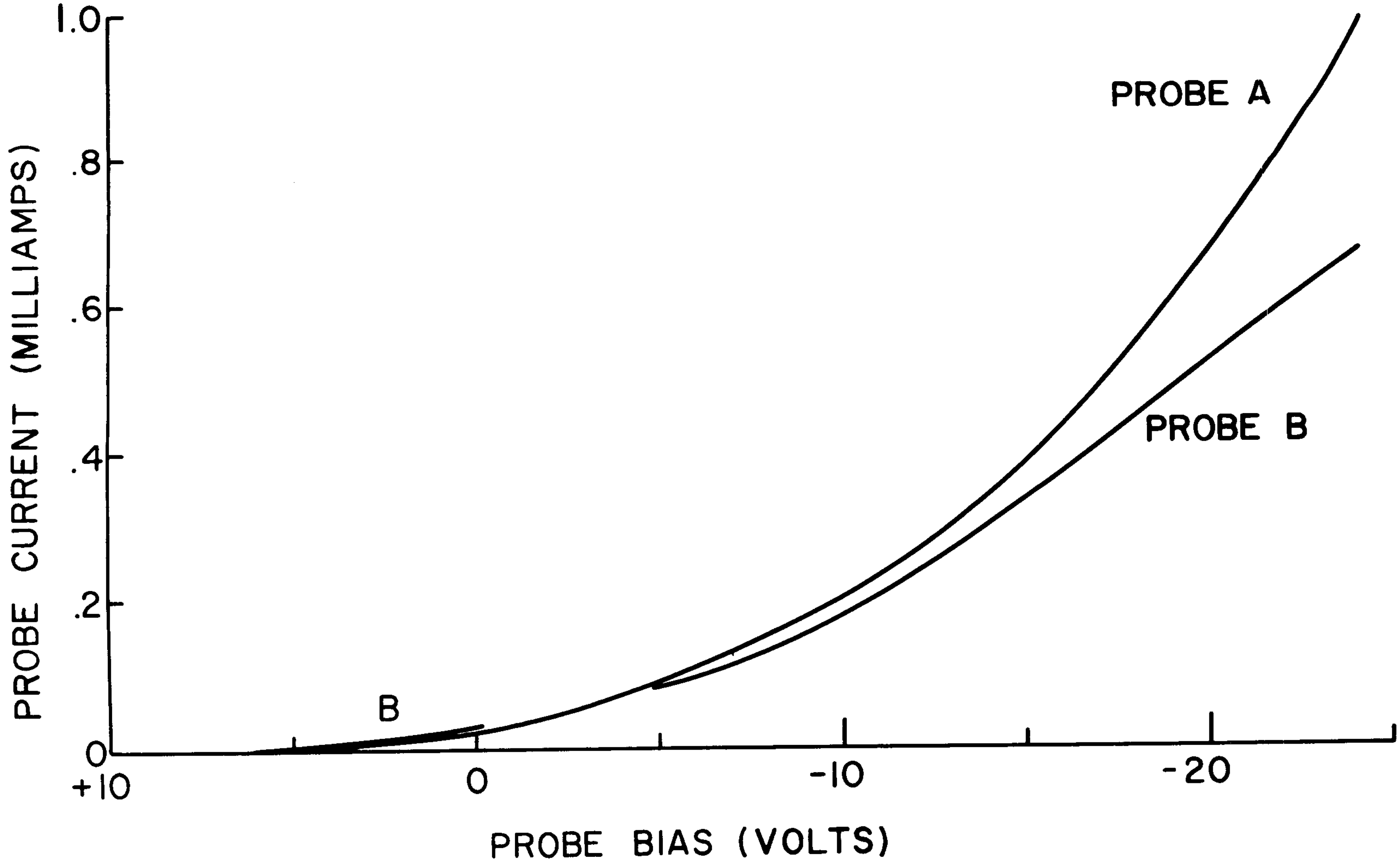

Figure 57. Hot Potential Probe Emission Current in Vacuum Tank. No Plasma Present

4.3.4 Energy Analyser Probe Measurements

For the Mark V-L accelerator measurements, the energy analyser probe data were recorded with an X-Y plotter. This yielded probe response I-V (current-voltage) curves such as shown in Figure 51. As mentioned elsewhere, the ion energy distribution is determined from these I-V curves by plotting dI/dV vs. $(V - V_p)$, where I is (ion) current, V is probe plate voltage, and V_p is local plasma potential. For this accelerator, the potential probe usually indicated plasma potentials of about 20 volts in the vicinity of the energy analyser probe.

The energy analyser probe results are indicated in Table VI.

TABLE VI.

Energy Analyser Probe Measurements - Mark V-L Accelerator.

Accel. Conditions			Plasma Jet Ions	
r-f Power (kw)	Gas	Gas Flow (mg/sec)	Avg. Energy (ev)	Energy Spread (ev)
1	N_2	0.42	62	31
1.5	Ar	0.22	61	38
2	Ar	0.26	57	41

Only three analyser probe runs were made on the Mark V-L accelerator because grid to plate leakage developed during the third analyser probe run, and rapidly became too serious for further use of the probe. However, for these three runs, we see that the main body of ions appears to reach the energy analyser probe with an energy spread of 30-40 electron volts, and in all cases with an average $e(V-V_p)$ energy of about 60 electron volts.

Another feature of these energy analyser probe I-V curves (see Figure 51) is the indication of another, smaller, body of particles centering at about -8 electron volts $[e(V-V_p)]$. In Figure 51 this group is indicated at a slightly positive potential because V_p has not yet been subtracted from the potential. This group of particles might be due to a relatively quiescent ion gas which enters the probe with little or no directed energy. Such a quiescent ion gas might be produced through collision of accelerator ions or electrons with any vacuum chamber ambient gas. That these particles center at an $e(V - V_p)$ energy of -8 rather than zero electron volts, is not understood, unless the V_p used is in error by that amount. This low energy group of particles may also have been present in the Mark IV-S runs reported elsewhere, but their presence would not have been discovered due to the very few data points read in that voltage range (X-Y plotter not used there).

4.3.5 R-f Probes

Data obtained from the r-f probes in the Mark V-L plasma chamber have been reduced and curves obtained from these data are plotted in Figures 58-61. These probes are antenna wires in the walls of the plasma chambers separated from the plasma by quartz covers. Probe details are shown in Figure 4. Probe locations on the Mark V-L accelerator are shown in Figure 7, probes #2, 3, 4 and 5 are, respectively, .2, .4, .6 and .8 inches beyond the plasma side of the dielectric window.

It is evident that a rather complex pattern exists, apparently something like a decaying standing wave pattern. Because of this complexity, it is difficult to make a quantitative measure of the attenuation parameter. The expected deep propagation at large fields is discernible from these curves.

4.4 MARK V-S ACCELERATOR (PERIPHERAL-INJECTION, SHORT VERSION)

A photograph of the exhaust stream emerging from the Mark V-S accelerator is shown in Figure 62. The stream is apparently well collimated.

A thermocouple located on the outer surface of the accelerator adjacent to the window monitors the plasma chamber wall temperature. A typical record of this temperature during a test is shown in Figure 32. It is seen that the accelerator approaches an equilibrium temperature which is a function of plasma conditions, with high magnetic fields resulting in lower accelerator temperatures (and higher calorimeter temperatures), confirming a result previously obtained with the wall calorimeters in the Mark IV-L accelerator.

The engine is cooled by flowing water through a ring-shaped duct adjacent to the window flange (see Figures 7 and 8). The flow rate is approximately 15 cc/sec., corresponding to 63 watt/^{o}C. The fact that after a test the accelerator cools much more rapidly with the water flowing than with the water turned off indicates that this water flow is the major means by which heat is taken away from the accelerator.

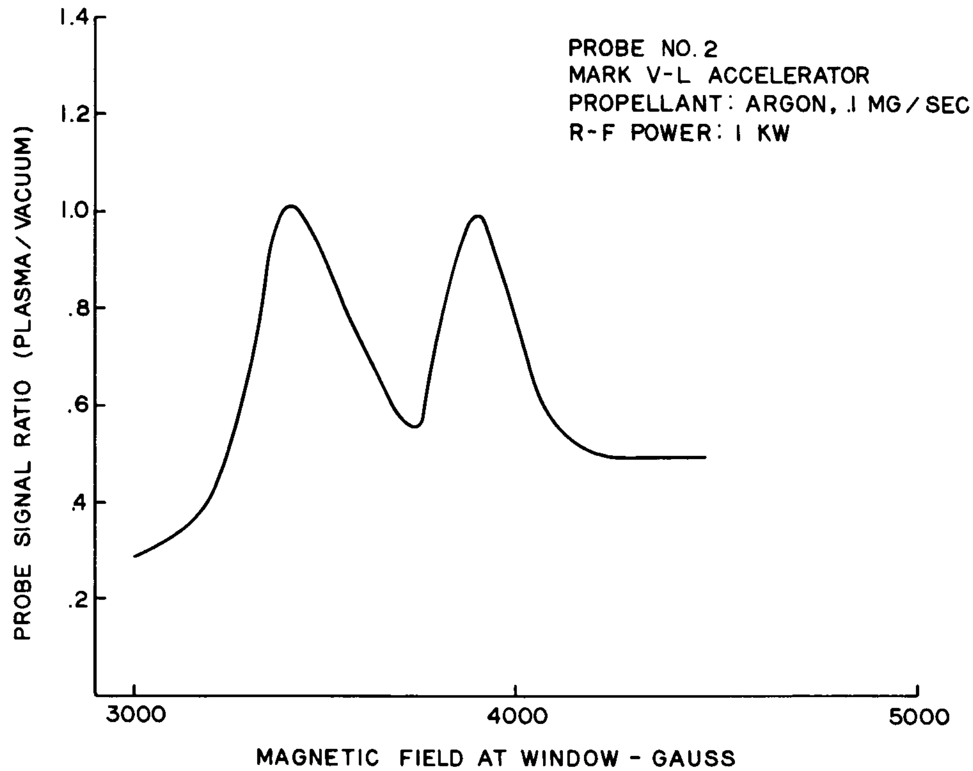

Figure 58. Dependence of R-f Probe Signal on Magnetic Field Strength

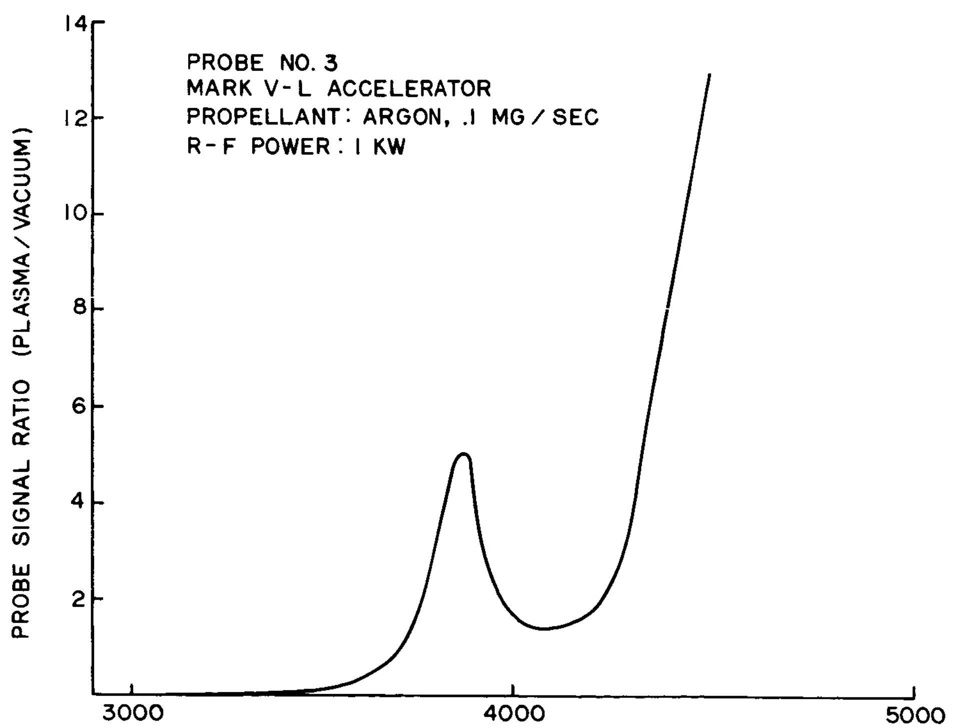

Figure 59. Dependence of R-f Probe Signal on Magnetic Field Strength

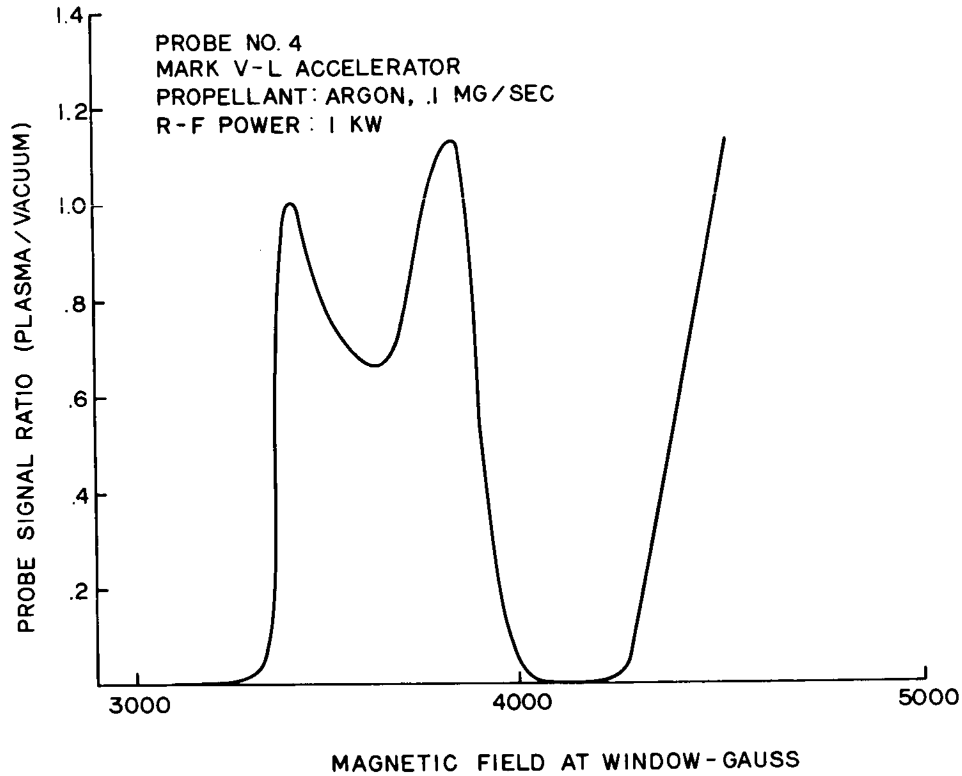

Figure 60. Dependence of R-f Probe Signal on Magnetic Field Strength

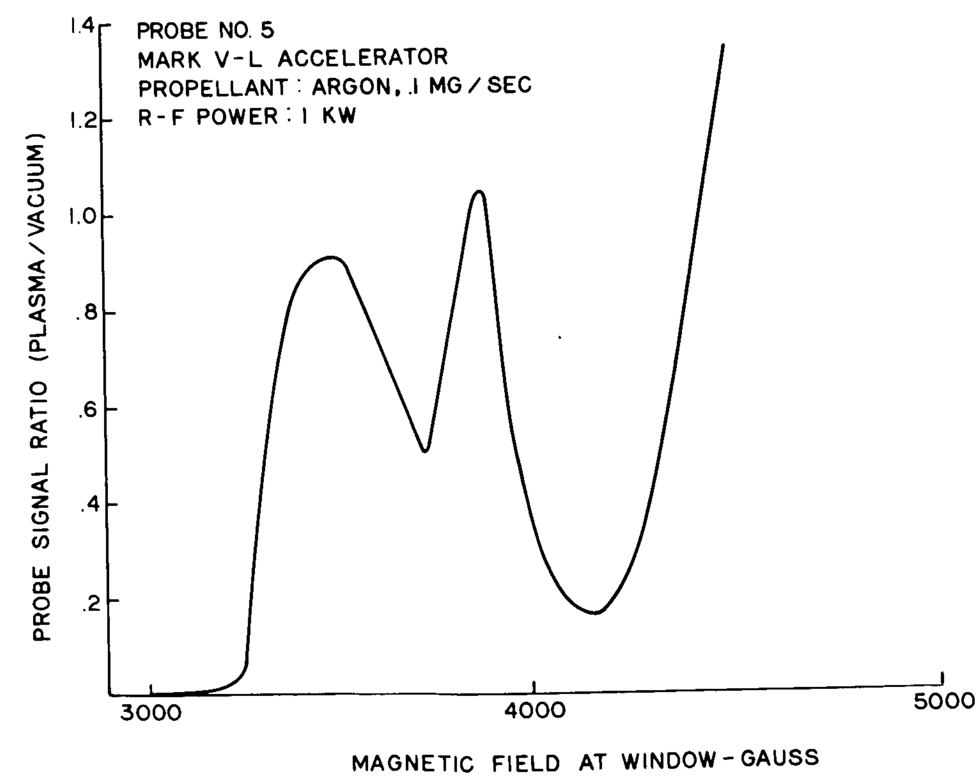

Figure 61. Dependence of R-f Probe Signal on Magnetic Field Strength

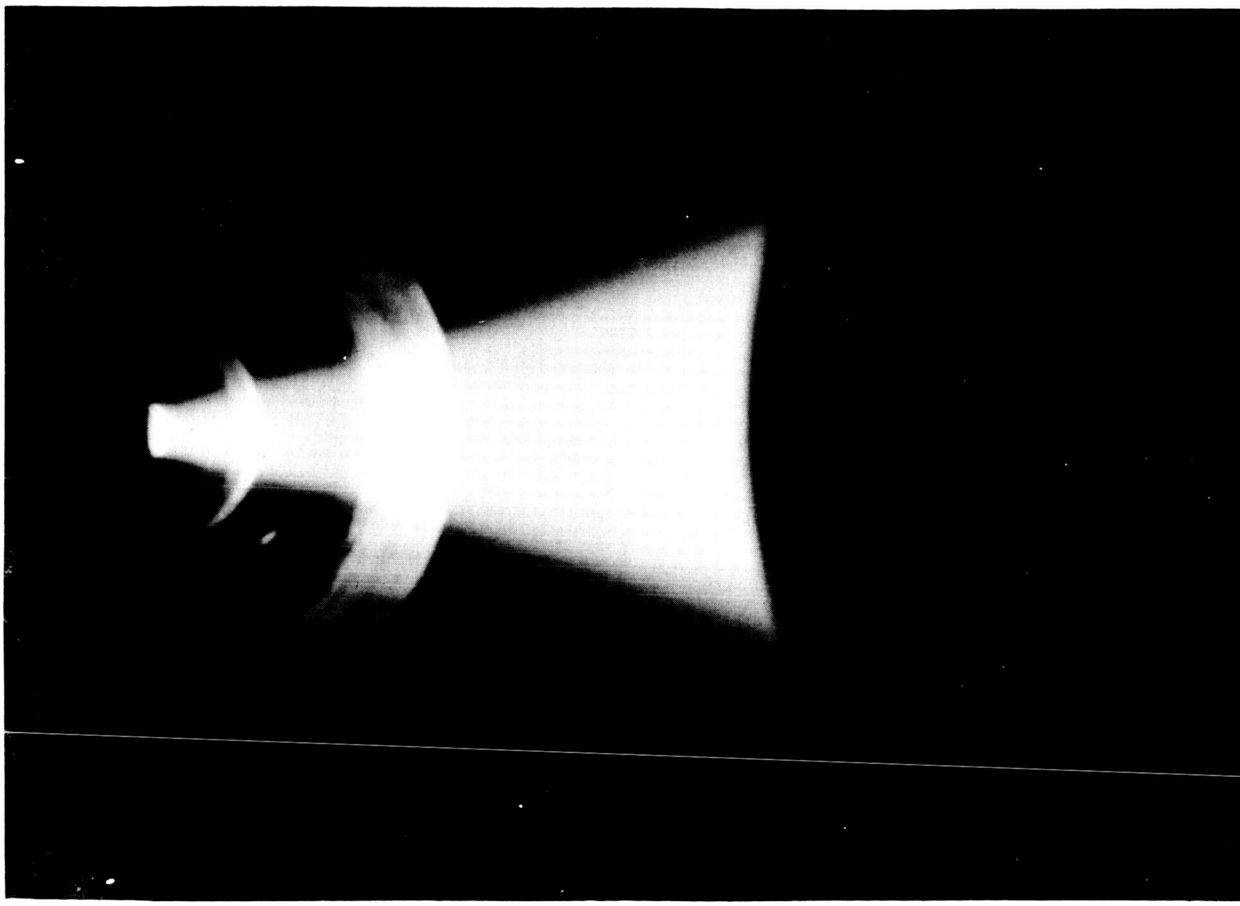

Figure 62. Exhaust Stream, Mark V-S Accelerator, Xenon 1500 watts r.f. Power; Exhaust Stream is Emerging from the Accelerator on the Left and is Flowing into the Open End of the 10" Diameter Calorimeter on the Right

The ability of the dielectric waveguide windows to remain in tact is apparently quite sensitive to accelerator temperature, since most beryllium oxide window failures can be traced to situations in which the accelerator temperature was allowed to reach high levels, e.g., 200°C. During recent tests, 125°C (5.5 mv) has been adopted as the maximum allowable temperature. Aluminum oxide (half-wave thickness) and sapphire (.010 thickness) windows both failed rapidly at low power (< 1000 watts).

Original tests with this accelerator revealed extreme difficulty in initiating the plasma, even at high power (up to 3 kw) and high pressure (up to 2×10^{-4} argon), probably due to the shortness of the plasma chamber. Insertion of a .020" diameter tungsten wire ring into the plasma chamber completely cured this problem, allowing dependable starting in all gases used over a wide range of pressure, field and power settings. The high electric field strength concentrations at the exposed ends of this igniter wire probably are accountable for this result. Since the r-f heats this wire to a visibly high temperature, thermionic emission may also be active in initiating the plasma. This white-hot wire ring can be seen in Figure 62.

The third recorder chart shown in Figure 32 is an example of the data recorded during each run on the multichannel light-beam-galvanometer recorder. In this case only the incident and reflected r-f powers and the magnetic field strength are measured. The importance of this data is to ensure the constancy of r-f power and magnetic field during a given test.

Note that, except at the lowest magnetic field setting, the reflected r-f power is essentially zero. This is a consequence of the tuner in the waveguide transmission line which carries the power from the r-f generator to the accelerator. For each new plasma condition (gas density, power level, magnetic field strength) this tuner is used to optimize the generator/plasma match and thereby minimize the reflection; in the reflected power trace in Figure 32, the periods in which the tuner was used to minimize reflection are evident. The importance of optimizing the match is also seen in the increased power received by the calorimeter when reflection is reduced to a minimum.

A further optimization has been made for the Mark V-S accelerator by adjusting the polarizer angle for maximum calorimeter heating. This empirically optimum angle is at the 45° point at which the right-hand circular polarization component should theoretically be maximum.

4.4.1 Power Efficiency Results

Initial Mark V-S tests were made using the 24" diameter x 10" deep calorimeter. The results, shown in Figure 63, indicated that very little had been gained by shortening the accelerator (compare Figures 63, 53 and 52).

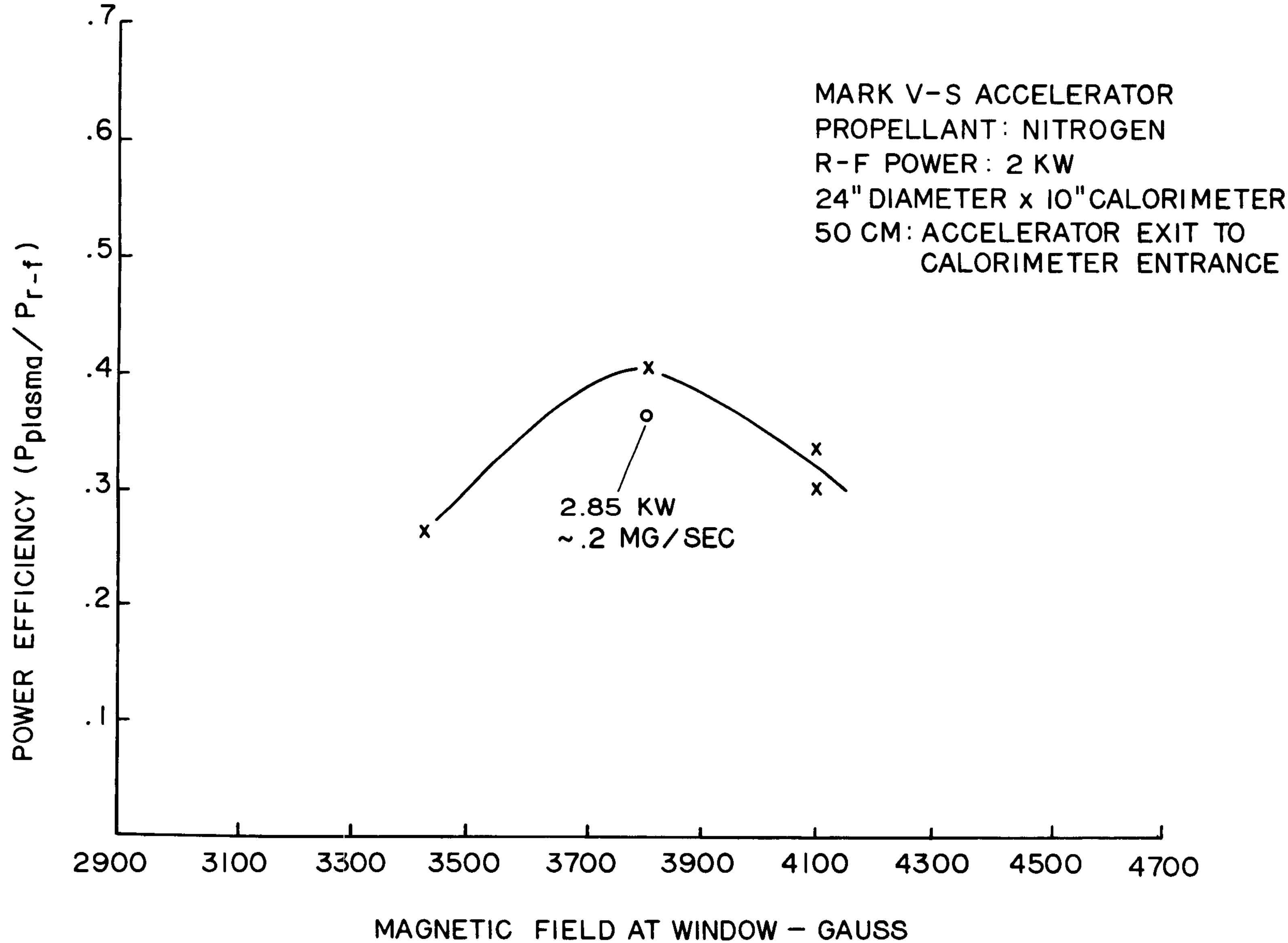

Figure 63. Dependence of Power Efficiency on Magnetic Field Strength

Before concluding that the efficiency of this type of accelerator was inherently low, a 10'' diameter by 20'' deep calorimeter (Figure 18) was employed to check the 24'' diameter calorimeter. Figures 64-68 show the results of the 10'' calorimeter tests with the Mark V-S accelerator. Up to 3700 gauss, efficiency is approximately the same. Beyond, the significantly higher efficiencies are obvious. Note that the calorimeter power goes up with increasing magnetic field strength and with increasing molecular weight. The functional relationships with r-f power level and gas flow rate are not clear, although indications are that the efficiency increases with increasing power and that an optimum flow rate exists for any given combination of gas species, r-f power level and magnetic field. These results are in agreement with Mark IV behavior.

A calorimeter efficiency maximum of .65 was achieved in these tests, using heavy propellant, high flow, high magnetic field and high power. Since the accelerator cooling water temperature was noted to rise about 5°C during its flow through the accelerator (at 1500-2000 watts), this accounts for approximately 15-20% of the input power. The remaining 15-20% must be lost in conduction away from the accelerator and in radiation from the plasma stream.

The actual edge of the exhaust jet is apparently not as sharp as is suggested by the photograph in Figure 62. This is evidenced by the data in Figure 69, showing a gradual falling off of calorimeter power as the calorimeter to accelerator distance is increased. The half power point on the curves in Figure 69 corresponds to a total jet angle of 25-27°.

The increase in calorimeter power with increasing magnetic field, especially at levels where the vacuum field is well above cyclotron resonance throughout the plasma chamber, may be related to plasma diamagnetism, as has frequently been suggested in the past. It may, however, also be caused by the enhanced r-f propagation which is present at high magnetic fields. It is possible that the r-f is propagating through the plasma and being absorbed within the calorimeter, therefore giving a falsely high measure of plasma stream power. This, it turns out, is not the case, as shown below.

4.4.2 R-f Probes

There are two specific reasons for measuring the spatial variation of the r-f field. In order to evaluate the fundamental processes in the accelerator, it is necessary to know the absorption and propagation characteristics of the electromagnetic field, as spelled out in the Contract work statement. It is further necessary to know the r-f field level within and in front of the calorimeter in order to determine to what extent the calorimeter heating is due to power absorbed from the r-f wave directly within the calorimeter.

Earlier attempts to map the r-f wave profile employed antennas fixed in the accelerator walls. Although a decaying pattern could in some cases be deciphered, in general the pattern was very complex; for example, see

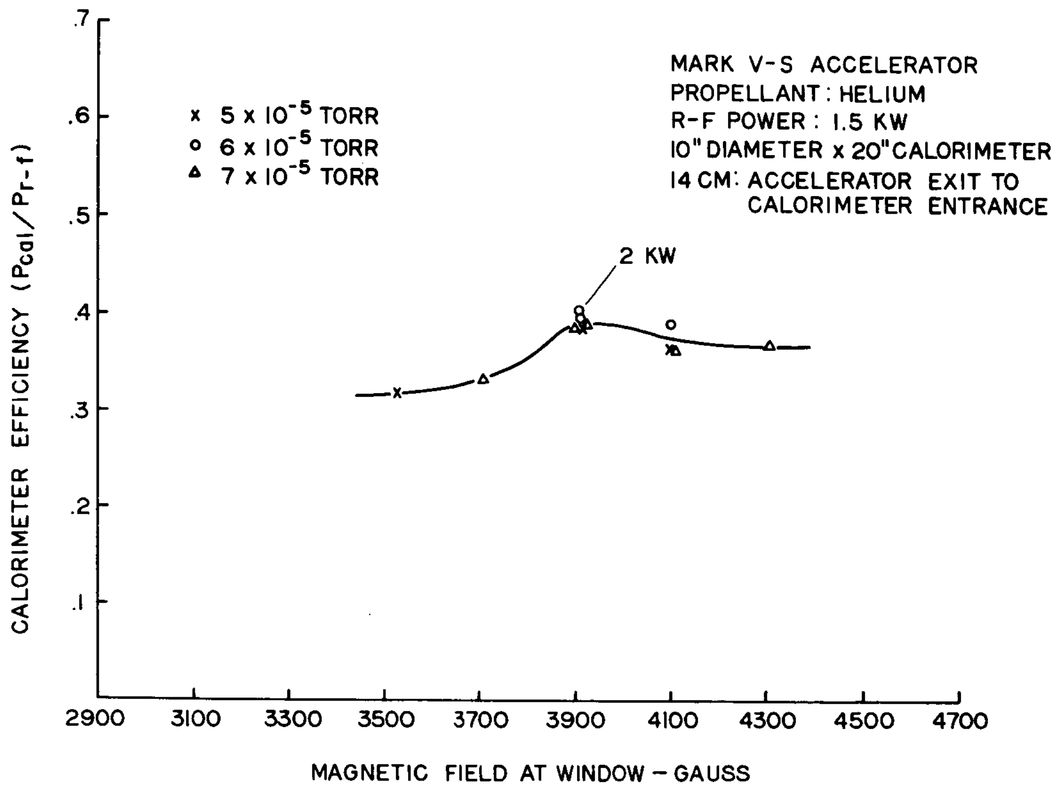

Figure 64. Dependence of Power Efficiency on Magnetic Field Strength

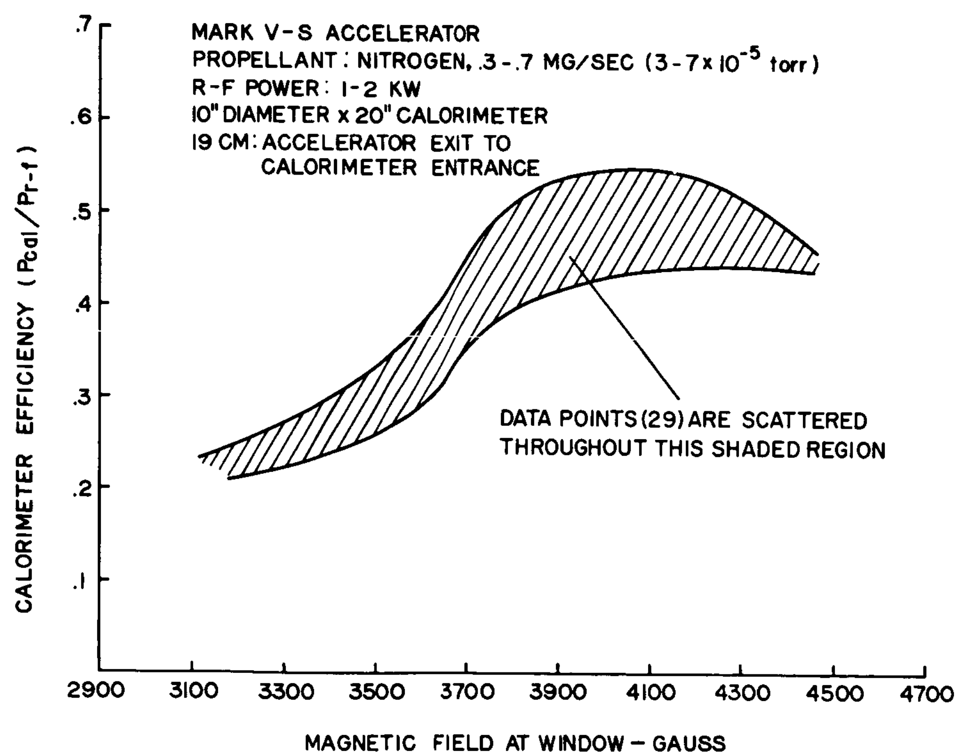

Figure 65. Dependence of Power Efficiency on Magnetic Field Strength

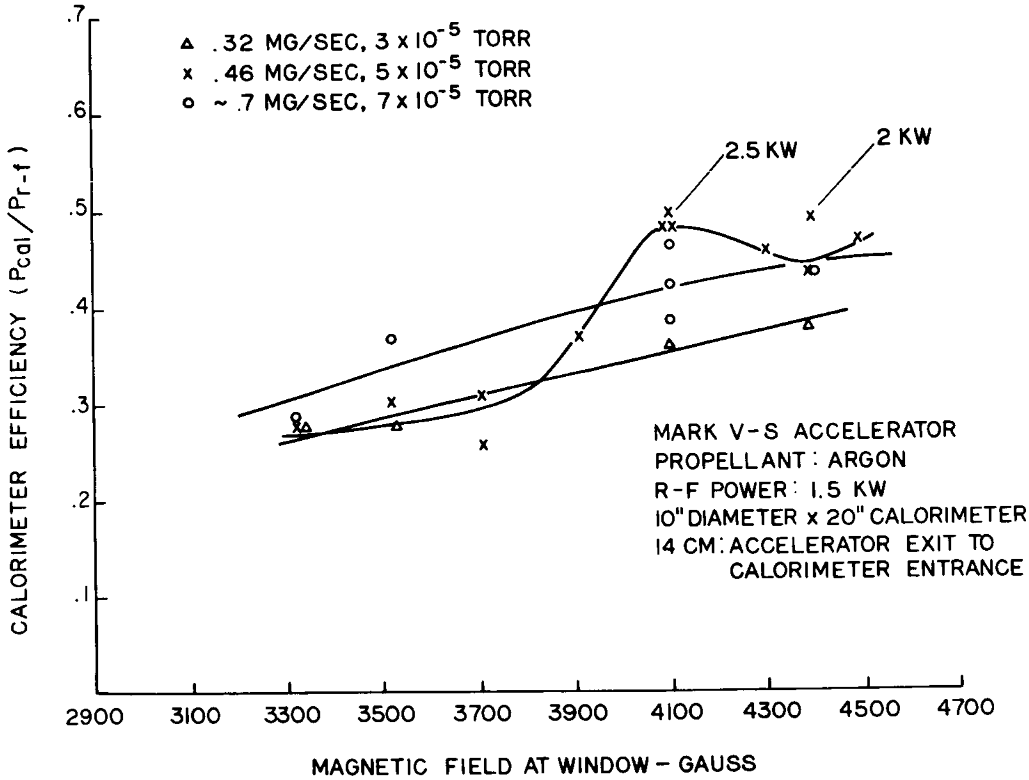

Figure 66. Dependence of Power Efficiency on Magnetic Field Strength

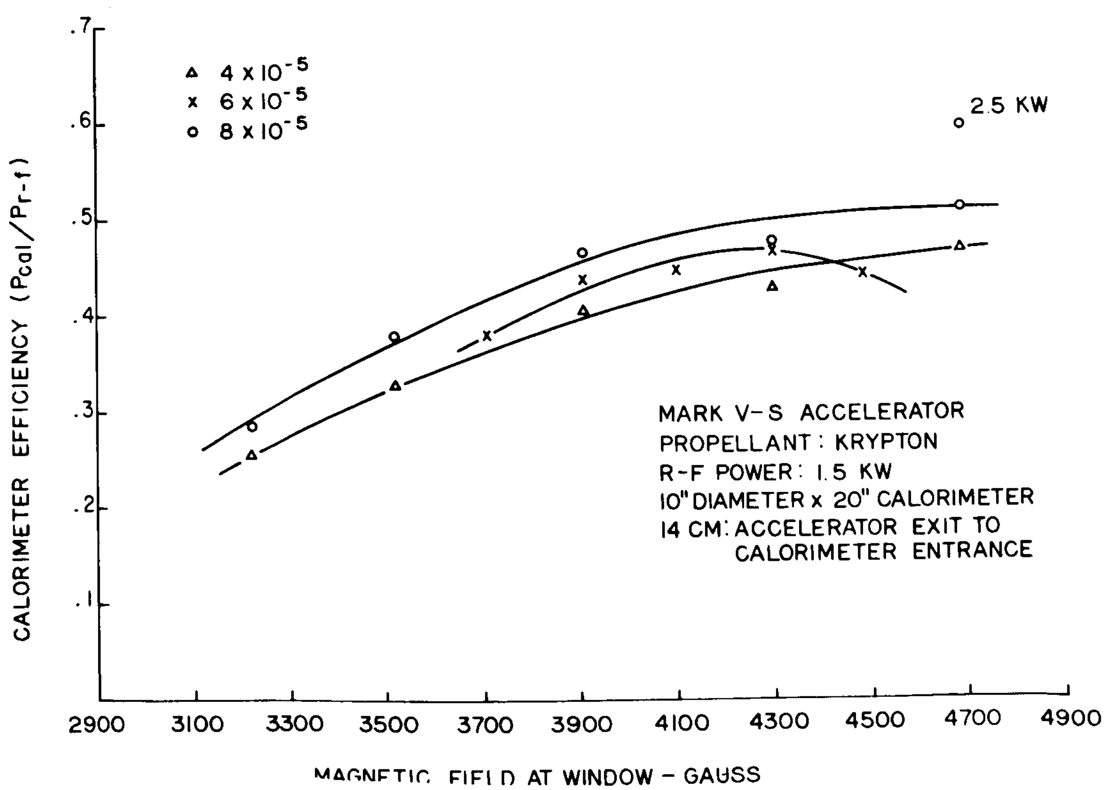

Figure 67. Dependence of Power Efficiency on Magnetic Field Strength

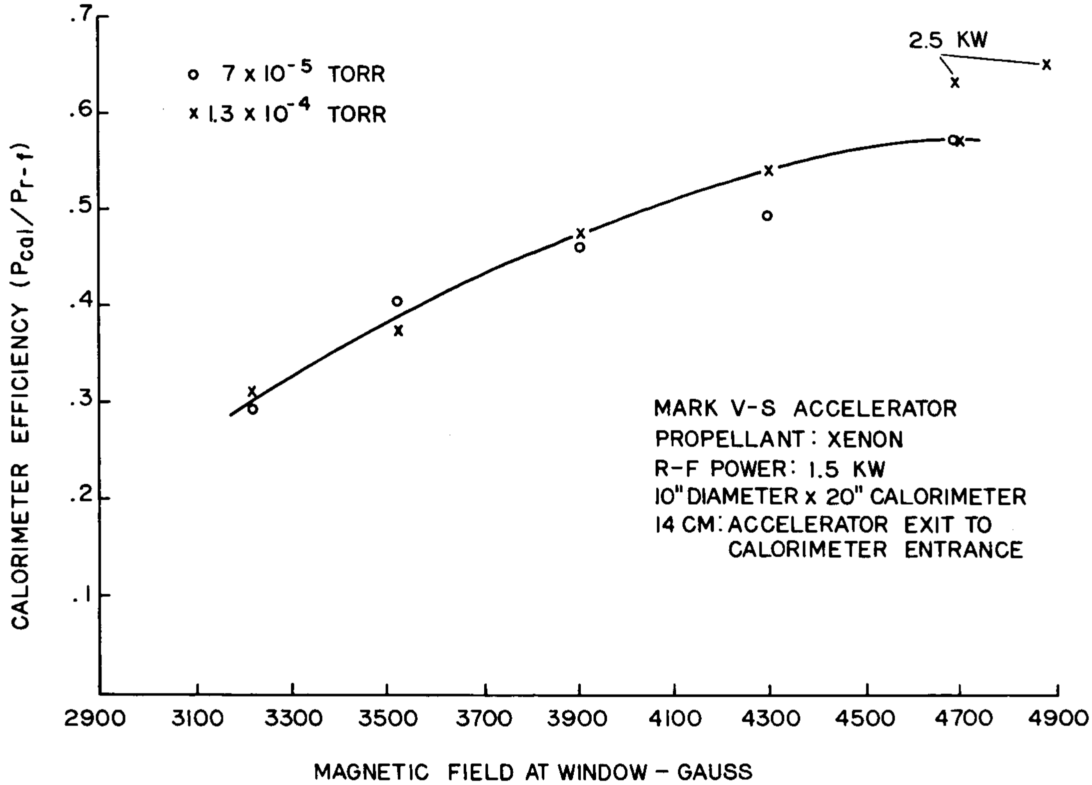

Figure 68. Dependence of Power Efficiency on Magnetic Field Strength

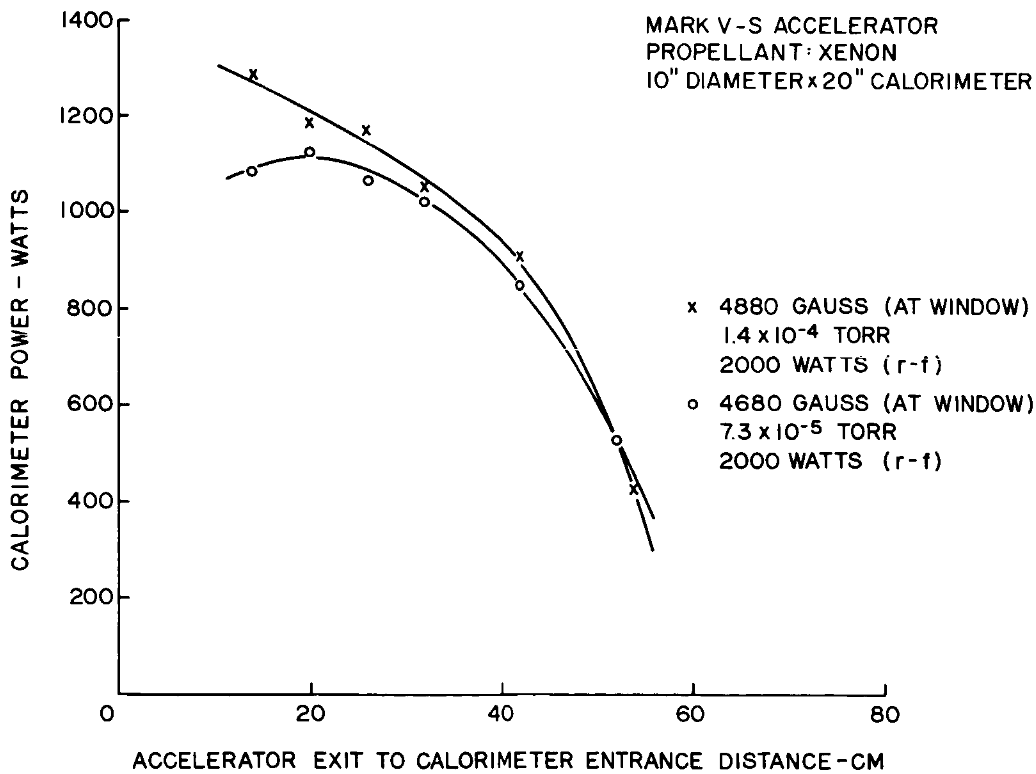

Figure 69. Dependence of Calorimeter Power on Calorimeter Position

Figures 58-61. This was predicted to be due to the electric field pattern being of a standing wave form. The current effort has been concerned with r-f antenna probes which can be moved and which can continuously map the r-f field both within and beyond the accelerator. A sketch of the movable probe is shown in Figure 15.

Before the Figure 15 probe was built, a fixed probe within the calorimeter and a larger movable antenna probe (of the same general design as Figure 15) were used. These showed that, under efficient Mark V-S operating conditions (i.e., with the calorimeter repeating the high power efficiency reported in Figure 68), the r-f electric field within and in front of the calorimeter was found to be less than one-one hundredth of the equivalent no plasma field strength. Thus, it is conclusively shown that an insignificant minority of the calorimeter power is entering the calorimeter as a propagating r-f wave and that the overwhelming majority of the calorimeter power is indeed plasma stream power.

In order to map the r-f electric field directly within the accelerator, the smaller, higher-temperature Figure 15 probe was employed. A set of curves taken with this probe is shown in Figures 70-74. Figure 70 shows the r-f electric field at 625 watts with no plasma present. The expected peaks and nulls in the radiating wave are clearly indicated. The remaining curves apply for the same r-f power, with argon flowing at .26 mg/sec, for various coil currents. Note that as the coil current increases, the depth of penetration increases. The equivalent vacuum magnetic field at which the final decay takes place also increases with increasing magnetic field strength.

Section 5 contains an analysis of the propagation of an r-f wave through a waveguide filled with magnetized plasma. The Mark V-S magnetic field shape is used, and an exponential electron density is assumed. The r-f electric fields thus calculated show a good correlation with the Figure 70-74 measured values, as further discussed in Section 5.

In Figures 71-74, we note that the r-f power is largely absorbed in a magnetic field range 10-15% higher than resonance (2970 gauss). The magnetic probe (Figure 30) indicated that the plasma diamagnetism was very small, as discussed in Section 3.13. The electric field patterns calculated in the waveguide analysis (Chapter 5) also exhibit this fall-off before the magnetic field has reached resonance, although the computed effect is not as pronounced as is the experimental result.

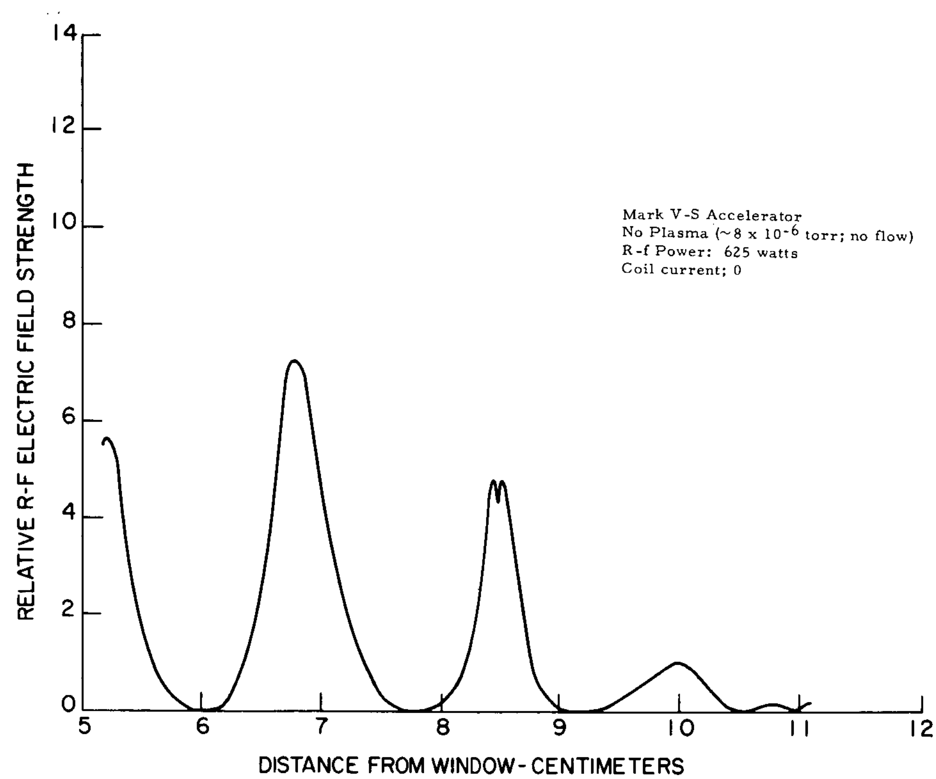

Figure 70. R-f Electric Field Strength as a Function of Position

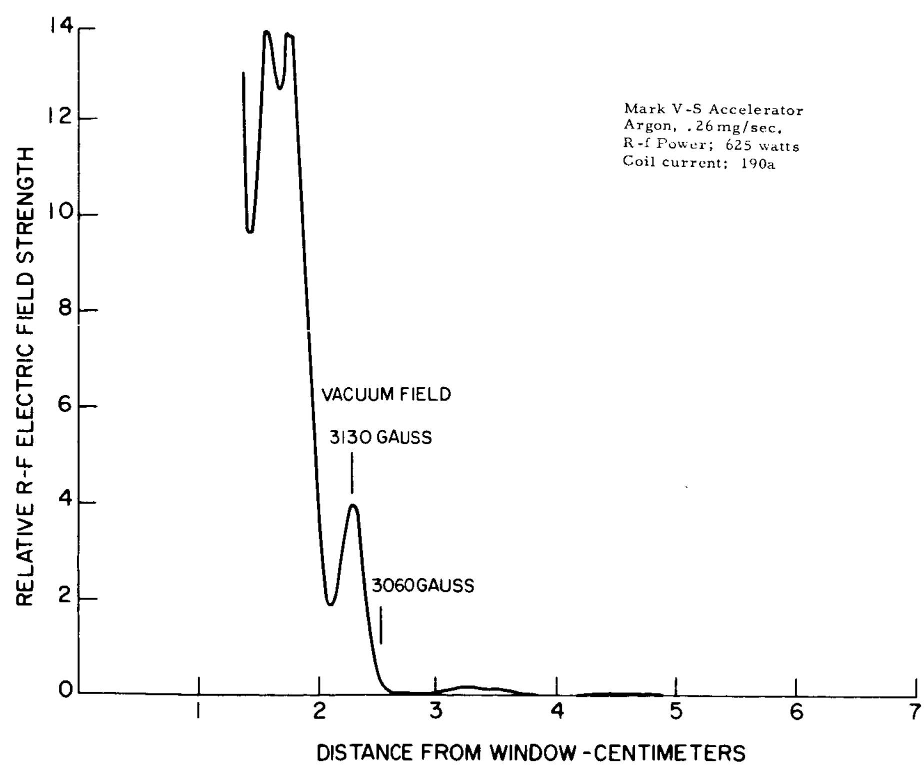

Figure 71. R-f Electric Field Strength as a Function of Position

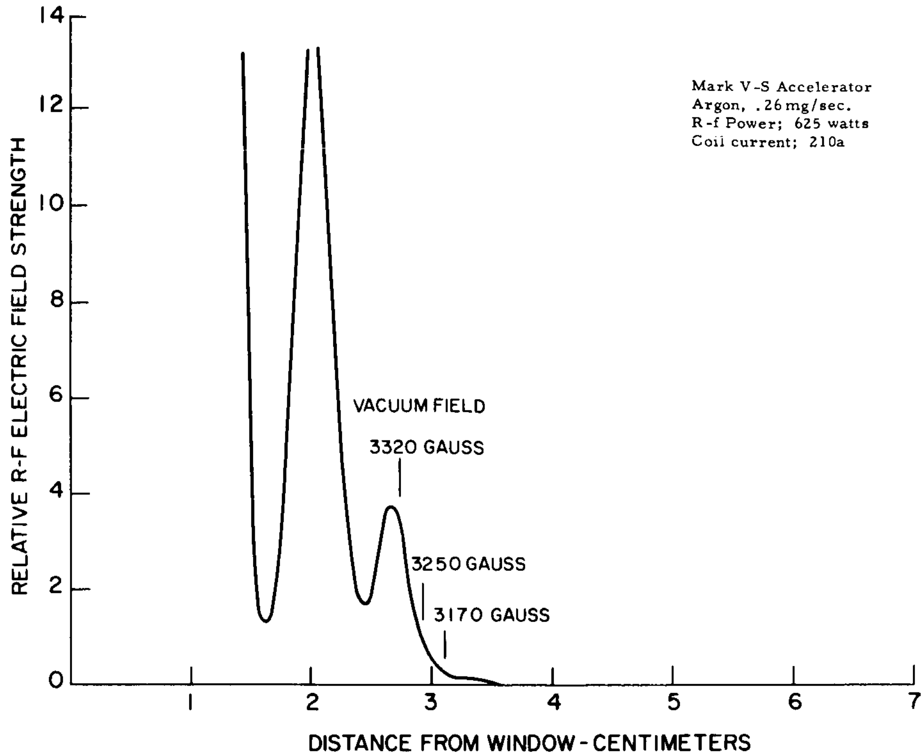

Figure 72. R-f Electric Field Strength as a Function of Position

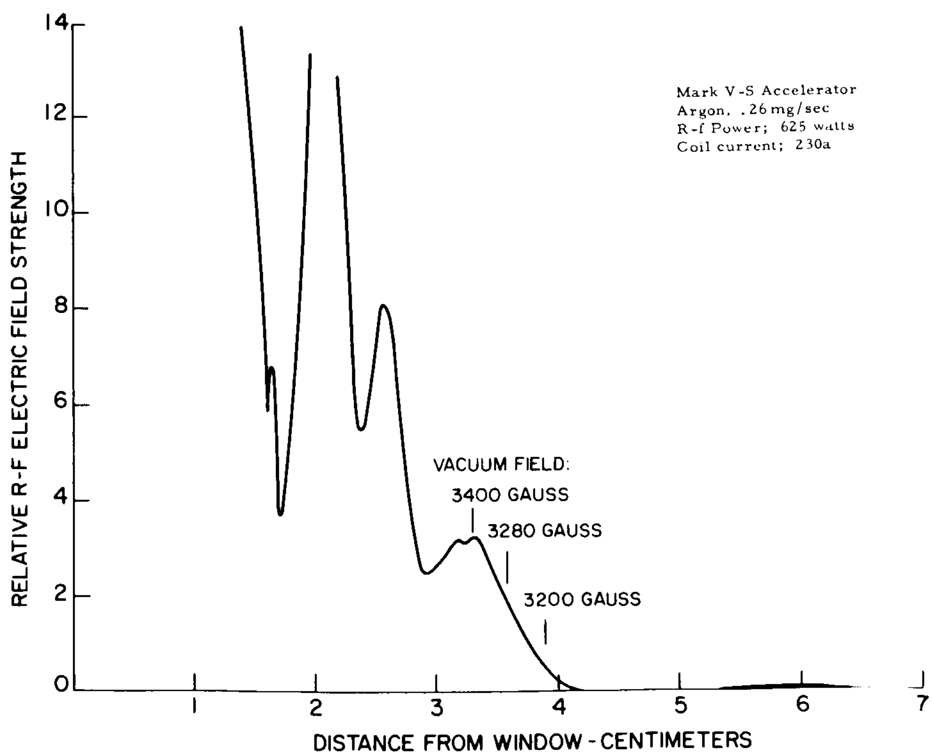

Figure 73. R-f Electric Field Strength as a Function of Position

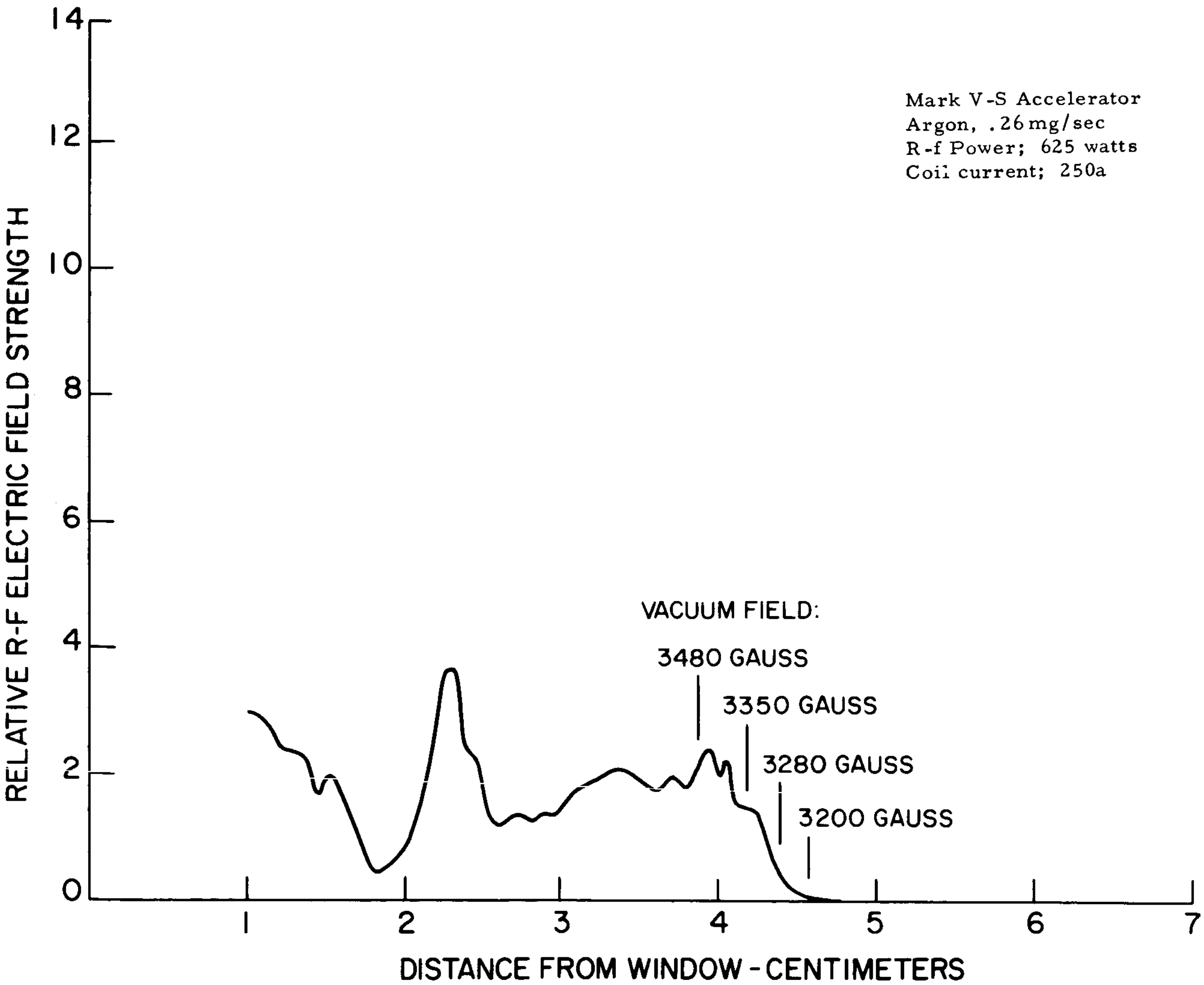

Figure 74. R-f Electric Field Strength as a Function of Position

4.4.3 Potential Probes

Potential probe measurements were made of the Mark V-S accelerator exhaust, the (grounded) accelerator being operated with argon and xenon gas, gas flow rates of ~ 0.5 and ~ 1.0 mg/second, magnetic field coil currents of 210 and 250 amperes (see Figure 12), and rf power levels of 1 and 2 kilowatts. Table VII shows the Mark V-S operating conditions for these measurements as a function of "run numbers" which will be used in subsequent discussions of the results.

It appears that the .002 inch diameter cylindrical tungsten (Langmuir) probes performed the best of the three types of potential probes employed (see Section 3.10 for descriptions). In addition, these cylindrical probes permitted the determination of approximate values for electron temperature and electron density as discussed below. As with the Mark IV-S and V-L emitting potential probe measurements discussed earlier, the emitting potential probes did not very clearly indicate a plasma potential. The .065 inch diameter thick ("flat") potential probes also yielded difficult-to-interpret response curves, due in part, to the plasma sheath being too large for these probes to be considered flat. Both the emitting and the "flat" potential probes also acquired unreasonably large ion currents when close to the accelerator, perhaps due to electron emission from the heated boron nitride-insulated surfaces.

All potential probe runs were recorded logarithmicly on a Visicorder using a special sawtooth bias voltage power supply, except for run 3b (see Table VII) for which all potential probe curves were recorded linearly vs bias voltage on an X-Y recorder. Figure 75 shows a typical X-Y recorder plot of a cylindrical Langmuir probe response curve. As stated in Section 3.10, probe voltages were always measured with respect to the grounded test chamber (Figures 1 and 2).

Since the plasma potential is not directly apparent from the cylindrical Langmuir probe response curve (see Figure 75), this information must be obtained through application of the appropriate probe theory to the probe response curve. To obtain the plasma potential (V_p) it is first necessary to determine the electron temperature (T_e). For flat and convex probes in the electron-retarding region of the current response curve,

$$T_e = \frac{e}{k}\left(\frac{d\ell n\, I_e}{dV}\right)^{-1} = \frac{5040}{(d \log I_e / dV)} \ {}^{o}K. \qquad (4.1)$$

where

$$I_e = I - I_i \qquad (4.2)$$

Table VII. Mark V-S Operating Conditions for Potential Probe and Energy Analyser Probe Measurements*.

Accel. Run No.	Gas	RF Power (kw)	Gas Flow (mg/sec)	Mag. Field Coil Current (amp)
1	Argon	1.0	0.4	210
2	Argon	1.0	0.4	250
3a & 3b	Argon	1.0	0.9	210
4	Argon	1.0	0.9	250
5	Argon	2.0	0.4	210
6	Argon	2.0	0.4	250
7	Argon	2.0	0.9	210
8	Argon	2.0	0.9	250
9	Xenon	1.0	~0.5	210
10	Xenon	1.0	~0.5	250
11	Xenon	1.0	1.2	210
12	Xenon	1.0	1.3	250
13	Xenon	2.0	~0.5	210
14	Xenon	2.0	~0.5	250
15	Xenon	2.0	~1.1	210
16	Xenon	2.0	~1.1	250

* All these runs were made on 7/22/65 and 7/23/65.

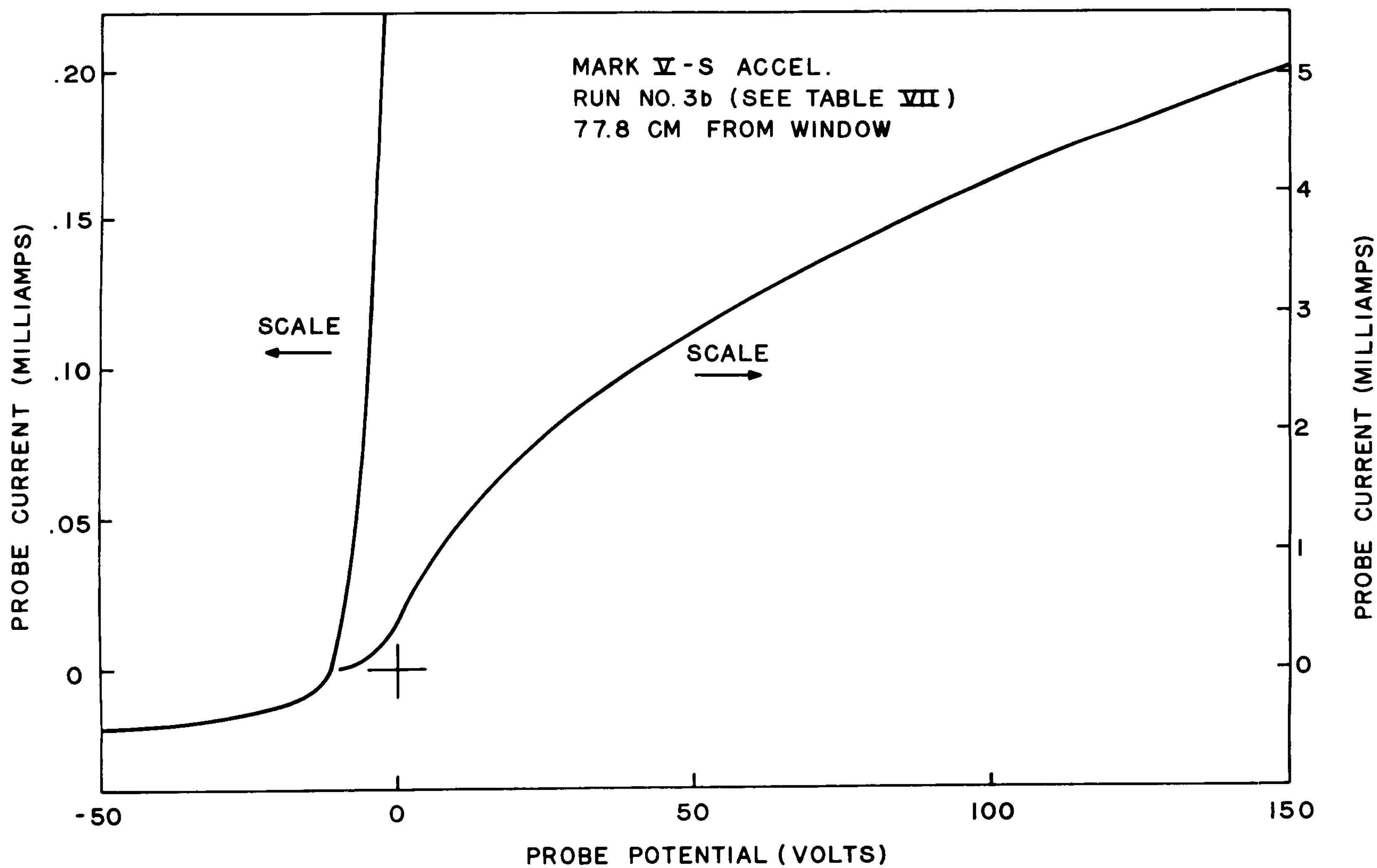

Figure 75. Typical Cylindrical Langmuir Probe Response Curve

and where e is the electronic charge, k is the Boltzman constant, I_e is the probe electron current, V is the probe voltage as measured, I_i is the probe ion current, and I is the total probe current.

Now (Reference 25)

$$I_{es} = I_{er} f = A_p J_{er} f \tag{4.3}$$

where

$$I_{er} = A_p N_e e \left[k T_e / (2\pi m_e) \right]^{1/2} \tag{4.4}$$

$$= 2.49 \times 10^{-14} A_p N_e T_e^{1/2} \text{ amps.} \tag{4.5}$$

Here, I_{es} is probe electron saturation current, I_{er} is the probe random electron current, A_p is the probe area (cm^2), J_{er} is the random electron current density, N_e is the electron density (cm^{-3}), m_e is the electron mass, T_e is in ^oK, and f is a complex function (≥ 1) which has been graphed by Langmuir (Reference 25) as a function of η and the plasma sheath-to-probe radius ratio (r_s/r_p). Here,

$$\eta = -e(V - V_p)/(kT_e) = 11605\,(V - V_p)/T_e \tag{4.6}$$

where $(V - V_p)$ is the probe potential with respect to plasma potential. Finally, a combination of Langmuir's cylindrical probe orbital-limited and space charge-limited theories (Reference 25) yields

$$(-\beta)^2 \left[\frac{2}{f} \left(\frac{r_s}{r_p} \right) - 1 \right] = \frac{2}{9} \left(\frac{2e}{m_e} \right)^{1/2} \frac{L\,(V - V_p)^{3/2}}{r_p \cdot I_e} \tag{4.7}$$

where L is probe length, r_p is probe radius, and $(-\beta)$ is a complex function of (r_s/r_p) which is tabulated by Langmuir (Reference 25).

To obtain the desired T_e, V_p, and N_e information from the cylindrical Langmuir probe response curves, the following steps were taken: 1) Equations (4.1) and (4.2) were used to obtain T_e from the slope of a semi-log plot of the electron-retarding region of the probe response curve (about -15 to +5 volts in Figure 75). For the X-Y recorded curves a constant value for I_i was found (trial and error) which gave a straight semi-log plot. For the logarithmicly recorded (Visicorder) runs the slope was obtained in regions where $I_e >> I_i$, although here the desired slope was not always obvious, with a resulting uncertainty in the derived T_e. 2) An I_{es} and corresponding V were picked off the probe response curve, and the right side of equation (4.7) evaluated after guessing at V_p. 3) The left side of equation (4.7) was then solved for (r_s/r_p) and thus f through the use of equation (4.6) and Langmuir's tabulations and plots (Reference 25) for $(-\beta)^2$ and f. 4) Equation (4.3) was then solved for I_{er} using f and I_{es}. From the probe response curve, the V was located at which $I = I_{er}$ (this is justified because $I_{er} \gg I_{ir}$). This new V gave a newer and better approximate value for V_p. 5) Steps 2 through 4 were repeated until the value for V_p no longer changed. This iteratative process converged very rapidly, giving V_p. 6) Finally, equation (4.5) plus the last iterated value for I_{er} was used to obtain N_e.

The above method for reducing the potential probe data was rather tedious, though speeded up enormously through the use of graphed combined functions. Ideally, there are simpler and faster ways to determine V_p from cylindrical Langmuir probe curves, but they require replotting and judicious use of an appropriate part of the probe response curves. For the large number of (Visicorder semi-log) curves reduced, the method used was not only faster but also avoided the often self-conflicting results obtained by other methods.

One problem in evaluating the Langmuir probe data was the complicating effect of the accelerator magnetic field. This problem was avoided by always reducing the probe data at V sufficiently low to result in $r_s <$ electron cyclotron radius. Within this limit, the probe response curves followed the theory outlined by equations (4.1) to (4.7).

The potential probe results as determined by the above methods, are tabulated in Tables VIII, IX, and X for T_e, V_p, and N_e, respectively. To permit more general intercomparisons, these results are plotted in Figure 76 for T_e, Figures 77-80 for V_p and accelerator magnetic field strength, and Figure 81 for N_e. Curve numbers and table run numbers refer to the operating conditions listed in Table VII. From these tables and figures we see that through the axial distance range of 12.5 - 77.8 cm from the plasma-window interface, plasma potentials of 0 - + 55 volts, electron temperatures of $\sim$ 25,000 - > 150,000°K, and electron densities of $\sim 0.1 - 6 \times 10^{10}$/cc were obtained.

On intercomparing the Langmuir potential probe results, a number of trends can be seen with varying degrees of certainty: at distances from the accelerator plasma-window interface (D) of < 43 cm, T_e, V_p, and N_e all increase as D decreases. Furthermore, Figures 77-80 indicate that for $12 < D < 78$ cm in argon and for $12 < D < 23$ cm in xenon, V_p is very approximately proportional to the magnetic field strength. This conclusion is least correct in the case of runs 5-8 (argon gas and 2 kw rf power). These V_p vs magnetic field comparisons can be made more quantitative by noting that between the D limits given above, the Figures 77-80 V_p slopes (log-log) are about -1.7 for runs 1-4 (Figure 77), -1.0 for runs 5-8 (Figure 78), -2.4 for runs 9-12 (Figure 79), and -1.9 for runs 13-16 (Figure 80); while for D > 13 cm the magnetic field strength slope is -2.08 as plotted.

Additional qualitative trends to be noted from Tables VIII - X and Figures 76-81 are given below:

Table VIII. Mark V-S Electron Temperature as a Function of Accelerator Operating Conditions (see Table VII) and Distance from Plasma-Window Interface. Electron Temperatures are Calculated from Cylindrical Langmuir Probe Response Curves.

Run No.	Electron Temperature (x 10^4 °K)						
	Distance from Window (cm)						
	77.8	42.5	32.5	22.5	17.5	12.5	77.8
1	-	-	-	-	-	-	-
2	2.8	2.6	3.5	5.5	5.6	14.	3.8
3a	4.6	3.0	4.8	6.0	8.4	8.7	4.2
3b	3.72	4.37	-	4.46	-	7.65	-
4	4.4	8.0	6.1	9.4	9.6	10.	3.2
5	4.8	7.4	9.2	15.	>15.	>15.	5.0
6	6.7	7.3	11.	2.6	3.6	-	-
7	5.0	5.8	5.7	8.8	9.2	9.5	4.5
8	5.0	6.3	7.2	9.2	9.5	10.	4.2
9	3.2	3.8	4.0	6.3	10.	14.	4.0
10	3.6	4.0	4.4	4.9	10.	-	4.4
11	3.6	3.6	3.8	4.6	8.0	10.	3.2
12	3.4	3.7	3.5	4.2	7.0	9.4	3.6
13	4.1	4.0	5.4	7.6	9.6	12.	3.6
14	3.3	3.7	3.8	4.2	5.4	11.	3.2
15	3.8	4.0	4.2	5.2	9.2	10.	3.4
16	4.5	4.6	4.7	5.9	8.7	10.	4.4

Table IX. Mark V-S Plasma Potential as a Function of Accelerator Operating Conditions (see Table VII) and Distance from Plasma-Window Interface. Plasma Potentials are Calculated from Cylindrical Langmuir Probe Response Curves.

Run No.	Plasma Potential (volts)						
	Distance from Window (cm)						
	77.8	42.5	32.5	22.5	17.5	12.5	77.8
1	1.5	4.5	--	15.5	26.	37	-0.5
2	2.0	6.5	11.5	23	28.5	48	3.5
3a	1.8	2.5	7.2	13	21.5	26	0
3b	2.9	6.7	--	9.3	--	25.0	--
4	3.5	6	8.5	14.5	22.5	29.5	1.1
5	6.5	14	19	28	37	55	7.0
6	10.5	17	28	26	34.5	--	--
7	7.3	9.5	12	18.5	27	30.5	5.0
8	7.5	10.5	13.5	18.5	27	27.6	6.0
9	3.5	4.8	4.8	8.5	25	39	4.5
10	4.5	5	5	7.5	15	~50	6.2
11	6.0	3.7	5	6.5	22	29.5	2.5
12	5.0	4	5	5.5	10.5	17	3.5
13	5.0	4.5	6	11.5	20.5	36	4.0
14	4.6	7	6	6.5	12	25	3.5
15	7.5	5.5	5	8	18	27.5	8.5
16	10.5	7.2	7.5	9	16.5	26	8.0

Table X. Mark V-S Electron Density as a Function of Accelerator Operating Conditions (see Table VII) and Distance from Plasma-Window Interface. Electron Densities are Calculated from Cylindrical Langmuir Probe Response Curves.

Run No.	Electron Density ($\times 10^9$/cc)						
	Distance from Window (cm)						
	77.8	42.5	32.5	22.5	17.5	12.5	77.8
1	2.9	4.6	--	9.6	16.	18.	2.0
2	2.1	2.3	1.9	2.4	2.0	3.0	1.2
3a	9.3	11.	18.	22.	38.	56.	7.6
3b	7.54	7.07	--	10.9	--	44.8	--
4	8.0	7.6	12.	16.	30.	40.	7.0
5	4.3	4.5	6.2	7.8	~15.	~17.	2.8
6	2.8	3.5	4.5	3.9	3.8	--	--
7	9.9	7.5	10.	16.	35.	46.	8.2
8	11.	9.6	11.	15.	32.	43.	8.5
9	10.	6.1	6.4	9.0	19.	26.	6.6
10	11.	1.6	5.4	4.6	5.2	--	4.5
11	14.	8.6	8.2	8.4	22.	26.	8.4
12	13.	11.	9.7	9.8	13.	18.	12.
13	14.	9.1	7.4	11.	16.	25.	8.2
14	8.6	5.6	6.8	6.7	7.6	9.1	7.3
15	16.	10.	9.2	11.	16.	58.	20.
16	30.	15.	16.	14.	15.	23.	16.

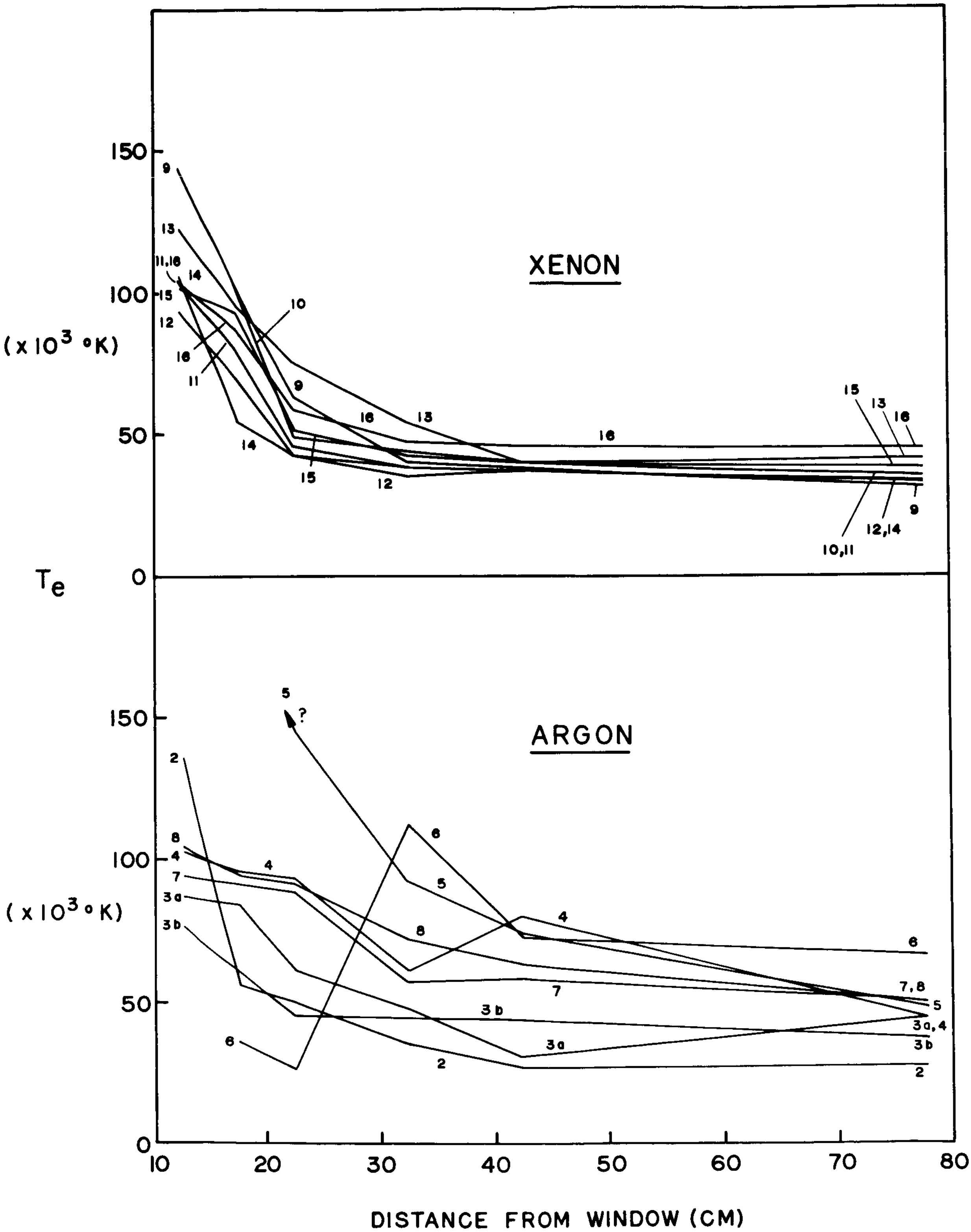

Figure 76. Mark V-S Electron Temperature as a Function of Accelerator Operating Conditions and Distance from the Plasma-Window Interface. Curve Numbers Refer to the Operating Conditions Listed in Table VII.

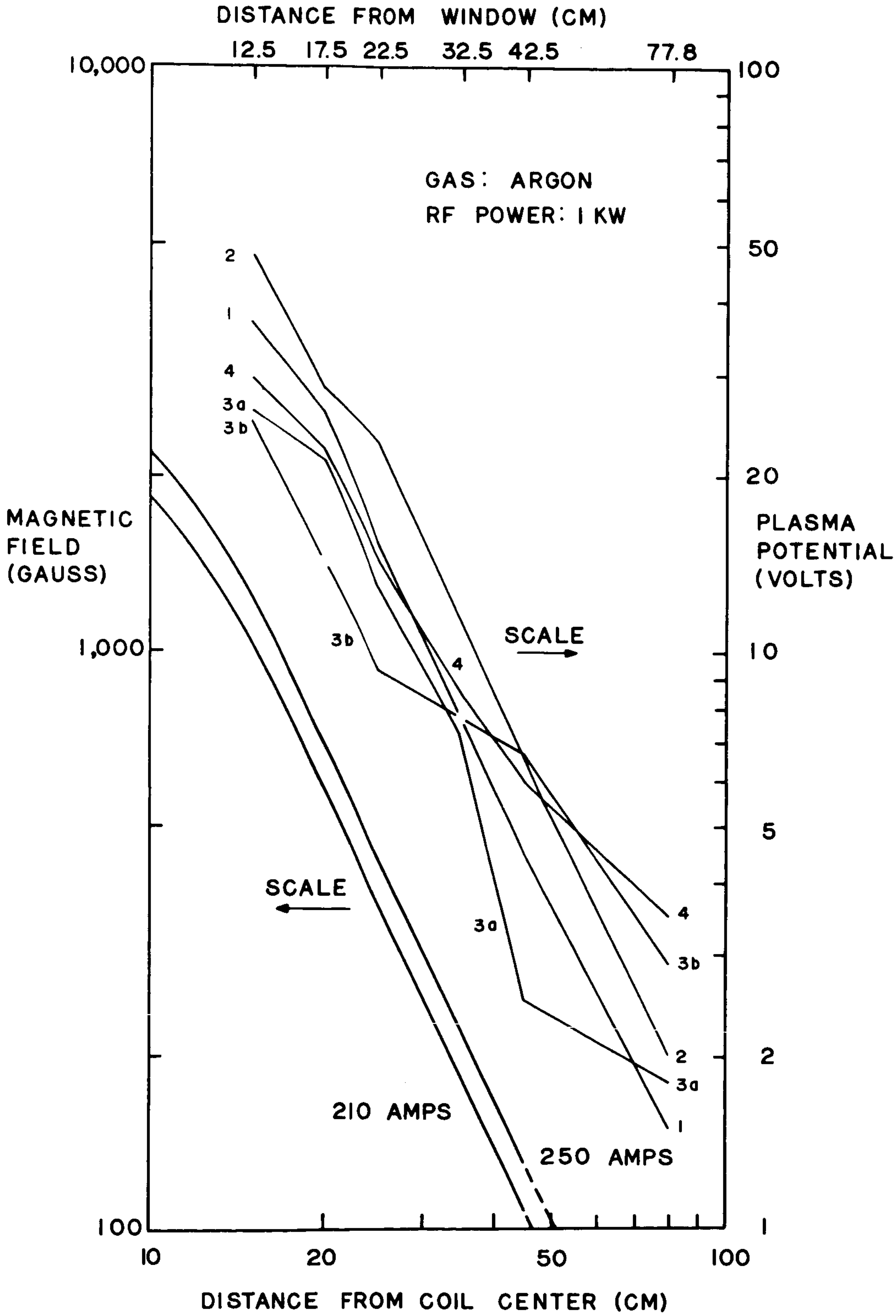

Figure 77. Mark V-S Plasma Potential as a Function of Accelerator Operating Conditions and Distance from the Plasma-Window Interface. Curve Numbers Refer to the Operating Conditions Listed in Table VII. A Plot of Magnetic Field Strength is Included for Comparison.

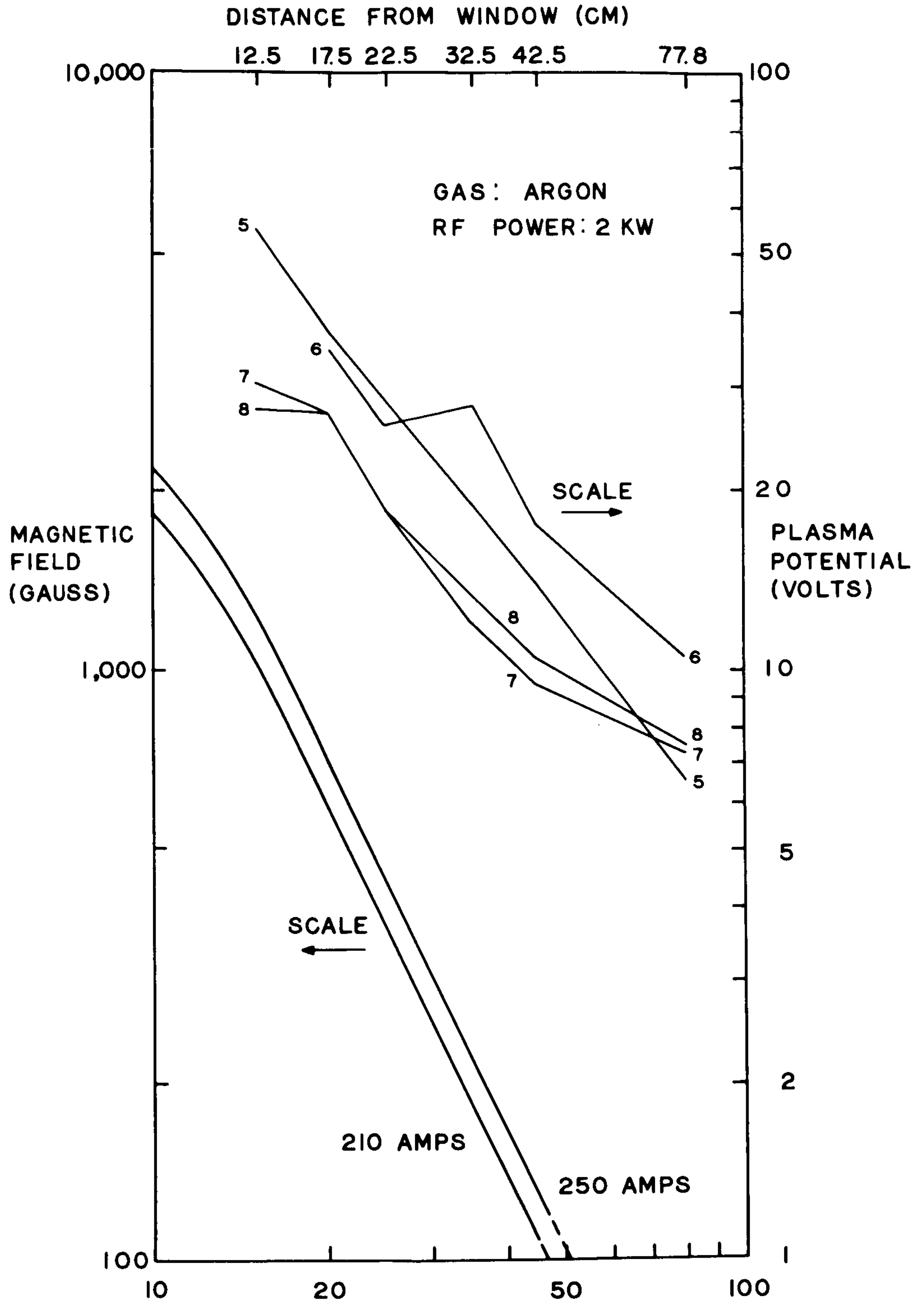

Figure 78. Mark V-S Plasma Potential as a Function of Accelerator Operating Conditions and Distance from the Plasma-Window Interface. Curve Numbers Refer to the Operating Conditions Listed in Table VII. A Plot of Magnetic Field Strength is Included for Comparison.

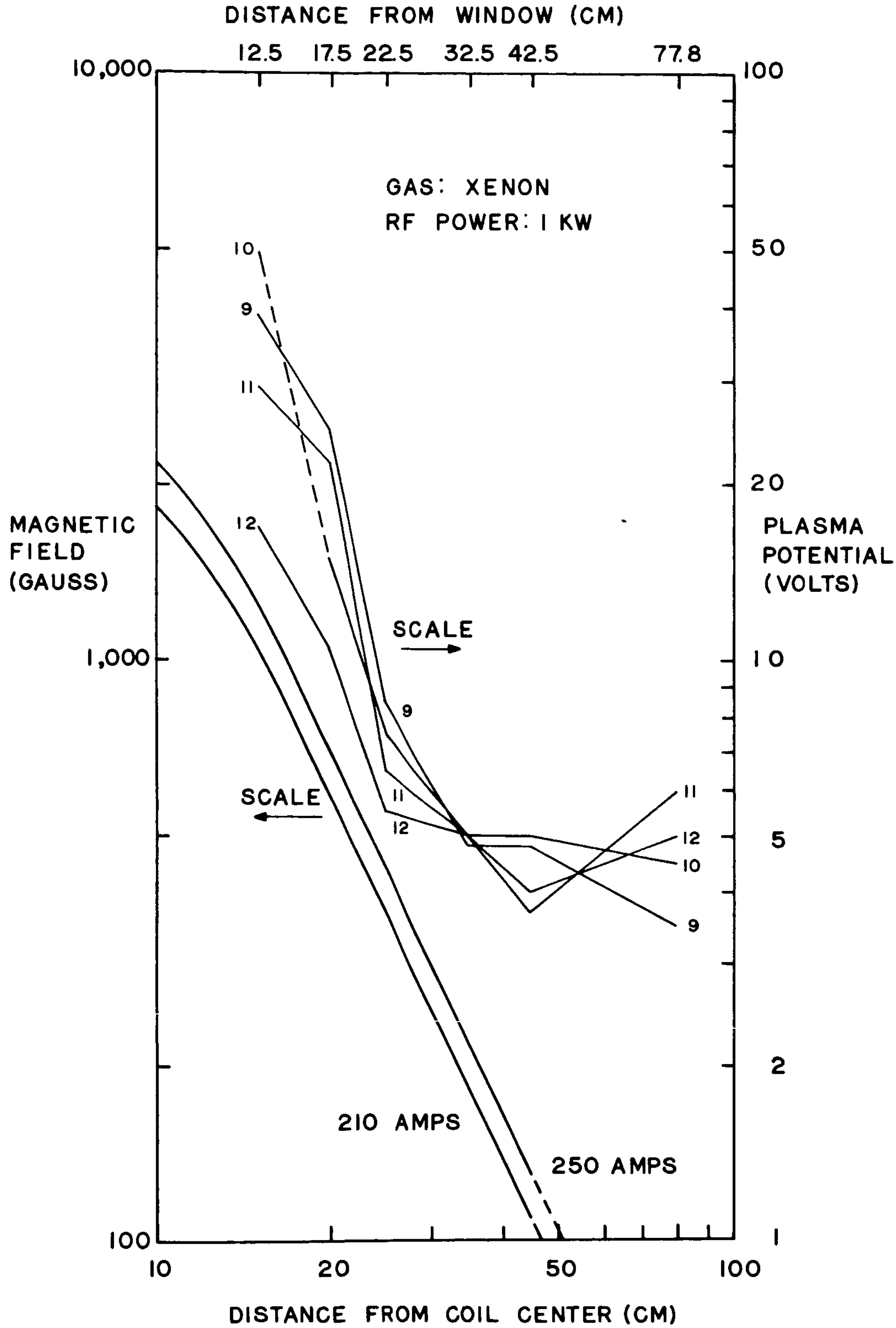

Figure 79. Mark V-S Plasma Potential as a Function of Accelerator Operating Conditions and Distance from the Plasma-Window Interface. Curve Numbers Refer to the Operating Conditions Listed in Table VII. A Plot of Magnetic Field Strength is Included for Comparison.

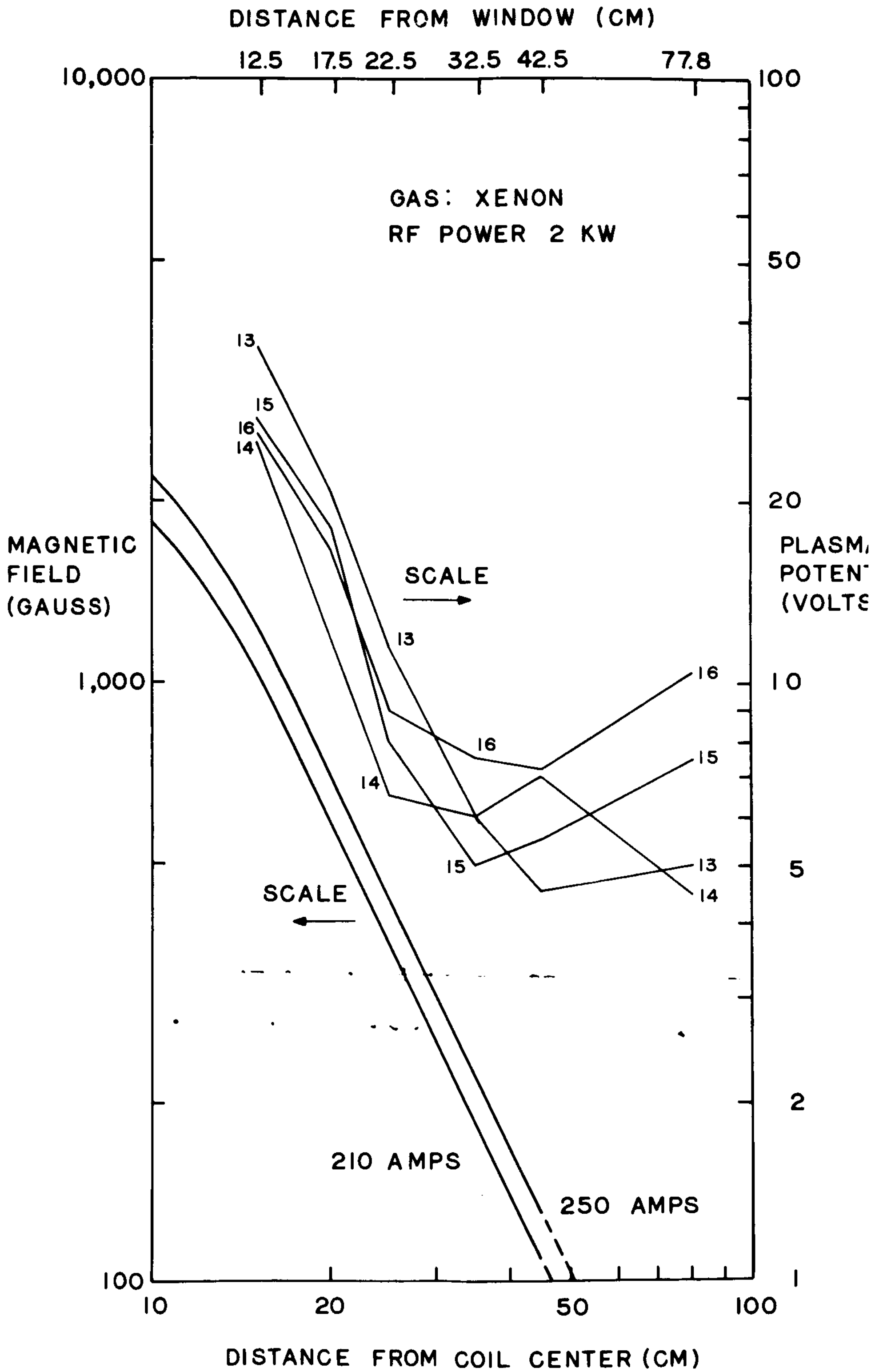

Figure 80. Mark V-S Plasma Potential as a Function of Accelerator Operating Conditions and Distance from the Plasma-Window Interface. Curve Numbers Refer to the Operating Conditions Listed in Table VII. A Plot of Magnetic Field Strength is Included for Comparison.

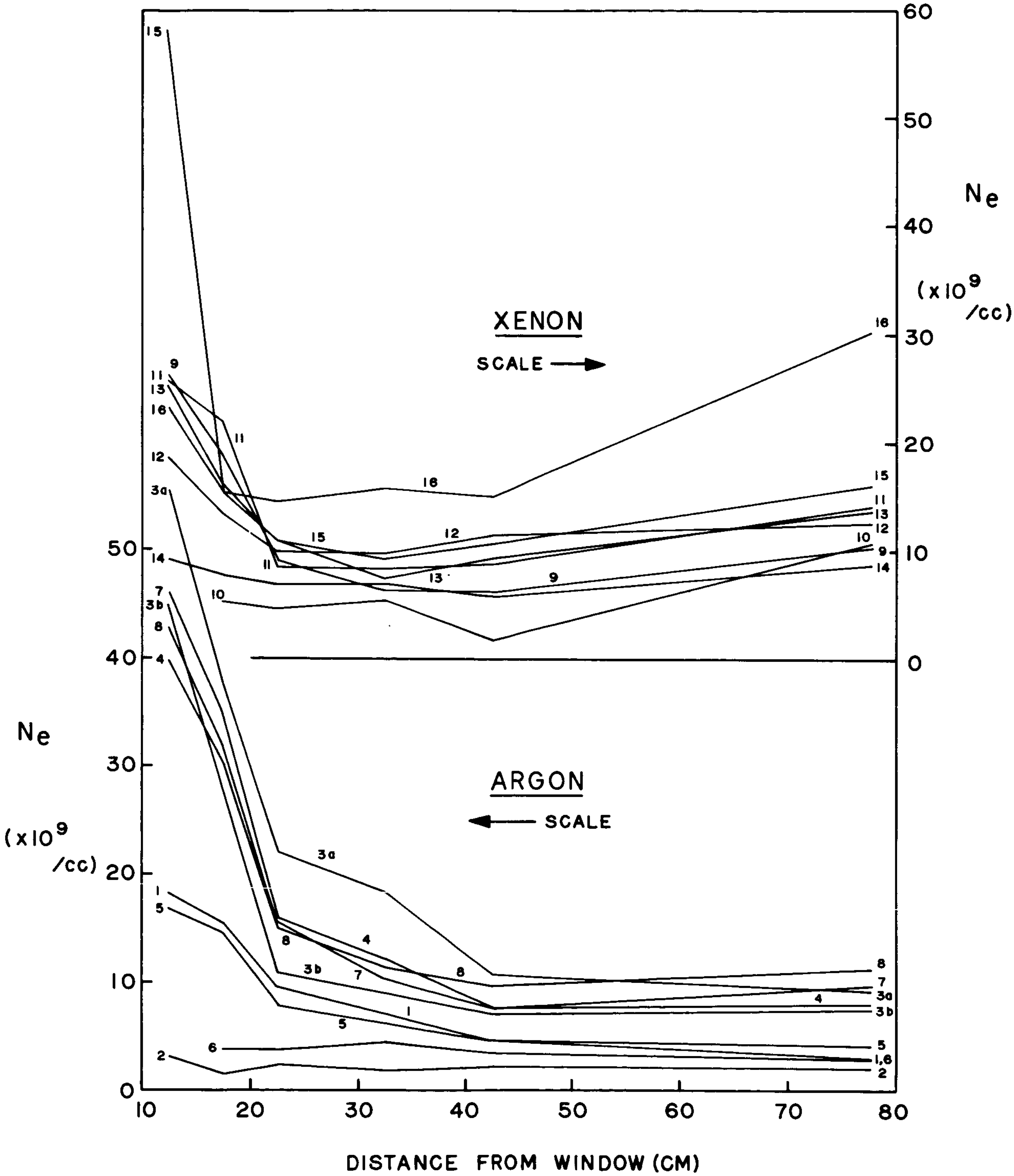

Figure 81. Mark V-S Electron Density as a Function of Accelerator Operating Conditions and Distance from the Plasma-Window Interface. Curve Numbers Refer to the Operating Conditions of Table VII.

1) On changing from argon to xenon gas, T_e tends to decrease at $D \geq 22$ cm and to remain unchanged at $D < 22$ cm, V_p shows variable (random?) changes, and N_e usually increases when at a gas flow rate of ~0.5 mg/sec and showed variable changes at ~1 mg/sec flow rate.

2) On increasing the gas flow rate from ~0.5 to ~1 mg/sec, T_e shows variable changes, V_p usually decreases (especially so for argon) at $D \leq 33$ cm, and N_e increases (again, especially so for argon).

3) On increasing the magnetic field by increasing the magnetic field coil current from 210 to 250 amperes, T_e shows little to no change, V_p increases for argon and shows variable changes for xenon, and N_e usually decreases.

4) On increasing the rf power from 1 to 2 kilowatts, T_e usually shows a slight increase, V_p increases for argon and shows variable changes for xenon, and N_e has a slight tendency to increase.

These trends plus some others discussed later are summarized in Table XI.

4.4.4 Energy Analyser Probe

Energy analyzer probe measurements were made of the Mark V-S accelerator exhaust, with the (grounded) accelerator being operated at the same conditions as for the potential probe measurements. In fact, the energy analyser probe and potential probe measurements were made simultaneously for all runs except run 3b, where the two types of probes were operated at different times. Thus, the run numbers of Table VII apply to both the energy analyser and the potential probe measurements.

Throughout all these Mark V-S runs the energy analyser probe appeared to operate satisfactorily, and survived with no shorting, leakage, or grid burn-out.

Similar to the Mark IV-S and V-L accelerator runs described earlier (see Figure 51), the Mark V-S energy analyser probe response curves (of plate current (I) vs plate voltage (V)) typically showed three inflection points. This is illustrated by the lower curve of Figure 82. Since the actual particle distribution as a function of probe plate voltage (i.e., particle energy in electron volts) is given by the derivative of the analyser probe response curve, a semi-quantitative plot of the resulting relative ion distribution curve is shown by the upper curve of Figure 82.

Rather than try to differentiate and re-plot every energy analyser probe curve, certain features of the probe direct response curve have been evaluated and listed in Table XII. These features are identified in Figure 82 by the voltages V_1, V_2, V_3, and V_4 for the turning points; by the voltages V_a, V_b and V_c for the inflection points; and by the derivatives $(dI/dV)_a$,

Table XI. Summarized Qualitative Results of Energy Analyser Probe and Potential Probe Measurements on Mark V-S Accelerator.* "Ion Energy" is $e(V_c - V_p)$, "Energy Spread" is $\Delta(e V_c)$, and "Current Ratio" is the Ratio of Quiet Ion Current to Jet Ion Current.

Probe	Item	Approach accel. [77.8 → 12.5 cm from window]	Change Gas Ar → Xe	Increase Flow Rate (~.5→~1 mg/sec)	Increase B Field (210→250 amps)	Increase RF Power (1 kw→2 kw)
Potential Probes	T_e	Inc at < 43 cm	Tend Dec at ≥ 22 cm NC at < 22 cm	Var	NC to Var	Us Sl Inc
	V_p	Inc (esp at < 43 cm)	Var	Us Dec (esp Ar) at ≤ 33 cm	Argon Inc Xenon Var	Argon Inc Xenon Var
	N_e	Inc at < 43 cm	Us Inc low flow Var high flow	Inc (esp in Ar)	Us Dec	Sl Tend Inc
Potential Probe	T_e	(77.8 cm only)	Tend Dec.	Tend Dec	Var	Us Inc
	V_p	" " "	Us Inc	Var	Some Tend Inc	Us Inc
	N_e	" " "	Inc	Inc (esp in Ar)	Sl and Var	Us Inc
Energy Analyser Probe (Ions)	Ion Energy	(77.8 cm only)	Var	Strongly Dec	Var (Us Dec)	Var
	Energy Spread	" " "	Us Inc	Us Dec	Var and Sl	Var (Tend Inc)
	Current Ratio	" " "	Inc	Inc	Us Dec	Argon Inc Xenon Var

*Abbreviations used in Table:

Dec = Decreases
esp = especially
Inc = Increases
NC = No change
Sl = Slight, Slightly
Tend = Tendency
Us = Usually
Var = Variable

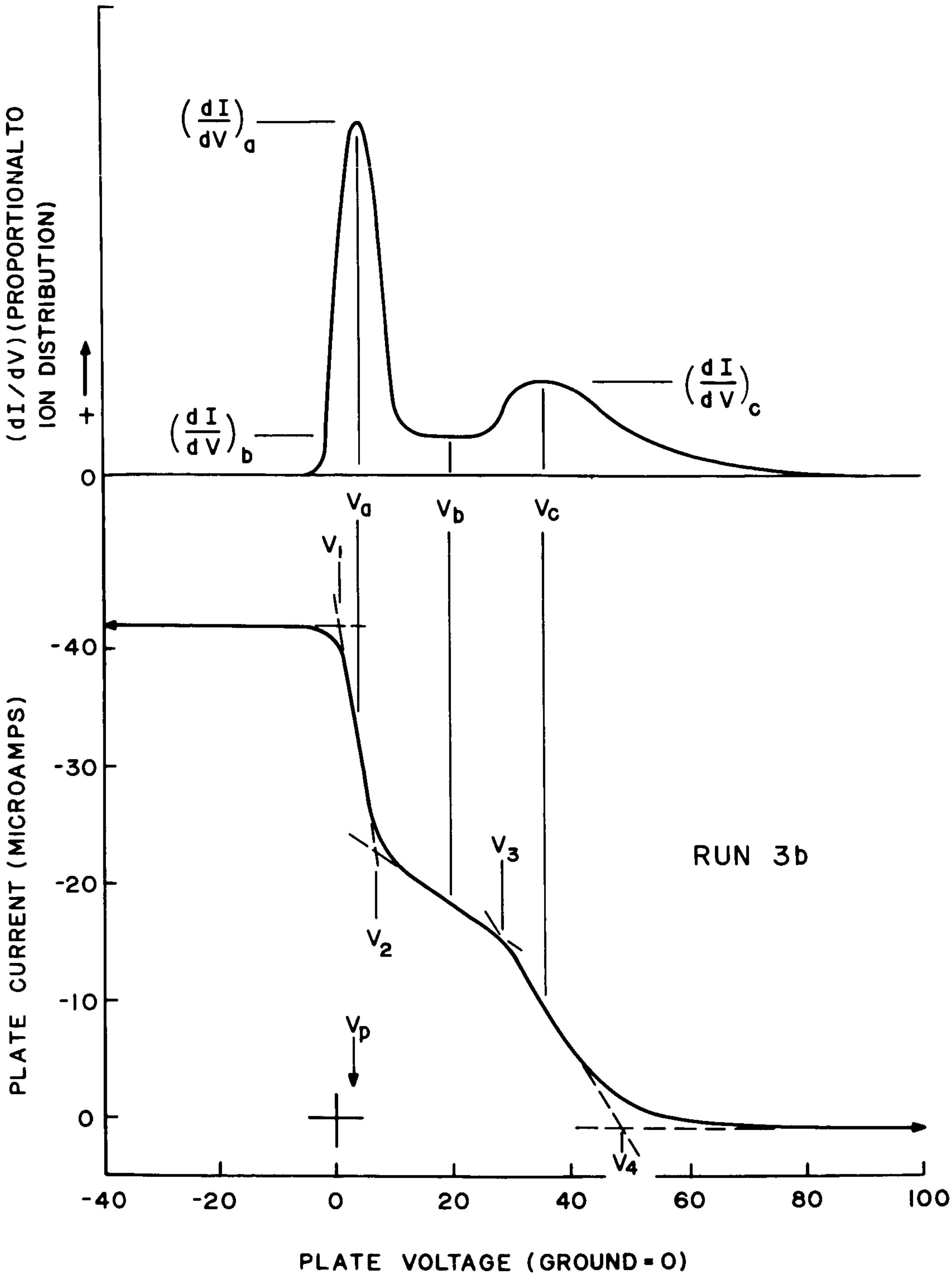

Figure 82. Typical Energy Analyser Probe (see Figure 25) Signal from Mark V-S Accelerator. The Lower Curve Shows the Analyser Probe Signal from Run 3b (see Table VII). The Upper Curve Represents the Resulting Ion Distribution as Obtained from a Semi-Quantitative Differentiation of the Lower Curve. The Items Listed in Table XII are Also Defined Here, with V_p Being Plasma Potential.

Table XII. Energy Analyser Probe Results from Mark V-S Accelerator. The Column Headings are Explained by Figure 82, with the Voltages being Referenced to Time-Averaged Plasma Potentials (V_p) as Determined with the Potential Probes (see Table IX). Run Numbers Refer to the Operating Conditions Listed in Table VII. The Energy Analyser Probe was Located 77.8 cm from the Accelerator Window.

Run No.	Potentials (volts)								μ amps/volt		
	V_p	(V_1-V_p)	(V_a-V_p)	(V_2-V_p)	(V_b-V_p)	(V_3-V_p)	(V_c-V_p)	(V_4-V_p)	$\left(\frac{dI}{dV}\right)_a$	$\left(\frac{dI}{dV}\right)_b$	$\left(\frac{dI}{dV}\right)_c$
1	0	≤ -2	2	10	~36	57	77.5	108	0.58	~.053	~.17
2	3	-7.5	3	16.5	29	35.5	53	82	0.33	.14	.23
3a	1	-6.5	-2	2	19	30	37	53	3.0	.24	.52
3b	2.9	-3	1	4	17	26	33.5	46	3.0	.32	.80
4	2	-5	0	4.5	19	28.5	43	60	2.0	.23	.40
5	7	-9	-3	5	33	65	89	121	1.00	.072	.17
6	10	-12	0	14	28	32	50	88	0.37	.14	.20
7	6	-8	-3	2	20	29.5	42	57	3.1	.21	.51
8	7	-7	-4	1	15	30	42	58.5	4.3	.33	.64
9	4	-7	-3	0	24	51.5	~69	~96.5	1.5	~.039	.085
10	5	-8	-4	~1	~24	~33	~55	87	1.4	.063	.090
11	4	-6	-3	0	~20	43	~58	82	2.2	.057	.11
12	4	-8	-3.5	0	14	23	~35	59	2.4	.12	.22
13	4	-8	-3.5	0	26	51.5	73	104	1.6	.038	.11
14	4	-7	-2	3	31	70	81	~105	1.6	.050	.33
15	8	-13	-6.5	-3.5	13	26	~42	~67	2.5	.059	~.16
16	9	-8	-6	-3	9	~20	31	57	~5.0	.17	.44

$(dI/dV)_b$, and $(dI/dV)_c$. Figure 82 also illustrates how these quantities refer to the relative ion distribution curve. As noted in the Table XII heading, all energy analyser probe potentials have been reduced by the average plasma potentials (V_p) as determined by the adjacent cylindrical Langmuir probes (see Table IX). Electron-repelling negative grid (Figure 25) potentials varied from -150 to -400 volts, depending on the run.

4.4.4.1 Jet Ion Exhaust

V_c of Figure 82 defines the high velocity directed ("jet") ion exhaust. The peak of the jet ion distribution curve is at an energy of $e(V_c - V_p)$ electron volts, and the jet ion energy spread is defined as

$$\Delta(eV_c) = e(V_4 - V_3)$$

If the ions are assumed to be singly ionized, the ion velocity and velocity spread can be calculated from

$$v_x = \left[2e(V_x - V_p)/m_i\right]^{1/2} \qquad (4.8)$$

where m_i is ion mass and sub -x refers to sub -1, -2, -3, -4, -a, -b, or -c. Thus, in Table XIII are listed the ion energy and ion velocity (v_c) at the peak of the jet distribution curve, and the energy spread and velocity spread of the ion jet. The ion jet velocity spread is defined as

$$\Delta v_c = v_4 - v_3 \ .$$

For reference, Table XIII also lists the plasma potentials (V_p) used.

From a comparison of Tables VII and XIII, we can see that both the ion energy and ion velocity of the ion jet distribution curve peak [i.e., $e(V_c - V_p)$ and v_c] show variable (random) effects on changing the Mark V-S accelerator gas from argon to xenon and also when increasing the rf power from 1 kw to 2 kw. However, $e(V_c - V_p)$ and v_c usually decrease on increasing the field coil current from 210 to 250 amps, and strongly decrease on increasing the gas flow rate from $\sim$0.5 to $\sim$ 1.0 mg/sec. A similar comparison shows the ion jet energy spread and velocity spread to usually increase on changing from argon to xenon, to usually decrease on increasing the gas flow rate from $\sim$ 0.5 to $\sim$ 1.0 mg/sec, to show only slight variable changes on increasing the field coil current from 210 to 250 amps, and to perhaps show a tendency to increase on increasing rf power from 1 kw to 2 kw. These trends are summarized in Table XI.

Table XIII. Summary of Mark V-S plasma characteristics as calculated from energy analyser probe (Table XII) and potential probe (Table IX) results. Plasma potential (V_p) is the time-averaged potential probe value at the energy analyser probe, $e(V_c - V_p)$ and v_c are the ion energy and ion velocity, respectively at the peak of the ion jet distribution curve, $\Delta(e V_c)$ and Δv_c are ion energy spread and velocity spread, respectively of the ion jet (see Figure 82), V_{pw} is the calculated plasma potential at the window, and D_i is the distance from the window at which most of the ionization is calculated to occur. See Table VII for accelerator operating conditions.

Run No.	77.8 cm from Window (Volts) V_p	(ev) $e(V_c-V_p)$	(ev) $\Delta(e V_c)$	($\times 10^5$ cm/sec) v_c	($\times 10^5$ cm/sec) Δv_c	(Volts) V_{pw}	(cm) D_i
1	0	77.5	51	19.3	6.2	149	6.1
2	3	53	46.5	16.0	6.8	194	11.2
3a	1	37	23	13.4	4.0	105	9.1
3b	2.9	33.5	20	12.7	3.7	101	9.1
4	2	43	31.5	14.4	5.3	119	8.7
5	7	89	56	20.7	6.4	222	7.5
6	10	50	56	15.5	8.2	~202	~10.9
7	6	42	27.5	14.2	4.6	123	8.5
8	7	42	28.5	14.2	4.8	111	7.4
9	4	~69	~45	~10.1	~3.2	157	~7.0
10	5	~55	~54	~9.0	~4.4	~202	~10.9
11	4	~58	39	~9.2	3.0	119	~6.0
12	4	~35	36	~7.2	3.5	68	~5.4
13	4	73	52.5	10.4	3.7	145	5.9
14	4	81	~35	10.9	~2.3	101	2.0
15	8	~42	~41	~7.9	~3.7	111	~7.2
16	9	31	~37	6.7	~3.7	105	8.7

4.4.4.2 Quiescent Ion Gas

All of these energy analyser probe response curves showed a sharp drop in plate current near zero volts at V_a in addition to the anticipated plate current drop at V_c due to the plasma jet ions (see Figure 82). Since V_a is close to plasma potential (see Table XII) and also since the plate current drop at V_a is relatively sharp, it would appear that the current drop at V_a is due to "quiescent" ions as opposed to the "jet" ions causing the plate current drop at V_c. This current inflection at V_a could not be the onset of some electron current (as the plate voltage goes positive) because any electrons that get past the negative grid or are produced through secondary processes at the grid, would not be attracted to the plate unless the plate potential became more negative than that of the negative grid (which is at -150 to -400 volts).

To possibly aid in determining the source of this "quiescent" ion gas that produces the inflection at V_a, the ratio of "quiet ion" current to "jet ion" current was examined as a function of accelerator operating conditions. Specifically, the above quiet to jet ion current ratio is $(I_1 - I_2)/(I_3 - I_4)$, where I_1 is the plate current at V_1, I_2 is plate current at V_2, etc. (see Figure 82). This current ratio is approximately the ratio of quiescent gas ion random current density to the product of jet ion velocity, jet ion density, and ion charge. It was observed that the above ratio (0.75 to 4.1, averaging at 1.5 for argon and 2.7 for xenon) increases on changing from argon to xenon, increases on increasing the gas flow rate from ~ 0.5 to ~ 1 mg/sec, usually decreases on increasing the magnetic field coil current from 210 to 250 amps, and increases for argon on increasing rf power from 1 kw to 2 kw. These observations are also summarized in Table XI.

It should be noted that a few exploratory energy analyser probe measurements (not those discussed here) have been made during some Mark V-S accelerator runs for which the accelerator was isolated. During those floating accelerator runs, the few exploratory analyser probe measurements showed only "jet ions" (V_c of Figure 82), but did not show any "quiescent ions" (V_a of Figure 82).

As discussed elsewhere, isolation of the accelerator eliminated a large accelerator-exhaust collector (calorimeter) current. Since the accelerator runs discussed in this section had the accelerator and vacuum tank grounded, the resulting large accelerator-tank current was probably due to ion loss to the accelerator walls. This ion loss is due to both diffusion and the radial electric field between the positive plasma and the grounded accelerator wall. This accelerator ion loss in turn would produce an ion defficiency in the accelerator exhaust. Consequently, to preserve charge neutrality in the exhaust, the few remaining engine exhaust ions must move slower than the electrons. If instead we assume the plasma in the exhaust jet to consist of full velocity electrons, some full velocity ions, and enough quiescent (non-exhaust) ions to give net charge neutrality, we meet the reduced ion current condition above and we have the quiescent ion gas which is observed by the measurements discussed here. The large mean-free-path in the accelerator exhaust could permit the two ion populations to co-exist.

Assuming the "quiescent ion" gas explanation to be the correct interpretation of the V_a inflection point (Figure 82, Table XII), appropriate semi-log plots and equation (4.1) have yielded temperature estimates for the quiescent ion gas of several runs. These temperatures ranged from 15,000 to 109,000^{o}K and averaged at 36,000^{o}K.

4.4.4.3 Intercomparison of Potential and Energy Analyser Probe Results

As indicated earlier, Table XI summarizes trends of the various measured potential probe and energy analyser probe-determined plasma parameters as a function of Mark V-S accelerator operating conditions.

To permit a more direct comparison of potential probe and energy analyser probe results, we may make use of the earlier observation that for any given run, the accelerator plasma potential is approximately proportional to the magnetic field. Thus, in Table XIII we have listed the plasma potential at the plasma-window interface (V_{pw}) as calculated from the 12.5 cm -from-window (D = 12.5 cm) measured plasma potential (see Table IX) while assuming proportionality between magnetic field and plasma potential. If it is assumed that the ions are formed at the window and the ion energy (in electron volts) is equal to the plasma potential through which the ions fall, then $V_{pw} - V_p$ (at D = 77.8 cm) should numerically equal $e(V_c - V_p)$. In all cases, we see that $[V_{pw} - V_p$ (at D = 77.8 cm)$] > e(V_c - V_p)$.

If we interpret the above observation to mean that the ions are formed well away from the accelerator window and thus have a smaller plasma potential difference through which to fall, it is possible to calculate the (ionizing) distance (D_i) from the window at which the difference between calculated plasma potential (calculated by the same method as V_{pw}) and V_p at the energy analyser probe (at D = 77.8 cm) equals $e(V_c - V_p)$, the ion kinetic energy at the energy analyser probe. This ionizing distance (D_i) is also listed in Table XIII as a function of accelerator operating conditions. D_i does not appear to vary in any consistent way with accelerator operating conditions, nor do the D_i values agree very well with the independently measured and calculated microwave penetration distance of about 3-5 cm from the plasma-window interface.

4.4.5 Thrust Stand Results

Original thrust stand tests were made with the waveguide evacuated. An arc immediately formed within the waveguide destroying the waveguide window. The waveguide section leading through the vacuum tank to the thrust stand was then sealed, using O-ringed choke flanges, so that the guide was at atmospheric pressure all the way to the beryllium oxide window in the engine. In spite of the flexible waveguide section and the many guide flanges, a good vacuum tank base pressure was achieved (4 x 10^{-6} mm Hg), the flexible guide section was not noticeably stiffened by the positive internal pressure, and successful engine operation was achieved.

The thrust stand sensitivity is sufficiently high to detect the reaction to the engine thrust. A number of instrumentation problems have been uncovered which currently limit the applicability and precision of this device. These are listed below, with suggestions for improvement.

1. Magnetic effect: Detectable forces are exerted on the thrust stand due purely to the interaction of the d-c magnetic field with miscellaneous magnetic pieces in the laboratory. For any given field level this is constant and known and so can be subtracted out.

2. Thermal effects: When the r-f is turned on, with or without plasma, a slow position shift results, probably due to the waveguide heating and expanding. One procedure which has been used is to turn the r-f on first and let the thrust stand seek a new equilibrium zero before igniting the plasma by turning up the magnetic field. Cooling of the guide may reduce this effect.

3. Vibration: The large mechanical pump creates a vibration signal on the thrust stand transducer output comparable in magnitude to the thrust signal. The vacuum tank is mounted on vibration absorbing pads and is further isolated from the pump by a bellows section in the vacuum line. It is believed, however, that much of this vibration is being carried into the thrust stand by water lines. Attempts will be made to reduce this vibration level, perhaps by installing a flexible section in the pump water line.

The following actions were taken to reduce these interference problems.

1. Magnetic effect: Steel rails and calorimeter carriage wheels originally located in the vacuum tank were removed. It was also discovered that contrary to the design specifications, the flexible thrust stand legs were magnetic; these were replaced by one .030" nonmagnetic stainless steel leg at each of the four corners. These changes reduced the magnetic problem, but a substantial shift in thrust stand location still takes place due to the d-c accelerator magnetic field.

2. Vibration: The actual thrust measurement is made by measuring the difference in equilibrium thrust stand positions immediately before and immediately after shutdown as indicated by Figure 33. During this short period around shutdown, the large mechanical pump is turned off, thereby greatly reducing the vibrational level of the stand. During this period, the diffusion pumps are fore-pumped by smaller mechanical pumps.

3. Thermal effects: Nothing has yet been done to reduce the slow thrust stand drift probably accountable to waveguide thermal expansion. This effect does not interfere with the thrust measurement made by the above outlined shutdown procedure.

Initial thrust measurements, using the Mark V-S accelerator resulted in very low thrust, relative to mass flow and power. Placing a current meter between the calorimeter and ground showed that a very large (~ 1 ampere) electron current was flowing through the calorimeter, undoubtedly coming from the grounded engine through the plasma stream. (This was later confirmed; see below.) The calorimeter during these thrust stand tests is rather closely positioned to the engine due to limited vacuum tank length; the engine exit plane to calorimeter entrance plane distance is 8 centimeters. Since the calorimeter efficiencies were still high (Table XIV), it is possible that a significant portion of this power was being carried to the calorimeter by electrons and that ions were merely drifting back to the accelerator walls. The calorimeter efficiency remained as high or higher, however, when the calorimeter was ungrounded, indicating either that the ions were now being accelerated or that the electrons were finding another path to ground after depositing their energy at the calorimeter. The calorimeter assumed a potential of about -25 v relative to ground during these grounded-accelerator, ungrounded-calorimeter tests.

TABLE XIV

Power Efficiency (P_{plasma}/P_{r-f})

Mark V-S Accelerator, 1 kw

(Accelerator on thrust stand, grounded)

Gas	Flow mg/sec.	Window Field gauss	Power Efficiency
Ar	1.4	4290	.53
	.26	4290	.67
	.26	3900	.68
	.26	3900	.75
Kr	.56	4290	.79

The thrust stand was modified so that the engine would be isolated from ground, in hopes of eliminating this short-circuiting electron current. In order to isolate the accelerator the following changes had to be made:

1. A teflon spacer was placed between the engine flange and the thrust stand cover mounting surface, and nylon bushings were used to insulate the mounting bolts from the engine flange. This was a very difficult change since the coil housing is at atmospheric pressure and the bolts have to sustain the very large force built up between the two coil housing covers. Originally, teflon and nylon both were tried, but these proved to be inadequate.

2. Rubber hoses were added within the coil housing to carry the propellant gas and coolant water to the accelerator.

3. A nylon sleeve was made and the back cover was modified so that the waveguide could be brought into the coil housing without being grounded to the thrust stand.

4. Choke flanges and a thin boron nitride spacer were added to the waveguide before it enters the thrust stand. By this type of coupling the engine waveguide need not be d-c electrically tied to the grounded waveguide from the klystron.

Although considerable time was spent making these modifications and achieving a good vacuum, some thrust measurements with the isolated accelerator were obtained before the end of the contract period. Since there have not been sufficient tests to clearly establish parametric dependencies, the results to date are presented in tabular form (Table XV) rather than as plotted curves. Tank pressures during these tests were in the range 2×10^{-4} to 2×10^{-5} torr. The following items are noted from this table:

1. Thrust levels were substantially increased over original results. Whether or not this is directly ascribable to isolating the accelerator, however, is not clear, as discussed below.

2. Measured thrust efficiencies are now large enough to indicate that this type of accelerator is not inherently a low efficiency device. Further study is required to determine just what the best attainable efficiency is and under what operating conditions ($\dot{m}$, P_{r-f}, B, etc.) this maximum is obtained.

3. A heavier molecule (xenon) appears to improve thrust efficiency, which agrees with the earlier result that calorimeter efficiency also increases with increasing molecular weight.

TABLE XV. Thrust and Calorimeter Measurements. Isolated Mark V-S Accelerator. Isolated 10" Dia. x 20" Long Calorimeter. Accelerator-to-Calorimeter Distance 8 cm.

Date	Test No.	Gas Species	Gas Flow mg/sec (in)	R-f Power Inc Wt (P_{rf})	R-f Power Refl wt	Coil Current amp	Resonance Position* cm	Calorimeter Plasma Power wt (P_p)	η_p (P_p/P_{rf})	Thrust Millinewton (T)	η_t ($T^2/2\dot{m}P_{rf}$)	I_{sp}+ sec ($T/\dot{m}g$)
9/28	9	Argon	.85	680	0	230	4.6	441	.65	9.0	.07	1100
	10	"	.85	1824	0	230	4.6	--	--	23	.16	2700
	12	"	.48	1824	0	230	4.6	--	--	23	.31	4800
9/29	2	"	.10	1824	0	230	4.6	--	--	6.8	.13	6800
	3	"	.39	1824	0	230	4.6	--	--	14	.14	3500
	4	"	.86	1824	0	230	4.6	--	--	20	.13	2300
	5	"	.93	1824	0	230	4.6	--	--	32	.31	3500
	7	"	.99	1824	0	230	4.6	--	--	24	.16	2400
	8	"	.31	912	0	230	4.6	647	.71	7.5	.09	2400
	9	"	.56	912	0	230	4.6	483	.53	17	.29	3000
	10	"	.91	912	0	230	4.6	565	.62	14	.11	1500
	11	"	1.11	912	0	230	4.6	537	.59	14	.09	1200
	12	"	2.8	912	0	230	4.6	438	.48	17	.06	600
9/30	3	"	.79	912	0	230	4.6	510	.56	20	.28	2500
	4	"	.79	912	0	210	3.6	510	.56	25	.42	3200
	5	"	.80	912	0	250	5.3	614	.67	21	.30	2600
	6	"	.83	912	0	190	2.8	290	.32	9.5	.06	1100
	8	Xenon	.82	912	0	230	4.6	680	.75	--	--	--
	12	"	.82	912	-	230	4.6	--	--	26	.46	3200

*Distance on axis away from window.

+A specific impulse (I_{sp}) of 3000 sec. corresponds to an exhaust velocity of 29,400 m/sec. This is equivalent to 180 ev Ar^+ ions or 585 ev Xe^+ ions.

4. Flow and field dependencies appear to exist, but further data are required to define these quantitatively. It is obvious that low field (190 amperes) and low flow (.10 and .31 mg/sec) give low thrust efficiency.

During these tests, both the accelerator and the calorimeter were isolated. The accelerator, however, appeared to assume a potential very near ground (within $\pm$ 2 volts) while the calorimeter ran typically at -25 to -30 volts, depending on operating conditions. When the calorimeter was grounded but the accelerator left isolated, the accelerator potential relative to ground rose to about 24 volts, at 1 kw r-f power level. Contrary to earlier results, grounding the accelerator and calorimeter, so that a large (~ 600 ma) electron current flowed, did not clearly cause a marked decrease in thrust. These results need further corroboration, but it is possible that improvements in thrust measurement procedure in fact caused the noted thrust improvement.

These voltage measurements also raise the possibility that the observed thrust is merely an electrostatic effect. To check this, a d-c voltage (up to 50 volts) was placed between the isolated accelerator and calorimeter; no thrust stand deflection resulted.

Unfortunately, mechanical failures in the d-c coil unit and in the accelerator mounting structure necessitated an early termination of the xenon tests.

In order to confirm the relatively high measured thrust efficiencies, an attempt was made to obtain thrust and energy probe data simultaneously. Coil cooling, engine structure and probe leakage current problems continued to plague these tests, however, so that no simultaneous thrust and ion energy data were obtained.

4.5 MARK VIII (SCREEN WAVEGUIDE) ACCELERATOR

A photograph of the exhaust stream from the Mark VIII accelerator is shown in Figure 83. Comparison of this photo with a similar one taken for the Mark V-S accelerator (Figure 62) suggests that this stream may be narrower. This is confirmed by the calorimeter power data in Figure 84 which indicate that the calorimeter collects a greater percentage of the exhaust power for greater distances away from the engine exit (compare Figure 69). It is also interesting to note that the peak calorimeter power occurs some distance out from the accelerator.

Power efficiency data for the Mark VIII accelerator are plotted in Figures 85 and 86. Xenon again (as with the Mark V-S accelerator) enables operation at greater than 60% efficiency; a peak of 65% was recorded on one run. Argon efficiency is slightly higher than for the Mark V-S accelerator.

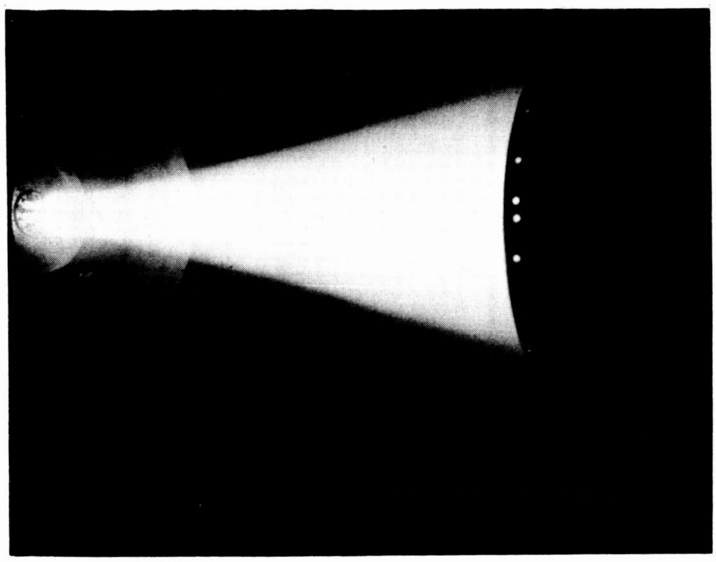

Figure 83. Photograph of Exhaust Stream Emerging from Mark VIII Accelerator on the Left and Incident on 10" Diameter x 20" Long Calorimeter on the Right. Argon, 1 kw.

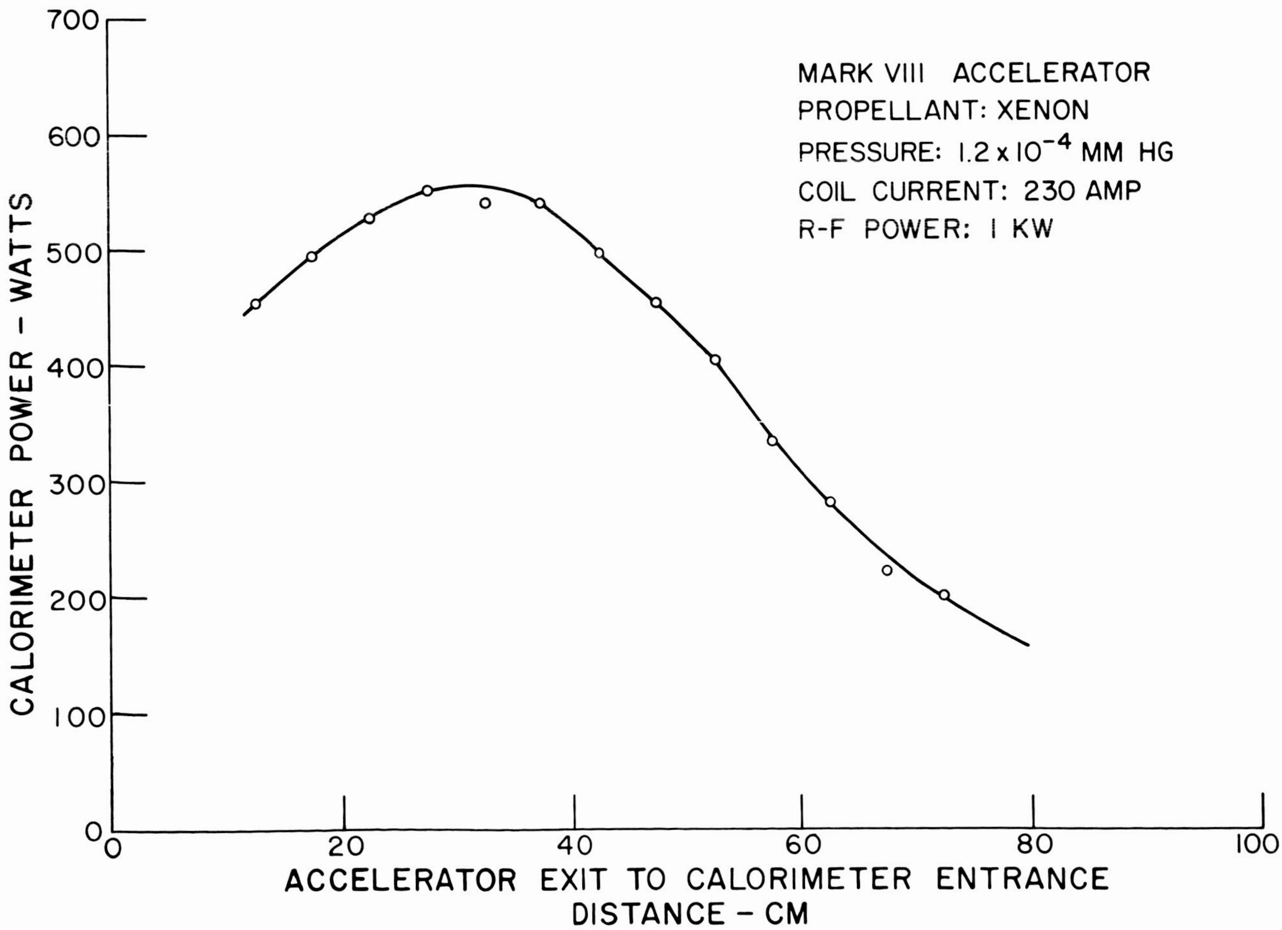

Figure 84. Dependence of Power on Calorimeter Position

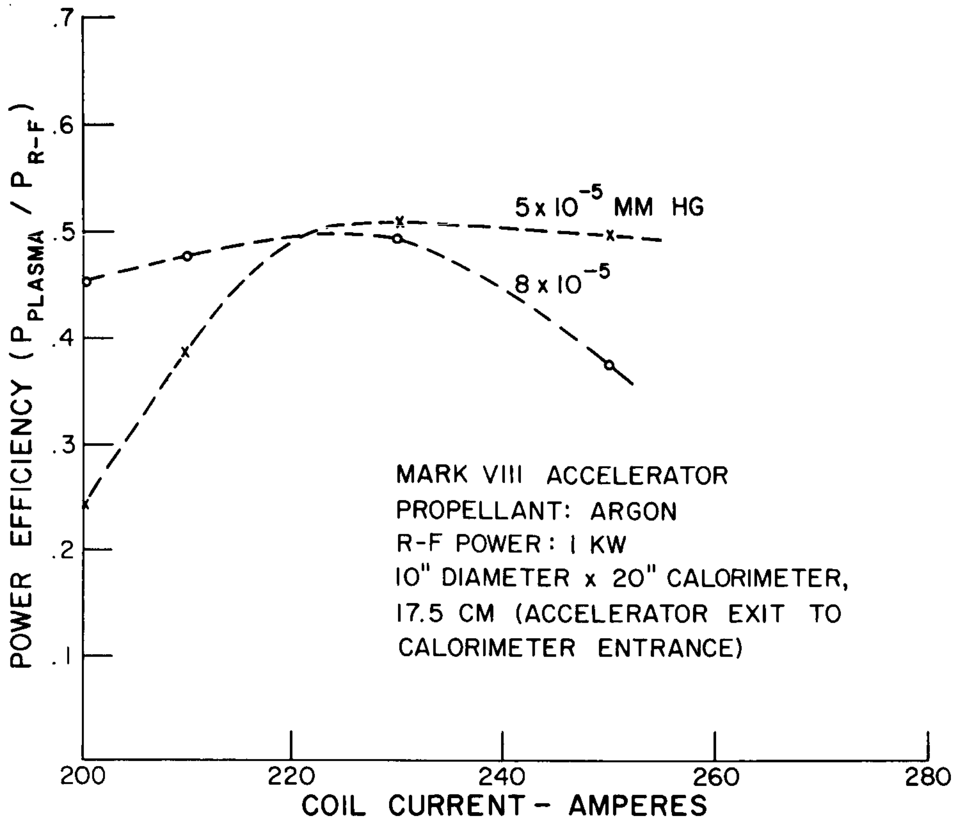

Figure 85. Power Efficiency Data Mark VIII, Argon

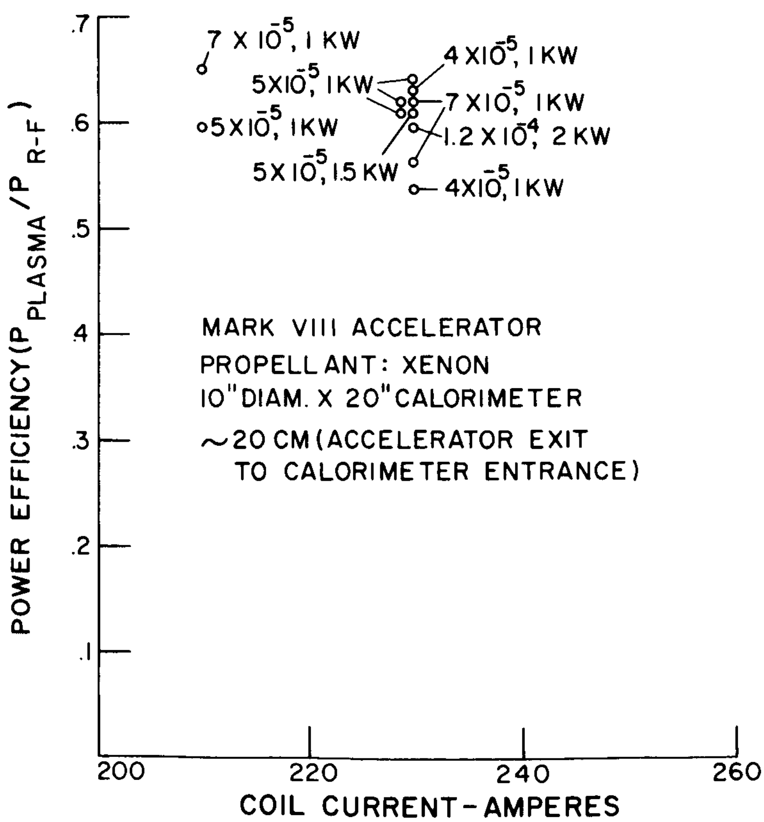

Figure 86. Power Efficiency Data Mark VIII, Xenon

The efficiency at low power (1 kw) is about the same as at higher power (2 kw); this design is more efficient than the Mark V-S accelerator at lower power levels.

These results indicate that an accelerator of this general design will run as efficiently as do the solid wall accelerators. Being capable of removing the injection point further from the window and in addition being able to pump on this region without loss of efficiency is very significant since it most certainly reduces the power loading on the window.

At 2 kw in xenon some erosion and burning away of the copper screen occurred. At the same power level in argon, the screen operated at a lower temperature. If future designs of this type are attempted, a higher temperature assembly is recommended.

5. PROPAGATION WITHIN A MAGNETOPLASMA-FILLED WAVEGUIDE

5.1 INTRODUCTION

As an aid in the analysis of the experimental r-f probe measurement data shown in Figures 71-74, it is desirable to correlate these results with those of some model which the theory supports. To do this, we would like to ascertain the electron density of the plasma, and relate this, in light of known damping mechanisms, to the propagation properties of the EM wave in the plasma. Eventually, then, we should be able to compute the field intensity, and reflected power from the model, and compare these with experimental evidence.

An electron density model, as a function of distance from the dielectric window, is assumed. This model is then used to derive the complex propagation constant, as a function of distance along the waveguide. A lumped parameter equivalent circuit analysis is then performed on the plasma filled waveguide, and the desired computations for the pertinent comparisons are made from this circuit. The theory behind this analysis follows.

5.2 THEORETICAL MODEL

First, from the equations of motion of an electron in an electromagnetic field, with a constant magnetic intensity in the direction of propagation, the wave propagation constant is obtained in a manner similar to Stratton (Reference 26). The resulting dispersion relation, incorporating the effect of electron collision interactions, is

$$h^2 = \left(\frac{\omega}{c}\right)^2 \left[1 - \left(\frac{\omega_p}{\omega}\right)^2 \frac{1}{1 - \frac{\omega_B}{\omega} - j\,\frac{\nu}{\omega}} \right] \tag{1}$$

where, ω = r-f frequency

c = free space velocity of light

$\omega_p^2 = \frac{n_e e^2}{\epsilon_o m}$, plasma frequency

$\omega_B = \frac{qB}{m}$, electron cyclotron frequency

ν = collision frequency

and the input field has been assumed to be circularly polarized, and proportional to exp - j (h z - ωt).

It is found, however, that another damping effect is more pronounced than that of actual particle collisions. This is the Doppler frequency shifting effect (References 2 and 3) by which the r-f field frequency influencing an electron is a function of the electron's velocity parallel to the direction of field propagation. The effective frequency experienced by the electron is:

$$\omega' = \omega + h_r v, \tag{2}$$

where h_r is the real part of the propagation constant, and v is the electron velocity in the direction of field propagation. This may be shown to be the chief contributor to the damping effect by introducing this effective frequency into the dispersion relation, averaging this relation according to a maxwellian velocity distribution over all velocities, and allowing the particle collision frequency ν to go to zero. The details of this derivation may be found in Appendix I. The resulting general solution for the conductivity is:

$$\sigma = \frac{2\epsilon_o \omega_p^2}{V_{te} h_r^2} \Lambda \left\{ \frac{\sqrt{\pi}}{2} \frac{h_r}{\Lambda} - j \int_0^{\frac{1}{V_{te}}} \exp\left(y \frac{\Lambda}{h_r}\right)^2 dy \right\} \exp - \left(\frac{\Lambda}{V_{te} h_r}\right)^2 \tag{3}$$

where $V_{te} = \left(\frac{2kT}{m_e}\right)^{1/2}$ = electron velocity

$\Lambda = \omega - \omega_B$

$h = h_r + j h_i$

From Maxwell's equations for an input field proportional to exp-j (hz-ωt), the conductivity becomes,

$$\sigma = - j \omega \epsilon_o \left(1 - \frac{h^2}{\omega^2/c^2}\right) \tag{4}$$

Equating the real and imaginary parts of (3) and (4), respectively, yields

$$h_r = \frac{-\sqrt{\pi}\, \omega_p^2}{2 V_{te}} \frac{\omega/c^2}{h_r h_i} \exp - \left(\frac{\Lambda}{V_{te} h_r}\right)^2 \tag{5}$$

$$h_i = -\left\{h_r^2 + \left(\frac{\omega}{c}\right)^2 \left[\frac{2\omega_p^2}{V_{te}\,\omega h_r^2} \Lambda \exp^{-\left(\frac{\Lambda}{V_{te} h_r}\right)^2} \int_o^{\frac{1}{V_{te}}} \exp\left(y\frac{\Lambda}{h_r}\right)^2 dy - 1\right]\right\}^{1/2} \tag{6}$$

Note that the negative sign associated with the square root in equation (6) has been chosen.

A computer program has been written to solve Equations (5) and (6). An explanation of this program may be found in Appendix I.

Having obtained the complex propagation constant by the above methods, the equivalent circuit for the magnetoplasma-filled waveguide may be devised. This, of course, allows the inclusion of the appropriate boundary conditions for the waveguide and the mode of the input field. A detailed derivation of the equivalent circuit appears in Appendix II.

The waveguide and enclosed medium are then "segmented" into uniform increments starting from the dielectric window, similar to the procedure suggested by Mullin and Shane (Reference 27). In each increment, the axial magnetic intensity is assumed constant, and the wave propagation constant is computed. At some distance from the window, e.g., at the Nth increment the field is assumed to be completely attenuated. The characteristic impedance of the remainder of the guide, the Nth, $(N+1)^{th}$, etc. increments, then is assumed constant, and computed from the parameters at the N^{th} increment. This impedance is then used as the load for the T-equivalent circuit computed for the $(N-1)^{th}$ increment. The input impedance for this network is in turn used as the load for the $(N-2)^{th}$ increment, and so forth, until we have reached the dielectric window. Now that the equivalent circuit for each increment is specified, a normalized input field is introduced at the window. The drop across each incremental circuit is computed, and the corresponding output field intensity is computed. The magnitude of the resulting field versus distance from the dielectric window is shown in later Figures. The calculated reflection coefficient at the window is also shown.

The parameters which may be varied in the computer program which performs all of the preceeding calculations are as follows:

(1) Plasma frequency - the electron density model used for the presented results is an exponentially increasing one, as proposed by Yen (Reference 28), in which the maximum value and relaxation constant are variable parameters.

(2) Cyclotron frequency - an empirical model has been derived for the steady axial magnetic intensity along the guide, based on the actual measured field configuration (Figure 12); the coil current producing this field is a variable parameter.

(3) Segment size - the thickness and number of increments into which the guide is segmented is a variable parameter.

(4) Energy - the electron energy, 2 KT, from which the electron velocity is computed is a variable.

(5) The r-f frequency may be varied.

5.3 RESULTS AND INTERPRETATION

A typical computer output for the previously described program is shown on the following pages (Table XVI). The parameters chosen for this run are:

$$f = 8350 \quad \text{MC}$$

$$n_e = n_\infty (1 - \epsilon^{-\gamma x}) \quad \text{electrons/cm}^3$$

$$= 10^{12} (1 - \epsilon^{-0.1x})$$

$$\text{where } x = z\left(\frac{\omega}{c}\right)$$

$$\beta = 231 \exp\left[-\left(\frac{z}{2.54} + 2\right)^2 \Big/ \left(26 + \frac{z}{2.54}\right)\right] \text{gauss}$$

$$I = 230 \quad \text{AMPS}$$

$$2KT = 1.6 \times 10^{-12} \quad \text{ERGS } (= 1 \text{ ev})$$

On pages one and two of the output, respectively, from left to right[+] :

DIST = distance from dielectric window

WB = cyclotron frequency

WP = plasma frequency

V = collision frequency

H REAL = real part of propagation constant

H IMAG = imaginary part of propagation constant

TABLE XVI. TYPICAL COMPUTER OUTPUT

THE GAS USED IN THIS EXPERIMENT WAS ARGON

COMPLEX PROPAGATION, CONDUCTIVITY, IMPEDANCE, AND FIELD AT EACH POINT ALONG GUIDE G. CRIMI 8/65

DIST(CM)	WR(1/SEC)	WP(1/SEC)	V(1/SEC)	H REAL	H IMAG	E FIELD REAL	E FIELD IMAG
0.200	0.7884E 11	0.1046E 11	0.1755E 08	0.1818E 01	-0.	-0.6209E 00	0.4531E 00
0.400	0.7788E 11	0.1467E 11	0.1027E 08	0.1886E 01	-0.	0.1603E 00	-0.8419E 00
0.600	0.7690E 11	0.1781E 11	0.6632E 07	0.1955E 01	-0.	0.3208E 00	0.1106E 01
0.800	0.7590E 11	0.2039E 11	0.8122E 07	0.2024E 01	-0.	-0.7492E 00	-0.1196E 01
1.000	0.7489E 11	0.2260E 11	0.4689E 07	0.2096E 01	-0.	0.1050E 01	0.1086E 01
1.200	0.7386E 11	0.2455E 11	0.4689E 07	0.2170E 01	-0.	-0.1162E 01	-0.7828E 00
1.400	0.7282E 11	0.2630E 11	0.	0.2246E 01	-0.	0.1050E 01	0.3310E 00
1.600	0.7176E 11	0.2788E 11	0.4194E 07	0.2327E 01	-0.	-0.7241E 00	0.1863E 00
1.800	0.7070E 11	0.2932E 11	0.2097E 07	0.2412E 01	-0.	0.2406E 00	-0.6598E 00
2.000	0.6962E 11	0.3066E 11	0.3316E 07	0.2502E 01	-0.	0.2970E 00	0.9749E 00
2.200	0.6853E 11	0.3189E 11	0.3923E 07	0.2599E 01	-0.	-0.7561E 00	-0.1041E 01
2.400	0.6744E 11	0.3304E 11	0.	0.2705E 01	-0.	0.1005E 01	0.8206E 00
2.600	0.6634E 11	0.3411E 11	0.1483E 07	0.2821E 01	-0.	-0.9541E 00	-0.3585E 00
2.800	0.6523E 11	0.3511E 11	0.1483E 07	0.2949E 01	-0.	0.5955E 00	-0.2160E 00
3.000	0.6412E 11	0.3605E 11	0.1049E 07	0.3094E 01	-0.	-0.2957E-01	0.7095E 00
3.200	0.6301E 11	0.3694E 11	0.1816E 07	0.3258E 01	-0.	-0.5426E 00	-0.9228E 00
3.400	0.6189E 11	0.3778E 11	0.1483E 07	0.3450E 01	-0.	0.8745E 00	0.7357E 00
3.600	0.6077E 11	0.3857E 11	0.1049E 07	0.3676E 01	-0.	-0.7788E 00	-0.1949E 00
3.800	0.5965E 11	0.3932E 11	0.	0.3951E 01	-0.	0.2560E 00	-0.4442E 00
4.000	0.5854E 11	0.4003E 11	0.5243E 06	0.4297E 01	-0.	0.4185E 00	0.7865E 00
4.200	0.5742E 11	0.4070E 11	0.7415E 06	0.4751E 01	-0.	-0.7564E 00	-0.5245E 00
4.400	0.5631E 11	0.4134E 11	0.5243E 06	0.5388E 01	-0.	0.3784E 00	-0.2105E 00
4.600	0.5519E 11	0.4195E 11	0.4540E 06	0.6379E 01	-0.	0.4186E 00	0.6328E 00
4.800	0.5409E 11	0.4253E 11	0.	0.8255E 01	-0.9352E-08	-0.3683E 00	0.7208E-01
5.000	0.5298E 11	0.4308E 11	0.2022E 09	0.1455E 02	-0.5238E 01	-0.1118E 00	-0.6360E-01
5.200	0.5189E 11	0.4361E 11	0.	0.6913E 01	-0.2002E 02	-0.2310E-02	0.2174E-02
5.400	0.5080E 11	0.4411E 11	0.	0.9470E-06	-0.1062E 02	-0.3478E-03	0.3273E-03
5.600	0.4971E 11	0.4459E 11	0.2621E 06	0.	-0.6253E 01	-0.1079E-03	0.1016E-03
5.800	0.4864E 11	0.4505E 11	0.5243E 06	0.	-0.5280E 01	-0.3990E-04	0.3755E-04
6.000	0.4757E 11	0.4548E 11	0.5243E 06	0.	-0.4648E 01	-0.1654E-04	0.1557E-04
6.200	0.4651E 11	0.4590E 11	0.5243E 06	0.	-0.4194E 01	-0.7449E-05	0.7010E-05
6.400	0.4546E 11	0.4630E 11	0.	0.	-0.3848E 01	-0.3575E-05	0.3364E-05
6.600	0.4442E 11	0.4669E 11	0.	0.	-0.3571E 01	-0.1805E-05	0.1699E-05
6.800	0.4339E 11	0.4706E 11	0.1049E 07	0.	-0.3344E 01	-0.9509E-06	0.8948E-06
7.000	0.4237E 11	0.4741E 11	0.1049E 07	0.	-0.3152E 01	-0.5191E-06	0.4885E-06
7.200	0.4137E 11	0.4775E 11	0.1816E 07	0.	-0.2988E 01	-0.2922E-06	0.2750E-06
7.400	0.4037E 11	0.4807E 11	0.1049E 07	0.	-0.2845E 01	-0.1690E-06	0.1590E-06
7.600	0.3939E 11	0.4838E 11	0.	0.	-0.2718E 01	-0.1001E-06	0.9417E-07
7.800	0.3842E 11	0.4868E 11	0.1483E 07	0.	-0.2605E 01	-0.6053E-07	0.5697E-07
8.000	0.3746E 11	0.4897E 11	0.	0.	-0.2503E 01	-0.3733E-07	0.3513E-07
8.200	0.3652E 11	0.4924E 11	0.	0.	-0.2411E 01	-0.2343E-07	0.2205E-07
8.400	0.3559E 11	0.4950E 11	0.2966E 07	0.	-0.2327E 01	-0.1494E-07	0.1406E-07
8.600	0.3467E 11	0.4976E 11	0.2097E 07	0.	-0.2250E 01	-0.9666E-08	0.9096E-08
8.800	0.3377E 11	0.5000E 11	0.	0.	-0.2178E 01	-0.6339E-08	0.5966E-08
9.000	0.3288E 11	0.5024E 11	0.2097E 07	0.	-0.2112E 01	-0.4210E-08	0.3962E-08
9.200	0.3201E 11	0.5046E 11	0.2097E 07	0.	-0.2050E 01	-0.2828E-08	0.2661E-08
9.400	0.3115E 11	0.5068E 11	0.	0.	-0.1993E 01	-0.1920E-08	0.1806E-08
9.600	0.3031E 11	0.5089E 11	0.2097E 07	0.	-0.1939E 01	-0.1315E-08	0.1237E-08
9.800	0.2948E 11	0.5109E 11	0.	0.	-0.1888E 01	-0.9067E-09	0.8532E-09
10.000	0.2867E 11	0.5128E 11	0.2097E 07	0.	-0.1840E 01	0.	0.

TABLE XVI. TYPICAL COMPUTER OUTPUT (Cont'd)

Z0 REAL	Z0 IMAG	ZIN REAL	ZIN IMAG	COND REAL	COND IMAG	DIST(CM)	E MAG	EP
0.3864E 12	0.	0.2050E 12	0.1420E 12	0.	0.3675E-12	0.200	0.7686E 00	0.
0.3707E 12	0.	0.1752E 12	0.2658E 11	0.	0.7496E-12	0.400	0.8570E 00	0.
0.3562E 12	0.	0.1855E 12	-0.8320E 11	0.	0.1149E-11	0.600	0.1152E 01	0.
0.3426E 12	0.	0.2515E 12	-0.1948E 12	0.	0.1571E-11	0.800	0.1412E 01	0.
0.3297E 12	0.	0.4436E 12	-0.2671E 12	0.	0.2017E-11	1.000	0.1511E 01	0.
0.3175E 12	0.	0.6925E 12	0.1770E 10	0.	0.2495E-11	1.200	0.1401E 01	0.
0.3057E 12	0.	0.4150E 12	0.2735E 12	0.	0.3008E-11	1.400	0.1101E 01	0.
0.2943E 12	0.	0.2065E 12	0.1825E 12	0.	0.3566E-11	1.600	0.7477E 00	0.
0.2831E 12	0.	0.1402E 12	0.6417E 11	0.	0.4176E-11	1.800	0.7023E 00	0.
0.2722E 12	0.	0.1355E 12	-0.4375E 11	0.	0.4851E-11	2.000	0.1019E 01	0.
0.2614E 12	0.	0.1943E 12	-0.1532E 12	0.	0.5603E-11	2.200	0.1286E 01	0.
0.2506E 12	0.	0.4143E 12	-0.1905E 12	0.	0.6453E-11	2.400	0.1297E 01	0.
0.2397E 12	0.	0.4399E 12	0.1765E 12	0.	0.7424E-11	2.600	0.1019E 01	0.
0.2288E 12	0.	0.1762E 12	0.1564E 12	0.	0.8549E-11	2.800	0.6334E 00	0.
0.2176E 12	0.	0.1067E 12	0.4001E 11	0.	0.9872E-11	3.000	0.7102E 00	0.
0.2062E 12	0.	0.1148E 12	-0.6620E 11	0.	0.1146E-10	3.200	0.1071E 01	0.
0.1944E 12	0.	0.2420E 12	-0.1599E 12	0.	0.1340E-10	3.400	0.1143E 01	0.
0.1820E 12	0.	0.3511E 12	0.1258E 12	0.	0.1585E-10	3.600	0.8028E 00	0.
0.1690E 12	0.	0.1123E 12	0.9666E 11	0.	0.1904E-10	3.800	0.5127E 00	0.
0.1551E 12	0.	0.7718E 11	-0.1407E 11	0.	0.2336E-10	4.000	0.8909E 00	0.
0.1400E 12	0.	0.1597E 12	-0.1138E 12	0.	0.2960E-10	4.200	0.9205E 00	0.
0.1232E 12	0.	0.1840E 12	0.1159E 12	0.	0.3940E-10	4.400	0.4330E 00	0.
0.1039E 12	0.	0.5370E 11	0.1307E 11	0.	0.5708E-10	4.600	0.7587E 00	0.
0.8009E 11	0.9127E 02	0.1298E 12	-0.7628E 11	0.2342E-18	0.9872E-10	4.800	0.3752E 00	0.1283E-17
0.4014E 11	0.1448E 11	0.3538E 11	0.1611E 11	0.2312E-09	0.2747E-09	5.000	0.1286E 00	0.1297E 00
0.1015E 11	0.2942E 11	0.1015E 11	0.2941E 11	0.4198E-09	-0.5400E-09	5.200	0.3172E-02	0.
0.5506E 04	0.6197E 11	0.5653E 04	0.6244E 11	0.3051E-16	-0.1757E-09	5.400	0.4776E-03	0.
0.	0.1049E 12	0.	0.1065E 12	0.	-0.6396E-10	5.600	0.1482E-03	0.
0.	0.1240E 12	-0.	0.1262E 12	0.	-0.4693E-10	5.800	0.5479E-04	0.3000E 01
0.	0.1406E 12	0.	0.1432E 12	0.	-0.3741E-10	6.000	0.2271E-04	0.3000E 01
0.	0.1555E 12	-0.	0.1585E 12	0.	-0.3133E-10	6.200	0.1023E-04	0.3000E 01
0.	0.1691E 12	0.	0.1725E 12	0.	-0.2710E-10	6.400	0.4908E-05	0.3000E 01
0.	0.1818E 12	-0.	0.1855E 12	0.	-0.2399E-10	6.600	0.2479E-05	0.3000E 01
0.	0.1938E 12	0.	0.1977E 12	0.	-0.2161E-10	6.800	0.1306E-05	0.3000E 01
0.	0.2051E 12	-0.	0.2093E 12	0.	-0.1972E-10	7.000	0.7128E-06	0.3000E 01
0.	0.2159E 12	0.	0.2204E 12	0.	-0.1819E-10	7.200	0.4012E-06	0.3000E 01
0.	0.2263E 12	-0.	0.2310E 12	0.	-0.1692E-10	7.400	0.2320E-06	0.3000E 01
0.	0.2363E 12	0.	0.2412E 12	0.	-0.1585E-10	7.600	0.1374E-06	0.3000E 01
0.	0.2460E 12	-0.	0.2511E 12	0.	-0.1494E-10	7.800	0.8312E-07	0.3000E 01
0.	0.2554E 12	0.	0.2607E 12	0.	-0.1415E-10	8.000	0.5126E-07	0.3000E 01
0.	0.2646E 12	-0.	0.2701E 12	0.	-0.1346E-10	8.200	0.3217E-07	0.3000E 01
0.	0.2735E 12	0.	0.2792E 12	0.	-0.1286E-10	8.400	0.2051E-07	0.3000E 01
0.	0.2823E 12	-0.	0.2881E 12	0.	-0.1232E-10	8.600	0.1327E-07	0.3000E 01
0.	0.2908E 12	0.	0.2968E 12	0.	-0.1184E-10	8.800	0.8705E-08	0.3000E 01
0.	0.2992E 12	-0.	0.3053E 12	0.	-0.1141E-10	9.000	0.5781E-08	0.3000E 01
0.	0.3074E 12	0.	0.3135E 12	0.	-0.1102E-10	9.200	0.3883E-08	0.3000E 01
0.	0.3155E 12	-0.	0.3214E 12	0.	-0.1067E-10	9.400	0.2636E-08	0.3000E 01
0.	0.3235E 12	0.	0.3287E 12	0.	-0.1035E-10	9.600	0.1805E-08	0.3000E 01
0.	0.3313E 12	-0.	0.3349E 12	0.	-0.1005E-10	9.800	0.1245E-08	0.3000E 01
0.	0.3390E 12	0.	0.3390E 12	0.	-0.9782E-11	10.000	0.	0.3000E 01

THE COEFFICIENT OF REFLECTION = -0.2578E 00 +J 0.2934E 00   REFLECTED POWER/INCIDENT POWER = 0.1526E 00
VTE= 0.4191E 08 W= 0.5246E 11

E FIELD REAL	=	real part of the field intensity
E FIELD IMAG	=	imaginary part of the field intensity
ZO REAL	=	real part of the characteristic impedance of a given increment
ZO IMAG≠	=	imaginary part of the characteristic impedance of a given increment
ZIN REAL	=	real part of the input impedance of a given increment
ZIN IMAG	=	imaginary part of the input impedance of a given increment
COND REAL≠	=	real part of the conductivity
COND IMAG	=	imaginary part of the conductivity
DIST	=	distance from the dielectric window
E MAG	=	magnitude of the electric field
EP	=	1) ϵ *, where non-integer values apply to large $\Lambda < 0$ approximation; N.B. if $\epsilon < 10^{-38}$, the computer inserts 0.0 for these values 2) EP = 2.0 means the expandable region approximation is being employed 3) EP = 1.0 means the Λ very small region of approximation is being employed 4) EP = 0.0 means that the large $\Lambda > 0$ approximation is being employed; these are distinguishable from the values of $\epsilon < 10^{-38}$ due to their relative position in the results. 5) EP = 3.0 means that $h_r = 0$, and large $\Lambda > 0$ approximation is being employed. *See Appendix I, equation (42).

+ Note: The notation 0.2000 E ± 05 indicates $2.0 \times 10^{\pm 4}$ in scientific notation

≠ Impedances are in abohms (10^{-9} ohm) and conductances are in abmhos (10^{9}mho), the electromagnetic system of units being used throughout.

Also, at the bottom of page two:

VTE = electron thermal velocity, $\sqrt{\frac{2KT}{m}}$

W = ω = $2\pi f$, the r-f radian frequency.

Plots of the real and imaginary parts of the propagation constant for this run are given in Figure 87. It is obvious from this figure that a sudden region of high absorption occurs near the point of cyclotron resonance. This correlates well with the experimental evidence. A highly absorptive medium is indicated from this point on, as the real part of the propagation constant falls rapidly to zero.

As mentioned earlier, it is assumed that the damping effect due to the doppler frequency shift of the moving electrons is more pronounced than that of the actual particle collisions. We may now ascertain the validity of this assumption by solving for ν, the particle collision frequency, given the propagation constant from the dispersion relation shown in equation (1). This will give us the magnitude of what ν would have to have been, in order to have obtained that propagation constant. By this artifice, we may compare the ν to known particle collision frequencies, as for instance calculated from relations derived by Spitzer (Reference 29), based on electron coulomb interactions.

From equation (1),

$$(h_r^2 - h_i^2) + j2\, h_r h_i = \left(\frac{\omega}{c}\right)^2 \left\{ 1 - \frac{\omega_p^2/\omega}{\omega - \omega_B - j\nu} \right\} . \tag{7}$$

Rationalizing and equating the real parts,

$$\frac{h_r^2 - h_i^2}{(\omega/c)^2} = \frac{(\omega-\omega_B)^2 + \nu^2 - \frac{\omega_p^2}{\omega}(\omega-\omega_B)}{(\omega - \omega_B)^2 + \nu^2} \tag{8}$$

and solving for ν,

$$\nu = \left\{ \frac{\frac{\omega_p^2}{\omega}(\omega - \omega_B)}{1 - \frac{(h_r^2 - h_i^2)}{(\omega/c)^2}} - (\omega - \omega_B)^2 \right\}^{1/2} . \tag{9}$$

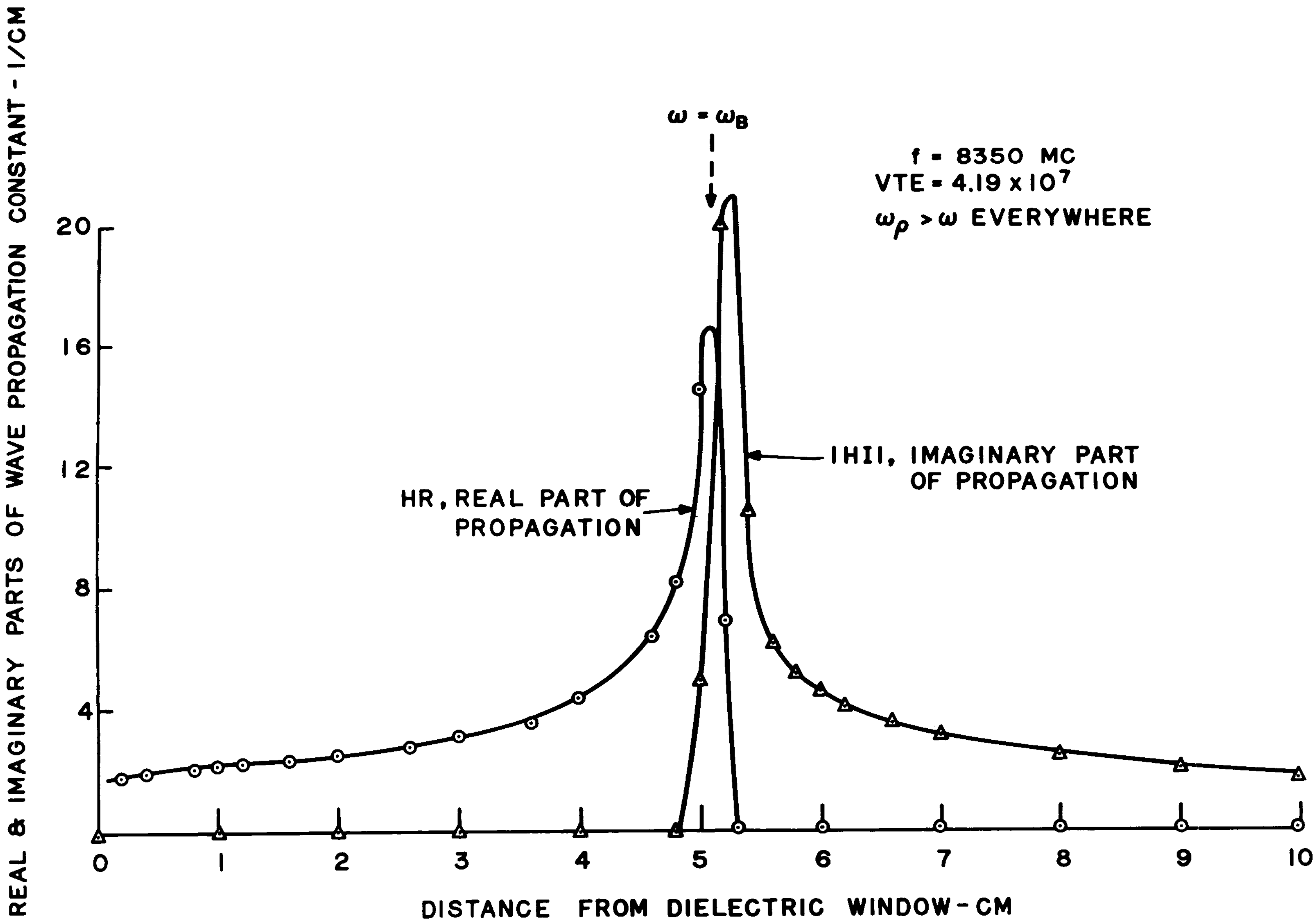

Figure 87. Real and Imaginary Parts of the Propagation Constant vs Distance from Dielectric Window

A plot of this result, from the data presented previously, is shown in Figure 88. For comparison purposes, Spitzer's Equation (5-26) may be used to evaluate the effective electron collision frequency arising from coulomb processes. Assuming $n = 10^{12}$ electrons/cc, and the transverse electron energy is 1000 ev, ν is approximately 2×10^3/sec. If the typical energy in electron cyclotron motion is only 10 ev, the collision frequency rises a thousand fold, to 2×10^6/sec. Thus, at and near the resonance point, the Doppler effect is considerably greater than the coulombic collision process, thereby justifying our initial assumption as to damping mechanisms.

Figures 89 thru 110 are typical plots of the magnitude of the electric field versus the distance from the dielectric window. These plots were produced by a Stromberg-Carlson 4020 plotter used in conjunction with the IBM 7094 computer. The data plotted was taken directly from the output of the computer program. As a simplification, straight lines were used to connect the points.

Figures 89 to 92 were chosen as those results which favorably correlate, at least qualitatively, with the experimental results shown in Figures 71 to 74. Note that the coil currents in the computed results are respectively identical to those in the experimental results. This then allows us to associate the quantitative parameters of the computer results, such as electron density profiles, and energy, with those of the experimental results. For example, we might now say that for the experimental 230 ampere curve shown in Figure 73, the electron energy was about 1 ev, with a slowly rising electron density profile to a maximum of $10^{12}/cm^3$. All of the data for this run is that given in Table XVI.

It is interesting to note that the computed results confirm the sharp drop-off of the r-f electric field near the point of cyclotron resonance. It will also be interesting in future experiments to compare the indicated reflection coefficients with experimental measurements.

Figures 93 to 110 are typical results from a parameter variation study. Here, the maximum electron density, electron energy, and electron density rise distance γ are all systematically varied, for a constant coil current of 230 amps. The corresponding parameters and the resulting ratio of reflected to input power are noted on each figure.

We notice from these plots that as the maximum electron density is decreased from 10^{13} to $10^{12}/cm^3$, the depth for wave propagation is slightly increased. This would be expected. We also note, however, that the highest absorption occurs consistently in the region of cyclotron resonance. This point, where $\omega = \omega_B$, and that where $\omega = \omega_p$ are indicated on the plots. If the point $\omega = \omega_p$ is indicated by an arrow to the right, it should be taken to mean that this point occurred at $z > 10$ cm.

Some of the plots clearly indicate that the distance between the standing wave peaks becomes shorter as the wave progresses from the dielectric window. This would indicate a wave compression, or an increase in the dielectric constant of the medium. This effect is especially pronounced in the low density, high energy region.

Finally, it should be noted that, in general, the reflection increases with the decrease of electron energy for constant γ and maximum density.

Figure 111 represents another type of parameter variation study performed. Here, the r-f frequency was allowed to vary from 8.5 to 10.0 gc, and the ratio of reflected to input power computed. In both cases, the coil current was 230 amps, the electron density rise constant γ was 0.1, and the electron energy was 1.6×10^{-12} ergs. However, the two cases shown represent different maximum electron densities, i.e., 10^{12} and $10^{13}/cm^3$ respectively.

In general, the higher electron density gives consistently lower reflection. These results should prove extremely interesting when the corresponding experimental measurements are made.

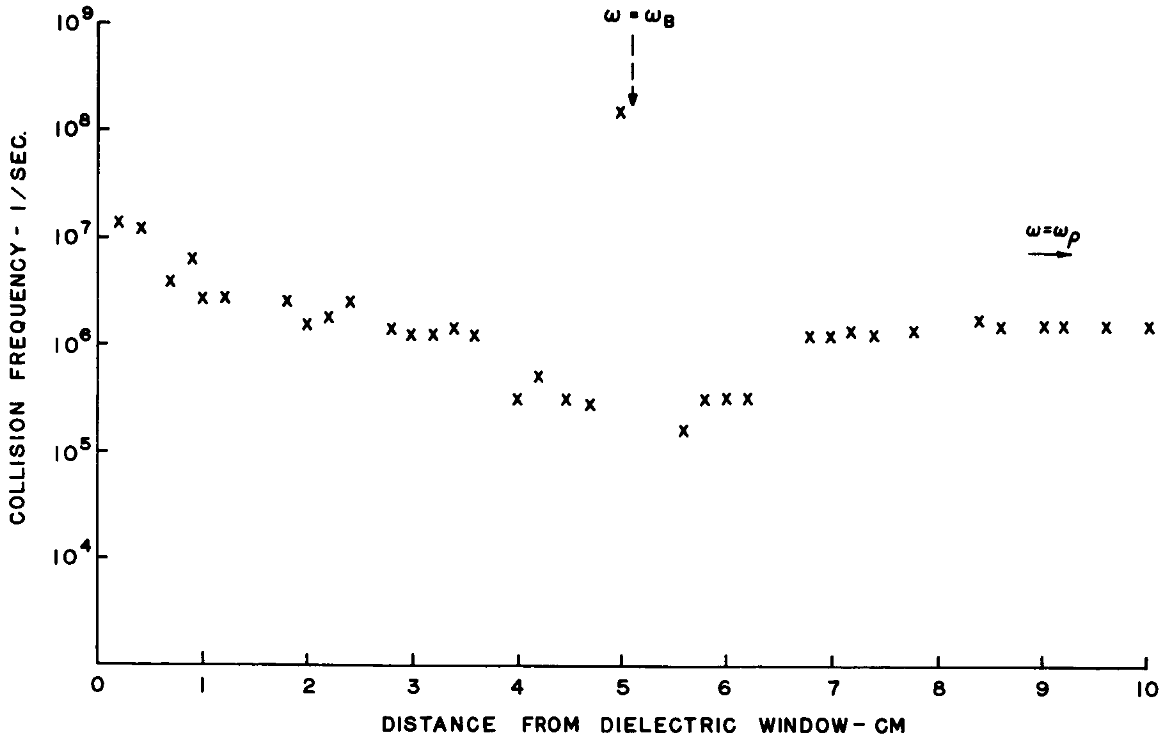

Figure 88. Collision Frequency (as Computed from Equation (9)) vs Distance from Dielectric Window

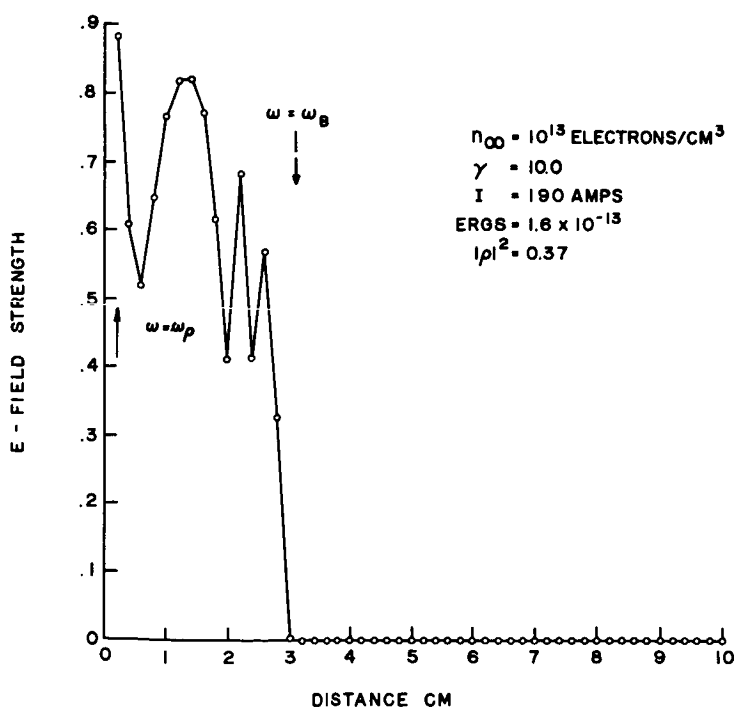

Figure 89. R-f Electric Field vs. Distance from Dielectric Window

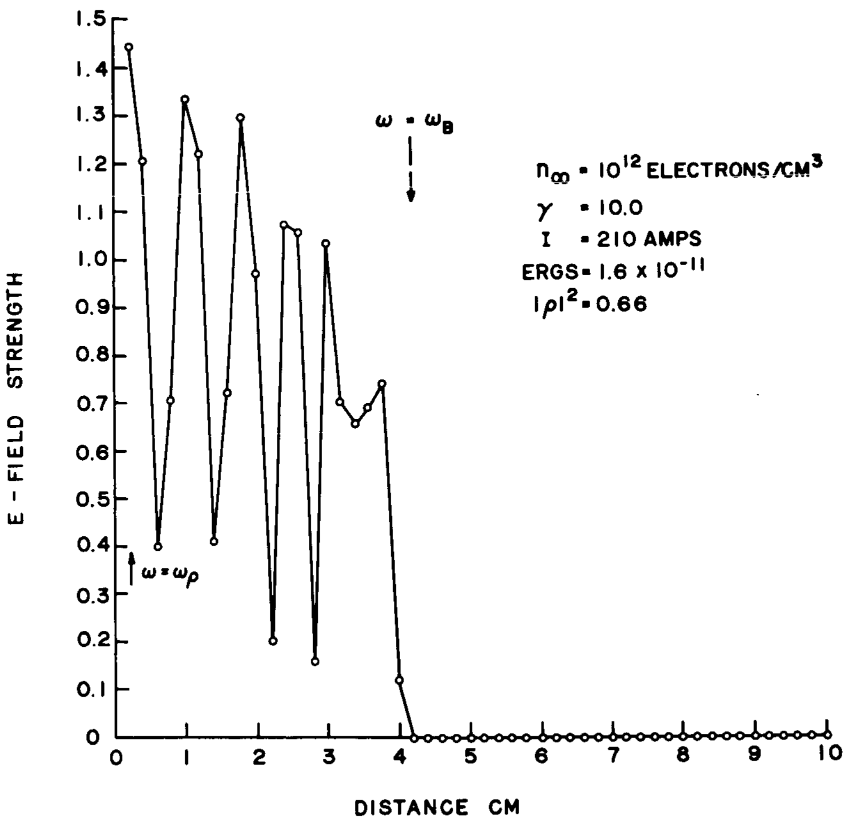

Figure 90. R-f Electric Field vs. Distance from Dielectric Window

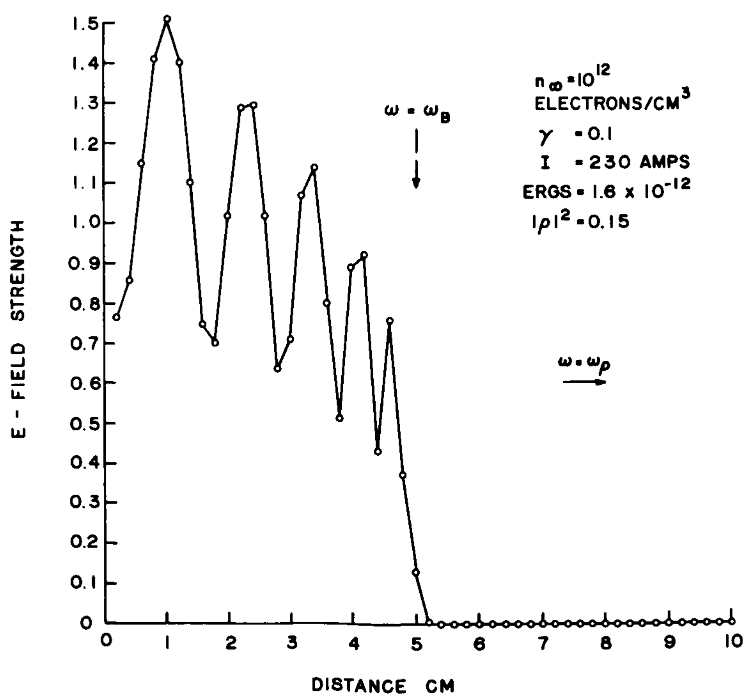

Figure 91. R-f Electric Field vs. Distance from Dielectric Window

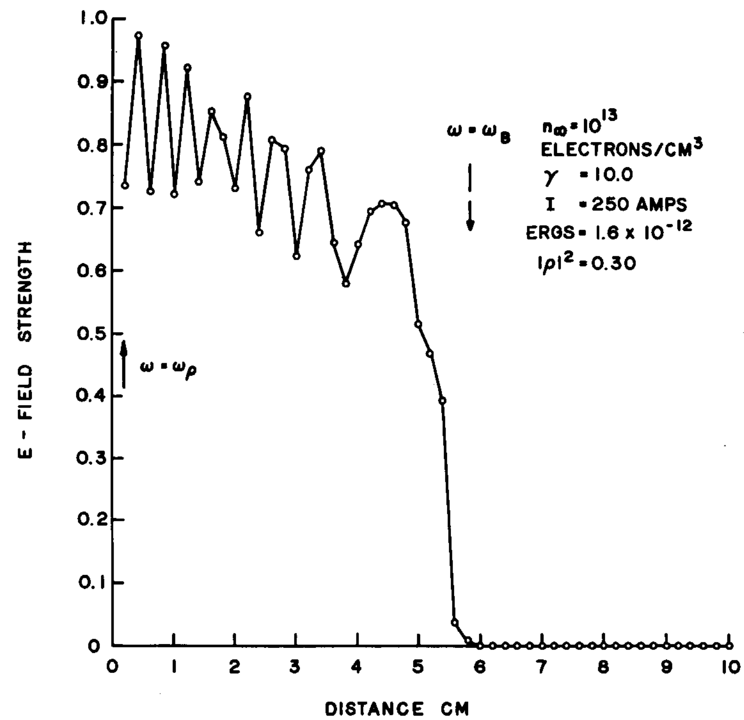

Figure 92. R-f Electric Field vs. Distance from Dielectric Window

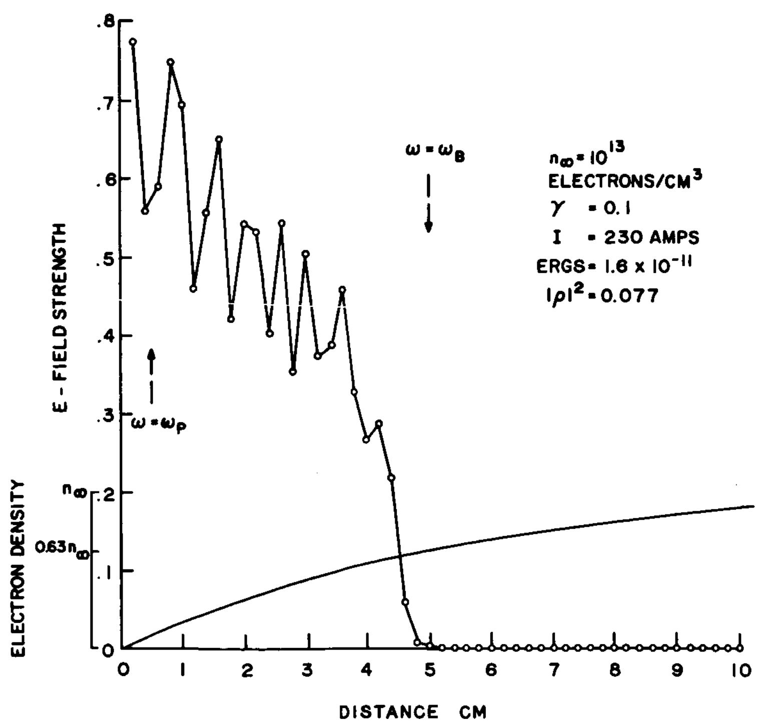

Figure 93. R-f Electric Field vs. Distance from Dielectric Window

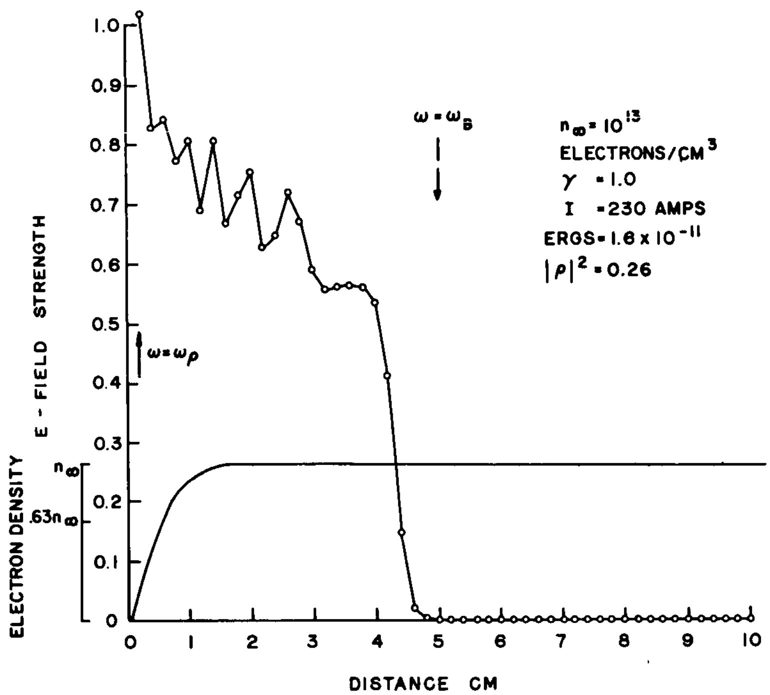

Figure 94. R-f Electric Field vs. Distance From Dielectric Window

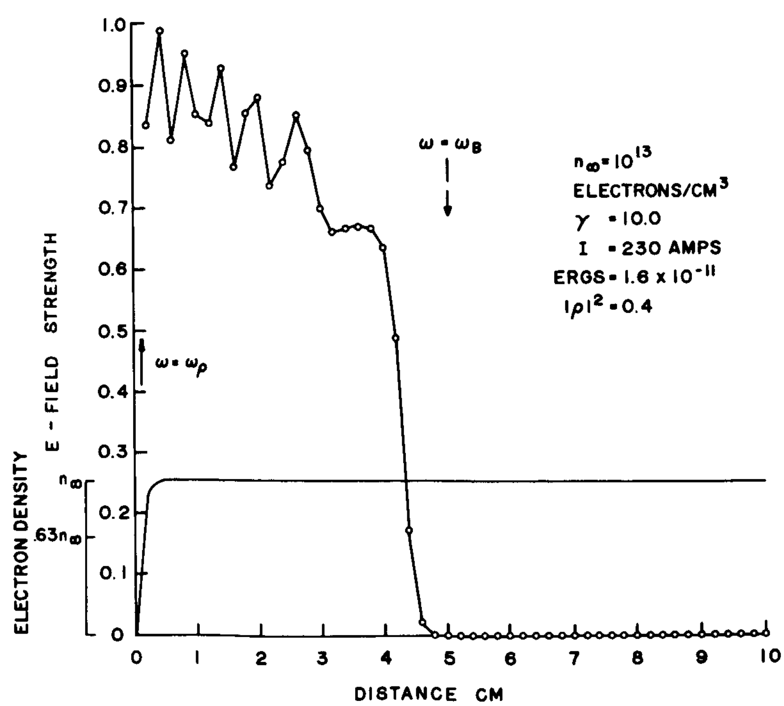

Figure 95. R-f Electric Field vs. Distance from Dielectric Window

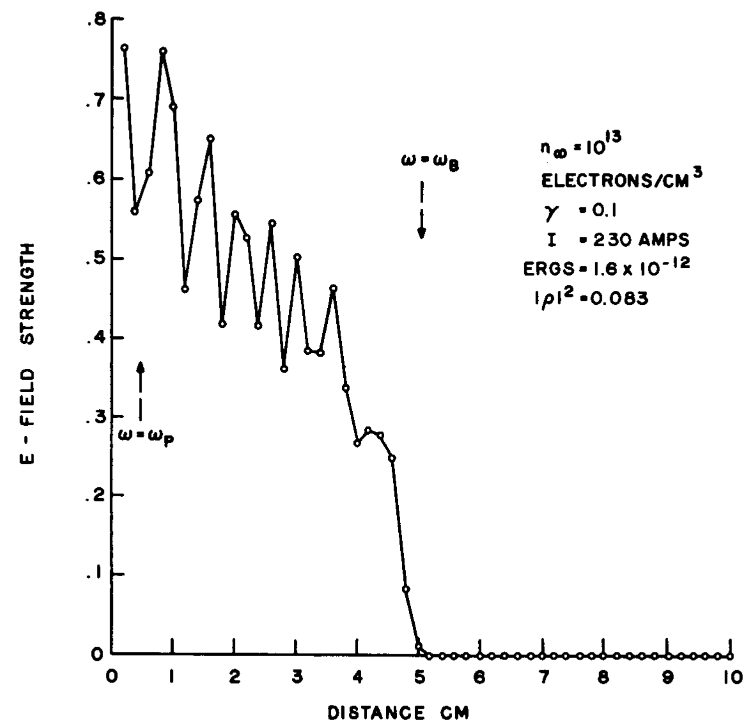

Figure 96. R-f Electric Field vs. Distance from Dielectric Window

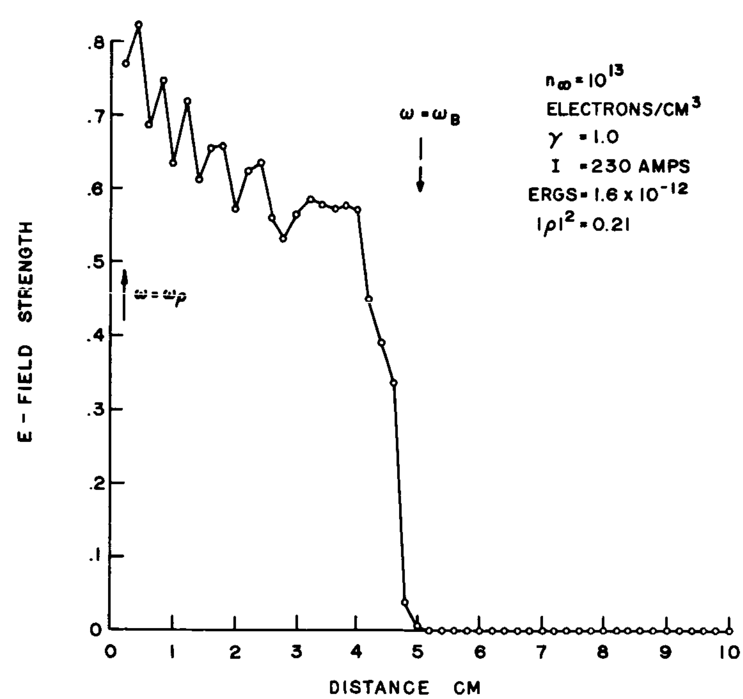

Figure 97. R-f Electric Field vs. Distance from Dielectric Window

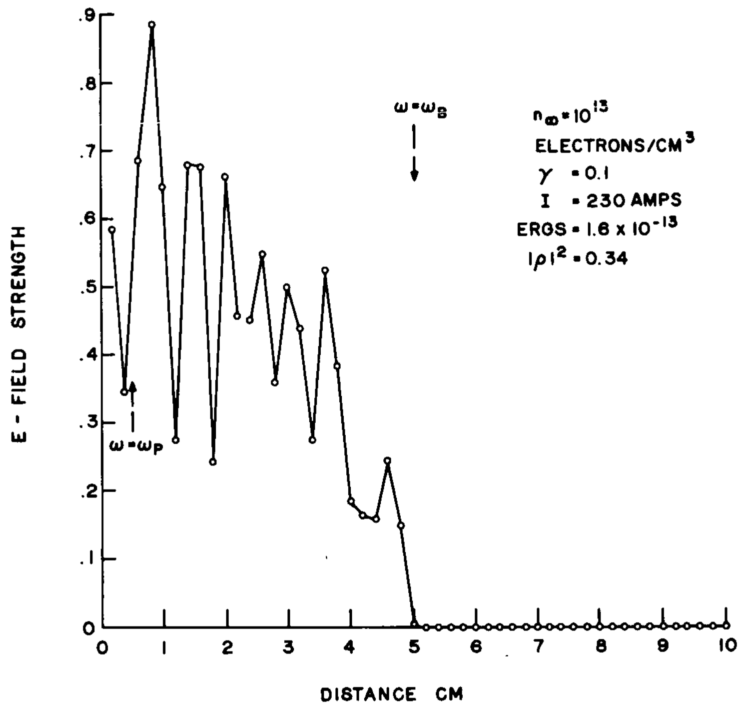

Figure 98. R-f Electric Field vs. Distance from Dielectric Window

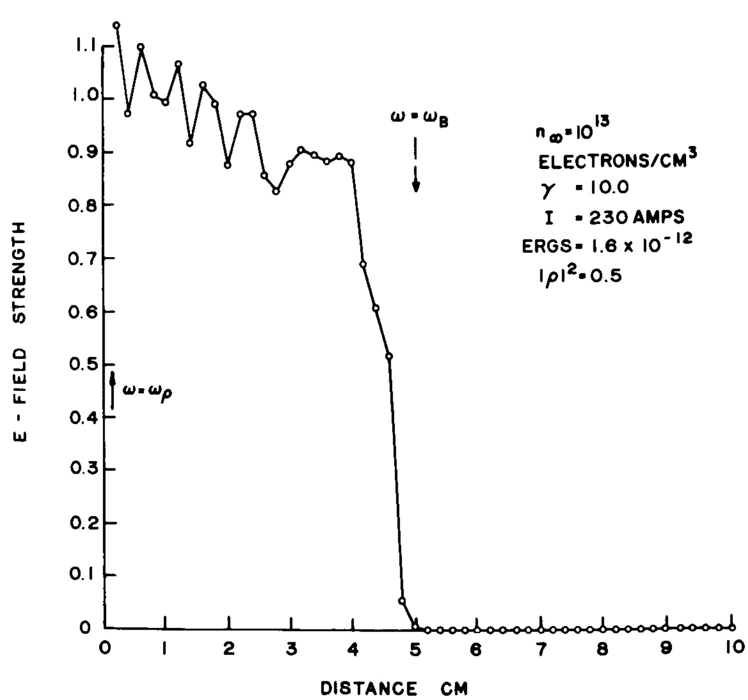

Figure 99. R-f Electric Field vs. Distance from Dielectric Window

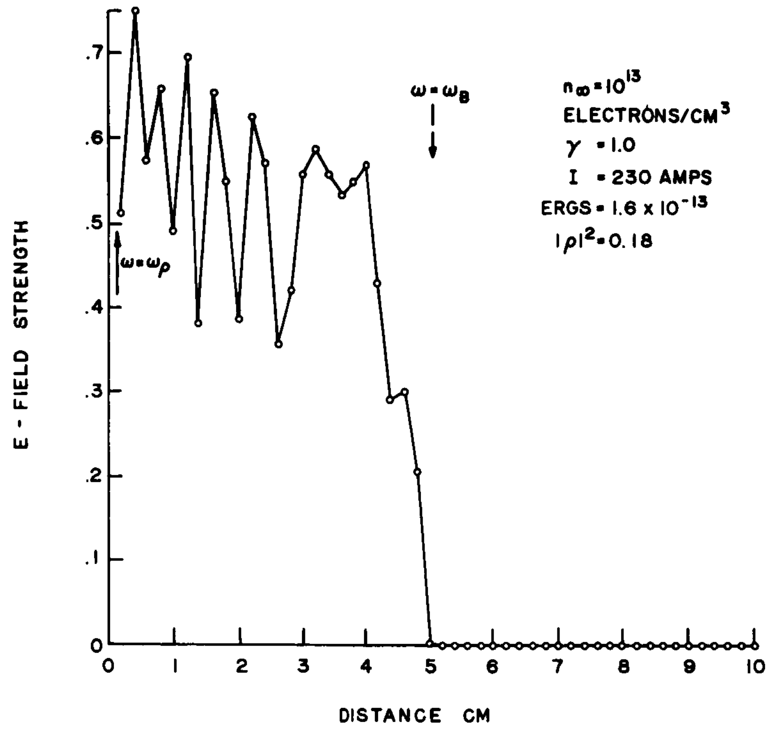

Figure 100. R-f Electric Field vs. Distance from Dielectric Window

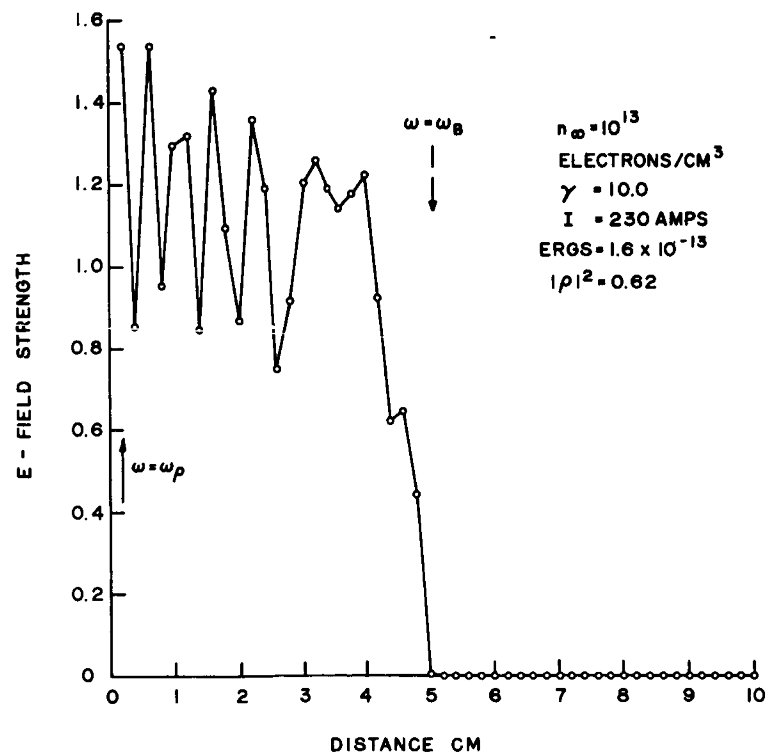

Figure 101. R-f Electric Field vs. Distance from Dielectric Window

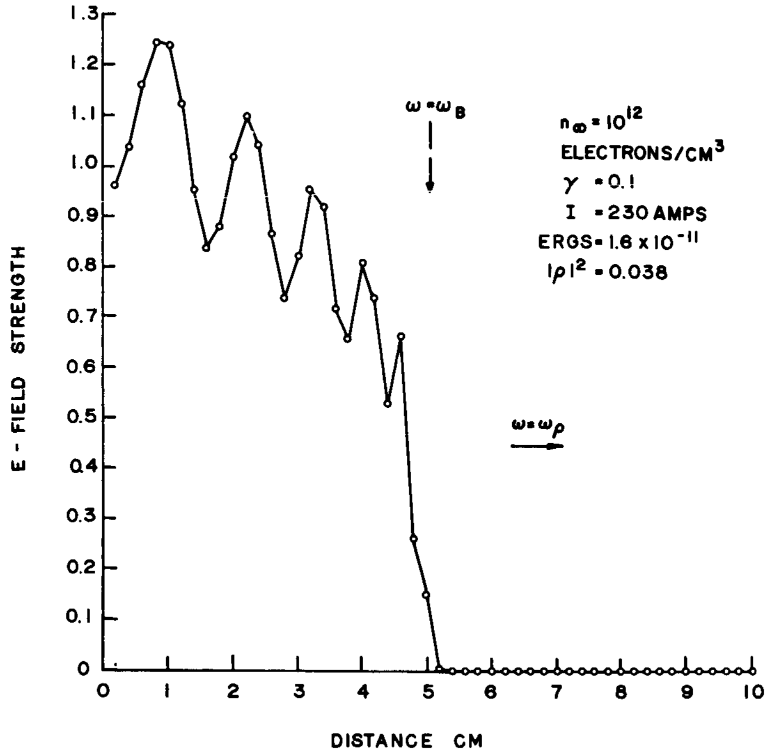

Figure 102. R-f Electric Field vs. Distance from Dielectric Window

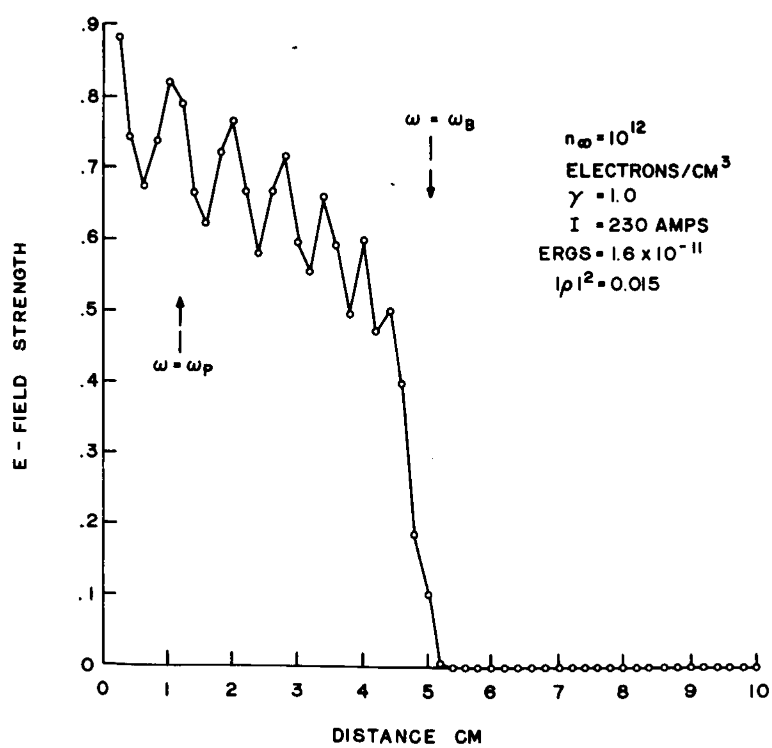

Figure 103. R-f Electric Field vs. Distance from Dielectric Window

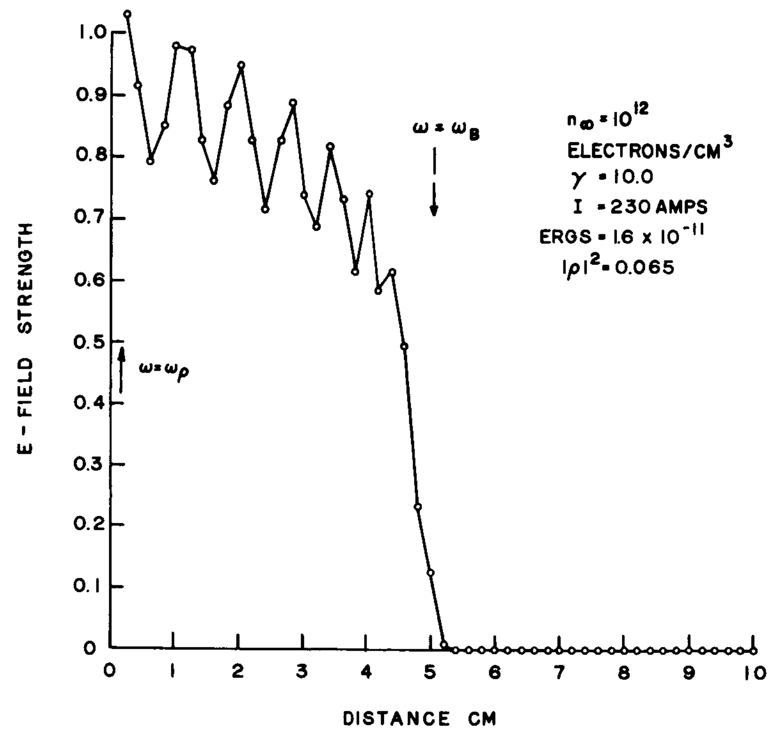

Figure 104. R-f Electric Field vs. Distance from Dielectric Window

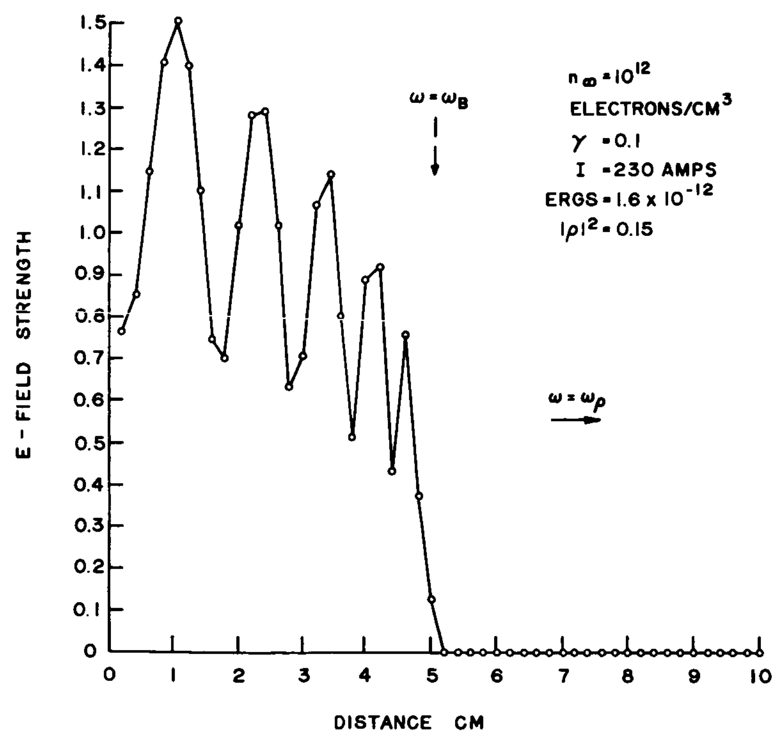

Figure 105. R-f Electric Field vs. Distance from Dielectric Window

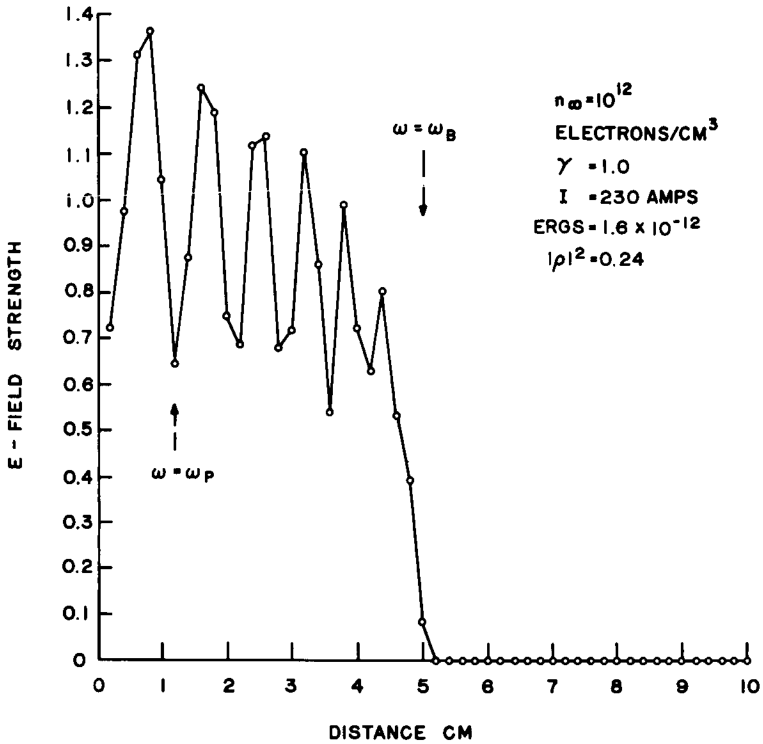

Figure 106. R-f Electric Field vs. Distance from Dielectric Window

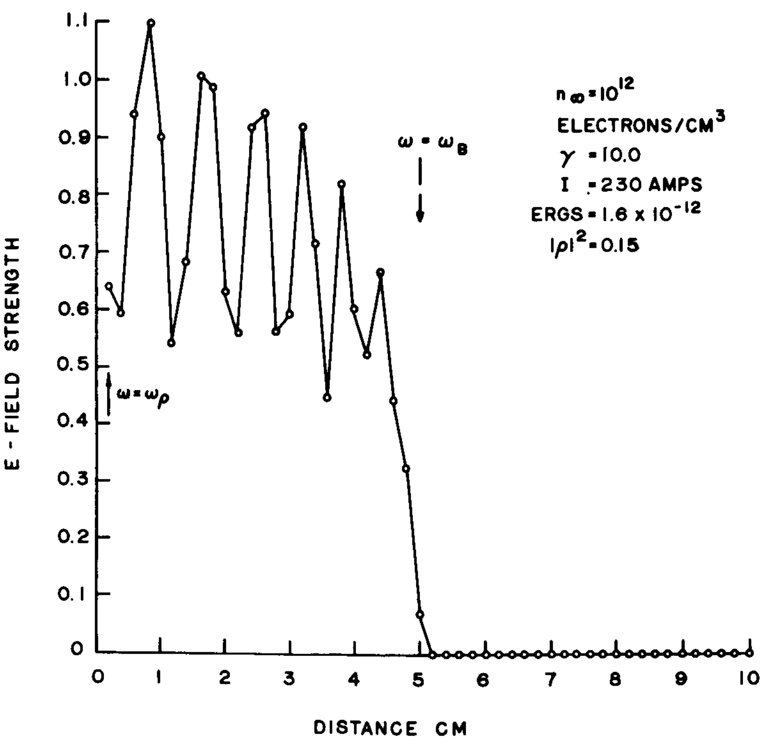

Figure 107. R-f Electric Field vs. Distance from Dielectric Window

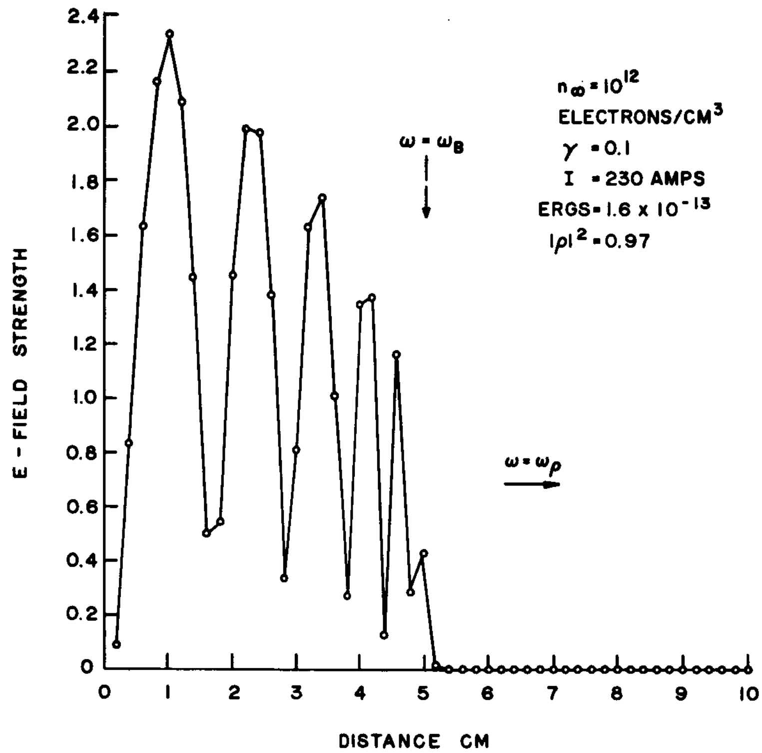

Figure 108. R-f Electric Field vs. Distance from Dielectric Window

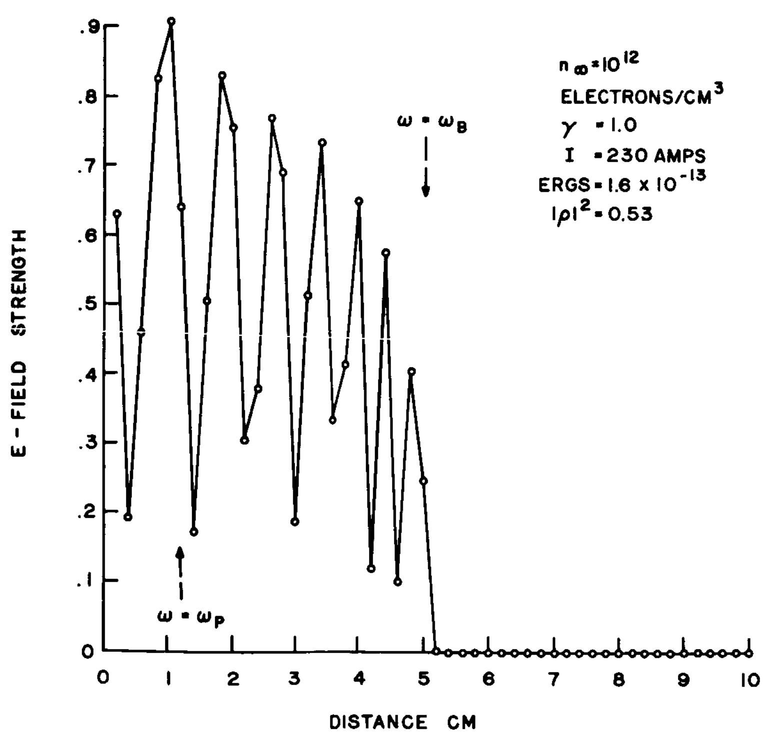

Figure 109. R-f Electric Field vs. Distance from Dielectric Window

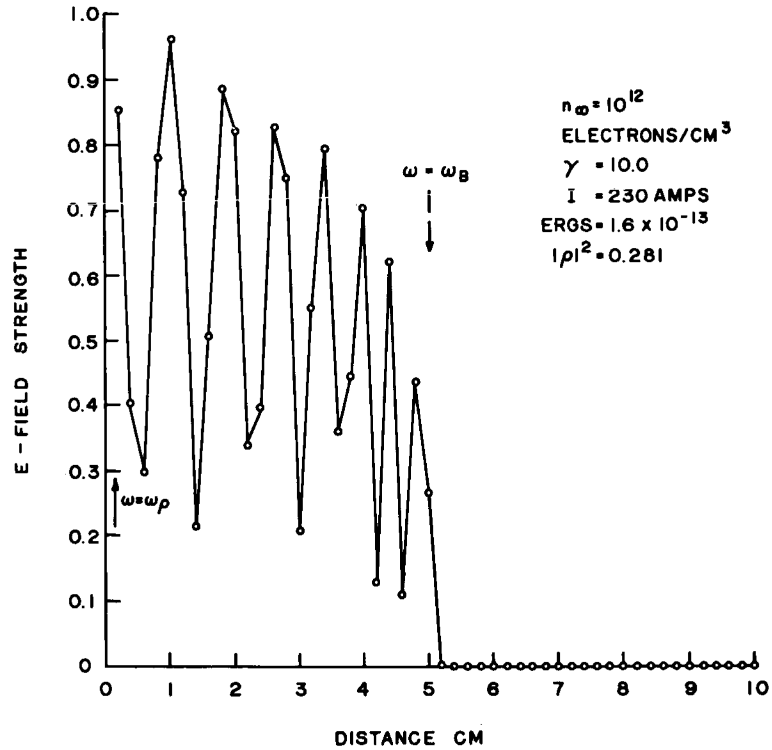

Figure 110. R-f Electric Field vs. Distance from Dielectric Window

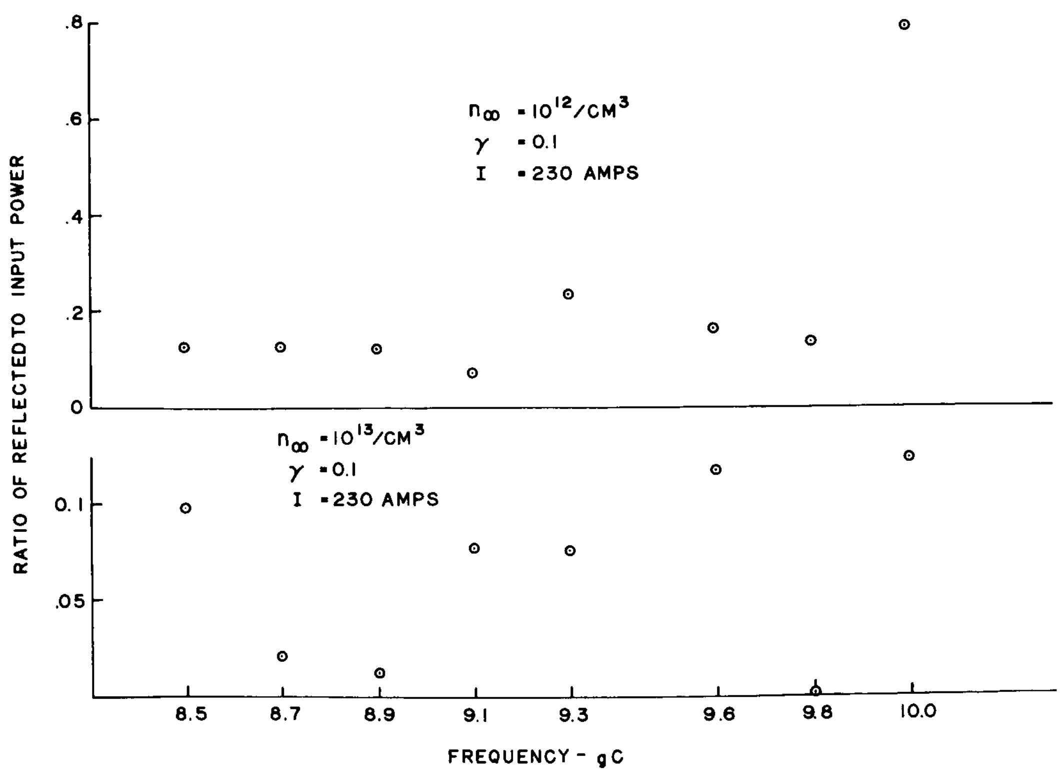

Figure 111. Frequency vs Reflected/Incident Power

APPENDIX I

G. F. Crimi, J. M. Levin

The calculation of the propagation constant, h, is a straightforward extension of the work of D. BenDaniel (Reference 3) who included the effect of Doppler shifts in his treatment of the dispersion relation. It is well-known (see e.g. Stratton (Reference 26) that the dispersion relation for a plane wave propagating parallel to a fixed magnetic field is

$$h^2 = \frac{\omega^2}{c^2}\left[1 - \left(\frac{\omega_p}{\omega}\right)^2 \frac{1}{1 \pm \frac{\omega_B}{\omega} \pm j\frac{\nu}{\omega}}\right] \tag{1}$$

where ω is the frequency of the wave, ω_p is the plasma frequency, ω_B is the cyclotron frequency, c is the velocity of light in the plasma, and ν is the collision frequency. Furthermore, the conductivity of the medium can be expressed by solving the inhomogeneous wave equation

$$\nabla^2 H - \mu_o \epsilon_o \frac{\partial^2 H}{\partial t^2} = \sigma \mu_o \frac{\partial H}{\partial t} \tag{2}$$

for the case of a plane wave

$$H = H_o e^{\pm j(hz - \omega t)} \tag{3}$$

Substitution of (3) into (2) yields

$$\sigma = \pm j\omega \epsilon_o \left(1 - \frac{h^2 c^2}{\omega^2}\right) \tag{4}$$

Choosing the minus sign in equations (1), (3) and (4) in order to examine the resonance phenomenon associated with the extraordinary wave, and substituting (1) into (4) yields

$$\sigma = \frac{-j\omega_p^2 \epsilon_o}{\omega - \omega_B - j\nu} \tag{5}$$

In the limit of zero collision frequency one would be tempted to say that σ becomes purely imaginary. However, from a heuristic standpoint we can see by inspection that σ will have a real part by recalling the Plemelj formulas (References 31 and 32),

$$\lim_{\epsilon \to o} \frac{1}{(X-X' \pm j\epsilon)} = P\left(\frac{1}{X-X'}\right) \pm \pi j \delta (X-X')$$

(where P indicates the Cauchy principal value integral), and therefore,

$$\lim_{\nu \to 0} \sigma = -j\,\omega_p^2\,\epsilon_o \left[P\,\frac{1}{\omega - \omega_B} - \pi j\,\delta\,(\omega - \omega_B) \right].$$

(These comments have been made only to indicate the plausibility of the existence of the real part of σ. In the rigorous considerations which follow we do not use the Plemelj formulas but actually perform the calculations for arbitrary values of ν, taking the limit as $\nu \to$ o only after the integrals have been evaluated.)

BenDaniel argued that many of the electrons had a component of velocity parallel to the wave and consequently "saw" a Doppler shifted frequency,

$$\omega_{eff} = \omega + h_r\,v_z \tag{6}$$

where z is the direction of propagation of the wave. Therefore, to find σ for the plasma, it was necessary to average equation (5) for σ over all possible values of v_z (with an appropriate weighting factor) after replacing ω by ω_{eff} from equation (6). Thus, at resonance, where $\omega_{eff} = \omega_B + h_r\,v_z$,

$$\bar{\sigma} = \frac{\int_{-\infty}^{+\infty} f\,(v_z) \left[j\,\omega_p^2\,\epsilon_o \left(\frac{-1}{h_r v_z - j\nu} \right) \right] dv_z}{\int_{-\infty}^{+\infty} f(v_z)\,dv_z} \tag{7}$$

If f (v_z) is Maxwellian, BenDaniel found that

$$\mathrm{Re}\,\bar{\sigma} = \frac{\sqrt{\pi}\,\epsilon_o\,\omega_p^2}{h_r\,V_{te}} \tag{8}$$

where

$$V_{te} = \sqrt{\frac{2\,KT}{m_e}}\,.$$

In the present calculation the fact that the longitudinal magnetic field is not homogeneous has been included. This inhomogeneity is reflected in the fact that the cyclotron frequency, ω_B, changes along the guide. Therefore, if $\omega = \omega_B$ at one point in the guide, it will certainly be off-resonance elsewhere. If we define a parameter Λ to be the difference between ω and ω_B (for an electron with $v_z = 0$) at a given point in the guide,

$$\Lambda \equiv \omega - \omega_B \tag{9}$$

then we will find that

$$\omega_{eff} - \omega_B = (\omega + h_r v_z) - \omega_B = \Lambda + h_r v_z \tag{10}$$

and hence, for a normalized $f(v_z)$,

$$\bar{\sigma} = -j\,\omega_p^2\,\epsilon_o \int_{-\infty}^{+\infty} \left[\frac{1}{(\Lambda + h_r v_z) - j\nu}\right] f(v_z)\,dv_z$$
$$= \bar{\sigma}_r + i\,\bar{\sigma}_i \tag{11}$$

Returning to equation (4) we see that if h is complex

$$\sigma = -\left[\frac{2\,h_i h_r c^2 \epsilon_o}{\omega}\right] - j\,\omega\epsilon_o\left[1 + (h_i^2 - h_r^2)\frac{c^2}{\omega^2}\right] \tag{12}$$

Equating (11) and (12) we can solve for h_r and h_i and thus the propagation constant is determined.

In the following analysis we will assume that the electrons have a Boltzmann distribution in their longitudinal velocities,

$$f(v_z) = \sqrt{\frac{m}{2\pi kT}}\; e^{-\frac{mv_z^2}{2kT}} \tag{13}$$

and therefore equation (11) becomes

$$\bar{\sigma} = -j\,\omega_p^2\,\epsilon_o \int_{-\infty}^{+\infty} \sqrt{\frac{m}{2\pi kT}}\;\frac{e^{-\frac{mv_z^2}{2kT}}}{(\Lambda + h_r v_z - j\nu)}\,dv_z \tag{14}$$

Evaluation of $\int_{-\infty}^{+\infty} \frac{e^{-\alpha v^2}\,dv}{(\Lambda + h_r v) - j\nu}$ follows:

Let us define

$$I(\alpha) \equiv \int_{-\infty}^{+\infty} \frac{e^{-\alpha v^2}\,dv}{(\Lambda + h_r v) - j\nu} \tag{15}$$

Then we can make the denominator an even function of v,

$$I = \frac{1}{h_r}\int_{-\infty}^{+\infty} \frac{\left[\left(\frac{\Lambda - j\nu}{h_r}\right) - v\right] e^{-\alpha v^2}}{\left[\left(\frac{\Lambda - j\nu}{h_r}\right)^2 - v^2\right]} dv$$

$$= \frac{(\Lambda - j\nu)}{h_r^2}\int_{-\infty}^{+\infty} \frac{e^{-\alpha v^2}}{\left(\frac{\Lambda - j\nu}{h_r}\right)^2 - v^2} dv$$

Define a function A (α) as follows:

$$A(\alpha) = \int_{-\infty}^{+\infty} \frac{e^{-\alpha\left[v^2 - \left(\frac{\Lambda - j\nu}{h_r}\right)^2\right]}}{\left(\frac{\Lambda - j\nu}{h_r}\right)^2 - v^2} dv \qquad (16)$$

Then

$$\frac{dA}{d\alpha} = \int_{-\infty}^{+\infty} e^{-\alpha\left[v^2 - \left(\frac{\Lambda - j\nu}{h_r}\right)^2\right]} dv = e^{+\alpha\left(\frac{\Lambda - j\nu}{h_r}\right)^2}\sqrt{\frac{\pi}{\alpha}}$$

Integrating this differential equation with respect to α, we find that

$$A(\alpha) = \int^{\alpha} e^{\alpha'\left(\frac{\Lambda - j\nu}{h_r}\right)^2}\sqrt{\frac{\pi}{\alpha'}}\, d\alpha' + \text{const.} \qquad (17)$$

Let $x = \sqrt{\alpha'}$, $dx = \frac{d\alpha'}{2\sqrt{\alpha'}}$. Then A ($\alpha$) becomes

$$A(\alpha) = 2\sqrt{\pi}\left[\int_0^{\sqrt{\alpha}} e^{\left(\frac{\Lambda - j\nu}{h_r}\right)^2 x^2} dx + L\right] \qquad (18)$$

where L is a constant of integration. Then recalling equations (15) and (16) we see that

$$I(\alpha) = \left(\frac{\Lambda - j\nu}{h_r^2}\right) e^{-\alpha\left(\frac{\Lambda - j\nu}{h_r}\right)^2} A(\alpha)$$

$$= 2\sqrt{\pi}\left(\frac{\Lambda - j\nu}{h_r^2}\right)\left\{\int_o^{\sqrt{\alpha}} e^{(x^2-\alpha)\left(\frac{\Lambda - j\nu}{h_r}\right)^2} dx + L\, e^{-\alpha\left(\frac{\Lambda - j\nu}{h_r}\right)^2}\right\} \qquad (19)$$

To evaluate the integration constant, L, consider I (α) for $\alpha = 0$. From (15) we see that

$$I(\alpha = 0) = \int_{-\infty}^{+\infty} \frac{dv}{\Lambda + h_r v - j\nu} = \int_{-\infty}^{+\infty} \frac{(\Lambda + h_r v + j\nu)\, dv}{(\Lambda + h_r v)^2 + \nu^2} \qquad (20)$$

let $y = \Lambda + h_r v$, $dy = h_r\, dv$

$$I(\alpha = 0) = \int_{-\infty}^{+\infty} \frac{y dy}{h_r (y^2 + \nu^2)} + \frac{j\nu}{h_r}\int_{-\infty}^{+\infty} \frac{dy}{y^2 + \nu^2} = +j\frac{\pi}{h_r} \qquad (21)$$

Letting $\alpha = 0$ in (19) and equating this expression to (21) we find that

$$2\sqrt{\pi}\left(\frac{\Lambda - j\nu}{h_r^2}\right) L = +j\frac{\pi}{h_r}$$

or

$$L = +j\frac{\sqrt{\pi}\, h_r}{2(\Lambda - j\nu)} \qquad (22)$$

Therefore,

$$I(\alpha) \equiv \int_{-\infty}^{+\infty} \frac{e^{-\alpha v^2} dv}{(\Lambda + h_r v - j\nu)} =$$

$$= \left(\frac{\Lambda - j\nu}{h_r^2}\right)\left\{2\sqrt{\pi}\int_o^{\sqrt{\alpha}} e^{(x^2-\alpha)\left(\frac{\Lambda - j\nu}{h_r}\right)^2} dx + j\frac{\pi h_r}{(\Lambda - j\nu)}\, e^{-\alpha\left(\frac{\Lambda - j\nu}{h_r}\right)^2}\right\} \qquad (23)$$

Returning to equation (14) we find that

$$\bar{\sigma} = -j\omega_p^2 \epsilon_o \sqrt{\frac{m}{2\pi kT}} \left\{ 2\sqrt{\pi}\left(\frac{\Lambda - j\nu}{h_r^2}\right) \int_o^{\sqrt{\alpha}} e^{(x^2-\alpha)\left(\frac{\Lambda - j\nu}{h_r}\right)^2} dx + \frac{j\pi}{h_r} e^{-\alpha\left(\frac{\Lambda - j\nu}{h_r}\right)^2} \right\} \tag{24}$$

where

$$\alpha \equiv \sqrt{\frac{m}{2kT}}\,. \tag{25}$$

If we now go to the limit of zero collision frequency (24) becomes

$$\lim_{\nu \to 0} \bar{\sigma} = -j\omega_p^2 \epsilon_o \sqrt{\frac{m}{2\pi kT}} \left\{ \frac{2\sqrt{\pi}\Lambda}{h_r^2} \int_o^{\sqrt{\alpha}} e^{(x^2-\alpha)\left(\frac{\Lambda}{h_r}\right)^2} dx + j\frac{\pi}{h_r} e^{-\alpha\left(\frac{\Lambda}{h_r}\right)^2} \right\} \tag{26}$$

It is interesting to note that in the limit as $\Lambda \to 0$, equation (25) reduces to the BenDaniel result already quoted in equation (8).

As is explained in the text, the real and imaginary parts of equations (26), and (12) are equated, respectively, giving

$$h_r = -\frac{\sqrt{\pi}\,\omega_p^2}{2V_{te}} \frac{\omega/c^2}{h_r h_i} \exp -\left(\frac{\Lambda}{V_{te} h_r}\right)^2 \tag{27}$$

$$h_i = -\left\{ h_r^2 + \left(\frac{\omega}{c}\right)^2 \left[\frac{2\omega_p^2}{V_{te}\,\omega h_r^2} \lambda \exp -\left(\frac{\Lambda}{V_{te} h_r}\right)^2 \int_o^{\frac{1}{V_{te}}} \exp\left(y\frac{\Lambda}{h_r}\right)^2 dy - 1 \right] \right\}^{1/2} \tag{28}$$

for the solution of the complex propagation constant at any given point in the waveguide. Note, as mentioned in the text, the negative sign on the square root in equation (28) is chosen. The reason for this is that in order to obtain any real values for h_r from equation (27), the h_i in the denominator must have a minus sign associated with it.

Due to computer limitations in dealing with large exponents, the solution of equations (27) and (28) must be performed by several different approximation techniques depending upon the value of the exponent $\frac{\Lambda}{V_{te} h_r}$. The methods of the approximations and their applicable ranges will be given in the following:

a) For $|\Lambda|$ large, we examine the integral in equation (28),

$$\exp - \left(\frac{\Lambda}{V_{te} h_r}\right)^2 \int_0^{\frac{1}{V_{te}}} \exp \left(y \frac{\Lambda}{h_r}\right)^2 dy$$

$$= \int_0^{\frac{1}{V_{te}}} \exp - \left(\frac{1}{V_{te}^2} - y^2\right) \left(\frac{\Lambda}{h_r}\right)^2 dy \qquad (29)$$

and realize that equation (29) represents the area under one of the curves of Figure A-1 depending on the value of (Λ / h_r).

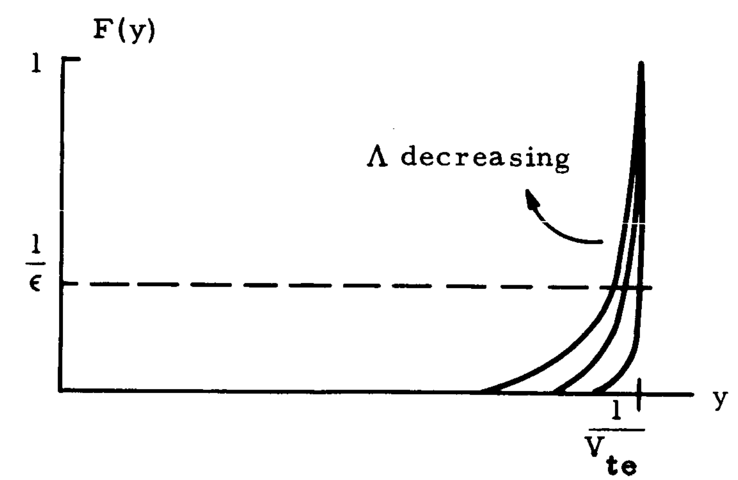

Figure (A-1)

But, to a good degree of accuracy, the area of such a function can be approximated by($\frac{1}{V_{te}}$ — ϵ - fold distance) times the height, 1. The ϵ -fold distance is found from

$$\left(\frac{1}{V_{te}^{2}} - y_{\epsilon}^{2}\right)\left(\frac{\Lambda}{h_r}\right)^2 = 1 \tag{30}$$

$$y_{\epsilon} = \left[\frac{1}{V_{te}^{2}} - \left(\frac{h_r}{\Lambda}\right)^2\right]^{1/2} \tag{31}$$

Then,

$$\text{AREA} = \Delta y_{\epsilon} \times 1 = \left[\frac{1}{V_{te}} - \left(\frac{1}{V_{te}^{2}} - \left(\frac{h_r}{\Lambda}\right)^2\right)^{1/2}\right] \tag{32}$$

Or, equation (32) may be written,

$$\text{AREA} = -\frac{1}{V_{te}}\left[1 - \left(\frac{h_r V_{te}}{\Lambda}\right)^2\right]^{1/2} + \frac{1}{V_{te}} \tag{33}$$

and for $|\Lambda| >> h_r V_{te}$ we may write (33) as

$$\text{AREA} = -\frac{1}{V_{te}}\left(1 - \frac{1}{2}\left(\frac{h_r V_{te}}{\Lambda}\right)^2\right) + \frac{1}{V_{te}} = \frac{1}{2} V_{te}\left(\frac{h_r}{\Lambda}\right)^2 \tag{34}$$

Substituting this into equation (28) gives,

$$h_i = -\left\{h_r^{2} + \left(\frac{\omega}{c}\right)^2\left[\frac{\omega_p^{2}}{\omega\Lambda} - 1\right]\right\}^{1/2} \tag{35}$$

Now, for $\omega_B > \omega$, then $\Lambda < 0$, and we may further simplify equation (35);

let $K = \left|\left(\frac{\omega}{c}\right)^2\left(\frac{\omega_p^{2}}{\omega\Lambda} - 1\right)\right| \qquad \lambda < 0$

then $h_i = -\left(h_r^{2} - K\right)^{1/2}$ (36)

and from equation (27),

$$h_r^{2} = \frac{-W}{h_i} \exp - \left(\frac{\Lambda}{V_{te} h_r}\right)^2 \tag{37}$$

where $W = \dfrac{\sqrt{\pi}\,\omega_p^{\,2}\,\omega}{2\,V_{te}\,c^2}$.

But, equation (37) requires that $h_r \to 0$ for this region of Λ, which is not the physical situation; therefore, $h_i \to 0$. To allow this, we define ϵ by,

$$h_r^{\,2} = K\,(1 + \epsilon\,) \tag{38}$$

then $$h_i = -\sqrt{K}\,\sqrt{\epsilon} \tag{39}$$

which makes equation (37) become

$$K\,(1 + \epsilon\,) = \frac{W}{\sqrt{K}\sqrt{\epsilon}} \exp - \left(\frac{\Lambda}{V_{te}}\right)^2 \frac{(1 - \epsilon + \epsilon^2 - - - -)}{K} \tag{40}$$

and as $\epsilon \to 0$

$$K^{3/2} = \frac{W}{\sqrt{\epsilon}} \exp - \left(\frac{\Lambda}{V_{te}}\right)^2 \frac{1}{K} \tag{41}$$

which, to a first-order approximation, we may solve for ϵ,

$$\epsilon = \frac{W^2}{K^3} \exp - \frac{2}{K} \left(\frac{\Lambda}{V_{te}}\right)^2 \tag{42}$$

which for $|\Lambda|$ large justifies our original assumption of ϵ small. This gives

$$h_r = \Big(K\,(1 + \epsilon)\Big)^{1/2} \tag{43}$$

$$h_i = \frac{-W}{K} \exp - \left(\frac{\Lambda}{V_{te}}\right)^2 \frac{1}{K} \tag{44}$$

For $\omega > \omega_B$ and $|\Lambda|$ large, the physical situation dictates that $h_r \to 0$, therefore, in this part of the program Equations (35) and (37) are used directly; the new h_i is calculated from the preceeding value of h_r and the new ω_p and Λ; and the new h_r is calculated from this new h_i, ω_p and Λ. No iterations are involved and the procedure simply provides a continuous function for h_r which rapidly approaches zero, while $h_i \to K$.

b) For this program the computer is capable of handling values of Λ such that $\left|\dfrac{\Lambda}{V_{te}\,h_r}\right| \gtrsim 0.9$. Therefore, for the intermediate range of Λ such that,

$$0.02 < \left| \frac{\Lambda}{V_{te} h_r} \right| \leq 0.9$$

an expansion of the integrand of equation (28) is completed, the number of terms used depending upon a selected error criterion, and a termwise integration is performed. This computation is used in conjunction with an iterative solution of equation (27) for h_r.

c) For Λ small, i.e. where $\left| \frac{\Lambda}{V_{te} h_r} \right| \leq 0.02$, a third approximation for the solution of the integral of equation (29) is employed. Here, near resonance, the program is allowed to compute from the first two terms of the integrated expansion, such that,

$$h_i = - \left\{ h_r^2 + \left(\frac{\omega}{c} \right)^2 \left[\frac{2\omega_p^2}{V_{te}\, \omega h_r^2} \left(\frac{\Lambda}{V_{te}} - \frac{2}{3h_r^2} \left(\frac{\Lambda}{V_{te}} \right)^3 \right) - 1 \right] \right\}^{1/2} \tag{45}$$

which is then used in an iterative solution for h_r.

Sequentially, a typical run consists of the following:

1) Initial values of h_r and h_i calculated directly from equations (43) and (44) for large negative Λ.

2) A region around resonance, using the integrated expansion described in (b) above, and an iterative solution for h_r, where each initial guess for h_r for a given point in the guide is the value of h_r computed for the previous point. Here, $\Lambda < 0$.

3) A region of small Λ, quite near resonance, as described in (c) above.

4) A second expansionable region, as we leave resonance, and $\omega > \omega_B$.

5) A region where $\Lambda \rightarrow \omega$, as described in (a) above.

APPENDIX II

G. F. Crimi

An equivalent circuit analysis, such as that found in Jordan (Reference 30) may be performed on the cylindrical waveguide for a TE mode once the propagation constant at each point has been specified. For this system the lumped parameter circuit is shown in Figure A-2.

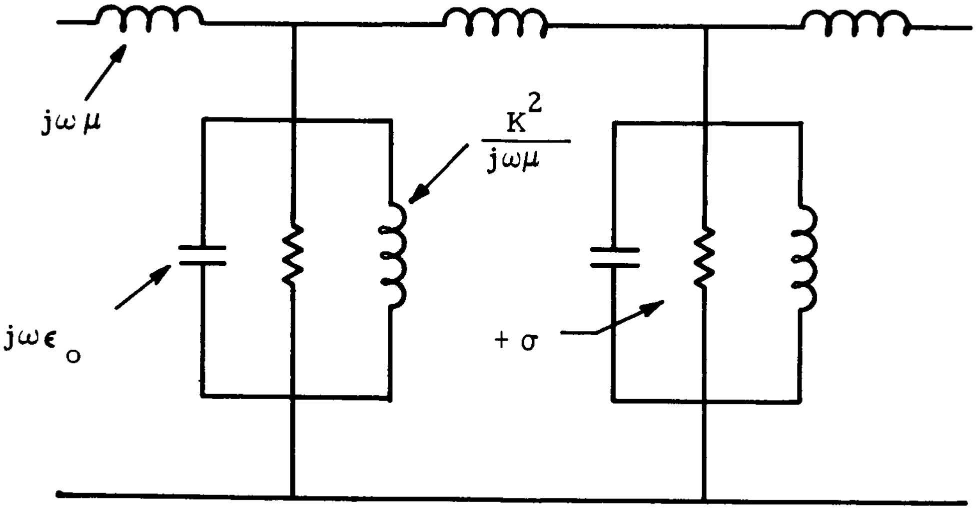

where $K^2 = \omega^2 \mu \epsilon_o - h^2 - j\omega\mu\sigma$

$$\sigma = - j\omega\epsilon_o \left(1 - \frac{h^2}{\omega^2/c^2}\right)$$

Figure A-2

Analogous to the transmission line, the characteristic impedance for the waveguide is found by

$$Z_O = \sqrt{X/Y}$$

$$= \sqrt{\frac{j\omega\mu}{j\omega\epsilon_o + \frac{K^2}{j\omega\mu} + \sigma}} \qquad (46)$$

$$= \frac{\eta}{\sqrt{1 - \left(\frac{\omega_c}{\omega}\right)^2 - j\frac{\sigma}{\omega\epsilon_o}}} \qquad (47)$$

where

$$\eta = \sqrt{\mu/\epsilon_o}$$

$$\omega_c = \frac{(\rho a)'_{mn}}{a\sqrt{\mu\epsilon}}$$

$(\rho a)' = 1.84$ for a TE_{11} mode

$a = 2.93$ cm.; radius of guide.

Since the conductivity σ is a function of position in the guide, equation (47) represents the characteristic impedance of any given increment of the segmented guide, as described in the text.

The field is assumed vanished at the point of the N^{th} element. The characteristic impedance of the N^{th} element is computed from equation (47) and it is assumed that this is the characteristic impedance for the (N + 1)th, (N + 2)th, etc. The guide is thus assumed terminated by this impedance. The input impedance for the (N - 1) th increment is found to be:

$$Z_{1N}(N-1) = Z_O(N-1)\,\frac{Z_L + j Z_O(N-1)\tan(hd)}{Z_O(N-1) + j Z_L \tan(hd)} \tag{48}$$

where

$Z_O(N-1)$ = characteristic impedance of the (N-1) th increment

Z_L = the load on the (N-1)th increment

= the input impedance of the Nth increment

d = thickness of the increment

In this particular case, at the end of the guide, Z_L is the characteristic impedance of the Nth increment.

Equation (48) allows us to resolve the increment into an equivalent T-circuit as shown in Figure A-3.

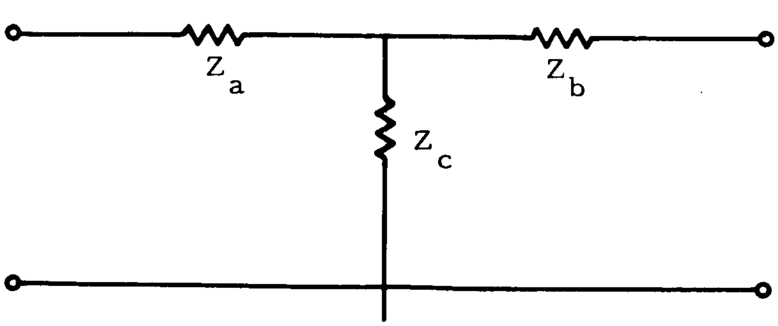

Figure A-3

$$Z_c = \sqrt{Z_{20}(Z_{10} - Z_{1S})}$$

$$Z_a = Z_{10} - Z_c$$

$$Z_b = Z_{20} - Z_c$$

We shall assume that the small increment is expressible as a balanced T, ∴

$$Z_{10} = Z_{20}$$

Now, Z_{10} implies $Z_L \to \infty$

$$\therefore \quad Z_{10} = -j\, Z_O \operatorname{ctn}(hd)$$

and, Z_{1S} implies $Z_L \to 0$

$$\therefore \quad Z_{1S} = j\, Z_O \tan(hd)$$

Finally,

$$Z_c = j\, Z_O \sqrt{1 + \operatorname{ctn}^2 (hd)} \qquad (49a)$$

$$Z_a = Z_b = -j\, Z_O \operatorname{ctn}(hd) - Z_c \qquad (49b)$$

We have now specified the circuit for any given increment of the guide, in terms of the parameters associated with that point in the guide. Equations (47) and (49) are then used to complete the ladder network to the window of the guide. A normalized input field is then assumed at the window, and simple circuit theory is applied to the T- equivalent circuits to find the output for each successive increment, starting from the first at the window, and ending with the output of the (N-1)th, at which point the field should have vanished.

APPENDIX III

SPECTROSCOPIC ANALYSIS; Be CONTAMINATION

D. B. Miller

Although various dielectric materials have been utilized for the waveguide window in the electron-cyclotron resonance accelerator ("Cyclops"), the only satisfactory solution at high r-f power levels has been beryllium. Since beryllium and beryllium compounds are considered to be highly toxic, however, care must be taken to make sure that dangerous situations do not arise.

Sax[33] reports that the major danger is to the lungs by inhalation of beryllium oxide dust particles, although skin irritation can also result from body contact. Thus the BeO windows have been carefully protected from any abrasive action during storage, handling or assembly. Of more importance are possible effects due to BeO eroded from the windows by energetic, impinging plasma particles. To study the extent and distribution of eroded beryllium, samples are occasionally taken from various exposed surfaces and analysed for Be content. The results are listed in the accompanying table.

We observe from this table that beryllium is on occasion detected in significant quantities; since the only source of beryllium in this system is the waveguide window, we must conclude that the Be deposits are due to window erosion. It seems likely that a good deal of this erosion takes place at lower magnetic field values, when the intense plasma is located directly within the accelerator; wall erosion is believed also to be more severe under low field conditions (see Section 4.1). Since wall erosion was most severe with the Mark IV accelerators, perhaps the window erosion also occurred most rapidly with these accelerators.

For some undetermined reason, the 18" tank wall showed relatively high Be content. This tank is not now in use but has been thoroughly cleaned before putting in storage. The 4' tank has relatively low contamination. Surfaces such as probe and calorimeter front faces, which directly intercept the beam at close range, show high Be content.

Action items based on these results are as follows:

1) Known and suspected contamination areas should be avoided. Abrasive (machining, grinding, filing) activity on such items as used calorimeters and probes will be done only after the pieces have been thoroughly cleaned, using a continuously submerged cleaning procedure. Work within the tank will be minimized and done only under good ventilation conditions.

Sample Date	Sample Origin	Occasion	Be Content
1/6/64	1. Oil - 3' "Reppac" Tank	Shortly after beginning Mark I tests	None detected (< .0005%)
4/20/64	1. Emery paper smear - front probe surface	After ~ 4 months Mk I testing	.001 - .005%
	2. Oil - 18" Tank wall	After ~ 4 months Mk I testing	.01 - .05%
5/20/65	1. Calorimeter - front face	After ~ 4 months Mk IV testing	None detected
	2. 4' Tank - back wall		None detected
	3. 4' Tank - Adj. to accel.		.00008 - .00013%
	4. Accel. flange deposit		.00008 - .00013%
10/20/65	1. 4' tank - back wall	After ~ 9 months Mk. IV and Mk V testing	.0001%
	2. Calorimeter - inside surface		.005%

2) Samples will continue to be spectroscopically analysed.

3) Low magnetic field tests with accelerators having BeO windows will be kept to a minimum.

4) Accelerator designs employing window materials other than BeO will be developed. In particular, the BN-windowed Mark VII design (see section 3.2) should be tested. Possibly the sapphire or alumina windows can be used successfully with a high-field, screened-waveguide accelerator such as the Mark VIII.

APPENDIX IV

CIRCULAR POLARIZER

D. B. Miller

Since r-f power couples into the cyclotron orbiting electrons only from that circularly-polarized component of the wave whose electric vector rotates with the electrons (known as the "extra-ordinary" wave*), best efficiency will result when the total wave power is in this "extra-ordinary" wave. The polarizer (see Figure 13) is incorporated into the r-f system to accomplish this objective. In order to test the circularity of the wave after passage through this polarizer, a special test section was added just beyond the polarizer. This special section consists of a piece of cylindrical guide having the same inside diameter as the output end of the polarizer and which is rotatable relative to the polarizer. A small antenna probe projecting radially through the guide wall then measures the r-f radial electric field as a function of azimuthal angle. Perfect circularity would result in this signal being independent of angle. For the best setting of the polarizer, the ratio of maximum to minimum signal was in fact measured to be 4:1. The influence of reflection was not evaluated in this test.

* Since the rotation direction depends on the direction of the magnetic field, this may be either a clockwise or counter-clockwise rotation. If the propagation is parallel to $\vec{B}$, then electrons rotate counter-clockwise viewing in the propagation direction, requiring the counter-clockwise rotating wave. This is usually referred to as the right hand wave (Ref. 26, p. 280).

REFERENCES

1. J. I. F. King, "Continuous Microwave Magnetic Accelerator," General Electric Space Sciences Laboratory Proposal G.E. 050-804, October, 1960.

2. P. Gloersen, D. Miller, E. Gibbons, "Microwave Driven Magnetic Plasma Accelerator," Annual Report, Contract NAS5-1046, February 1962.

3. D. B. Miller et. al, "Cyclotron Resonance Propulsion System," Engineering Aspects of Magnetohydrodynamics, Proceedings, 3rd Symposium, University of Rochester, March, 1962; Gordon and Breach Sciences Publishers, New York, 1964, p. 405.

4. R. J. Kerr, et. al., "Recent Experiments with the Electron Cyclotron Plasma," Bull. Amer. Phys. Soc. II 7, 290, 1962.

5. W. B. Ard, et al., "Neutron Production from a Steady-State, Hot-Electron Deuterium Plasma, Phys. Rev. Lett. 10, 87, February, 1963.

6. D. B. Miller, E. F. Gibbons, "Cyclotron Resonance Propulsion System," Annual Report, Contract NAS5-1046, February, 1963.

7. H. W. Hendel, T. T. Reboul, "Continuous Plasma Acceleration by Electron Cyclotron Resonance," AIAA Paper 63001, March, 1963.

8. D. B. Miller, et al, "Cyclotron Resonance Propulsion System," AIAA Paper 63002, March, 1963.

9. T. Consoli, R. B. Hall, "Acceleration de Plasma Par des Gradients de Champs Electromagnetique," Fusion Nucleaire 3, 237, 1963.

10. T. Consoli, R. Hall, "First Experimental Verification of the Acceleration of a Plasma by Gradients of a H. F. Field and Static Magnetic Field," C. R. Acad. Sci. France 257, 2804, November, 1963.

11. S. A. Ahmed, H. W. Hendel, "Space Charge Acceleration of Ions at Electron Cyclotron Resonance, "AIAA Paper 64-24, January, 1964.

12. D. B. Miller, E. F. Gibbons, "Experiments with an Electron Cyclotron Resonance Plasma Accelerator," AIAA Journal 2, 35, January, 1964.

13. R. Bardet, T. Consoli, R. Geller, "Results Experimentaux sur L'Acceleration de Plasma par les Gradients des Champs Magnetique Statique et Electromagnetique," Nuclear Fusion 4, 48, 1964.

14. R. A. Dandl et al, "Preliminary Results with a 50-Liter Electron Cyclotron Plasma," Bull. Amer. Phys. Soc. II 9, 332, 1964.

15. D. B. Miller, "Continuous Microwave Magnetic Accelerator," Summary Report, Contract NAS3-3567, August, 1964.

16. D. B. Miller, "X-Band Magnetic Resonance Plasma Accelerator," AIAA Paper 64-702, September, 1964.

17. R. Bardet, T. Consoli, R. Geller, "Mecanisme Physique de L'Entranement des Ions par la Charge D'espace des Electron Dans L'Acceleration par les Gradients de Champs Magnetique Statique et Electromagnetique," Fusion Nucleaire 5, 7, 1965.

18. E. C. Hutter, H. Hendel, T. Faith, "Plasma Acceleration by Electron Cyclotron Resonance," 4th Symposium on Advanced Propulsion Concepts; AFOSR, Palo Alto, April, 1965.

19. V. J. Veksler, et al, "Interactions of Plasmoids with an Electromagnetic Wave," Atomnaya Energiya 18, 14, 1965.

20. H. Hendel, T. Faith, E. C. Hutter, "Plasma Acceleration by Electron Cyclotron Resonance," RCA Review 26, 200, June, 1965.

21. D. B. Miller and G. W. Bethke, "Cyclotron Resonance Thrustor Design and Diagnostics Techniques," AIAA Paper 65-301, July, 1965.

22. R. Bardet, et al, "Acceleration and Reflexion de Faisceaux de Plasma par des Structures Mixtes," AGARD Propulsion and Energetics Panel Meeting, Pisa, Italy, September, 1965.

23. H. W. Hendel, T. Faith, "Electron Cyclotron Plasma Thrustor for Orbit Corrective Missions," AGARD Propulsion and Energetics Panel Meeting, Pisa, Italy, September, 1965.

24. D. B. Miller, "Microwave Powered Plasma Accelerators," AGARD Propulsion and Energetics Panel Meeting, Pisa, Italy, September, 1965.

25. C. G. Suits, The Collected Works of Irving Langmuir, Volumes III and IV, Pergamon Press, N. Y., 1961.

26. J. A. Stratton, Electromagnetic Theory, McGraw-Hill Book Co., New York, 1941, p. 328.

27. C. R. Mullin, E. D. Shane, "Comment on Microwave Reflection by Non-Uniform Plasmas with Exponential Electron Distribution," Proc. IEEE, 52, 1272, 1964.

28. K. T. Yen, "Microwave Reflection by Non-Uniform Plasmas with Exponential Electron Distribution," J. App. Phys. 35, 290, 1964.

29. L. Spitzer, Jr., Physics of Fully Ionized Gases, Interscience Publishers, New York, 1956.

30. E. C. Jordan, Electromagnetic Waves and Radiating Systems, Prentice-Hall Inc., Englewood Chffs., N. J., 1950, pp. 282-287.

31. Montgomery & Tidman, Plasma Kinetic Theory, McGraw-Hill, 1954 p. 56 equation (5. 23).

32. Muskhelishvili, N. I., "Singular Integral Equations," Erven P. Noordhoff, N. V. Groningen, Netherlands, 1953. (Rigorous treatment referred to by Montgomery and Tidman).

33. N. Irving Sax, Dangerous Properties of Industrial Materials, Reinhold Publishing Co. N. Y., 1963.

DISTRIBUTION LIST FOR SUMMARY REPORT

CONTRACT NAS 3-6266

	Addressee	Number of Copies
1.	NASA Headquarters FOB-10B 600 Independence Avenue, N. E. Washington, D C	
	Attn: RNT/J. Lazar	2
	RNT/J Mullin	1
	RRP/Dr K. H. Thom	1
2.	NASA-Marshall Space Flight Center Huntsville, Alabama	
	Attn: E. Stuhlinger	1
3.	Commander Aeronautical Systems Division Wright-Patterson AFB, Ohio	
	Attn: ASRMPE/R. River	1
4	NASA-Lewis Research Center 21000 Brookpark Road Cleveland, Ohio 44135 Attn: Electromagnetic Propulsion Division	
	G. Seikel	1
	W. Moeckel	1
	Attn: Spacecraft Technology Division	
	J. H. Childs	2
	Dr. H G Kosmahl	6
	Attn: Library	2
	Attn: Reports Control Office	1
	Attn: Spacecraft Technology Procurement Section	
	John H. DeFord	1
	Attn: Technology Utilization Office	
	John Weber	1
5	General Dynamics/Astronautics P O Box 1128 San Diego, California 92112	
	Attn: Dr. A. Larsen	1
6	General Electric Company Valley Forge Space Technology Center P. O. Box 8555 Philadelphia 1, Pennsylvania	
	Attn: Dr. P. Gloersen	1

Addressee	Number of Copies
7. Electro-Optical Systems, Inc. 125 North Vinedo Avenue Pasadena, California Attn: Dr. Gordon Cann	1
8. AVCO-Everett Research Laboratory A Division of AVCO Corporation 2385 Revere Beach Parkway Everett 49, Massachusetts Attn: Dr. S. Janes	1
9. Allison Division General Motors Corporation Indianapolis, Indiana Attn: Mr. T. Rosebrock	1
10. Litton Industries Beverly Hills, California Attn: Dr. A. Penfold	1
11. Research Division American Radiator and Standard Corp. P. O. Box 2003 New Brunswick, New Jersey Attn: Mr. E. C. Okress	1
12. TRW Space Technology Laboratories Thompson Ramo Wooldridge, Inc. One Space Park Redondo Beach, California Attn: Mr. C. L. Dailey	1
13. Massachusetts Institute of Technology Cambridge 39, Massachusetts Attn: Dr. E. Covert	1
14. AFWL WLPC/Capt. C. F. Ellis Kirtland Air Force, New Mexico	1
15. NASA Scientific and Technical Information Facility P. O. Box 33 College Park, Maryland 20740 Attn: NASA Representative RQT-2448	6

	Addressee	Number of Copies
16.	Aerospace Corporation P. O. Box 95085 Los Angeles, California 90045 Attn: Library Technical Documents Group	1
17.	Westinghouse Astronuclear Laboratories Pittsburgh 34, Pennsylvania Attn: H. W. Szymanowski, Mgr. Electrical Propulsion Laboratory	1
18.	Radio Corporation of America Astro Electrical Division Princeton, New Jersey Attn: Dr. W. H. Hendel	1
19.	General Technology Corporation 3510 Torrance Boulevard Torrance, California Attn: Dr. S. Ridgeway	1
20.	Republic Aviation Farmingdale, Long Island, New York 11735 Attn: Mr. A. Kunen	1
21.	United States Atomic Energy Commission Division of Technical Information Extension Oak Ridge, Tennessee	1
22.	Case Institute of Technology Engineering Division University Circle Cleveland, Ohio 44106 Attn: Dr. Eli Reshotko	1

ERRATA

NASA CONTRACTOR REPORT CR-54756

INVESTIGATION OF PLASMA ACCELERATOR
(CYCLOTRON RESONANCE PROPULSION SYSTEM)

by D. B. Miller, G. W. Bethke, and G. F. Crimi

General Electric

This subject report was incorrectly numbered as NASA CR-54746. Please change this number to NASA CR-54756 on the cover and title page.